TEL AVIV UNIVERSITY אוניברסיטת תל-אביב

High-Momentum Nucleons in Nuclei

Thesis submitted towards the degree of
Doctor of Philosophy

By

Or Hen

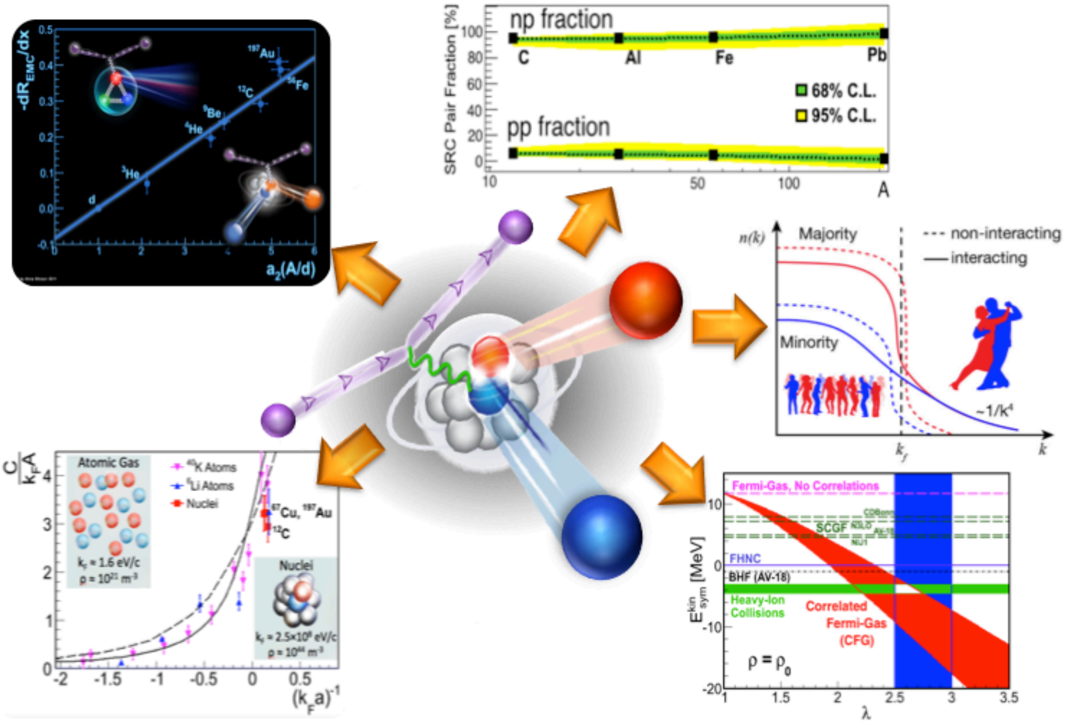

Submitted To The Senate of Tel-Aviv University
November 2015

This work was carried out under the supervision of
Professor Eli Piasetzky

Dedicated with love to Matty, my wife and best friend,
whose constant support, understanding, and endless
patience made this work possible.

Abstract

Nucleons at short distance experience a very strong short-range interaction, generating an extremely high-momentum tail to the nuclear wavefunction. The latter extends far beyond the Fermi momentum, k_F, of the nucleus. The creation of such a high-momentum tail, due to a strong short-range interaction, is a universal feature of two-component Fermi systems. As nucleons are composite objects, their internal structure may well be modified when the distance between them is smaller than their radii and there is a substantial overlap between their quark distributions.

While studied theoretically for many years, it is only recently, with the development of high-energy high-luminosity electron and proton accelerators, that experiments were able to start resolving this short-distance, high-momentum, structure of nuclei. Results from such experiments are revolutionizing our understanding of nuclei and the role played by Short-Range Correlated (SRC) nucleon pairs in various nuclear systems and astrophysical processes.

This work focuses on studies of SRC pairs in heavy atomic nuclei. It consists of two main parts: (1) *experimental* study of SRC pairs in medium and heavy nuclei and (2) *phenomenological* study of the effect of SRC on Deep Inelastic Scattering (DIS), Nuclei, Nuclear Matter, Neutron Stars, and on contact interactions in strongly interacting Fermi systems.

The experimental part of this thesis reports results from measurements of one- and two-proton knockout, $A(e,e'p)$ and $A(e,e'pp)$, from ^{12}C, ^{27}Al, ^{56}Fe, and ^{208}Pb using the CEBAF Large Acceptance Spectrometer (CLAS) at the Thomas Jefferson National Accelerator Facility (TJNAF). The measurements were performed at kinematics dominated by scattering off SRC pairs (Bjorken scaling variable $x_B > 1.2$, large momentum transfer squared $1.5 < Q^2 < 3.5$ $(GeV/c)^2$ and missing momentum $|P_{miss}| > 300$ MeV/c). The results of these measurements include the first direct identification of SRC pairs in nuclei heavier than ^{12}C, the extraction of the relative number of proton-proton to proton-neutron pairs in the measured nuclei, and a study of the nuclear transparency of proton knockout in the hard-breakup of SRC pairs.

The phenomenological part deals with the implications of the experimental results on a wide range of systems. It includes the correlation between the amount of SRC pairs in nuclei and the strength of the EMC effect (ratio of the inelastic structure function of nucleons bound in nuclei to deuteron) in different nuclei and the extraction of the IMC effect (ratio of the inelastic structure function of nucleons bound in deuterium to a *free* proton-neutron pair). The IMC was used to extract the free-neutron structure function which in turn improved our knowledge of the large-x d/u ratio of the proton. Data on the number of SRC pairs as a function of nuclear mass A allow us to extract the quantum numbers of mean-field nucleons subject to correlations. In addition, we study the effect of SRC pairs on the kinetic energy of symmetric nuclear matter, the nuclear symmetry energy, and the neutron star equation of state. Lastly, the possible universality of contact interactions in strongly interacting Fermi systems is

discussed in the case of SRC in nuclei.

The results presented in this work have wide ranging implications on our understanding of the structure and energy sharing mechanisms in heavy imbalanced nuclear systems and also inspired the development of three new follow-up experiments recently approved to run at TJNAF after its 12 GeV upgrade.

Acknowledgements

The work presented in this dissertation is by far the most challenging and satisfying scientific venture of my life to date. Many people contributed to this experience, and I apologize to the friends I failed to mention here.

First and foremost, my deepest gratitude and appreciation is given to my advisor, Eli Piasetzky, for making this experience so enjoyable. He has the rare ability to make any student feel like a colleague from day one. His insightful questions and crazy ideas have been a constant source of inspiration. I can only strive to be able someday to encourage young minds the way he does.

To my non-official-co-advisor, Larry Weinstein, for always being available to explore new results together and discuss their implications. For teaching me how to write in ‘proper English’ and make human-readable presentations and, along with Eli, for showing me how to handle science politics.

To Shalev Gilad, for sharing his careful and unique approach to experimental findings and what we can learn from them. For always questioning what we see and making sure we stay on solid grounds. His vast experience taught me a lot and for that I am grateful.

To my friends from the Theory Department, Jerry Miller, Jan Ryckebusch, Mark Strikman, Leonid Frankfurt, Misak Sargsian, Wim Cosyn, Bao-An Li, Wally Melnitchouk, Alberto Accardi, and Ciofi Degli Atti, for sharing with me their (sometime wildly) different views of nuclear and partonic dynamics, taking the time to teach me what I needed to learn, and always being open to discuss and develop new ideas together.

To Arie and Sharon Beck for showing me the beauty of low-energy tabletop experiments. For pushing me to master Geant4 simulations, exposing me to the unique use of nuclear probes in solid-state research, and for always being there with good advice and insightful ideas.

To my many collaborators and friends from the staff and users community of Jefferson Lab. In particular to Doug Higinbotham, Brad Sawatzky and Steve Wood, for teaching me what lab life is like, how to build detectors, set up electronics and data acquisition systems, run high-level experiments and constantly develop new ones. To Eileen Wood for all the Korean lunches, house parties, and making New-Port News feel like home. To Will Brooks and Hayk Hakobyan, for accepting a Hall-B ‘newbie’ to the EG2 analysis team and taking the time to teach me about the CLAS spectrometer and its ever changing, *non-compiling*, analysis software ☺. And to the members of my never-ending CLAS analysis-review committee, Stepan Stepanyan, Dan Watts and Lamiaa El Fassi, for putting up with endless iterations and constantly changing analysis notes. Your careful review of my work and deep, insightful comments tremendously improved the quality of my analysis.

To my fellow students and friends from Tel-Aviv University and Jefferson Lab, Igor Korover, Israel Yaron, Erez Cohen, Meytal Duer, Michael Braverman, Navaphon (Tai) Muangma, Taisiya Mineeva, Nicholas Zachariou, and

Daria Sokhan, for their help along the way, for enlightening discussions and for making sure there will always be plenty of beer around.

Last, but certainly not least, to my dear family and friends, for accepting with full understanding the frequent travels, late night Skype conference calls and long hours on weekends and holidays. Without your support and understanding this work would not amount to what it is.

Outline

Notations and Conventions

2N-SRC	Two-Nucleon Short-Range Correlations
3N-SRC	Three-Nucleon Short-Range Correlations
A	Mass number of a nucleus (#protons + #neutrons)
BNL	Brookhaven National Laboratory
CC	Cherenkov Counters
CEBAF	Continuous Electron Beam Accelerator Facility
CERN	European Organization for Nuclear Research
CFG	Correlated Fermi-Gas
CLAS	CEBAF Large Acceptance Spectrometer
CM	Center of Mass
DC	Drift Chambers
DIS	Deep Inelastic Scattering
DWIA	Distorted Wave Impulse Approximation
EC	Electromagnetic Calorimeter
EMC	European Muon Collaboration
EOS	Equation of State
FFG	Free Fermi-Gas
FG	Fermi-Gas
FSI	Final State Interactions
HIC	Heavy Ion Collisions
IA	Impulse Approximation
IC	Isobar Currents
JLab	Thomas Jefferson Laboratory
k_F	Fermi momentum
MEC	Meson Exchange Currents
MF	Mean-Field
N	Number of neutrons in a nucleus
NS	Neutron Star
PDF	Parton Distribution Function
PID	Particle Identification
PMT	Photo Multiplier Tube

PNM	Pure Neutron Matter
PWIA	Plain Wave Impulse Approximation
Q^2	Minus four-momentum transfer squared
SCE	Single Charge Exchange
SLAC	Stanford Linear Accelerator Center
SNM	Symmetry Nuclear Matter
SRC	Short-Range Correlations
TJNAF	Thomas Jefferson National Accelerator Facility
TOF	Time of Flight
VMC	Variational Monte Carlo
x_A	Bjorken-x scaling variable for a nucleus
x_B	Bjorken-x scaling variable for a proton
Z	Number of protons in a nucleus

1. Introduction

1.1. Short-Range Correlations in Nuclei: From Mean-Field to Many-Body Dynamics

> "*What holds the nucleons of the atom together? In the past quarter century physicists have devoted a huge amount of experimental and mental labor to this problem, probably more man hours than have been given to any other scientific question in the history of mankind*" (Hans Bethe, Scientific American 1953)

The atomic nucleus was first discovered in 1911, when Rutherford, Geiger, and Marsden scattered 'alpha particles' off a thin gold film and observed backward scattering, consistent with the existence of heavy point-like objects [1-4]. Several years later, in 1932, Chadwick discovered the neutron and the field of nuclear physics was born [5]. A main goal of nuclear physics research was, and still is, the understanding of the nature of the interactions between nucleons (nucleon-nucleon interaction) and how these interactions make up atomic nuclei and determine their properties.

From a theoretical point of view, neglecting possible contributions from non-nucleonic degrees of freedom, a full description of atomic-nuclei can be achieved by solving the many-body problem, defined by the Hamiltonian:
Eq. 1.1

$$H = T + \sum_{i<j}^{A} v_{2\text{body}}(i,j) + \sum_{i<j<k}^{A} v_{3\text{body}}(i,j,k) + \dots ,$$

where T is the kinetic energy term and $v_{2\text{body}}$ and $v_{3\text{body}}$ are the two and three nucleon potentials. The two-body potential is traditionally extracted from fits to phase-shifts extracted from nucleon-nucleon (NN) scattering measurements. The three-body potential is usually chosen such that a full calculation for light-nuclei will yield the experimentally-measured binding energies.

Using state-of-the-art Monte-Carlo techniques, one can now solve the many-body problem for systems containing up to 12 nucleons (i.e. up to ^{12}C) [6], and for infinite nuclear matter [7,8]. While these achievements are impressive, it is not clear that similar calculations for heavier nuclei will be feasible in the near future. In addition, the accuracy of these calculations is inherently limited by our knowledge of the input nuclear potentials.

For these and other reasons, effective nuclear theories are constantly being developed. From the commonly used Free Fermi Gas (FFG) model [9,10], through the highly successful nuclear shell model [11,12], to modern chiral expansion-based theories [13-16], effective theories are and have always been useful tools in nuclear physics research.

The nuclear shell model was the first successful effective description of atomic nuclei. Formulated in 1949 by M. Mayer and J. Jensen (1963 Nobel Prize), this model successfully predicts various low-energy, static properties of nuclei such as spins, parities, ground state energies, excitation spectra, and more. The model approximates the nucleus as a collection of independent nucleons, obeying the Pauli exclusion principle, moving under the influence of an attractive mean field created by all the other nucleons. Neutrons and protons are assumed to have independently-defined shell model states. Under this approximation, the nuclear Hamiltonian for protons and neutrons can be written as:

Eq. 1.2

$$H = \underbrace{T + \sum_{i=1}^{A} V_{\text{mean-field}}(i)}_{\equiv H_{\text{Shell-model}}} + \underbrace{\left[\sum_{i<j}^{A} v_{2\text{body}}(i,j) + \sum_{i<j<k}^{A} v_{3\text{body}}(i,j,k) + \ldots\right] - \sum_{i=1}^{A} V_{\text{mean-field}}(i)}_{\equiv H_{\text{Residual}}},$$

$$= H_{\text{Shell-model}} + H_{\text{Residual}}$$

where $V_{\text{mean-field}}$ is the effective mean-field term. In the mean-field approximation, the residual many-body interaction, H_{Residual}, is neglected. Neglecting H_{Residual} drastically simplifies the problem allowing, in certain cases, for analytical solutions.

The historical success of the nuclear shell model lays in its ability to predict many bulk properties of nuclei. Electron scattering proton knockout measurements A(e,e'p) in the early 1980s [17] showed that the energy and momentum distributions of bound protons matched shell model orbital predictions. However, the cross-sections for valence proton knockout turned out to be only about 60 to 70% of that expected for electron scattering from bound protons (see Fig. 1-1) [18]. These "spectroscopic factors" showed a consistent depletion in the shell occupancy over a wide range of light to heavy nuclei, indicating that only 60-70% of the nucleons in the nucleus can be described as independent particles moving in the mean-field of the nucleus. The remaining 30-40% has to be part of higher order configurations. As the mean-field approximation is a single-body approximation, the next logical step is to look for two-body correlations.

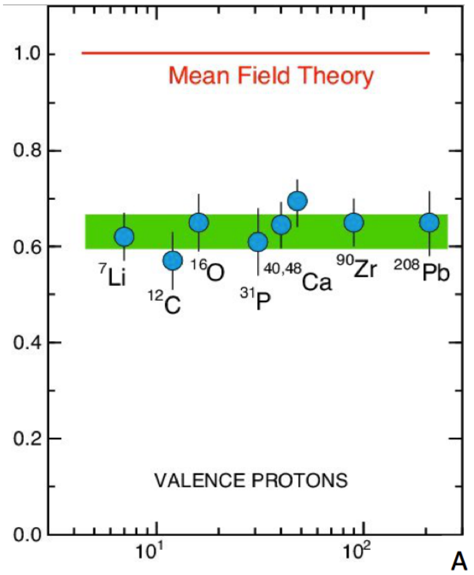

Fig 1-1: Spectroscopic factors for various nuclei, extracted by comparing A(e,e'p) valence knockout cross-sections to mean-field theory. See Ref. [18] for details.

Unlike the mean-field approximation, where effective average potentials can be used, two-body correlations depend directly on the details of the NN potential. Fig. 1-2 shows the radial dependence of the central part NN potential, extracted by three different groups, and, for one extraction, the contribution of different spin/isospin dependent interactions. While all extractions are experimentally valid (i.e., equally good fits ($\chi^2 \approx 1$) to the NN scattering phase shifts), considerable quantitative differences are evident. Currently, there are many commonly used NN potentials available, with numerous phase shift equivalent potentials [13-16,19-29].

One of the main differences among these NN potentials is their description of short distance behavior. This is due to the fact that potential descriptions of NN scattering data are far more complicated above the inelastic threshold (i.e., the pion production threshold). Thus NN potentials are typically fit to scattering data up to 350 MeV and are therefore not well constrained at short distances or high momentum. Despite this short distance uncertainty, Fig. 1-2 shows two short-range features common to all NN potentials: (1) a strong repulsive core at very short distances, and (2) overall dominance of the central part of the interaction, except for where it shifts from attractive to repulsive (at ~0.7 fm) and thus crosses zero. In this region, short-range spin/isospin dependent interactions dominate.

The repulsive core and the short-range spin/isospin dependent interactions are expected to create pairs of Short-Range Correlated (SRC) nucleons in the nuclear ground state: pairs of nucleons with high relative momentum and low center-of-mass momentum, where high and low are relative to the Fermi momentum of the nucleus (k_F ~ 250 MeV/c for medium and heavy nuclei). This definition implies that the interaction between the nucleons of the SRC pair is dominated by the short distance part of the NN interaction, and is therefore less sensitive to the many-body effects of the nuclear medium. Thus, SRC pairs can be thought of as naturally-occurring short range fluctuations in the ground state of the nucleus. By studying the abundance and detailed characteristics of SRC pairs, we can study the NN potential at short distances and its effect on the many-body nuclear medium.

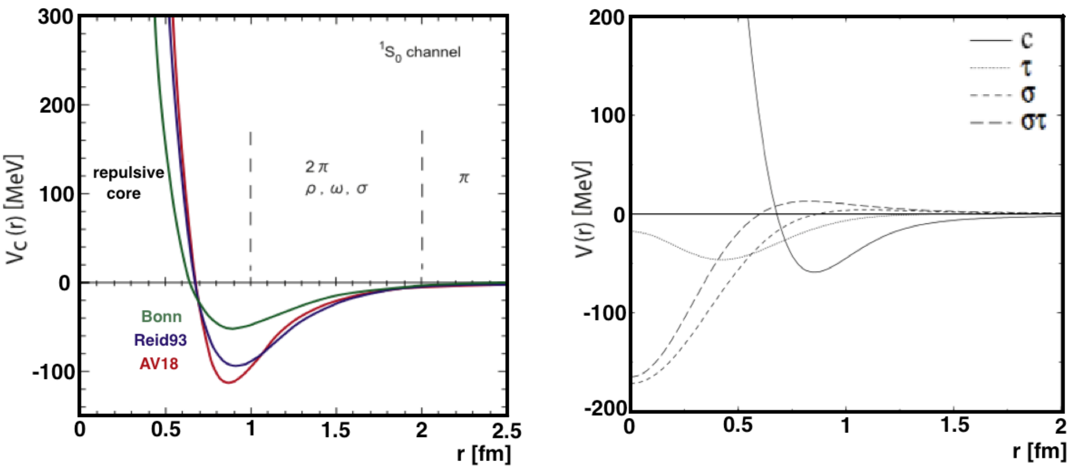

Fig 1-2: (left) The radial dependence of the central part of three different nucleon-nucleon potentials: RSC [26], Bonn [27,28], and AV18 [29]. (right) The central, isospin, spin, and spin-isospin components of the AV18 potential.

Experimental SRC studies were conducted at SLAC (Stanford Linear Accelerator Center), BNL (Brookhaven National Lab), and more recently at JLab (Thomas Jefferson Laboratory).

Inclusive electron scattering measurements, performed in kinematics corresponding to large four-momentum transfer, $Q^2 = \vec{q}^{\,2} - \omega^2 > 1.5$ GeV^2/c^2 [where $\vec{q}$ and ω are respectively the three-momentum and energy transferred to the nucleus], and Bjorken scaling parameter $x_B = Q^2/(2m_N \cdot \omega) > 1$ [where m_N is the nucleon mass] showed scaling of the cross-section ratio of nuclei relative to deuterium as a function of x_B for $1.5 < x_B < 2$. This scaling indicates that in all nuclei the nucleon momentum distribution above the Fermi level (i.e. $k > k_F$) has the same shape as in deuterium and that ~20% of the nucleons in medium and heavy nuclei have momentum greater than k_F [30-32].

Exclusive measurements of electron- and proton-induced two-nucleon knockout reactions, (e,e'pN) and (p,2pn), on ^{12}C and ^{4}He allowed the first direct observation of two-nucleon (2N) SRC pairs [33-37]. In these experiments, performed at high-duty cycle, high-energy, high intensity accelerators, high-energy electrons or protons scattered off a proton with large missing momentum, $|\vec{p}_{miss}| = |\vec{q} - \vec{p}_p| > 300$ MeV/c [where $\vec{p}_p$ is the measured knockout proton momentum], knocking it out of the nucleus, and looked for recoil nucleons emitted parallel to the missing momentum. They found that all high-momentum protons in the nucleus had a correlated nucleon partner, i.e. originated from 2N-SRC pairs [16]. They found that this correlated partner was almost always a neutron, showing the dominance of neutron-proton (np) pairs [34,36,37]. Additional analysis allowed reconstructing the pair in the ground state of the nucleus and studying their characteristics (see section 1.3 for further details).

The observed np-SRC dominance came as a surprise and highlighted the important role played by the tensor part of the NN interaction at short distances [38-40]. The tensor interaction acts only on NN pairs in spin (S) isospin (T) states ST = 11 and 10. In light nuclei it is difficult to create odd-*l* pairs, therefore tensor interactions can only act on np pairs in a *l*=0 ST=10 state. However, in heavy nuclei one can create odd-*l* pairs, giving rise to the appearance of ST = 11 proton-proton and neutron-neutron pairs, washing out the expected np-SRC dominance. Therefore, the isospin structure of 2N-SRC pairs in heavy nuclei is an open question with direct implications for the effect of correlations on massive nuclear systems such as neutron stars [41,42].

1.2. Scope of This Work

This work presents a study of 2N-SRC pairs in medium and heavy nuclei (^{12}C, ^{27}Al, ^{56}Fe, and ^{208}Pb), and their effect on various aspects of Deep Inelastic Scattering (DIS), nuclei, nuclear matter, neutron stars and contact interactions in strongly interacting Fermi systems. This dissertation is based on a collection of papers published in peer-reviewed journals and is structured as follows:

Chapter 1 is the introduction. It presents the motivation for studying 2N-SRC as part of the quest to understand many-body effects in the nuclear medium (section 1.1), followed by a review paper that provide a more detailed introduction to this work (section 1.3). In-between, we present the scope and layout of this dissertation (section 1.2).

The review paper reviews previous theoretical and experimental studies of SRC pairs in nuclei, deep-inelastic structure of bound nucleons (i.e. the EMC effect), and the connection between the two. It also includes a new analysis of the EMC effect in terms of the Bjorken scaling variable for nuclei, x_A, and a theoretical test of the ability to explain the EMC effect, using global modification of mean-field / SRC nucleons in nuclei.

Chapter 2 contains information on the experimental setup and analysis methods used in the study of the A(e,e'p) and A(e,e'pp) reactions in medium and heavy nuclei (^{12}C, ^{27}Al, ^{56}Fe, and ^{208}Pb). The data used in the analysis were taken from the EG2 experiment that ran in 2004 at Hall B of Jefferson-Lab using the CLAS spectrometer. The analysis is focused on kinematics that is dominated by scattering off SRC pairs and was done as part of the JLab data mining initiative [43].

This chapter was previously published as the supplementary materials of Hen et al. (CLAS Collaboration), Science **346**, 614 (2014).

Chapter 3 presents the results from the analysis described in chapter 2. These results include: (1) measurements of A(e,e'p)/^{12}C(e,e'p) cross-section ratios for the extraction of nuclear transparency ratios for protons knockout off a SRC pair, and (2) measurements of A(e,e'pp)/^{12}C(e,e'pp) cross-section ratios for the extraction of the relative number of proton-proton to proton-neutron SRC pairs.

Chapter 4 discusses the implications of SRC on different topics in Deep Inelastic Scattering (DIS), nuclei, nuclear matter, neutron stars and contact interactions in strongly interacting Fermi systems. Special emphasis is put on the specific implications of the observation that even in heavy, asymmetric nuclei, SRC pairs are predominantly neutron-proton (np) pairs (see chapter 3.1).

Chapter 5 presents a summary of the work and its main conclusions.

Appendix A contains a new database of EMC measurements, extracted using the Bjorken scaling variable for nuclei, x_A. This appendix is part of the publication presented in section 1.3.

Appendix B contains a short description of three future experiments, developed as part of this work, that will study the dependence of the proton and neutron inelastic structure function on its virtuality, and the energy-sharing between protons and neutrons in the A=3 system. These experiments were all approved by the Program Advisory Committee (PAC) of Jefferson Lab and are expected to run in the coming years as part of the 12 GeV program of JLab.

Appendix C contains a paper discussing the new insight gained into the origin of the EMC by the observation of the EMC/SRC correlation. This paper was the cover paper of the May-2013 edition of the CERN Courier magazine.

1.2. EMC and SRC Studies

“The EMC effect and High-Momentum Nucleons in Nuclei”
O. Hen et al., Int. J. Mod. Phys. E ***22****, 1330017 (2013).*

International Journal of Modern Physics E
Vol. 22, No. 7 (2013) 1330017 (30 pages)

DOI: 10.1142/S0218301313300178

THE EMC EFFECT AND HIGH MOMENTUM NUCLEONS IN NUCLEI

OR HEN*
Tel Aviv University, Tel Aviv 69978, Israel
or.chen@mail.huji.ac.il

DOUGLAS W. HIGINBOTHAM
Thomas Jefferson National Accelerator Facility, Newport News, Virginia 23606, USA
doug@jlab.org

GERALD A. MILLER
Department of Physics, University of Washington, Seattle, WA 98195-1560, USA
miller@phys.washington.edu

ELI PIASETZKY
Tel Aviv University, Tel Aviv 69978, Israel
eip@tauphy.tau.ac.il

LAWRENCE B. WEINSTEIN
Old Dominion University, Norfolk, Virginia 23529, USA
lweinste@odu.edu

Received 2 May 2013
Accepted 8 May 2013
Published 5 July 2013

Recent developments in understanding the influence of the nucleus on deep-inelastic structure functions, the EMC effect, are reviewed. A new data base which expresses ratios of structure functions in terms of the Bjorken variable $x_A = AQ^2/(2M_A q_0)$ is presented. Information about two-nucleon short-range correlations (SRC) from experiments is also discussed and the remarkable linear relation between SRC and the EMC effect is reviewed. A convolution model that relates the underlying source of the EMC effect to modification of either the mean-field nucleons or SRC nucleons is presented. It is shown that both approaches are equally successful in describing the current EMC data.

Keywords: EMC; SRC; 2N-SRC; high momentum nucleons.

1. Introduction

Basic models of nuclear physics describe the nucleus as a collection of free nucleons moving nonrelativistically under the influence of the sum of two-nucleon forces,

---

*Corresponding author.

which can be treated approximately as a mean field. In this picture, in the rest frame of the nucleon, the partonic structure functions of bound and free nucleons should be identical. Therefore, it was generally expected that, except for nucleon Fermi motion effects, Deep Inelastic Scattering (DIS) experiments which are sensitive to the partonic structure function of the nucleon would give the same result for all nuclei.

Instead, the measurements show a reduction in the structure function of nucleons bound in nuclei relative to nucleons bound in deuterium — the EMC effect. Since its discovery, over 30 years ago, a large experimental and theoretical effort has been put into understanding the origin of the effect. While theorists have had no difficulty in creating models that qualitatively reproduce nuclear DIS data by itself, there is no generally accepted model. This is because the models are either not consistent with or do not attempt to explain other nuclear phenomena. The use of most modern models shows that while traditional nuclear effects such as binding and Fermi motion contribute to the EMC effect, modification of the bound nucleon structure is also required.

Studies of the effects of the many-body nucleon–nucleon interaction on the structure of the nucleus predict the existence of Short-Range Correlated (SRC) pairs. These are pairs of nucleons at short distance whose wave functions strongly overlap, giving them large relative momentum and low center of mass (CM) momentum, where high and low is relative to the Fermi momentum (k_F) of the nucleus. Recent studies show that the magnitude of the EMC effect in any nucleus is linearly related to the number of two-nucleon SRC pairs in that nucleus. The observation of this phenomenological relationship raises a question of whether the medium modification of the nucleon structure is related to the nuclear mean field or to the SRC pairs. The answer to this question will give new insight regarding the origin of the EMC effect.

Sections 2 and 3 review the EMC and SRC research history, respectively. Section 2.3 presents a new formalism to correct the measured EMC data for the difference in the definition of the Bjorken scaling variable for different nuclei (the corrected EMC data is presented in Appendix A). Section 4 presents the EMC–SRC correlation, its implications, and a simple convolution model which compares treatments of the EMC effect based on nucleon modification occurring in SRC pairs with that based on nucleon modification occurring due to the mean field. Section 5 summarizes the paper.

2. The Nuclear EMC Effect

2.1. *Historical overview*

Unpolarized inclusive lepton scattering depends on two independent variables that can be chosen as the negative of the square of the transferred four-momentum, $Q^2 = -q^2$ and the Bjorken scaling variable for a proton $x_p = Q^2/(2m_p\omega)$, — commonly noted as x_B — where m_p is the proton mass and ω the transferred energy in the proton rest frame. In DIS, the momentum transfer is large ($Q^2 > 2$ (GeV/c)^2) and the invariant mass of the transferred photon plus the target nucleon is greater than the masses of individual nucleon resonances, $W > 2$ GeV. This allows a measurement of the proton's inelastic structure function, $F_2^p(x_p, Q^2)$, which gives the weighted average of the proton quark distribution function:

$$F_2^p(x_p, Q^2) = x_p \sum_q e_q^2 \cdot (q^p(x_p) + \bar{q}^p(x_p)) \,, \tag{1}$$

where $q^p(x_p)$ and $\bar{q}^p(x_p)$ are the proton's quark and anti-quark distribution, functions, respectively, e_q is the electric charge of the quark, and the sum runs over q — the different proton quark flavors (i.e., u, d and s). The neutron inelastic structure function, $F_2^n(x_p, Q^2)$, is given by substituting in Eq. (1) the proton quark distributions by that of the neutron. The latter can be expressed using the proton distribution, assuming isospin (charge) symmetry (i.e., $u^n(x_p) = d^p(x_p)$, $d^n(x_p) = u^p(x_p)$ etc.).

In the early 1980s, CERN's European Muon Collaboration (EMC) measured the per-nucleon DIS cross-section for scattering unpolarized muons from deuterium and iron nuclei and extracted the ratio of their structure functions[1] (i.e., $F_2^{\mathrm{Fe}}(x_p, Q^2)/F_2^d(x_p, Q^2)$). The latter are the average *bound* nucleon structure function in ^{56}Fe and Deuterium. For $x_p \leq 0.5 \sim 0.7$, where nucleon Fermi motion effects are negligible, they expected to measure a ratio of unity, indicating that the structure function of deeply bound (i.e., ^{56}Fe) and loosely bound (i.e., Deuterium) nucleons is identical. This would allow them to increase the experimental luminosity by using a denser target material such as iron, while still being sensitive to the free nucleon structure function. Instead, they discovered that the per-nucleon DIS cross-section ratio, which equals the structure function ratio, decreased from about 1 at $x_p \approx 0.3$ to as little as 0.8 at $x_p \approx 0.7$ (see Fig. 1). This unexpected result instantly became known as the EMC effect. The existence of the EMC effect was soon verified by analysis of existing target end-cap data from Stanford Linear Accelerator Center (SLAC),[2,3] and later by measurements at SLAC[4] and the BCDMS and NMC collaborations.[5–7]

A later experiment performed at SLAC showed that the EMC effect has the same qualitative behavior for all nuclei, differing only in the value of the ratio at the minimum.[8] It also showed that the EMC effect is independent of Q^2 for $2 \leq Q^2 \leq 40$ (GeV/c)^2 and that the depth of the minimum at $x_p \approx 0.7$ grows with nuclear mass. The growth seemed to increase with the average nuclear density[8] and this became a generally accepted feature of the EMC effect (see Ref. 9 and references therein).

As theorists provided several different, simple, explanations of the effect (see discussion in Sec. 2.2), an independent experimental test of these explanations was needed.[10] This came from Fermi National Accelerator Lab in the form of Drell–Yan measurements.[11] These experiments compared μ^+–μ^- production from q–$\bar{q}$ annihilation in proton–proton and proton–nucleus collisions. In the kinematic range

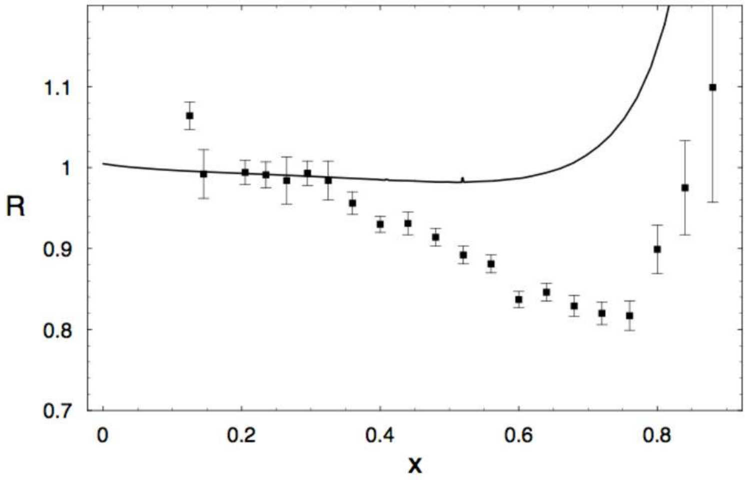

Fig. 1. Measurements of DIS cross-section ratio of gold relative to deuterium as a function of Bjorken-x_p from SLAC. The solid black line is the expected ratio taking into account only Fermi motion of nucleons in Gold. (Figure reprinted from Ref. 14. Copyright (2002) by the American Physical Society.)

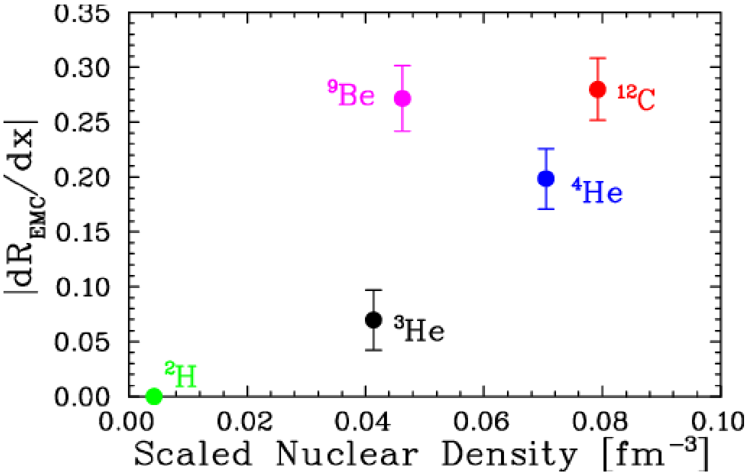

Fig. 2. The strength of the EMC effect, defined as the slope of the per nucleon DIS cross-section ratio for $0.3 \leq x \leq 0.7$, shown as a function of the scaled nuclear density for light nuclei. (Figure reprinted from Ref. 12. Copyright (2009) by the American Physical Society.)

covered by the measurement, they observed that the nuclear to proton ratio was consistent with unity. As this experiment was sensitive mainly to the nuclear sea quarks, the result pointed to the EMC effect being due to a change in the valence quark distributions.

It was not until 2009 that the simple nuclear density dependence of the EMC effect was challenged with new data.[12] A high precision measurement on light nuclei, including ^{3}He, ^{4}He, ^{9}Be and ^{12}C, showed that the effect was not related to the average nuclear density. The most significant outlier was ^{9}Be which has a low average nuclear density, similar to that of ^{3}He, and a large EMC effect, similar to that of ^{4}He and ^{12}C (see Fig. 2). This anomaly was consistent with variational Monte Carlo calculations which show that local, high density configurations occur in nuclei.[13] These calculations describe ^{9}Be as a collection of two alpha clusters and an orbiting neutron. In this picture, ^{9}Be has a low average density and a much higher local density similar to that of ^{4}He. Thus, the phenomenological explanation of the EMC effect shifted, based on the new data, from an average density effect to a local density effect.

2.2. *Theory status*

In QCD, the nucleon structure function, $F_2(x, Q^2)$, gives the weighted probability for finding a parton (quark) in the nucleon that carries a fraction x of the total nucleon momentum. The different partons contribute with a weight equal to the square of their electric charge. The primary theory interpretation of the reduction of the nuclear structure function in the valence quark region was simple.[9,15–19] Quarks in nuclei carry less momentum than quarks in nucleons and, as the uncertainty principle implies, move throughout a larger confinement volume. This notion gave rise to a host of models: bound nucleons are larger than free ones; quarks in nuclei move in 6-quark or 9-quark or even $3A$ quark bags.[20–22] But more conventional explanations such as the influence of nuclear binding or enhancement of pion cloud effects were successful in reproducing some of the nuclear DIS data.[23–27] And one could combine various different models.[10,28] This led to a plethora of models that reproduced the data, causing one of the present authors to write that EMC means Everyone's Model is Cool.[29] It is interesting to note that none of the earliest models were concerned with the role of two nucleon correlations, except as relating to 6-quark bags.

The initial excitement tapered off as nuclear DIS became more understood, the experimental data became more precise, and the need to include the effects of nuclear shadowing was acknowledged.[30] Indeed some of the more extreme models were ruled out by a failure to match well-known nuclear phenomenology. Moreover, inconsistency with the baryon and momentum sum rules led to the downfall of many models.[31] Some models predicted an enhanced nuclear sea, but others did not. As results from Drell–Yan measurements were published, none of the existing models survived the challenge of providing an accurate description of both the EMC and Drell–Yan data sets — a challenge that remains to this day.

It is now understood that conventional nuclear binding effects can account for the EMC effect up to values of $x_p \approx 0.5$ or so[14,32–35] but fail at larger values. Therefore, the effects of the nuclear modification of the nucleon structure function must be included. Currently viable models of nucleon modification include (a) the quark meson coupling model in which quarks in nucleons (either bags or eigenstates of the NJL model)[36,37] exchange mesons with quarks in other nucleons, (b) the chiral quark soliton model in which quarks in nucleons also exchange mesons with other nucleons,[38] and (c) the suppression of point-like-configurations of the nucleon by the nuclear medium.[39,40] A successful phenomenology that includes the effects of shadowing, binding, pion enhancement and a medium-modification of the quark structure function can be fitted to the extant data.[41]

A modern model which incorporates the influence of nucleon–nucleon correlations in a manner consistent with nuclear physics knowledge to describe both nuclear DIS and Drell–Yan data does not yet exist.

2.3. *EMC data analysis*

Following the EMC collaboration, other experiments measured the ratios of per-nucleon DIS cross-sections for nuclei and the deuteron at equal values of Q^2 and $x_p = Q^2/2m_p\omega$. In these kinematical conditions, the DIS cross-section ratio for nuclei A_1 and A_2 is given by[42]

$$\frac{\sigma_{A_1}}{\sigma_{A_2}} = \frac{F_2^{A_1}(x_p, Q^2)}{F_2^{A_2}(x_p, Q^2)} \cdot \frac{\left[1 + 2\dfrac{1+\omega^2/Q^2}{R_{A_1}-1}\tan^2\dfrac{\theta}{2}\right]}{\left[1 + 2\dfrac{1+\omega^2/Q^2}{R_{A_2}-1}\tan^2\dfrac{\theta}{2}\right]}\,, \tag{2}$$

where θ is the lepton scattering angle and $R_A = \sigma_L^A/\sigma_T^A$ is the ratio of the longitudinal to transverse cross-section for nucleus A. Assuming R_A independent of A, the cross-section ratio of Eq. (2) is reduced to the F_2 structure function ratio.

Recently, Frankfurt and Strikman (FS) pointed out that the structure functions of nucleons bound in nuclei should be extracted in the reference frame of the nucleus.[34] This is done by using the x_A scaling variable, defined as

$$x_A = \frac{Q^2}{2q \cdot P_A/A} = \frac{AQ^2}{2\omega m_A} = x_p \cdot \frac{Am_p}{m_A}\,, \tag{3}$$

where q and P_A are the four-momentum vectors of the virtual photon and target nucleus respectively, and m_A is the mass of the target nucleus. Note that, for the same values of Q^2 and ω, x_A differs from x_p by the ratio of the bound nucleon mass to the free mass. Therefore, a cross-section measured at Q^2 and ω on nucleus A will depend on the nucleon structure function evaluated at x_A rather than at x_p.

This means that the standard EMC cross-section ratio at the same Q^2 and ω (and hence the same x_p) is actually proportional to the nucleon structure function in nucleus A evaluated at parton momentum fraction $x_A = AQ^2/2m_A\omega$ divided by the nucleon structure function in deuterium evaluated at parton momentum fraction $x_d = 2Q^2/2m_d\omega$. For symmetric nuclei this is

$$\frac{2}{A}\frac{\sigma^A_{\text{DIS}}(x_p, Q^2)}{\sigma^d_{\text{DIS}}(x_p, Q^2)} = \frac{F_2^A(x_A, Q^2)}{F_2^d(x_d, Q^2)}\,, \tag{4}$$

where $\frac{\sigma^A_{\text{DIS}}}{\sigma^d_{\text{DIS}}}$ is the DIS cross-section ratio measured at the same (Q^2, ω, x_p), and $\frac{F_2^A(x_A,Q^2)}{F_2^d(x_d,Q^2)}$ is the ratio of structure functions at the same (Q^2, ω) but different x.

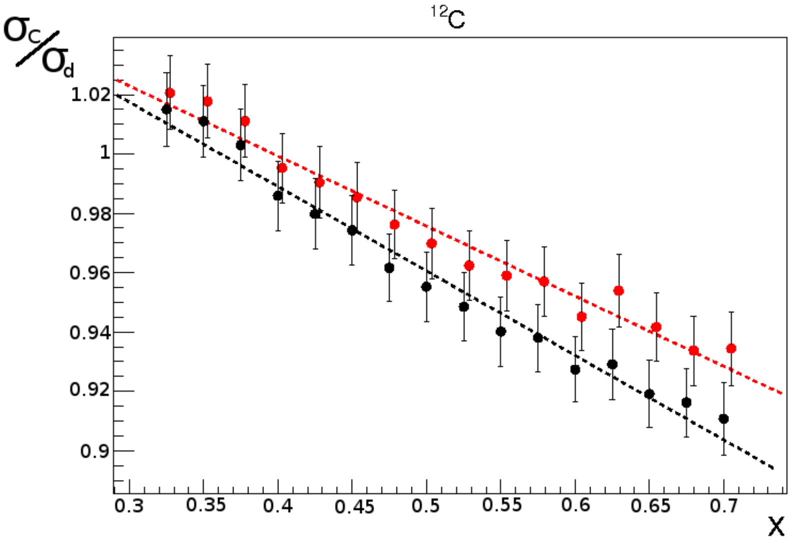

Fig. 3. (Color online) Example of the effect of the x_A correction to the data. The black points are the original Seely data plotted as a function of x_p. The red points are the corrected data, plotted as a function of x_A. Dashed lines are linear fits to the two data sets. The difference between the slope of the two fits is about 20%.

Since we want to compare the structure functions at the same parton momentum fractions, we want to correct this using

$$\frac{F_2^A(x_A,Q^2)}{F_2^d(x_d,Q^2)} = \frac{F_2^A(x_A,Q^2)}{F_2^d(x_A,Q^2)} \cdot \frac{F_2^d(x_A,Q^2)}{F_2^d(x_d,Q^2)} \tag{5}$$

and

$$\frac{F_2^A(x_A,Q^2)}{F_2^d(x_A,Q^2)} = \frac{\sigma_{\rm DIS}^A(x_p,Q^2)}{\sigma_{\rm DIS}^d(x_p,Q^2)} \cdot \frac{F_2^d(x_d,Q^2)}{F_2^d(x_A,Q^2)}\,, \tag{6}$$

where $\frac{F_2^A(x_A,Q^2)}{F_2^d(x_A,Q^2)}$ is the ratio of structure functions in the different nuclei evaluated at the same parton momentum fraction (i.e., the quantity we wish to extract), and $\frac{F_2^d(x_A,Q^2)}{F_2^d(x_d,Q^2)}$ is a correction factor. This correction factor can be evaluated using well-known parametrizations of the deuteron structure function.[43,44]

Figure 3 shows the effect of the correction factor of Eq. (6) on the measured DIS cross-section ratio for ^{12}C relative to deuterium from recent Jefferson Lab measurements. As can be seen, the x_A correction reduces the size of the EMC effect (i.e., its slope). It replaces part of the model-dependent binding energy corrections with a systematic, transparent and model-independent correction.

For asymmetric nuclei ($N \neq Z$), following Aubert *et al.* and Bodek *et al.*,[1–3] an additional isoscalar correction factor ($R_{\rm ISO}$) is applied to the measured cross-section ratio, making it related to a hypothetical nucleus with equal number of protons and neutrons ($N = Z = A/2$):

$$\frac{\sigma_{\rm DIS}^A(x_A,Q^2)_{\rm ISO}}{\sigma_{\rm DIS}^d(x_A,Q^2)_{\rm ISO}} = \frac{\sigma_{\rm DIS}^A(x_A,Q^2)}{\sigma_{\rm DIS}^d(x_A,Q^2)} \cdot R_{\rm ISO}(x_A)\,, \tag{7}$$

with $R_{\rm ISO}(x_A)$ defined as:

$$R_{\rm ISO}(x_A) = \frac{A}{2}\frac{F_2^p(x_A,Q^2)+F_2^n(x_A,Q^2)}{Z\cdot F_2^p(x_A,Q^2)+N\cdot F_2^n(x_A,Q^2)} = \frac{A}{2}\frac{1+R_{np}(x_A,Q^2)}{Z+N\cdot R_{np}(x_A,Q^2)}\,, \tag{8}$$

where $F_2^p(x_A,Q^2)$ and $F_2^n(x_A,Q^2)$ are the free proton and neutron structure functions, and $R_{np}(x_A,Q^2) = F_2^n(x_A,Q^2)/F_2^p(x_A,Q^2)$. The free neutron structure function used in this correction is usually extracted from world data on DIS scattering off deuterium and the proton, corrected for the Fermi motion of protons and neutrons in deuterium (i.e., smearing effect), see Refs. 45 and 46 for details.

Using the isoscalar correction for asymmetric nuclei and the description of the measured cross-section ratios in terms of F_2^A and F_2^d (Eq. (5)), we extract the structure function ratio of nucleons bound in nuclei relative to deuterium as:

$$\begin{aligned}\frac{F_2^A(x_A,Q^2)}{F_2^d(x_A,Q^2)} &= \frac{2}{A}\frac{\sigma^A_{\rm DIS}(x_p,Q^2)}{\sigma^d_{\rm DIS}(x_p,Q^2)}\cdot\frac{F_2^d(x_d,Q^2)}{F_2^d(x_A,Q^2)}\cdot R_{\rm ISO}(x_A)\\ &= \frac{2}{A}\frac{\sigma^A_{\rm DIS}(x_p,Q^2)_{\rm ISO}}{\sigma^d_{\rm DIS}(x_p,Q^2)_{\rm ISO}}\cdot\frac{F_2^d(x_d,Q^2)}{F_2^d(x_A,Q^2)}\cdot\frac{R_{\rm ISO}(x_A)}{R_{\rm ISO}(x_p)}\,.\end{aligned} \tag{9}$$

Appendix A presents the EMC ratios, extracted as a function of x_A for $0.3 \lesssim x_A \lesssim 0.7$, for all nuclei measured at SLAC[12] and Jefferson Lab (JLab).[8] The isoscalar correction applied is identical for both data sets, making them more consistent.

3. High Momentum Nucleons in Nuclei

This section describes nucleon–nucleon (or "two-nucleon") correlations. A correlated two-nucleon pair is one where the two-nucleon density is significantly different from the product of two single-nucleon densities. Both tensor and central forces can produce SRC.

3.1. *Theoretical need for high momentum nucleons in nuclei*

The strong interactions between nucleons in nuclei are dominated by two and three nucleon terms. Therefore, the fact that nucleons in nuclei are correlated is self-evident. There is no fundamental one-body potential in the nucleus, unlike the one-body Coulomb potential in atomic physics. The fundamental question of nuclear physics was: how does the very successful shell model of the nucleus emerge in spite of the strong short-ranged interactions between nucleons? An answer was provided early on by Brueckner and Goldstone, see the review by Bethe.[47] The strong two-nucleon interactions encoded by the potential V, constructed to reproduce experimentally measured scattering observables and believed to include strong repulsion at short distance and attraction at longer ranges, are summed to form the T-matrix of scattering theory and the G-matrix for bound states. The operator G is obtained from T by modifying the propagator to include the effects of the

Pauli principle and to use the appropriate self-consistent (single) nucleon energies. The G-matrix is considerably weaker than V, and can therefore be used in perturbation theory. One forms the nuclear mean field U throughout the Hartree–Fock method employing the G-matrix, and the first approximation to the wave function is the anti-symmetrized product of single particle wave functions engendered by U. However, the complete nuclear wave function is obtained in a perturbative hole-line expansion that includes two-particle — two-hole excitations and other excitations which incorporate correlations. Later work formulated a relativistic version of Brueckner theory in which the Dirac equation replaces the Schrödinger equation.[48,49] There is also a light front version.[50,51]

The Brueckner theory approach described above presumes that the two-nucleon potential contains strong short-distance repulsion. Early attempts to construct soft potentials lacking the strong repulsion that also reproduce scattering data did not succeed in obtaining interactions that could be used perturbatively in the nuclear bound state problem.[47] In modern times, the use of effective field theory provides a low-energy version of QCD, guided by chiral symmetry, in which one obtains the potential as an expansion in powers of (Q/Λ_χ) where Q is a generic external momentum (nucleon momentum) and Λ_χ is the chiral symmetry breaking scale of about 1 GeV. See the review in Ref. 52. In such theories the short distance interaction can be treated as a contact interaction, modified by the inclusion of a cutoff, and the longer ranged interactions are accounted for by one and two pion exchange interactions. The softness (involving low-momentum) or hardness (involving higher momentum) of the potential is determined by the value of the cutoff. For sufficiently soft potentials nuclear matter can be treated using perturbation theory in terms of the two and three nucleon chiral interactions. Nevertheless, two-nucleon correlations occur, primarily as a result of the second iteration of the one pion exchange potential.

Another approach uses renormalization group methods to generate a soft NN potential from a hard interaction either by integrating out high momentum components (in the case of $V_{\text{low-}K}$), or by using the similarity renormalization group.[53] Then one obtains a potential that is mainly restricted to small values of momentum. This potential is perturbative in the sense that the Born series for scattering converges and perturbation theory can be applied to the nuclear bound state problem. However, once again the second-order term in the potential generates correlations.

The renormalization group can be used to eliminate matrix elements of the nucleon–nucleon potential connecting low and high relative momentum states. Such a procedure simplifies the computations of nuclear binding energies and spectra, and would also lead to wave functions without high-momentum components and truly SRCs. However, it would be necessary to consistently transform all other operators. For high-momentum transfer reactions, the renormalization group changes a known simple probe, described by a single-nucleon operator into a complicated probe describable by unknown (in practice) A-nucleon operators. This prevents the analysis of any high momentum transfer experiment.

To summarize, there are two basic approaches to fundamental nuclear structure — perturbation in the G-matrix or perturbation in the potential. In either case there will be two-nucleon correlations. Theoretically, the key remaining question concerns the quantity and range of the correlations.

3.2. *SRC measurements*

Experimentalists at electron scattering facilities such as SACLAY and NIKHEF observed the need for high momentum components in nuclei, not from direct observation, but rather from a dramatic lack of cross-section in $A(e, e'p)A$–1 valence shell knock-out experiments where the independent particle models overestimated the measured cross-sections.[54] Since the shell model accurately predicts energy levels and spins, this reduced the range of possible explanations. The most straightforward explanation was that the "missing nucleons" were in nucleon–nucleon correlations. When the electron scattered from a nucleon in a correlated pair, its partner was also ejected from the nucleus. This shifted strength from excitation energies typical of valence states to much higher excitation energies.

Many experiments were done at these facilities to probe for more direct evidence of correlations; but as history would show, the necessary kinematic requirements, $x_B > 1$ and $Q^2 > 1$ $(\mathrm{GeV}/c)^2$, were practically inaccessible. Thus most of the early experiments ended up being studies of reaction mechanisms such as meson-exchange currents (MECs) and final-state interactions.

With the availability of continuous, high intensity, high momentum proton and electron beams, identifying SRCs in Quasi-Elastic (QE) scattering off nuclei became feasible. In this section, we review results from measurements of inclusive QE (e, e') cross-section ratios and exclusive, triple-coincidence, $(e, e'pN)$ and $(p, 2pn)$, large momentum transfer (hard), reactions performed at SLAC, Brookhaven National Lab (BNL) and more recently at JLab.

3.2.1. *Inclusive SRC measurements*

In inclusive scattering of unpolarized particles from an unpolarized target, there are only two independent kinematical variables. In the case of inclusive QE electron scattering these are normally chosen to be Q^2 and x_p. In the Plain Wave Impulse Approximation (PWIA) it is assumed that the virtual photon is fully absorbed on a single nucleon, which leaves the nucleus without rescattering, leaving the remaining $A - 1$ nuclear system unperturbed. Energy and momentum conservation for such a reaction define a minimum value for the component of the initial momentum of the scattered nucleon in the direction of the virtual photon as a function of Q^2 and x_p.[55] At $x_p = 1$, for all Q^2 values, the minimum value of this momentum component equals zero. As one increases or decreases x_p at fixed Q^2, its value increases. At moderate values of Q^2 ($\sim 2 - 4$ GeV$/c^2$) and $x_p \geq 1.4 - 1.5$ ($\leq \sim 0.6$), this minimum value is larger than the Fermi momentum (k_F) of the nucleus, and the reaction is dominated by scattering from high momentum ($\geq k_F$) nucleons in the nucleus. At these Q^2 values and $x_p < 1$, the virtual photon carries a large amount of energy compared to its momentum and the reaction, while sensitive to high momentum nucleons, has large inelastic contributions from Δ production and MECs. On the other hand, for the same Q^2 values and $x_p > 1$, the virtual photon transfers a small amount of energy compared to its momentum, inelastic processes are suppressed, and the reaction is more directly sensitive to the nature of the high momentum tail of the nuclear wave function.[56,57] In both cases, large values of Q^2 suppress MEC contributions.[58,59]

Inclusive electron scattering cross-section ratios for nucleus A relative to deuterium and to ^{3}He were measured at SLAC and later at Hall-B and Hall-C of JLab.[55,60–62] Figure 4 shows the x_p dependence of the per nucleon cross-section ratio of nuclei relative to ^{3}He measured at Hall-B. As can be seen, for x_p values which correspond to scattering off high momentum ($\geq k_F$) nucleons in the nucleus (i.e., $1.5 \leq x_p \leq 2$ and $x_p \geq 2.25$) the cross-section ratio scales (i.e., does not depend on x_p). The contribution of Final State Interactions (FSI) to the measured

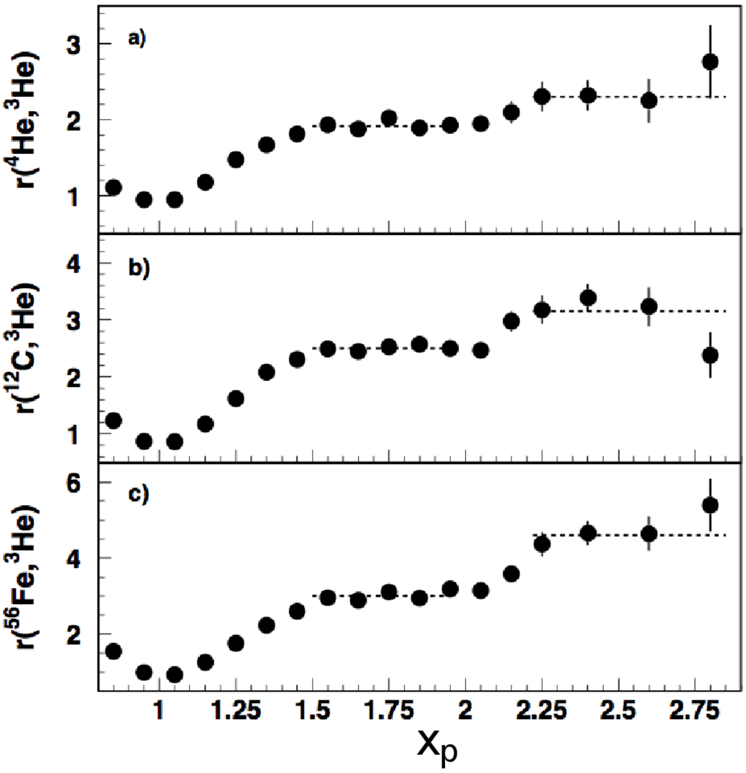

Fig. 4. Per nucleon QE inclusive (e, e') scattering cross-section ratios for nuclei relative to ^{3}He plotted as a function of x_p. Two plateaus are observed for $1.5 \leq x_p \leq 2$ and $x_p \geq 2.25$. The magnitude of these plateaus are labeled as a_2 and a_3, respectively. In the SRC model of the high momentum tail of the nuclear wave function, they are taken as a measure of the relative amount of 2N and 3N SRC pairs in the measured nuclei. See text for more details. (Figure reprinted from Ref. 61. Copyright (2006) by the American Physical Society.)

cross-sections are expected to rapidly decrease as a function of Q^2. Calculations of FSI in inclusive scattering at large Q^2 and $x_p \geq 1$ show they are largely confined to within the nucleons of the initial-state SRC pair.[56] The contribution of FSI of this kind will cancel in the cross-section ratio of two nuclei. This is supported by the small observed Q^2 dependence of the cross-section scaling plateau. This scaling reflects the scaling of the high momentum tail of the nuclear wave function and is usually interpreted using SRC model.[60,63] The latter states that the high momentum tail of the nuclear wave function is dominated by correlated, multi-nucleon, configurations. Due to their strong interaction at short distances, the structure of these configurations is independent of the surrounding nuclear environment, resulting in the same shape of the high momentum tail in all nuclei (i.e., scaling). Different nuclei have different amounts of SRC clusters. In this model, the observed scaling of the per-nucleon cross-section ratios for $1.5 \leq x_p \leq 2$ and $x_p \geq 2.25$ are indicative of scattering off two-nucleon (2N) and three-nucleon (3N) SRC configurations, respectively. The scaling factors, noted as a_2 and a_3 are then a measure of the relative amount of 2N and 3N SRC, respectively, in the measured nuclei.

3.2.2. *Exclusive* $(p, 2pn)$ *and* $(e, e'pN)$ *measurements*

Inclusive measurements alone do not prove that high momentum nucleons are a result of initial-state SRC pairs. To study the contribution of 2N-SRC pairs to the high momentum tail of the nuclear wave function exclusive two-nucleon-knockout experiments were done. The concept behind such experiments is that, in the PWIA, in the absence of FSI, when a nucleon that is part of a 2N-SRC pair is knocked out of the nucleus, in order to conserve momentum, its correlated partner nucleon has to recoil with momentum that is equal in size and opposite in direction to the initial momentum of the knocked-out nucleon. This back-to-back correlation between the initial momentum of the knocked-out nucleon and the momentum of the recoil nucleon, both above the Fermi sea level k_F, is a clear signature for scattering off a 2N-SRC configuration. Due to CM motion of the 2N-SRC pair with respect to the residual $A - 2$ nuclear system, this correlation will not be exactly back-to-back. The measured angular correlation can be used to extract the c.m. momentum distribution of the pair. If the 2N-SRC model is correct, the nucleons in the pair will have large relative momentum ($\geq k_F$) and small c.m. momentum ($\leq k_F$).

Two nucleon knockout experiments, measuring the $^{12}\mathrm{C}(p, 2pn)$ and $^{12}\mathrm{C}(e, e'pN)$ reactions, were done at BNL and JLab, respectively.[64–67] These experiments scattered protons and electrons off high initial momentum ($300 \leq P_{\text{initial}} \leq 600$ MeV$/c$) protons in ^{12}C and looked for the emission of a correlated recoil nucleon. In the absence of FSI, the initial momentum of the struck nucleon equals the missing momentum of the $^{12}\mathrm{C}(e, e'p)$ and $^{12}\mathrm{C}(p, 2p)$ reactions. FSI will make this relationship more approximate. For simplicity, we will ignore FSI The JLab measurement was sensitive to both proton and neutron recoils but the BNL measurement was only

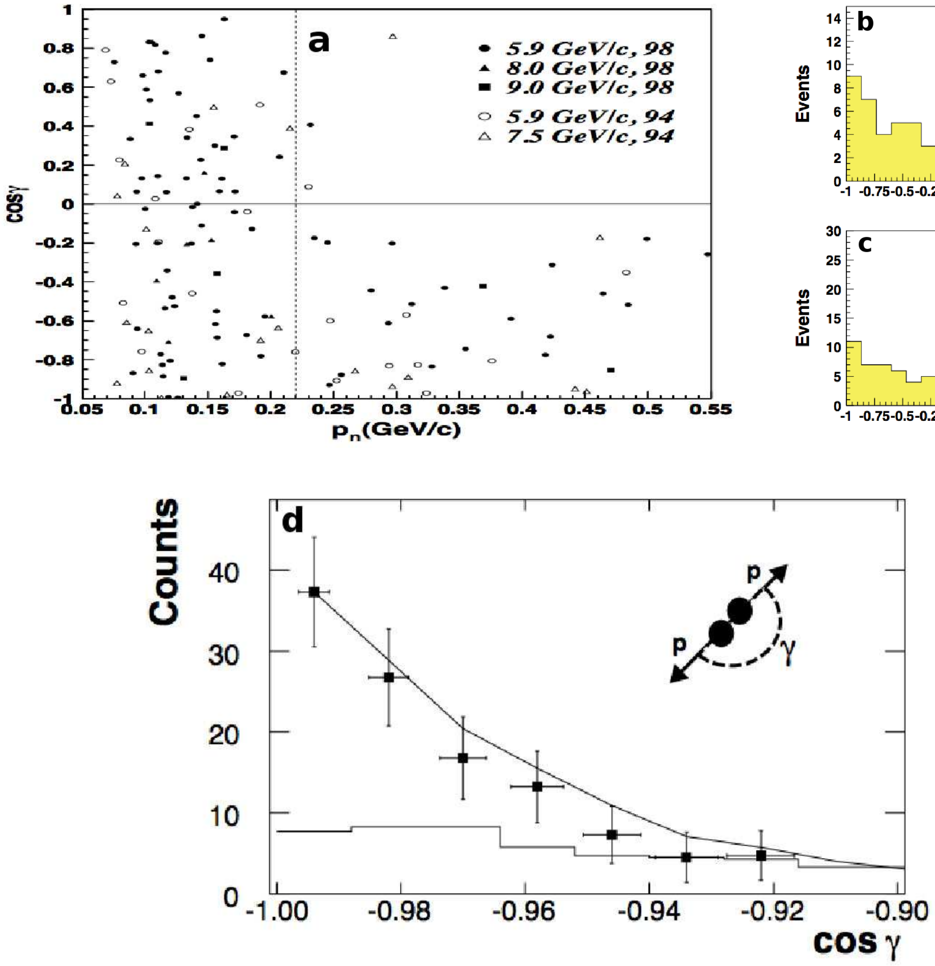

Fig. 5. Distributions of the relative angle (γ) between the reconstructed initial momentum of the knockout proton and the recoil nucleon. Top: Results for proton induced proton–neutron pair knockout (i.e., $^{12}\mathrm{C}(p, 2pn)$) measurements from BNL, shown and a function of: (a) the momentum of the recoil neutron, (b) for events with recoiling neutron with momentum greater than the Fermi momentum, and (c) for events with recoiling neutron with momentum lower than the Fermi momentum. These results show a clear transition from an isotropic distribution to a back-to-back correlated distribution as the recoil neutron momentum reaches the Fermi momentum of ^{12}C. Bottom: Results for electron induced proton–proton pair knockout (i.e., $^{12}\mathrm{C}(e, e'pp)$) measurements from JLab, shown for events in which the initial momentum of the knockout proton, $|\mathbf{p} - \mathbf{q}|$, equals $\sim$ 500 MeV/c. (Figures reprinted from Refs. 64–66. Copyright (2003, 2006, 2007) by the American Physical Society.)

sensitive to recoiling neutrons. These experiments were performed at large momentum transfer ($Q^2 \approx 2$ GeV/c^2) where competing effects such a MECs and Isobar Contributions (IC) are suppressed and FSI are mainly confined to be between the nucleons of the pair. The main results of these experiments are shown in Figs. 5 and 6. Figure 5 shows the distribution of the cosine of the opening angle between the initial momentum of the knocked-out proton and the recoil nucleon. The c.m. motion of the pairs in both cases was found to be consistent with a gaussian in each direction, with $\sigma = 143 \pm 17$ (BNL) and $\sigma = 136 \pm 20$ (JLab). The BNL results show a clear threshold around the Fermi momentum where recoiling neutrons above this momentum show a clear angular correlation, and those below it do not. Figure 6 shows the ratio of single nucleon knockout events to two nucleon knockout events, corrected for finite acceptance effects, as a function of the initial momentum of the knocked-out proton. As can be seen, within statistical uncertainties, all single proton knockout events were accompanied by the emission of a recoil nucleon. The ratio of proton recoil to neutron recoil was found to be approximately 1:20.[67] This is a clear evidence of the importance of the tensor part of the nucleon–nucleon interaction at these momentum scales.[68,69]

The effect of these measurements on our understanding of the short distance nuclear structure is illustrated by the pie chart shown in Fig. 6. From the inclusive cross-section ratio measurements and from $A(e,e'p)$ measurements we know that in medium and heavy nuclei (i.e., $A \geq 12$) $\sim$ 75–80% of the nucleons are "Mean-Field" nucleons, whereas $\sim$ 20–25% have momentum greater than the Fermi momentum of the nucleus. Combined with results from exclusive two-nucleon knockout measurements we know that these high momentum nucleons are dominated by $2N$-SRC pairs, which are in turn dominated by neutron-proton pairs.

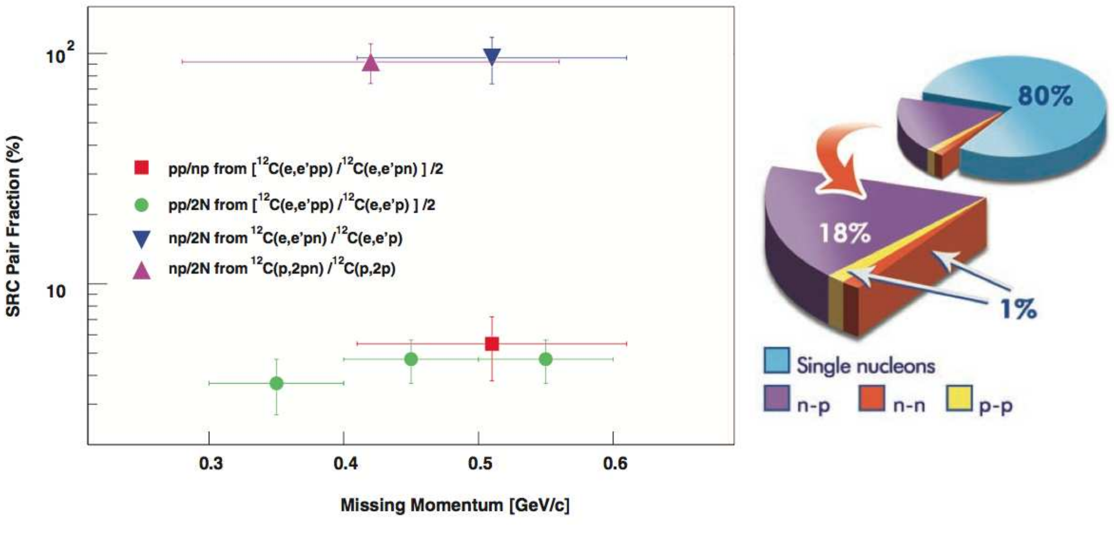

Fig. 6. The ratio of ^{12}C$(e,e'pN)$ double knockout events to ^{12}C$(e,e'p)$ single knockout events, shown as a function of the reconstructed initial (missing) momentum of the knocked-out proton from the ^{12}C$(e,e'p)$ reaction. Triangles and circles mark ^{12}C$(e,e'pn)$ and ^{12}C$(e,e'pp)$ events, respectively. The square shows the ^{12}C$(e,e'pp)/^{12}$C$(e,e'pn)$ ratio. A clear dominance of ^{12}C$(e,e'pn)$ events is observed, evidence of the tensor nature of the nucleon–nucleon interaction in the measured momentum range. The pie chart on the right illustrates our understanding of the structure of ^{12}C, composed of 80% mean-field nucleons and 20% SRC pairs, where the latter is composed of $\sim$ 90% np-SRC pairs and 5% pp and nn SRC pairs each. (Figure reprinted with permission from American Association for Advancement in Science.)[67]

4. SRC and the EMC Effect

4.1. *The EMC–SRC correlation*

Analysis of world data on inclusive DIS and QE scattering cross-section ratios showed that the magnitude of the EMC effect in nucleus A is linearly related to the probability that a nucleon in that nucleus is part of a $2N$-SRC pair, see Fig. 7.[70,71] Here we used the x_A corrected EMC data-base shown in Appendix A and defined the magnitude of the EMC effect, following Ref. 12, as the slope of the ratio of the per-nucleon DIS cross-section of nucleus A relative to deuterium, dR_{EMC}/dx, in the region $0.35 \le x_A \le 0.7$. The probability that a nucleon belongs to an SRC pair is characterized by the SRC scale factor, $a_2(A/d)$, the ratio in the plateau region ($Q^2 \ge 1.5$ $(\mathrm{GeV}/c)^2$ and $x_p \ge 1.5$) of the per-nucleon QE (e, e') cross-sections for nucleus A and deuterium.

The EMC effect correlates imperfectly with other A-dependent quantities (see Refs. 12 and 72 and references therein). In general, nuclei with $A \ge 4$ fall on one straight line but deuterium and ^{3}He do not. This is true when the EMC effect is plotted versus A, $A^{-1/3}$, or the average nuclear separation energy. When plotting the EMC effect versus average nuclear density, ^{9}Be is a clear outlier. This indicates that the excellent correlation with the SRC scale factor is not just a trivial by-product of their mutual A dependence.

The correlation between the EMC effect and the SRC scale factor is robust.[71] It applies to both new SRC data sets of Egiyan *et al.*[61] and Fomin *et al.*[62] The quality of the correlation also does not depend on the corrections applied to the

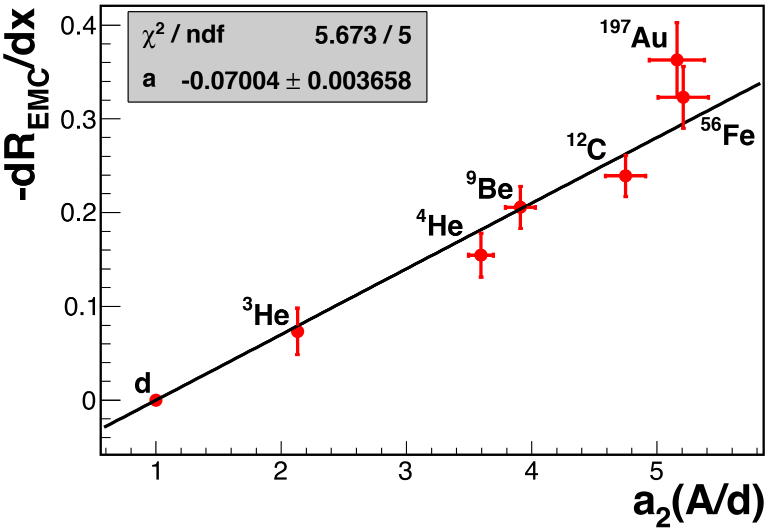

Fig. 7. The slope of the EMC effect (R_{EMC}, ratio of nuclear to deuteron cross-section) for $0.35 \le x_A \le 0.7$ plotted versus $a_2(A/d)$, the SRC scale factor (the relative probability that a nucleon belongs to an SRC NN pair) for a variety of nuclei.[71] The fit parameter, $a = -0.084 \pm 0.004$ is the intercept of the line constrained to pass through the deuteron (and is therefore also the negative of the slope of that line).

SRC data. These corrections include isoscalar cross-section corrections, CM motion corrections and isoscalar pair-counting corrections. The isoscalar correction to the SRC scale factors accounts for the different elementary electron–neutron and electron–proton cross-sections. This has a negligible effect on the fit quality and the extracted fit parameter. Fomin *et al.* did not apply this correction, arguing that SRC are dominated by *np* pairs. Fomin *et al.* argued that the SRC scale factors measured the relative probability of finding a high-momentum nucleon in nucleus A relative to deuterium and that these scale factors needed to be corrected for cm motion of the pair in order to determine the relative probability that a nucleon in nucleus A belongs to an SRC pair. As shown in Refs. 71 and 72, including the pair c.m. motion correction improves the EMC–SRC correlation only slightly.

This EMC–SRC correlation gives new insight into the origin of the EMC effect. Many different explanations of the EMC effect have been proposed since 1983. After accounting for the standard nuclear effects of binding energy and Fermi motion, explanations for the EMC effect fall into two general categories, those that require modifications of mean-field nucleons and those that require modifications of high-momentum nucleons. The linear correlation between the strength of the EMC effect and the SRC scale factors indicates that possible modifications of nucleon structure occurs in nucleons belonging to SRC pairs. This implies that the EMC effect, like SRC, is a short-distance, high virtuality, and high density phenomenon.

Additionally, one can use the EMC–SRC correlation as a phenomenological tool to constrain the deuteron IMC effect,[a] and thus extract the free neutron structure function. Following Weinstein *et al.*[70] we can extrapolate the linear fit to the EMC–SRC correlation to the limit of $a_2(A/d) \to 0$. If the EMC effect and the SRC scale factor both stem from the same cause, then both will vanish at the same point. The value $a_2(A/d) \to 0$ is the limit of free nucleons with no SRC. The extrapolation to the y-axis gives $dR_{\mathrm{EMC}}/dx = -0.070 \pm 0.004$. Since the EMC effect is linear for $0.3 \le x_A \le 0.7$ for all nuclei with $A > 2$, we assume that the EMC effect is also linear in this region for the free proton plus neutron. This gives the EMC effect for the free proton plus neutron:

$$\frac{\sigma_d}{\sigma_p + \sigma_n} = 1 - a(x_p - b) \quad \text{for } 0.3 \le x_p \le 0.7\,,$$

where σ_d and σ_p are the measured DIS cross-sections for the deuteron and free proton, σ_n is the free neutron DIS cross-section that we want to extract, $a = |dR_{\mathrm{EMC}}| = 0.070 \pm 0.004$ and $b = 0.34 \pm 0.02$ is the average value of x_p, where the EMC ratio is unity.[b] This implies that $\sigma_d/(\sigma_p + \sigma_n)$ decreases linearly from 1 to 0.97 as x_p increases from 0.3 to 0.7. We can then use this relationship to extract the free neutron cross-section in this x_p range. Incorporating this free neutron DIS

---

[a] The deuteron In Medium Correction (IMC) effect was first introduced in Ref. 70 and refers to the difference between the DIS cross-section for the deuteron and the sum of the cross-sections for a free proton and neutron.

[b] While the x_A correction does not change much the slope of the EMC–SRC correlation, the b parameter extracted here, while consistent within errors, is larger than that reported in Ref. 70.

cross-section into the global QCD analysis,[73] one can better constrain the d/u ratio at $x_p \to 1$ to be equal to 0.23 ± 0.09 at the 90% confidence level.[74]

The uncertainty quoted above is the uncertainty due to the data and the fit. It does not include the uncertainty of corrections to the data. As stated above, if we include the correction for the cm motion of the correlated pair, then the fit parameter increases by 25% and so does the free proton plus neutron EMC effect. Arrington *et al.* claim that if we also consider including the isospin pair counting correction and alternative fitting methods, then the range of fits expands to $0.59 \leq a \leq 1.04$. The effect of these uncertainties on the extraction of the free neutron structure function and the d/u ratio at large x_p are discussed in Ref. 75.

4.2. *Mean-field versus SRC contributions to the EMC effect*

We want to know whether the linear relation between the EMC slope and the SRC plateau parameter $a_2(A/d)$ is more than a coincidence. Any of the nuclear models discussed in Sec. 3.1 has correlations that would yield a value of $a_2(A/d)$ roughly consistent with the measured values. None of these models incorporate quark modifications of nuclear structure. Therefore existence of NN correlations is not a sufficient condition for the EMC effect to occur. The key questions are whether the quarks confined in the two nucleons in an SRC pair have different distribution functions than those of two free nucleons. Thus the minimum input necessary to test the existence of a relation between SRC and EMC is a model of a modified two-nucleon structure function consistent with a good nuclear model of SRC and with the EMC data. Here we make a first attempt at providing a link between SRC and EMC, by seeing if a modified two-nucleon structure function associated with the SRC can be used to describe DIS on nuclei. We also consider the other possibility, that medium modifications associated with the mean-field aspect of nuclei can describe nuclear DIS.

The treatment of FS[31] is very useful for such an aim, because the nuclear structure information needed to compute DIS is encoded in only three integrals that can be evaluated reliably. FS derive a convolution formula

$$\frac{1}{A}F_2^A(x_A, Q^2) = \int_0^A \alpha\rho_A(\alpha)F_2^N(x_A/\alpha, Q^2)d\alpha\,, \tag{10}$$

where $\alpha \equiv \frac{Ak\cdot q}{p_A\cdot q}$ is the fraction of the plus component of the nucleon momentum, with k the struck nucleon initial momentum and $p_A = (m_A, 0)$ is the nucleus four-momentum. $\rho_A(\alpha)$ is the probability that a nucleon in the nucleus carries momentum fraction α and F_2^N is the free nucleon structure function ($F_2^N = \frac{1}{2}(F_2^p + F_2^n)$).

Specifically $\rho(\alpha)$ is computed from the nonrelativistic structure function, $S_{A,NR}(k)$

$$\rho_A(\alpha) = \int d^4k S_{A,NR}(k)\delta\left(\alpha - \frac{k^0 + k^3}{m_N}\right)\,, \tag{11}$$

where

$$S_{A,NR}(k,E) \equiv \langle A|a_k^\dagger \delta(E-H) a_k|A\rangle \,. \tag{12}$$

The function $\rho(\alpha)$ is narrowly peaked about unity, so FS expand the nucleon structure function appearing in Eq. (10) about $\alpha = 1$ to find

$$\frac{1}{A}F_2^A(x_A) \approx F_2^N(x_A) I_1(A) + x_A F_2'^N I_2(A) + \left[x_A F_2'^N + \frac{1}{2}x_A^2 F_2''^N\right] I_3(A)\,, \tag{13}$$

where for simplicity we neglect the Q^2 term in the structure function notation. The integrals $I_n(A)$ are given by

$$I_n(A) \equiv \int \rho_A(\alpha)\alpha(1-\alpha)^{n-1} d\alpha, \quad n = 1,2,3\,. \tag{14}$$

Note that $I_1(A) = 1$, which is the normalization condition.

FS proceed (see also Ref. 32) by isolating the leading relativistic corrections of order ϵ_A/m and k^2/m^2 and then using the Koltun sum rule[76] to find

$$n_A(k) \equiv \langle A|a_k^\dagger a_k|A\rangle, \quad I_1(A) = \int d^3k n_A(k)\,, \tag{15}$$

$$I_2(A) = \int d^3k n_A(k)\left(2\epsilon_A/m + \frac{A-4}{A-1}k^2/6m^2\right) \equiv \frac{2\epsilon_A}{m} + \frac{A-4}{A-1}\left\langle \frac{k^2}{6m^2}\right\rangle\,, \tag{16}$$

$$I_3(A) = \int d^3k n_A(k) k^2/3m^2 = \left\langle \frac{k^2}{3m^2}\right\rangle\,. \tag{17}$$

FS used the above formalism to show that a nucleons-only model without modified structure functions could not reproduce DIS data.

To proceed with the calculation, we need a model of $n_A(k)$. The model of Ciofi degli Atti and Simula[63] is ideal for our purposes. This is based on a realistic nuclear calculation of the spectral function that leads to nuclear densities that yield qualitative agreement with quasi elastic electron scattering. The model yields reasonably good agreement with the plateau values $a_2(A/d)$. Furthermore, the contributions of the mean-field and correlation terms are enumerated in terms of the intermediate-state energy E appearing in the spectral function of Eq. (12). This association with continuum energies, E, above about 20 MeV with SRC is approximate but sufficiently accurate for the present schematic calculation. The spectral function leads to the momentum probability $n_A(k)$ such that

$$n_A(k) = n_A^{(0)}(k) + n_A^{(1)}(k)\,, \tag{18}$$

where the superscript 0 refers to that obtained from low energy terms dominated by the nuclear mean field and the superscript 1 refers to high energy terms (above the continuum threshold) dominated by the effects of nucleon–nucleon correlations. Ciofi degli Atti and Simula provide functional forms for $n_A(k)$ for several different nuclei. This separation using the excitation energy is not exactly the same as a separation in terms of relative momentum but is qualitatively reasonable. With this separation, terms involving correlations have about 20% of the probability.

Using Eq. (18) one can obtain the separate contributions to $I_n(A)$ as $I_n(A) = I_n^{(0)}(A) + I_n^{(1)}(A)$.

We next proceed by assuming that nucleons in high energy excited states (correlated nucleons) have a different structure function $\tilde{F}_{2N}(x)$ than free ones $F_{2N}(x)$. Thus we make the replacements

$$I_1(A)F_2 \to I_1^{(0)}(A)F_2^N + I_1^{(1)}(A)\tilde{F}_2^N = I_1^{(0+1)}(A)F_2^N + I_1^{(1)}(A)\Delta F_{2N}\,, \text{ etc}\,, \tag{19}$$

where

$$\Delta F_2^N(x_A) = \tilde{F}_2^N(x_A) - F_2^N(x_A)\,. \tag{20}$$

An alternate version in which the medium modification is associated with the mean-field components of the density can be obtained by using

$$I_1(A)F_2^N \to I_1^{(0)}(A)\tilde{F}_2^N + I_1^{(1)}(A) = I_1(A)F_2^N + I_1^{(0)}(A)\Delta F_2^N\,, \text{ etc}\,. \tag{21}$$

A condition on ΔF_2^N derived from the baryon sum rule is that $\int_0^2 dx_A \frac{\Delta F_2^N(x_A)}{x_A} = 0$. This means that ΔF_2^N must pass through 0 at some value of x_A.

The analysis proceeds by calculating Eq. (13) with the supplement of Eq. (19) (Eq. (21) for the case of Mean-Field modification), assuming $\Delta F_2^N(x_A)$ is a second-order polynomial in x_A. The parameters of $\Delta F_2^N(x_A)$ are fitted to the x_A corrected EMC data (see Appendix A) for all nuclei for which momentum distributions are available (i.e., ^{4}He, ^{12}C, ^{40}Ca, ^{56}Fe, and ^{197}Au). Note that the functional form of $\Delta F_2^N(x_A)$ is assumed to be universal independent of A.

The results of the fits for individual nuclei are shown in Fig. 9 (Fig. 11 for the case of Mean-Field modification). The description of the data is very good for all

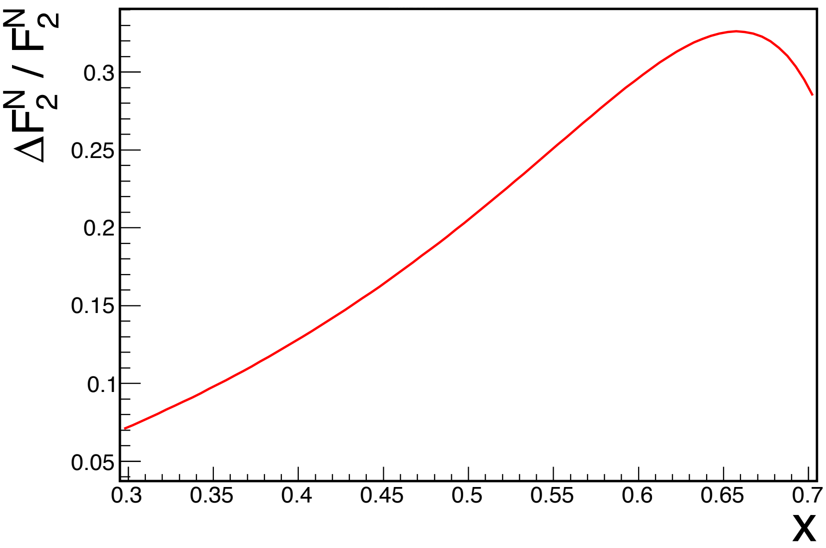

Fig. 8. The ratio of the modification term, ΔF_2^N to the free nucleon structure function, F_2^N.

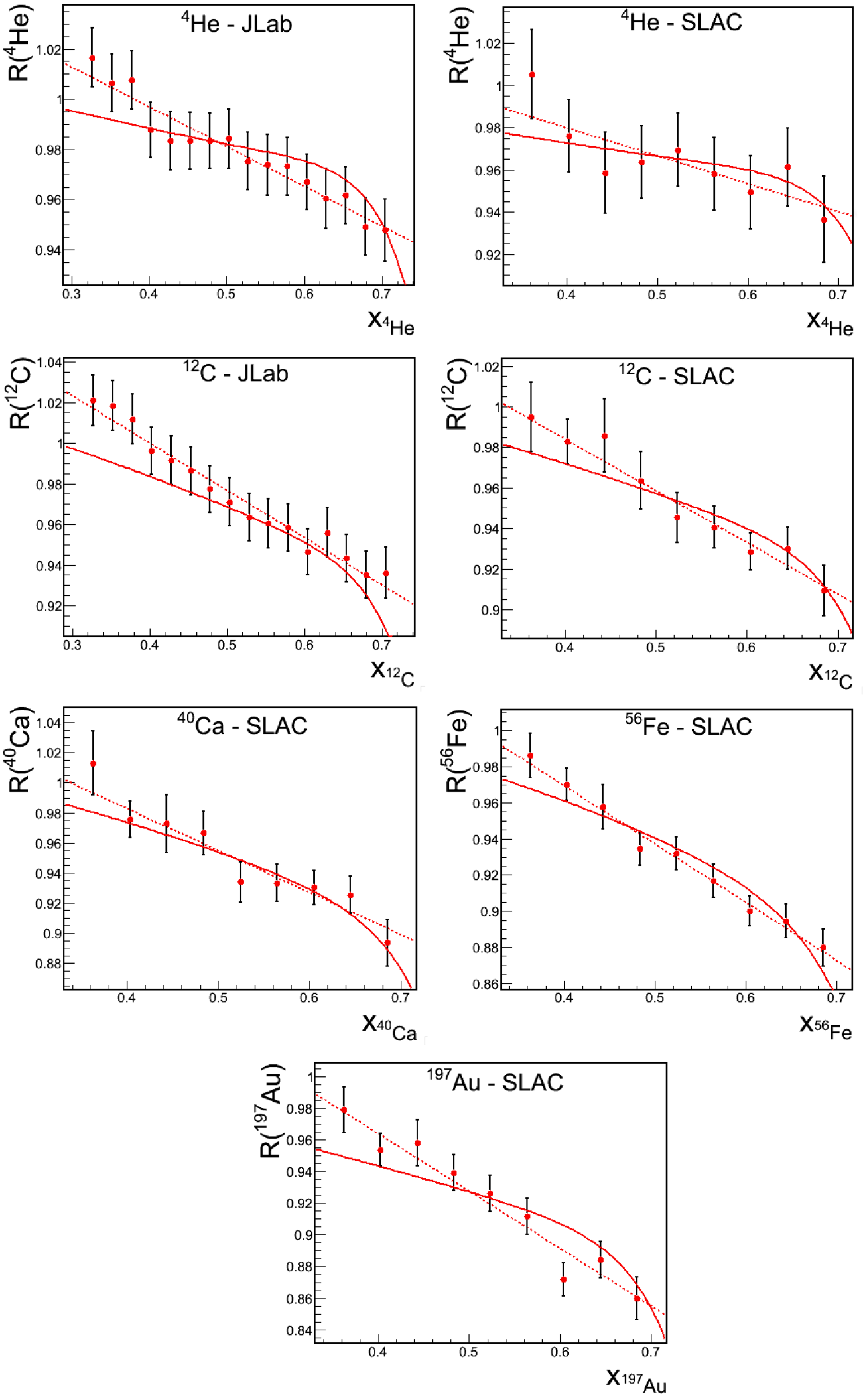

Fig. 9. (Color online) The ratios of free to bound structure functions for various nuclei, extracted in the nucleus reference frame as detailed in Eq. (9). The dashed line is the result of a linear fit to the data. The solid red line is the result of the medium-modification fit, assuming an A-independent modification to SRC nucleons.

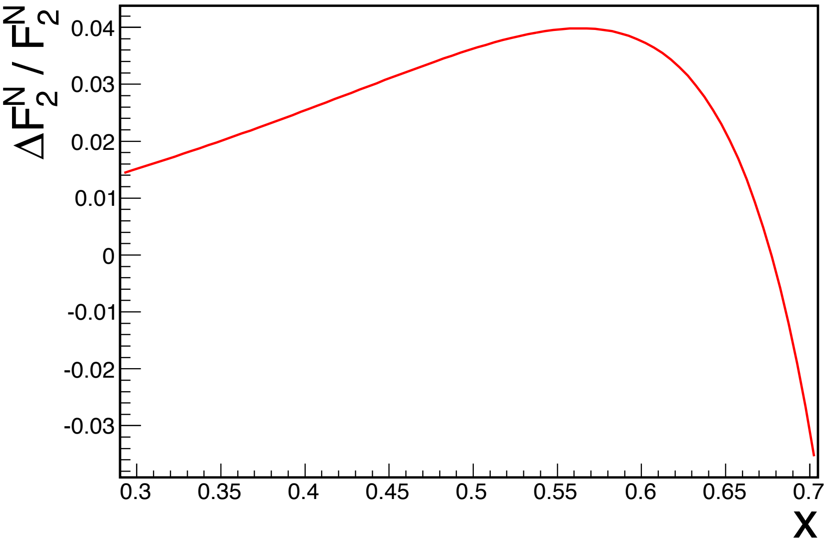

Fig. 10. Same as Fig. 8, assuming universal modification to Mean-Field nucleons. It is assumed that deuterium has no Mean-Field component, see text for details.

nuclei with a χ^2 per degree of freedom of ≈ 1 for both the SRC and Mean-Field fits. These results were obtained using the parametrization of Ref. 21 for the free-nucleon structure function, F_2^N. The modified-to-free structure function ratio is shown in Fig. 8 (Fig. 10 for the case of Mean-Field modification).

The present results show that a model incorporating either universal modification of Mean-Field nucleons or modification of nucleons in SRC pairs can explain the EMC effect. As expected, the required medium modification of Mean-Field nucleons is on the order of a few percent while that of SRC nucleons is a few tens of percent. This model does not prove or disprove that the underlying cause of the EMC effect is the unique association with SRC. Note that ^{9}Be was not included in the model calculations since a ^{9}Be spectral function was not available. Note also that this model does not separate valence and sea quark distributions and therefore cannot make predictions about the Drell–Yan data.

Further experiments are needed to determine whether the Mean-Field or SRC nucleons are modified by the nuclear medium. For example, quasi-elastic electron scattering would be sensitive to the former but not the latter.

5. Summary

We have reviewed recent data showing that the detailed A dependence of the EMC effect provides important hints in understanding the origin of that effect. The EMC effect seems to depend on local density rather than the average density. We present the EMC ratio data (the ratio of nuclear to deuterium structure functions) in terms of an improved Bjorken variable $x_A = AQ^2/(2M_A q_0)$ (see Appendix A). We review SRC data and discuss the linear relation between the EMC effect and SRC. We

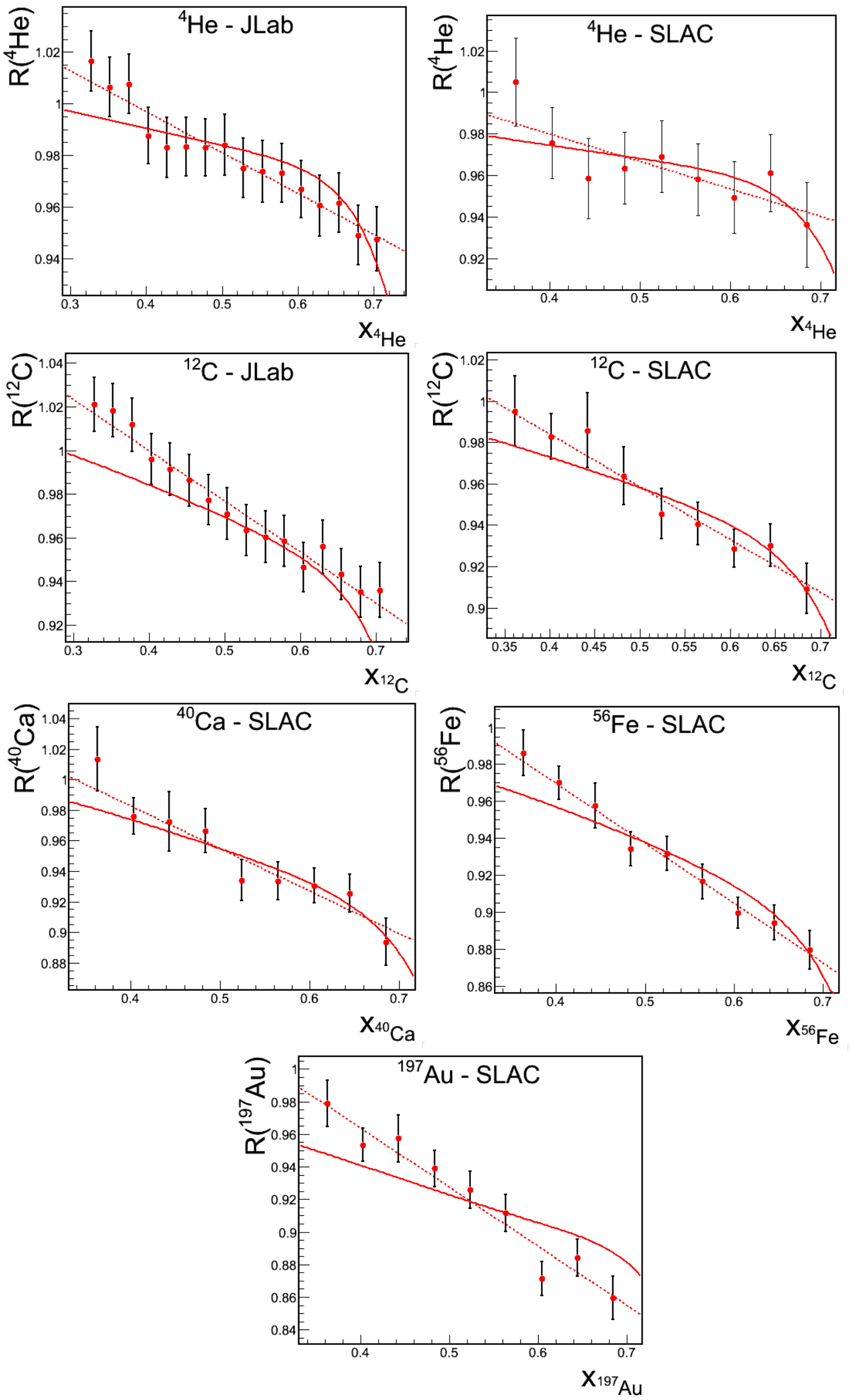

Fig. 11. Same as Fig. 9, assuming universal modification to Mean-Field nucleons. It is assumed that deuterium has no Mean-Field component, see text for details.

present a phenomenological model including modification of either Mean-Field or SRC nucleons and find that modification of either is capable of accounting for the existing data.

Acknowledgments

This work was supported in part by the Israel Science Foundation, the US-Israeli Bi-National Science Foundation and the United States Department of Energy (Grant Nos. FG02-97ER41014 and DE-FG02-96ER40960).

References

1. European Muon Collab. (J. Aubert *et al.*), *Phys. Lett. B* **123** (1983) 275.
2. A. Bodek *et al.*, *Phys. Rev. Lett.* **50** (1983) 14311434.
3. A. Bodek *et al.*, *Phys. Rev. Lett.* **51** (1983) 534537.
4. R. Arnold *et al.*, *Phys. Rev. Lett.* **52** (1984) 727.
5. S. Dasu *et al.*, *Phys. Rev. Lett.* **60** (1988) 2591.
6. BCDMS Collab. (G. Bari *et al.*), *Phys. Lett. B* **163** (1985) 282.
7. New Muon Collab. (P. Amaudruz *et al.*), *Z. Phys. C* **51** (1991) 387.
8. J. Gomez *et al.*, *Phys. Rev. D* **49** (1994) 4348.
9. D. F. Geesaman, K. Saito and A. W. Thomas, *Annu. Rev. Nucl. Part. Sci.* **45** (1995) 337.
10. R. Bickerstaff, M. Birse and G. A. Miller, *Phys. Rev. Lett.* **53** (1984) 2532.
11. D. Alde *et al.*, *Phys. Rev. Lett.* **64** (1990) 2479.
12. J. Seely *et al.*, *Phys. Rev. Lett.* **103** (2009) 202301.
13. S. C. Pieper and R. B. Wiringa, *Annu. Rev. Nucl. Part. Sci.* **51** (2001) 53.
14. J. R. Smith and G. A. Miller, *Phys. Rev. C* **65** (2002) 055206.
15. L. Frankfurt and M. Strikman, *Phys. Rep.* **160** (1988) 235.
16. M. Arneodo, *Phys. Rep.* **240** (1994) 301.
17. G. Piller and W. Weise, *Phys. Rep.* **330** (2000) 1.
18. M. Sargsian *et al.*, *J. Phys. G* **29** (2003) R1.
19. G. A. Miller, *Eur. Phys. J. A* **31** (2007) 578.
20. R. Jaffe, *Phys. Rev. Lett.* **50** (1983) 228.
21. C. Carlson and T. Havens, *Phys. Rev. Lett.* **51** (1983) 261.
22. H. J. Pirner and J. P. Vary, *Phys. Rev. Lett.* **46** (1981) 1376.
23. M. Ericson and A. W. Thomas, *Phys. Lett. B* **128** (1983) 112.
24. E. L. Berger and F. Coester, *Annu. Rev. Nucl. Part. Sci.* **37** (1987) 463.
25. C. L. Smith, *Phys. Lett. B* **128** (1983) 107.
26. H. Jung and G. A. Miller, *Phys. Lett. B* **200** (1988) 351.
27. H. Jung and G. A. Miller, *Phys. Rev. C* **41** (1990) 659.

28. R. Bickerstaff, M. Birse and G. A. Miller, *Phys. Rev. D* **33** (1986) 3228.
29. G. A. Miller, Nuclear wave functions in deep inelastic scattering and Drell–Yan processes, in Nuclear and Particle Physics on the Light Cone, eds. M. B. Johnson and L. S. Kisslinger (World Scientific Press, 1988).
30. L. Frankfurt and M. Strikman, *Nucl. Phys. B* **316** (1989) 340.
31. L. Frankfurt and M. Strikman, *Phys. Lett. B* **183** (1987) 254.
32. C. Ciofi degli Atti and S. Liuti, *Phys. Rev. C* **44** (1991) 1269.
33. A. Dieperink and G. A. Miller, *Phys. Rev. C* **44** (1991) 866.
34. L. Frankfurt and M. Strikman, *Int. J. Mod. Phys. E* **21** (2012) 1230002.
35. G. A. Miller and J. R. Smith, *Phys. Rev. C* **65** (2002) 015211.
36. H. Mineo, W. Bentz, N. Ishii, A. W. Thomas and K. Yazaki, *Nucl. Phys. A* **735** (2004) 482.
37. I. Cloet, W. Bentz and A. W. Thomas, *Phys. Lett. B* **642** (2006) 210.
38. J. R. Smith and G. A. Miller, *Phys. Rev. Lett.* **91** (2003) 212301.
39. L. Frankfurt and M. Strikman, *Nucl. Phys. B* **250** (1985) 143.
40. M. Frank, B. Jennings and G. A. Miller, *Phys. Rev. C* **54** (1996) 920.
41. S. A. Kulagin and R. Petti, *Nucl. Phys. A* **765** (2006) 126.
42. F. Halzen and A. D. Martin, *Quarks and Leptons: An Introductory Course in Modern Particle Physics* (Wiley, New York, USA, 1984).
43. L. W. Whitlow, E. M. Riordan, S. Dasu, S. Rock and A. Bodek, *Phys. Lett. B* **282** (1992) 475482.
44. P. E. Bosted and M. E. Christy, *Phys. Rev. C* **77** (2008) 065206.
45. A. Bodek *et al.*, *Phys. Rev. D* **20** (1979) 14711552.
46. J. Arrington, F. Coester, R. J. Holt and T.-S. H. Lee, *J. Phys. G: Nucl. Part. Phys.* **36** (2009) 025005.
47. H. Bethe, *Annu. Rev. Nucl. Part. Sci.* **21** (1971) 93.
48. M. Anastasio, L. Celenza, W. Pong and C. Shakin, *Phys. Rep.* **100** (1983) 327.
49. R. Brockmann and R. Machleidt, *Phys. Lett. B* **149** (1984) 283.
50. G. A. Miller and R. Machleidt, *Phys. Rev. C* **60** (1999) 035202.
51. G. A. Miller, *Prog. Part. Nucl. Phys.* **45** (2000) 83.
52. P. F. Bedaque and U. van Kolck, *Annu. Rev. Nucl. Part. Sci.* **52** (2002) 339.
53. S. Bogner, R. Furnstahl and A. Schwenk, *Prog. Part. Nucl. Phys.* **65** (2010) 94.
54. J. Kelly, *Adv. Nucl. Phys.* **23** (1996) 75.
55. CLAS Collab. (K. Egiyan *et al.*), *Phys. Rev. C* **68** (2003) 014313.
56. L. L. Frankfurt, M. M. Sargsian and M. I. Strikman, *Phys. Rev. C* **56** (1997) 1124.
57. M. M. Sargsian, *Int. J. Mod. Phys. E* **10** (2001) 405.
58. R. G. Arnold *et al.*, *Phys. Rev. C* **42** (1990) R1.
59. M. J. Laget *et al.*, *Phys. Lett. B* **199** (1987) 493.
60. L. Frankfurt, M. Strikman, D. Day and M. Sargsian, *Phys. Rev. C* **48** (1993) 2451.
61. CLAS Collab. (K. Egiyan *et al.*), *Phys. Rev. Lett* **96** (2006) 082501.
62. N. Fomin *et al.*, *Phys. Rev. Lett.* **108** (2012) 092502.
63. C. Ciofi degli Atti and S. Simula, *Phys. Rev. C* **53** (1996) 1689.
64. A. Tang *et al.*, *Phys. Rev. Lett.* **90** (2003) 042301.
65. E. Piasetzky, M. Sargsian, L. Frankfurt, M. Strikman and J. Watson, *Phys. Rev. Lett.* **97** (2006) 162504.
66. R. Shneor *et al.*, *Phys. Rev. Lett.* **99** (2007) 072501.
67. R. Subedi *et al.*, *Science* **320** (2008) 1476.
68. M. Sargsian, T. Abrahamyan, M. Strikman and L. Frankfurt, *Phys. Rev. C* **71** (2005) 044615.
69. R. Schiavilla, R. B. Wiringa, S. C. Pieper and J. Carlson, *Phys. Rev. Lett.* **98** (2007) 132501.

70. L. B. Weinstein, E. Piasetzky, D. W. Higinbotham, J. Gomez, O. Hen and R. Shneor, *Phys. Rev. Lett.* **106** (2011) 052301.
71. O. Hen, E. Piasetzky and L. B. Weinstein, *Phys. Rev. C* **85** (2012) 047301.
72. J. Arrington *et al.*, *Phys. Rev. C* **86** (2012) 065204.
73. A. Accardi *et al.*, *Phys. Rev. D* **84** (2011) 014008.
74. O. Hen, A. Accardi, W. Melnitchouk and E. Piasetzky, *Phys. Rev. D* **84** (2011) 117501.
75. E. Piasetzky, O. Hen and L. Weinstein, arXiv:1209.0636 (2012).
76. D. Koltun, *Phys. Rev. Lett.* **28** (1972) 182.

2. Experimental Setup and Data Analysis

*O. Hen et al., Science **346**, 614 (2014) – Supplementary materials.*

Supplementary Materials for

Momentum Sharing In Imbalanced Fermi Systems

O. Hen*, M. Sargsian, L.B. Weinstein, E. Piasetzky, H. Hakobyan, D. W. Higinbotham, M. Braverman, W.K. Brooks, S. Gilad, K. P. Adhikari, J. Arrington, G. Asryan, H. Avakian, J. Ball, N. A. Baltzell, M. Battaglieri, A. Beck, S. May-Tal Beck, I. Bedlinskiy, W. Bertozzi, A. Biselli, V. D. Burkert, T. Cao, D. S. Carman, A. Celentano, S. Chandavar, L. Colaneri, P. L. Cole, V. Crede, A. D’Angelo, R. De Vita, A. Deur, C. Djalali, D. Doughty, M. Dugger, R. Dupre, H. Egiyan, A. El Alaoui, L. El Fassi, L. Elouadrhiri, G. Fedotov, S. Fegan, T. Forest, B. Garillon, M. Garcon, N. Gevorgyan, Y. Ghandilyan, G. P. Gilfoyle, F. X. Girod, J. T. Goetz, R. W. Gothe, K. A. Griffioen, M. Guidal, L. Guo, K. Hafidi, C. Hanretty, M. Hattawy, K. Hicks, M. Holtrop, C. E. Hyde, Y. Ilieva, D. G. Ireland, B.I. Ishkanov, E. L. Isupov, H. Jiang, H. S. Jo, K. Joo, D. Keller, M. Khandaker, A. Kim, W. Kim, F. J. Klein, S. Koirala, I. Korover, S. E. Kuhn, V. Kubarovsky, P. Lenisa, W. I. Levine, K. Livingston, M. Lowry, H. Y. Lu, I. J. D. MacGregor, N. Markov, M. Mayer, B. McKinnon, T. Mineeva, V. Mokeev, A. Movsisyan, C. Munoz Camacho, B. Mustapha, P. Nadel-Turonski, S. Niccolai, G. Niculescu, I. Niculescu, M. Osipenko, L. L. Pappalardo, R. Paremuzyan, K. Park, E. Pasyuk, W. Phelps, S. Pisano, O. Pogorelko, J. W. Price, S. Procureur, Y. Prok, D. Protopopescu, A. J. R. Puckett, D. Rimal, M. Ripani, B. G. Ritchie, A. Rizzo, G. Rosner, P. Rossi, P. Roy, F. Sabatié, D. Schott, R. A. Schumacher, Y. G. Sharabian, G. D. Smith, R. Shneor, D. Sokhan, S. S. Stepanyan, S. Stepanyan, P. Stoler, S. Strauch, V. Sytnik, M. Taiuti, S. Tkachenko, M. Ungaro, A. V. Vlassov, E. Voutier, N. K. Walford, X. Wei, M. H. Wood, S. A. Wood, N. Zachariou, L. Zana, Z. W. Zhao, X. Zheng, and I. Zonta, Jefferson Lab CLAS Collaboration†

*Corresponding author. E-mail: or.chen@mail.huji.ac.il

†The collaboration consists of all listed authors. There are no additional collaborators.

Published 16 October 2014 on Science Express
DOI: 10.1126/science.1256785

This PDF file includes:

Materials and Methods
Figs. S1 to S30
Tables S1 to S8
Full Reference List

Materials and Methods

1. Calculations of <Tp> and <Tn>

1.1. Light nuclei (A<12)

Recently, state-of-the-art calculations of single-nucleon momentum distributions for a variety of light nuclei in the range of A = 2 - 12 became available (*26*). These are many-body variational Monte Carlo calculations (VMC) using the phenomenological AV18 two-nucleon and Urbana-X three-nucleon potentials (AV18+UX). By integrating these single-nucleon momentum distributions one can obtain the average proton and neutron kinetic energy for the different nuclei:

Eq. S1

$$\left\langle T_{p(n)} \right\rangle = \int n_{p(n)}(k) \cdot \frac{k^2}{2m} \cdot d^3k \ ,$$

where $n_{p(n)}(k)$ is the VMC calculated proton (or neutron) momentum distribution normalized according to: $\int n_{p(n)}(k) \cdot d^3k = 1$.

Table S1 lists the average proton and neutron kinetic energy for a variety of light nuclei as calculated using Eq. S1 and the VMC momentum distributions of (*26*). As can be seen, the average kinetic energy of the minority nucleons is larger than that of the majority nucleons in asymmetric nuclei, and this effect increases with the nuclear asymmetry. This non-trivial result can be naturally explained by the dominance of neutron-proton pairs in the high momentum tail of the nuclear momentum distribution. Model calculations within the np-SRC dominance model for heavier nuclei are presented below.

Table S1: The proton and neutron average kinetic energies as extracted from VMC single-nucleon momentum distribution calculations (*26*). As can be seen, the average kinetic energy of the minority nucleons is larger than that of the majority nucleons. This difference increases with the nuclear asymmetry

Nucleus	Asymmetry (N-Z) / A	$<T_p>$	$<T_n>$	$<T_p>/<T_n>$
^{8}He*	0.50	30.13	18.60	1.62
^{6}He*	0.33	27.66	19.60	1.41
^{9}Li	0.33	31.39	24.91	1.26
^{3}He	-0.33	14.71	19.35	0.76
^{3}H	0.33	19.61	14.96	1.31
^{8}Li	0.25	28.95	23.98	1.21
^{10}Be	0.20	30.20	25.95	1.16
^{7}Li	0.14	26.88	24.54	1.09
^{9}Be	0.11	29.82	27.09	1.10
^{11}B	0.09	33.40	31.75	1.05

*Neutron Halo

1.2. Heavy nuclei (A>12)

The average momentum distribution of nucleons in nuclei is given by the weighted sum of proton and neutron contributions:

Eq. S2

$$n_A(k) = \frac{1}{A}\left[Z \cdot n_p(k) + N \cdot n_n(k)\right],$$

where $n_p(k)$ and $n_n(k)$ are the proton and neutron momentum distributions, Z and N are the number of protons and neutrons in the nucleus, and A = Z+N is the nucleus mass number.

To study the effect of observed np-SRC dominance in heavy asymmetric nuclei (Fig. 1 in the main paper), we propose a simple model for the proton and neutron momentum distributions. This model describes the proton and neutron momentum distribution as two independent nucleon distributions up to a transition momentum, near the nuclear Fermi sea level, and a high momentum tail above it. The momentum distribution below the transition momentum is taken from mean-field nuclear wave-function calculations (*40-42*).

The high momentum tail must satisfy two experimental criteria: 1. the per-nucleon amount of high momentum nucleons in nucleus A relative to deuterium should equal $a_2(A/d)$, a scaling factor extracted from inclusive (e,e') cross-section measurements at $x_B>1.5$ (*10,11*), and 2. The absolute amount of high-momentum protons and neutrons should be equal for all nuclei (see Fig. 1 and 3 in the main paper). The resulting proton and neutron momentum distributions are given by (*25*):

Eq. S3

$$n_p(k) = \begin{cases} \eta \cdot n_p^{M.F.}(k) \ldots\ldots\ldots\ldots\ldots\ldots\ldots\ldots\ldots & k < k_0 \\ \frac{A}{2Z} \cdot a_2(A/d) \cdot n_d(k) \ldots\ldots\ldots & k > k_0 \end{cases},$$

where $n_p^{\mathrm{M.F.}}(k)$ is the mean field proton momentum distribution in nucleus A, $n_d(k)$ is the deuteron momentum distribution, $a_2(A/d)$ is the experimentally determined per-nucleon probability of finding a high-momentum nucleon in nucleus A relative to deuterium (*10,11,43*), k_0 is a transition momentum, and η is a normalization factor chosen such that $4\pi\int_0^\infty n_{p(n)}(k)k^2\,dk = 1$. The neutron momentum distribution is obtained by replacing $n_p^{\mathrm{M.F.}}(k)$ with $n_n^{\mathrm{M.F.}}(k)$ and Z with N in Eq. S3.

Using Eq. S1 and the momentum distributions of Eq. S3 we calculate the average proton and neutron kinetic energies in C, Al, Fe and Pb. The calculation is done using three different models for the mean-field momentum distribution: Ciofi and Simula (*40*), Woods-Saxon (*41*), and Serot-Walecka (*42*), $n_d(k)$ is taken from the Argonne V18 NN potential (*44*), $a_2(A/d)$ is taken from column 6 of Table-I of Ref. (*43*) based on inclusive A(e,e') scattering measurements at $x_B>1.5$ (*10,11*); k_0 is chosen to be equal to 300 MeV/c. As a sensitivity study we also consider a transition around the Fermi sea level ($k_0 = k_F$), which is below our experimental sensitivity limit. This correspond to k_0 = 221, 260, 260, and 260 (280) MeV/c for C, Al, Fe, and for protons (neutrons) in Pb respectively (*45*).

The different proton and neutron Fermi momenta in Pb is due to its large neutron excess, which increases the average neutron density.

The resulting proton and neutron average kinetic energies for C, Al, Fe, and Pb, calculated using the proposed np-dominance model, are shown in Fig. S1, and listed in Tables S2 and S3. The uncertainties in the calculations are due to the difference in the results obtained using the different input parameters described above (i.e. mean-field momentum distributions, k_0 transition momenta). The experimental uncertainties in the extraction of $a_2(A/d)$ are taken as 10% to include the effect of different corrections.

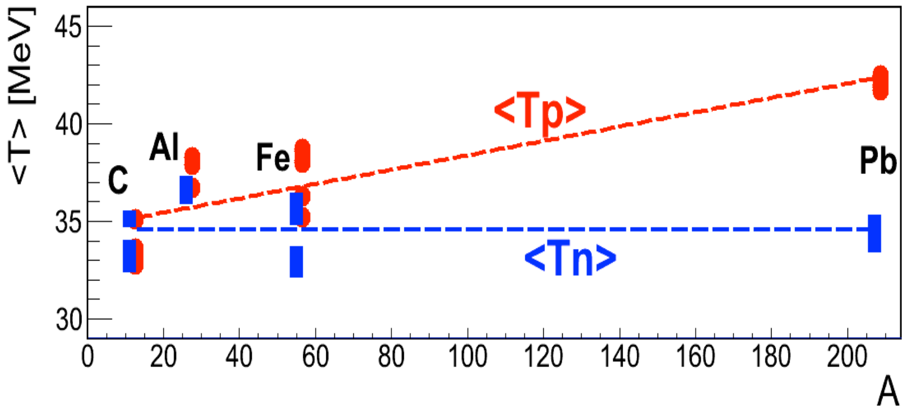

Fig. S1: The average proton and neutron kinetic energy calculated within the np-dominance model described by Eq. S3. See text for details.

Table S2: The average proton kinetic energy calculated within the np-dominance model, using the momentum distribution defined in Eq. S3, and three different mean-field momentum distributions and two different Mean-Field to SRC transition momentum.

Model $\langle T_p \rangle$	Wood-Saxon		Serot-Walecka		Ciofi and Simula	
	$k_0 = 300$ MeV/c	$k_0 = k_F$	$k_0 = 300$ MeV/c	$k_0 = k_F$	$k_0 = 300$ MeV/c	$k_0 = k_F$
C	33.2±1.7	32.8±2.0	35.1±1.7	33.5±2.0	33.6±1.7	33.1±2.0
Al	36.7±1.9	36.7±2.1	38.3±1.9	37.9±2.0	N/A	N/A
Fe	38.0±1.9	38.1±2.1	38.7±2.0	38.6±2.1	35.2±2.0	36.3±2.2
Pb	41.9±2.3	42.4±2.5	42.0±2.3	42.5±2.5	41.7±2.3	42.2±2.5

Table S3: Same as Table S2 for neutrons.

Model $<T_n>$	Wood-Saxon		Serot-Walecka		Ciofi and Simula	
	$k_0 = 300$ MeV/c	$k_0 = k_F$	$k_0 = 300$ MeV/c	$k_0 = k_F$	$k_0 = 300$ MeV/c	$k_0 = k_F$
C	33.2±1.7	32.8±2.0	35.1±1.7	33.5±2.0	33.6±1.7	33.1±2.0
Al	36.6±1.9	36.7±2.1	36.9±1.7	36.3±1.9	N/A	N/A
Fe	35.3±1.7	35.2±1.8	36.0±1.7	35.7±1.8	32.5±1.7	33.3±1.9
Pb	34.0±1.5	34.9±1.8	34.1±1.5	34.2±1.7	33.8±1.5	33.8±1.9

2. CLAS Detector

The measurement described in this paper was carried out using the CEBAF Large Acceptance Spectrometer (CLAS) (*20*), located in Hall-B of the Thomas Jefferson National Accelerator Facility (TJNAF) in Newport News, Virginia.

CLAS is a magnetic spectrometer optimized for coincidence measurements of nuclear reactions with multi-particle final states. It operates with incident electron and photon beams at luminosities up to ~ 10^{34} $cm^{-2}s^{-1}$. CLAS uses a toroidal magnetic field, generated by six flat super-conducting coils, and six identically instrumented detection sectors. These sectors are each based on three main detection sub-systems (see Fig. 2 and S2):

1. Charged-particle tracking system composed of three regions of drift chambers (DC), consisting of 34 layers of drift cells. The Region 1, 2, and 3 drift chambers are positioned between the target and the magnetic field region, in the magnetic field region, and after the magnetic field region, respectively.
2. Time-Of-Flight (TOF) measurement system consisting of an array of 336 plastic scintillation counters,
3. Electron/pion separation system using a set of gas threshold Cherenkov counters (CC) and segmented electromagnetic calorimeters (EC) divided into inner and outer super-layers.

The combination of the information obtained from all detector subsystems allows for high-momentum particle identification and momentum reconstruction. Details on the particle identification scheme of CLAS are given in the following sections. The momentum of charged particles is extracted from the measured curvature of their trajectories due to the influence of the toroidal magnetic field, as determined by the DC system.

The active charged particle detection region of CLAS covers about 70% of the full 4π solid angle. The azimuthal acceptance is maximal at polar angle of 90 degrees and decreases at forward and backward angles. The polar angle acceptance for hadrons such as protons ranges from about 8^o to 140^o. The polar acceptance for scattered electrons is limited by the coverage of the CC and EC sub-systems that extend up to 45^o.

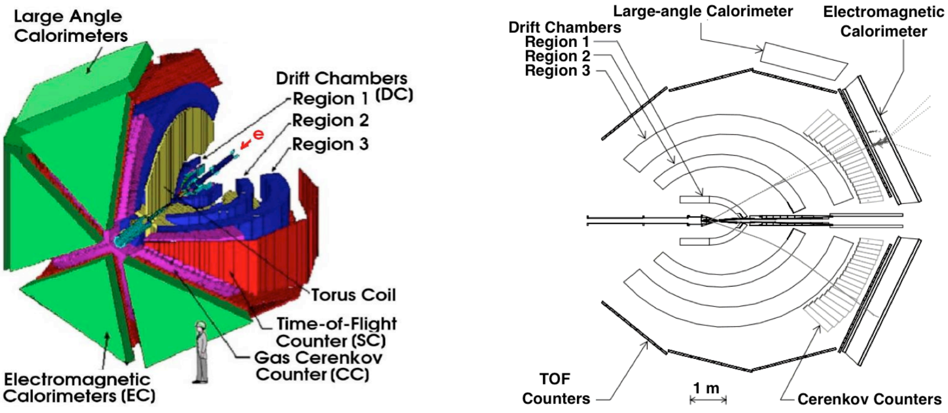

Fig. S2: A 3D-representation (left) and a cross-sectional image (right) of CLAS. See text for details.

3. Particle Identification

3.1. Electron Identification

Electron candidates are all negatively charged tracks (determined by the CLAS tracking system) with good hits in the Time-Of-Flight (TOF) system, Electro-Magnetic Calorimeter (EC) and Cerenkov Counter (CC). Additional cuts are applied to the CC and EC to better define the acceptance and separate electrons from pions. The cuts applied are:

- The reconstructed electron track passed through the target region.
- The reconstructed hit position is within the EC fiducial limits, ensuring full containment of the electromagnetic shower, see Fig. S3.
- More than 2.5 photo-electrons are produced in the CC, see Fig. S4.
- More than a specified amount of energy is deposited in the inner parts of the EC, see Fig. S5.
- The total energy deposited in the inner plus outer parts of the EC, divided by the particle momentum, exceeds a specified value, see Fig. S6.

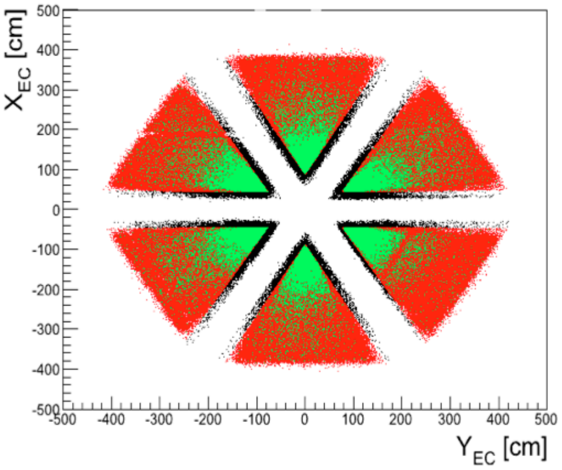

Fig. S3: Fiducial region of the CLAS Electro-Magnetic Calorimeter for electron candidates, which pass the initial vertex cut. The axis values marks the hit location along the face of the EC. Black: All events. Red: After applying the fiducial cuts. Green: After applying the fiducial cuts and demanding $x_B > 1$. The effect of the fiducial cuts on all the inner and outer edges of the EC (Red vs. Black points) is clear.

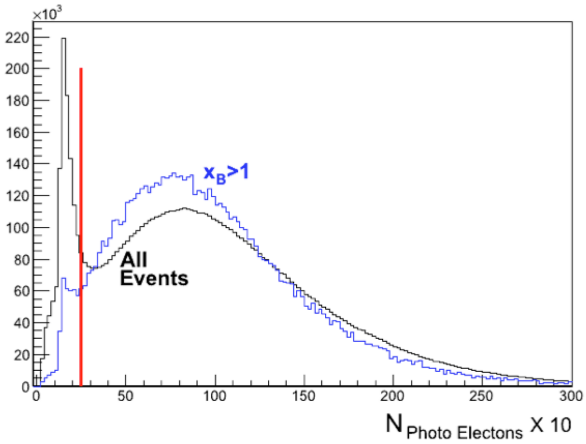

Fig. S4: CC photo-electron detection distribution for electron candidates which pass the initial vertex cut and EC fiducial cuts. Black: All events. Blue: $x_B > 1$ events (with an arbitrary scale factor). The peak at small values is associated with negative pions with momentum $p < 2.8$ GeV/c. The applied cut of #photo-electrons > 2.5 is shown in red.

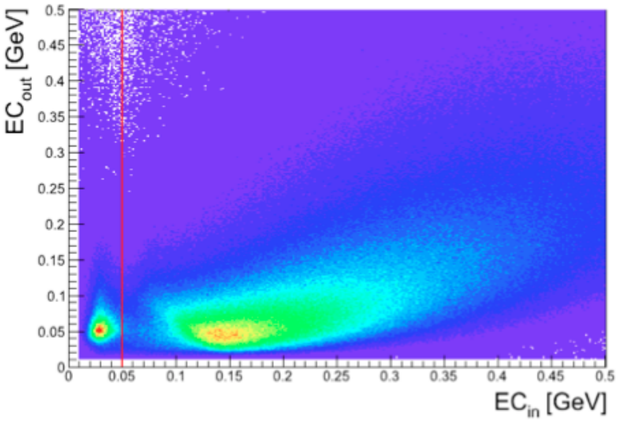

Fig. S5: Energy deposited in the inner vs. outer parts of the EC. Events shown are electron candidates that pass the initial vertex cut, the EC fiducial cuts, and the CC photo-electron cut. The peak at low energy deposited in the inner layer of the EC is associated with pions. The EC$_{in}$ energy cut is marked by the red line.

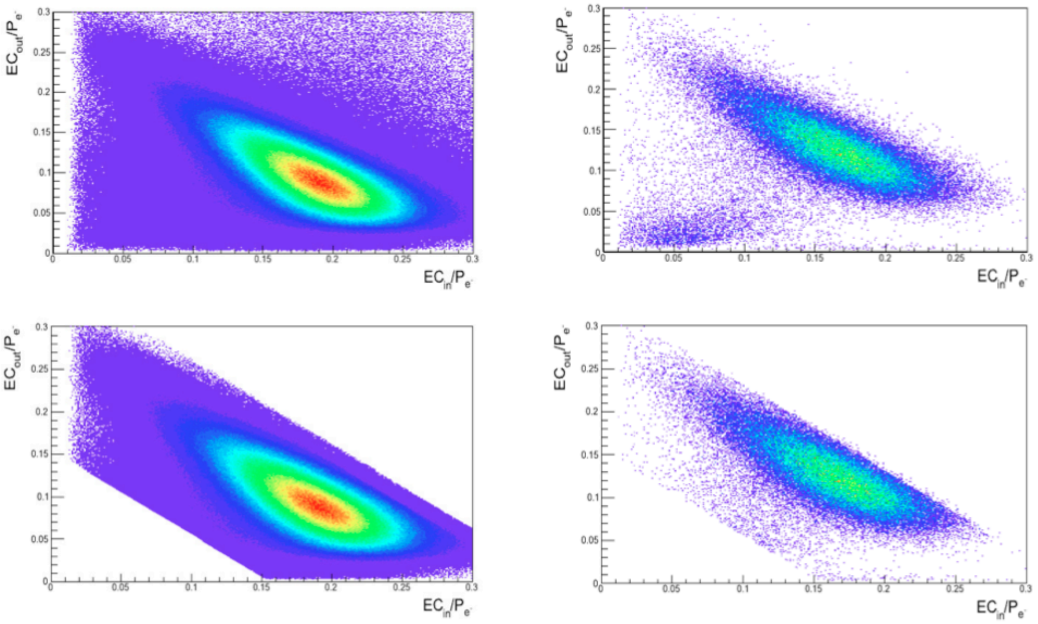

Fig. S6: Momentum normalized energy deposited in the inner vs. outer parts of the EC for all events (left) and for x_B>1 events (right). Top: Events shown are electron candidates that pass the initial vertex, EC fiducial, CC photo-electrons, and EC$_{in}$ energy cuts. The electron band can be seen stretching from the upper left to the lower right corners of the plots. Bottom: Events that pass the mentioned cuts and the additional cut on (EC$_{in}$ + EC$_{out}$)/p.

3.2. Proton Identification

Two detection systems are used for proton identification: the wire-chamber based tracking system, and the scintillator-counter based Time-Of-Flight (TOF) system.

Protons are identified by comparing the reconstructed momentum of positively charged particles, as measured by the tracking system, with their measured flight time. The difference between the measured TOF and that calculated using the reconstructed momentum and path-length, assuming the particle is a proton, is known as the "corrected TOF". If the measured particle is a proton, then the corrected TOF will equal zero within the measurement resolution. Fig. S7 shows the corrected TOF distribution vs. momentum for a random sample of positively charged particles.

For each of 50 bins in proton momentum, the corrected TOF was histogrammed and fitted with a Gaussian function. In order to extract a continuous parameterization, we fit the ±2σ values to a polynomial function of the momentum up to 2.8 GeV/c. Particles are identified as protons if their corrected TOF is within ±2σ of the mean as determined by this polynomial function, see Fig. S7.

Fig. S8 shows the energy deposited in the TOF counters vs. momentum for protons selected using the procedure described above. The observed energy deposit profile is characteristic of protons and is evidence for the quality of the proton identification.

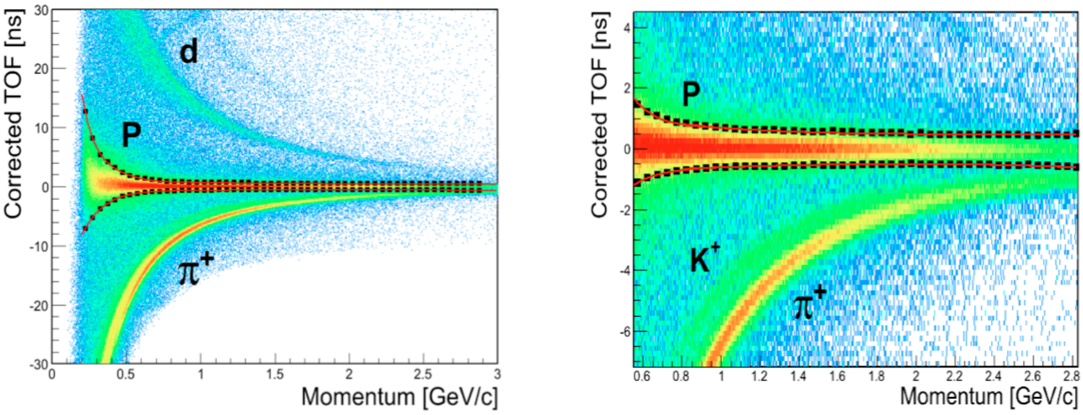

Fig. S7: Corrected TOF vs. momentum for a randomly chosen sample of positively charged particles. Left: the full proton momentum acceptance of CLAS. Right: For the higher momentum region alone. The protons should be centered at Corrected TOF = 0. The black squares mark the ±2σ limits for each bin for identifying protons, centered at Corrected TOF = 0. The red lines show the polynomial fit to the black squares, used to select protons for further analysis. See text for more details.

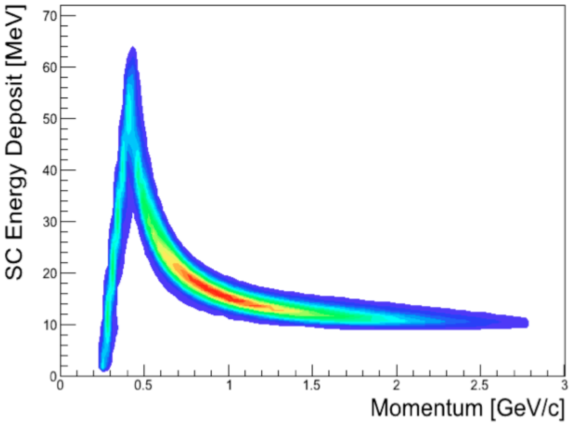

Fig. S8: Energy deposited in the TOF counters vs. momentum for identified protons.

4. Target setup and vertex reconstruction

The CLAS-EG2 run period used a specially designed double target, consisting of a 2 cm long liquid deuterium cryo-target followed by a solid-target (*46*). The cryo-target and the solid-target were separated by 4 cm and were both kept simultaneously in the beam-line. A special control system allowed changing between six different solid targets (thin and thick Al, Sn, C, Fe, and Pb, all in natural abundance) during the experiment, see Fig. S9. This double target setup was meant to allow a precise comparison of scattering off medium and heavy nuclei relative to deuterium for Hadronization and Color Transparency studies. Table S4 lists the physical characteristics of the different solid targets. The density of the solid targets was chosen to be about the same as the deuterium target, except the Pb target due to background considerations. The main data collected during the experiment was for a target configuration of deuterium + C, Fe, and Pb. The data analyzed here is for scattering from the solid targets alone and also includes data from Al runs with an empty cryo-target cell.

Electrons and protons scattering from the solid target were selected using vertex cuts. Figs S10 and S11 show the reconstructed vertex distribution of electrons and protons as detected in different sectors of CLAS. The red lines mark the regions used to define the cryo-target and the solid-target. The small bump observed between the solid and cryo-target target is due to a reference foil placed 2 cm downstream the cryo-target. The vertex distributions shown are corrected for beam misalignment effects that add a systematic (sector dependent) angular dependence to the reconstructed vertex. As can be seen, the corrected vertex distributions from all sectors agree for the different target locations. Fig S10 also shows agreement between the reconstructed vertex for all events and for x_B>1 events alone. The latter corresponds to higher electron momenta and smaller scattering angles.

Fig S12 shows the vertex reconstruction resolution extracted from a Gaussian fit to the corrected vertex distribution in the solid target region. The effect of the scattering angle on the resolution is removed by multiplying the observed resolution with the sine of the particle scattering angle. This is equivalent to extracting the resolution at 90^{o}. The observed decrease in the resolution at low momentum is due to multiple scattering. As can be seen, even at the smallest electron and proton momentum and scattering angles (15^{o} and 20^{o} respectively), the vertex resolution is good enough to separate the targets which are 4 cm apart.

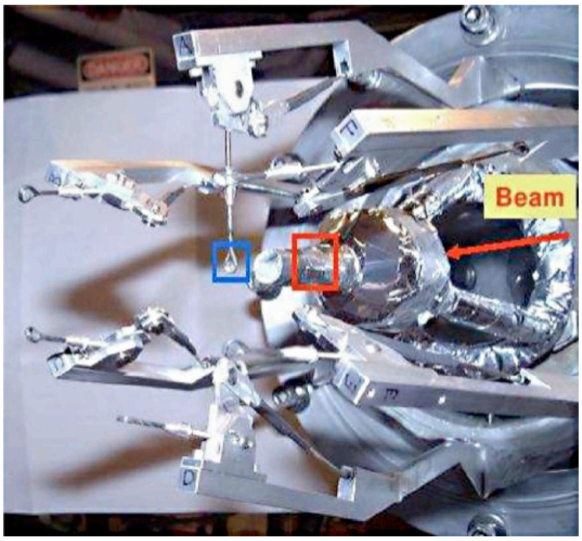

Fig. S9: The EG2 target. The red square shows the center of the LD_2 target cell. The blue square shows the solid target. The red arrow marks the approximate beam direction. As can be seen, the beam passes throughout both targets simultaneously.

Table S4: The physical characteristics of the different solid targets used during the EG2 run period. Note that all targets are natural isotopic abundance

Target	Radius [cm]	Thickness [mm]	Thickness [g/cm^2]	Radiation Length
C	0.15	1.72	0.300	0.009
Al (thin)	0.15	$1.5\text{x}10^{-3}$	~0	~0
Al thick	0.15	0.58	0.156	0.007
Fe	0.15	0.4	0.315	0.023
Sn	0.15	0.31	0.228	0.026
Pb	0.15	0.14	0.159	0.025

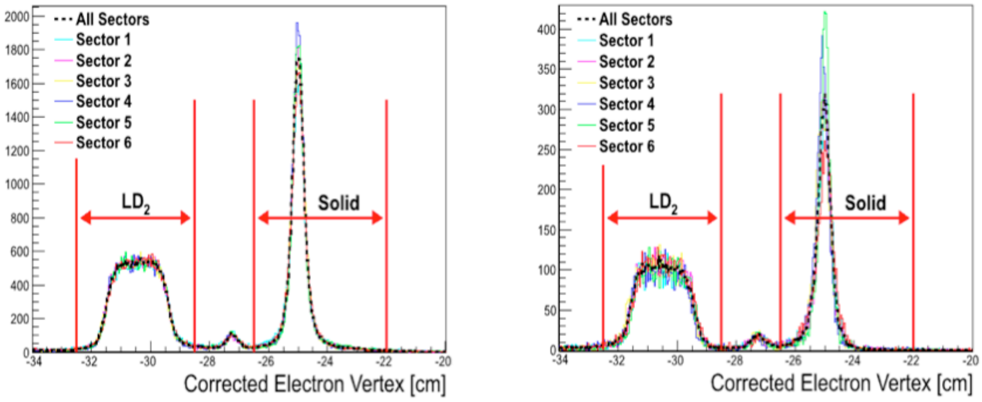

(a) All Events (b) $x_B > 1$

Fig. S10: The corrected electron vertex distribution for each sector separately (solid colored lines) and for all sectors combined (dashed black line). All distributions are normalized to the same number of events. The solid red lines show the software cut defining the region of the solid and liquid targets. The small bump in between the two targets is due to a reference foil placed 2 cm downstream the cryo-target.

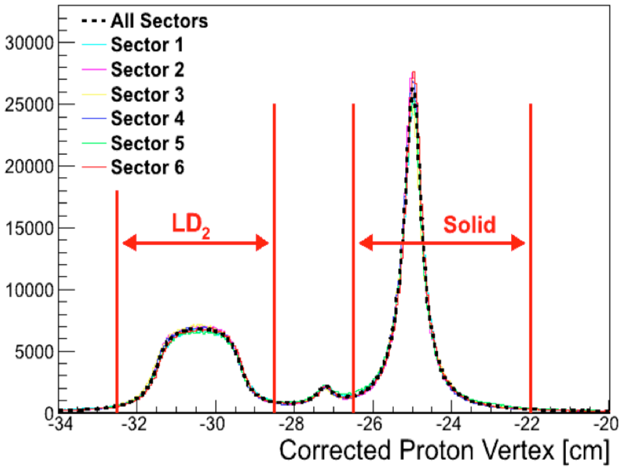

Fig. S11: Same as Fig S12 for protons.

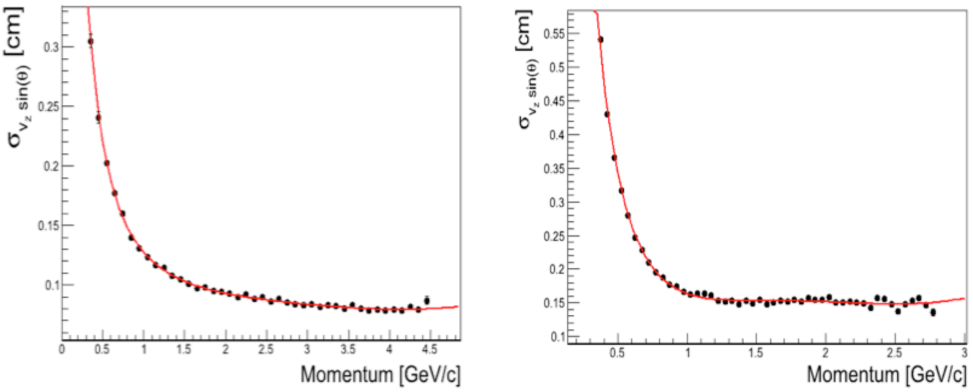

(a) Electrons (b) Protons

Fig. S12: Vertex reconstruction resolution for electrons and protons as a function of their momentum. The effect of the scattering angle on the resolution was removed by multiplying the vertex distribution by sin(θ). The red line is a fit to the resolution as a function of the momentum.

5. Event Selection and Characterization

5.1. Selection of A(e,e'p) events

To identify events where the electron scattered from a pn- or pp- SRC pair in the nuclear ground state, one must work in a kinematic regime in which competing processes are suppressed. Such processes include: Meson Exchange Currents (MEC), Isobar Configurations (IC), and Final State Interactions (FSI). Fig S13 shows the different Feynman diagrams associated with these reaction channels. In the figure, the bottom left diagram describes FSI between the nucleons in the SRC pair and bottom Right diagram describes FSI with the A-2 system. Notice that the FSI within the SRC pair conserve its nucleonic composition and c.m. momentum. In what follows (except if mentioned otherwise) FSI refers to the process described in the bottom right diagram.

The amplitude of the MEC diagram decreases faster then the SRC one by a factor of $1/Q^2$. Additionally, for a given value of four-momentum transfer Q^2, IC are suppressed in the $x_B = Q^2/(2m_p\omega) > 1$ region. An added advantage of measuring at large-Q^2 is that the struck (leading) proton has high momentum ($|P_{lead}| > 1$ GeV/c), and one can use the Glauber approximation to evaluate the contribution of FSI.

To simultaneously minimize both FSI and IC, we choose $x_B>1$, large-Q^2, anti-parallel kinematics, in which the initial momentum of the struck proton is directed opposite (anti-parallel) to the virtual photon (i.e., to the transferred momentum). In such kinematics, after absorbing the virtual photon, the struck proton is emitted in the same direction as the virtual photon, but with smaller momentum. See (*47,13*) and references within.

We used the following cuts to select A(e,e'p) events that are dominated by scattering off 2N-SRC pairs (*9,48*):

1. $x_B > 1.2$,
2. $300 < |\vec{P}_{\rm miss}| < 1000$ MeV/c,
3. $\theta_{pq} < 25^o$,
4. $0.62 < |\vec{P}|/|\vec{q}| < 0.96$ and
5. $m_{\rm miss} < 1.1$ GeV/c^2,

where $\vec{P}_{\rm miss} = \vec{P} - \vec{q}$ is the initial (missing) momentum of the leading proton and $m^2_{\rm miss} = [(\vec{q},\omega) + (\vec{0},m_d) - (\vec{P},E_p)]^2$ is the missing mass of the reaction assuming scattering off a stationary nucleon pair. m_d is the deuteron mass and E_p is the proton final energy, $E_p = \sqrt{\vec{P}^2 + m_p^2}$. Cuts (2-5), and mainly cut (1), together with the CLAS acceptance are sufficient to obtain large Q^2, i.e. largely > 1.5 GeV/c^2, with a small tail extending down to ~1.3 GeV/c^2 (see Fig. S15). Cut (2) selects scattering off high initial-momentum protons (*21*). Cuts (3) and (4) are used to select the leading protons of the reaction (see details below) and cut (5) is used to further suppress pion production and isobar contribution.

Protons knocked out of the nucleus with high momentum and a small angle with respect to the momentum transfer vector, $\vec{q}$, are more likely to be the ones struck by the virtual photon. Fig. S16 shows the relative angle between the virtual photon and the detected proton (θ_{pq}) vs. the ratio between the detected proton momentum and the momentum transfer, $|\vec{P}|/|\vec{q}|$. This plot includes only A(e,e'p) events that pass the kinematical cuts described above ($x_B > 1.2$ and $300 < |\vec{P}_{\rm miss}| < 1000$ MeV/c). To select these struck (i.e., leading) protons, we cut on $\theta_{pq} < 25^o$ and $0.62 < |\vec{P}|/|\vec{q}| < 0.96$.

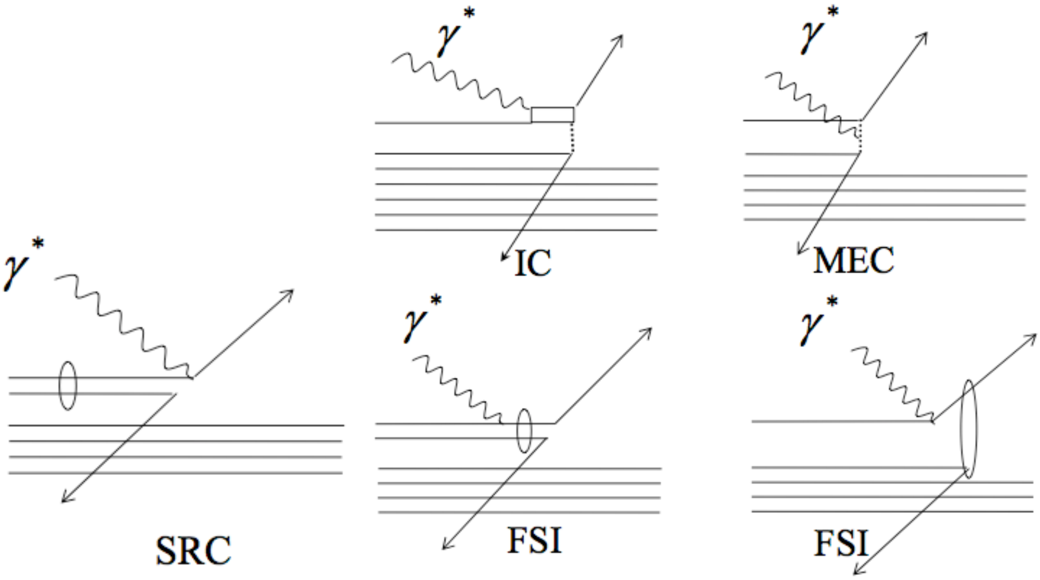

Fig. S13: Feynman diagrams of the different possible reaction channels, leading to a two-nucleon final state. The γ^* indicates the virtual photon that carries the momentum and energy transferred from the electron to the proton. The double line indicates an excited state of the proton, the dashed line indicates a meson, and the ellipse indicates an interaction between two nucleons. See text for details. The difference between the two FSI diagrams shown is that one entails FSI between the nucleons of the pair (left diagram) and the other FSI of uncorrelated nucleons (right diagram).

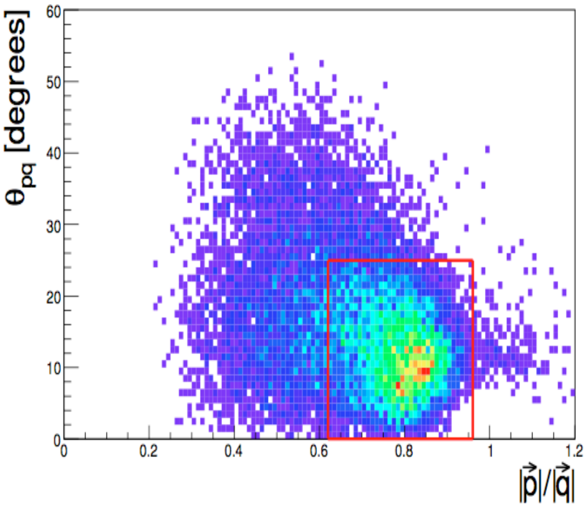

Fig. S14: The relative angle between the detected proton and the momentum transfer $\vec{q}$ vs. the ratio of the detected proton momentum and the momentum transfer, $|\vec{P}|/|\vec{q}|$. Only C(e,e′p) events with $x_B > 1.2$ and $300 \leq |P_{miss}| \leq 1000$ MeV/c are shown. The red box shows the cut applied to select leading protons.

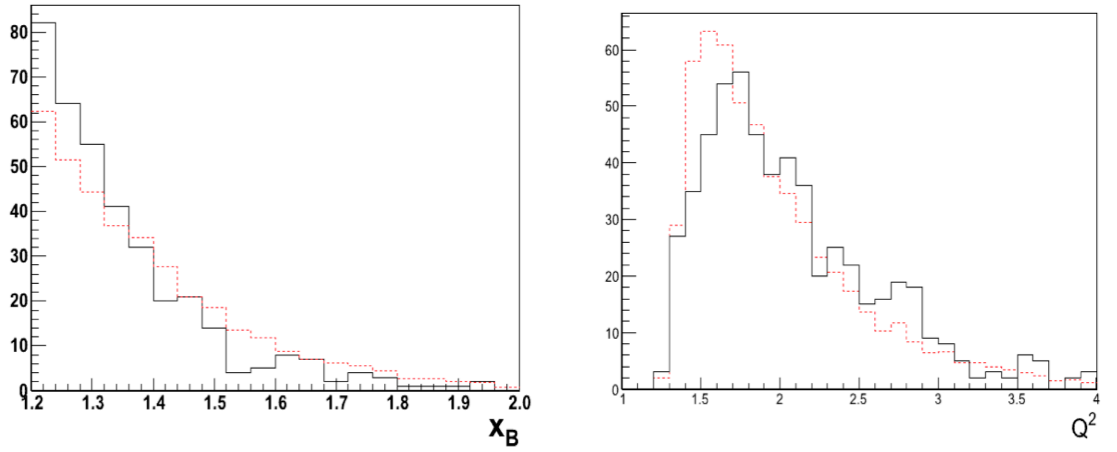

Fig. S15: x_B and Q^2 distributions for the selected C(e,e'pp) events (solid black) and C(e,e'p) (dashed red) events, normalized according to the number of C(e,e'pp) events. Within statistical uncertainties the distributions agree and the detection of the additional, recoil, proton in the C(e,e'pp) case does not bias the distribution.

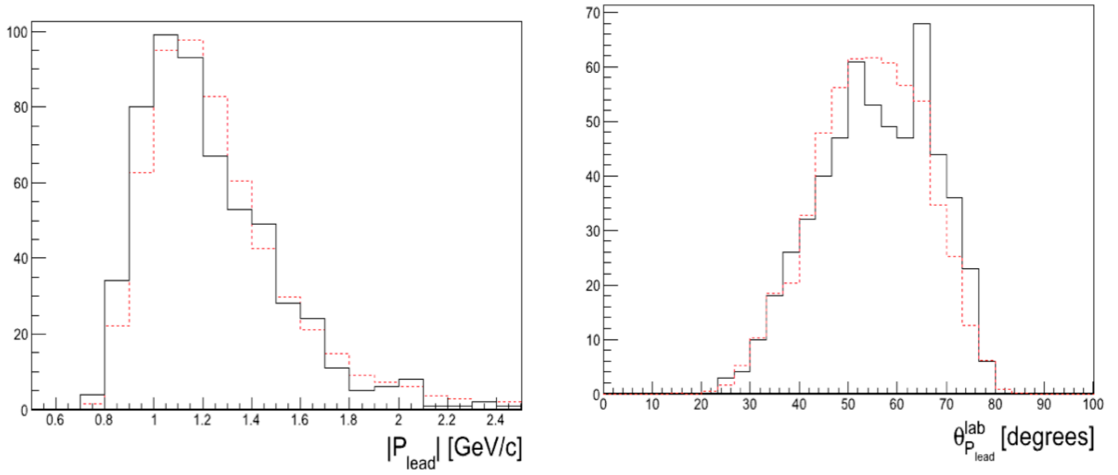

Fig. S16: Same as Fig. S15 for the momentum and angle distribution of the leading proton.

5.2. Selection of A(e,e'pp) events

A(e,e′pp) events are defined as A(e,e'p) events with an additional "recoil" proton detected with momentum $|\vec{P}_{\text{recoil}}| > 350$ MeV/c, the threshold for efficient proton detection in the CLAS. There were no A(e,e'pp) events in which both protons passed the leading proton selection cuts described above.

5.3. Characterization of the A(e,e'p) and A(e,e'pp) events

The kinematical distributions for C(e,e'p) and C(e,e'pp) events that pass the event-selection cuts described above are shown below (Fig S15 to S18). Equivalent distributions were obtained for the other nuclei, see section 2.4.4.

The missing energy distributions presented in Fig S20 are defined as:
Eq. S4

$$\begin{aligned} E_{miss} &= \omega - KE_p^{lead} - KE_{A-1} \\ E_{2miss} &= \omega - KE_p^{lead} - KE_p^{recoil} - KE_{A-2} \end{aligned},$$

where ω is the energy transferred by the virtual photon, KE_p^{lead} and KE_p^{recoil} are the measured leading and recoil proton kinetic energies, and KE_{A-1} and KE_{A-2} are the reconstructed (small) kinetic energies of the undetected recoiling ($A-1$) and ($A-2$) nuclei.

Fig. S19 shows the angular distribution of the recoil proton relative to the missing momentum of the leading proton. The data show a strong backward peak. In the absence of FSI, this angle equals the opening angle of the two protons in the initial state. To ensure that this distribution is due to the measured reaction and not to the CLAS acceptance and our event selection cuts, we also examine the opening angle distribution of two protons from mixed events, i.e. the opening angle distribution of events where the leading and recoil proton are taken from two different events that pass the cuts. This distribution is shown by the dashed line in Fig. S19. As can be seen, the data is far more backward-peaked than the mixed-events. We note that a mixed-event sample in which events were only mixed within the same electron kinematics bin (x_B and Q^2) gave the same result, for each bin separately, as the full mixing shown here.

This distribution is a strong signature for pp-SRC pairs (*49*), providing the first observation of pp-SRC pair knockout from nuclei heavier than carbon. In the absence of FSI, the width of the distribution is due to the center-of-mass motion of the pp-SRC pairs. This motion is predicted to depend only weakly on A (*40,49*). FSI, which increase strongly with A, would broaden this backwards peak. The width of the backwards peak is similar for all nuclei. This is consistent with the weak A dependence of the pp-SRC c.m. momentum distribution and it is inconsistent with FSI. We note that the c.m. momentum reconstruction resolution was estimated from exclusive d(e,e'ppπ^-) measurements to be about 20 MeV/c. This has a negligible effect of ~2% on the measured width of the c.m. momentum distribution.

Fig. S20 shows the opening angle of the recoil proton, $\vec{P}_{recoil}$ and the momentum transfer, $\vec{q}$. This distribution peaks between 30° and 50°. Knockout of the leading proton followed by a collision (FSI) with the second proton would produce a peak at around 70° – 90° (depending on q). This is further evidence that the two protons came from knockout of one proton and emission of its correlated partner, rather than from knockout of one proton followed by final state rescattering.

To fully characterize the kinematics of the measured reaction, Fig S21 shows the angular distribution of the missing momentum of the leading proton and the momentum transfer vector. As can be seen, this distribution also peaks at large backward angles (~150°), evidence of the anti-parallel nature of our kinematics.

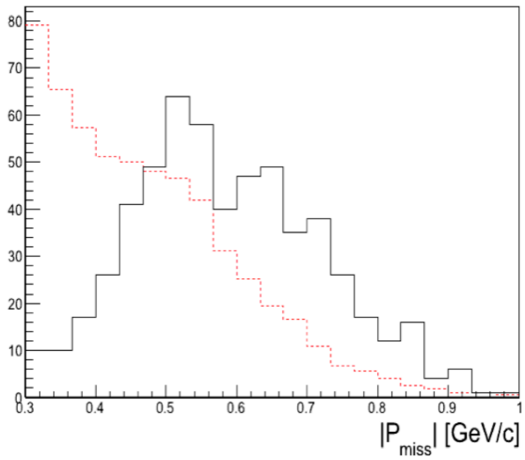

Fig. S17: Same as Fig. S15 for the missing momentum distribution. Note that in the case of ^{12}C(e,e'pp), the missing momentum shown is calculated in the same way as that of the ^{12}C(e,e'p) reaction, and is calculated using the leading proton of the event: $\vec{p}_{miss} = \vec{p}_{leading} - \vec{q}$. See text for details.

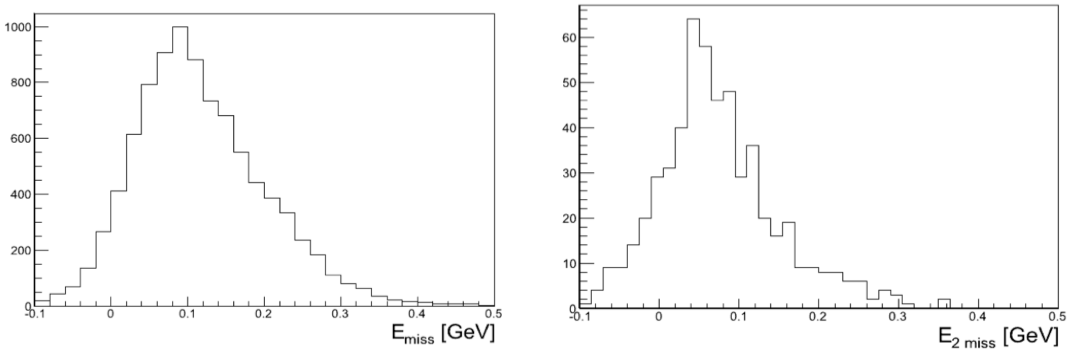

Fig. S18: Missing energy distribution for C(e,e'p) (left) and C(e,e'pp) (right) events. The non-physical tail at $E_{\text{miss}} < 0$ is due to the experimental resolution.

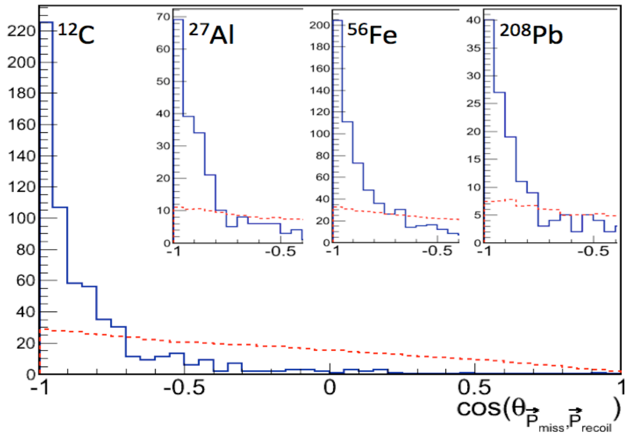

Fig. S19: The distribution of the cosine of the recoil proton angle relative to the missing momentum of the leading proton for C. The insert shows the distribution for other nuclei (Al, Fe, and Pb). The dashed red line is the distribution of the random phase-space extracted from mixed-events. See text for details.

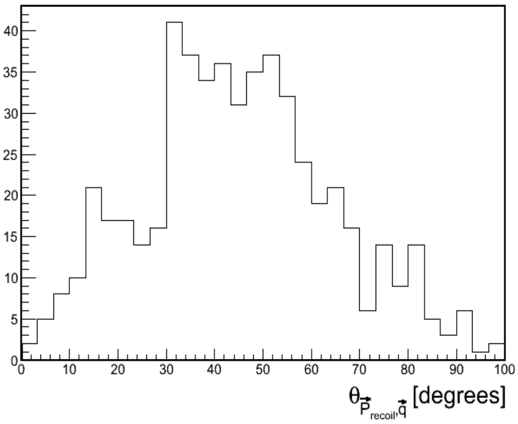

Fig. S20: The relative angle of the momentum transfer vector and the recoil proton. See text for details.

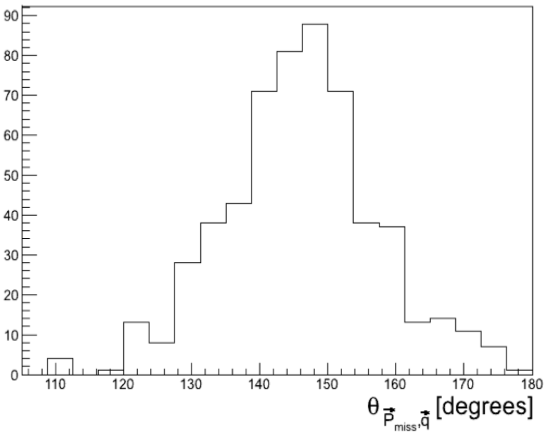

Fig. S21: The relative angle of the momentum transfer vector and the missing momentum of the leading proton. See text for details.

5.4. Kinematical distribution from different targets

Fig S22 to S26 show the electron (x_B, Q^2) and proton (θ_p, |P|) kinematics for (e,e'p) and (e,e'pp) events from C (Black), Al (Red), Fe (Green), and Pb (Blue). Within statistical uncertainties the kinematical distributions for all targets are consistent.

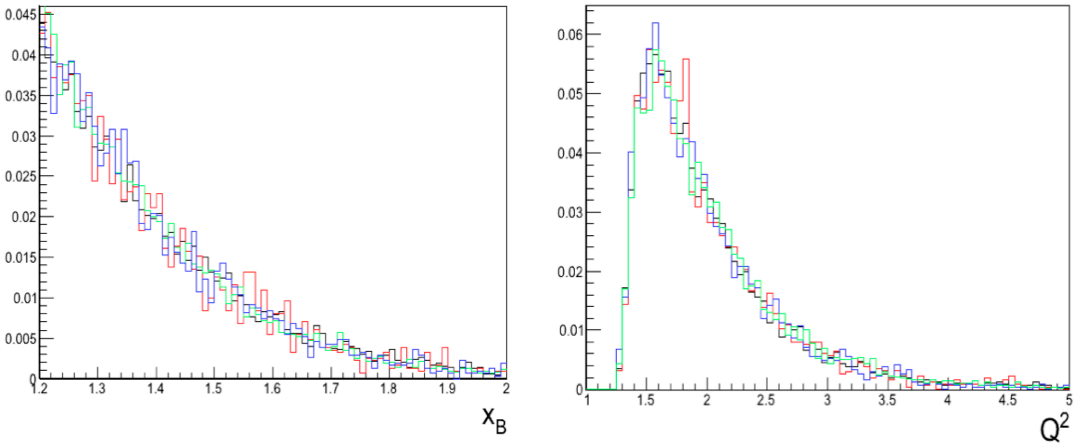

Fig. S22: The electron kinematics (x_B and Q^2) for A(e,e'p) events from all measured nuclei: C (Black), Al (Red), Fe (Green), and Pb (Blue), normalized to the same number of events.

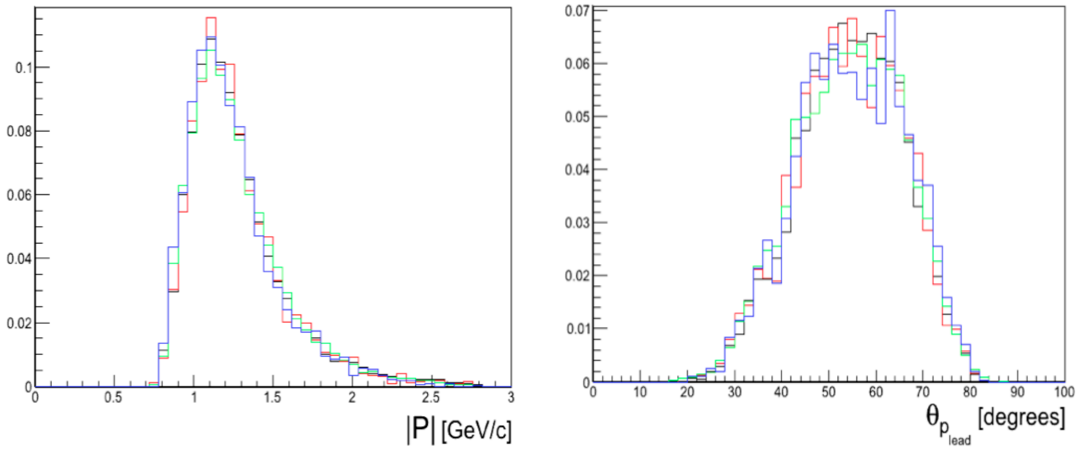

Fig. S23: The leading proton kinematics (|P| and θ) for A(e,e'p) events from all measured nuclei: C (Black), Al (Red), Fe (Green), and Pb (Blue).

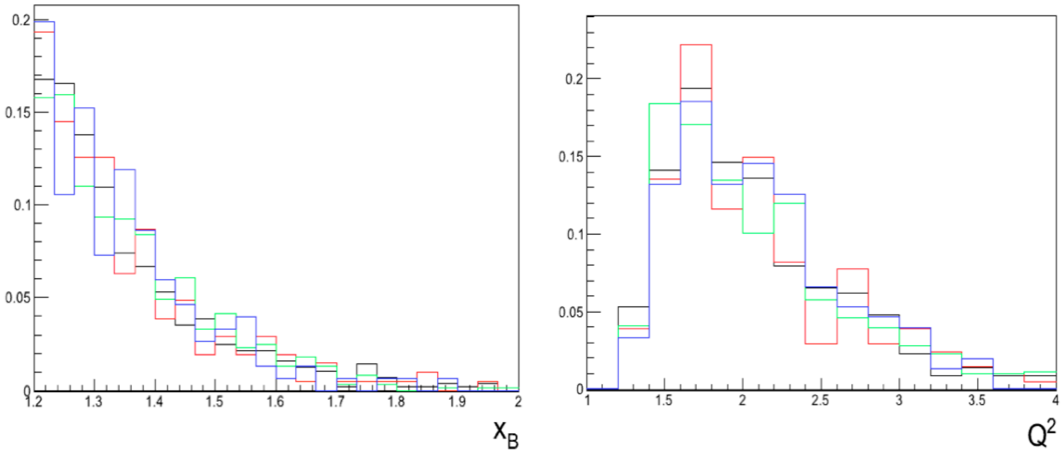

Fig. S24: The electron kinematics (x_B and Q^2) for A(e,e'pp) events from all measured nuclei: C (Black), Al (Red), Fe (Green), and Pb (Blue).

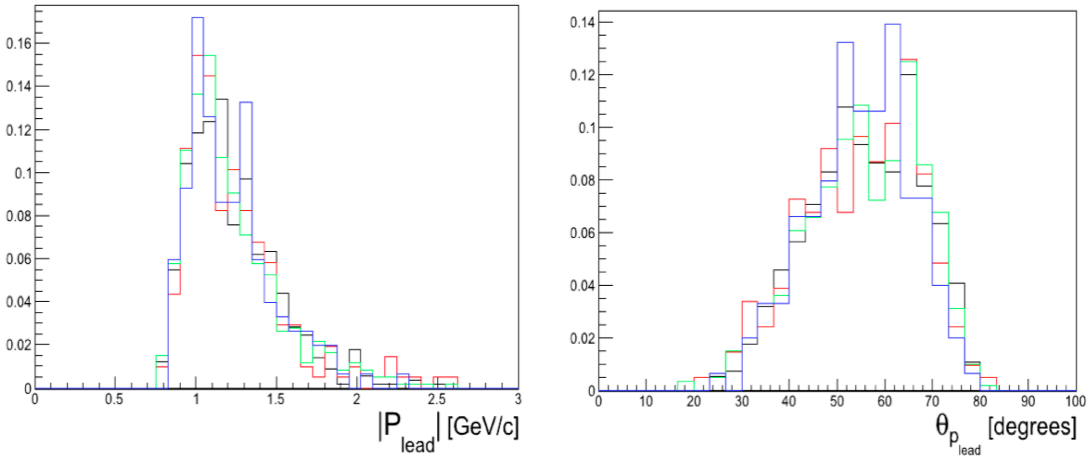

Fig. S25: The leading proton kinematics (|P| and θ) for A(e,e'pp) events from all measured nuclei: C (Black), Al (Red), Fe (Green), and Pb (Blue).

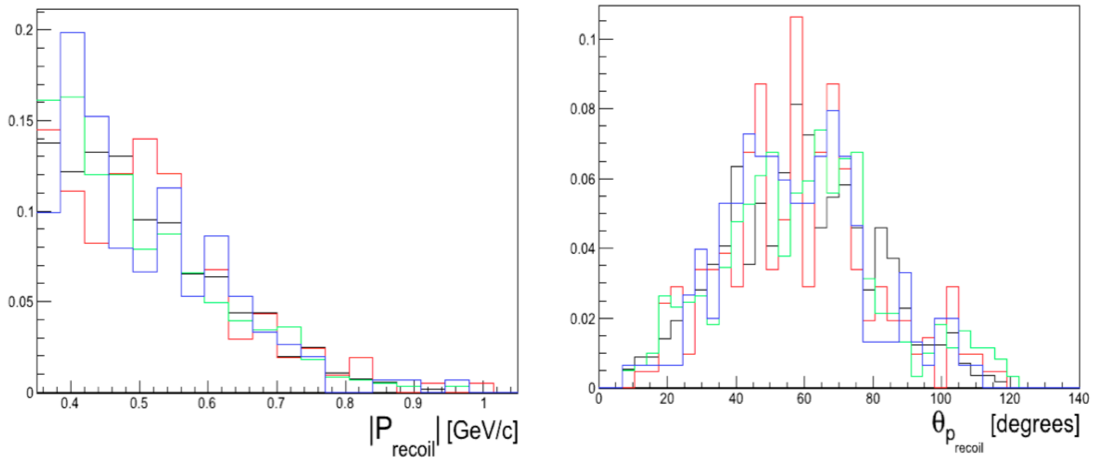

Fig. S26: The recoil proton kinematics (|P| and θ) for A(e,e'pp) events from all measured nuclei: C (Black), Al (Red), Fe (Green), and Pb (Blue).

6. Analysis and Results

6.1. Extraction of the cross section double-ratio

The extraction of the A(e,e'p)/C(e,e'p) and A(e,e'pp)/C(e,e'pp) cross-section ratios and the [A(e,e'p)/C(e,e'p)] / [A(e,e'pp)/C(e,e'pp)] cross-section double-ratio from the measured yields (number of events), requires three corrections:

1. Detector acceptance corrections,
2. Radiative corrections,
3. Overall normalization corrections for target density and accumulated beam charge.

Acceptance correction. As the momentum density for all target nuclei has the same shape at high momentum (*10,11*), and because during the experiment all solid targets were held in the same location, the detector instantaneous rate was kept constant, and the kinematics of the measured events from all target nuclei are identical (see Figs S22 – S26), detector acceptance effects cancel in each of the A(e,e'p)/C(e,e'p) and A(e,e'pp)/C(e,e'pp) cross section ratios.

Radiative corrections. Due to the large acceptance of CLAS, radiative effects affect mainly the electron kinematics. Such corrections were previously calculated (*21*) for the extraction of the A(e,e'p)/C(e,e'p) cross section ratio. As the electron kinematics are the same for the A(e,e'p) and A(e,e'pp) reactions (see Fig S15), the same corrections are used in the extraction of the A(e,e'pp)/C(e,e'pp) cross-section ratio and therefore cancel in the extraction of the A(e,e'p)/C(e,e'p) / A(e,e'pp)/C(e,e'pp) cross-section double-ratio.

Target density and beam charge corrections. The A(e,e'p) and A(e,e'pp) reactions were measured simultaneously and therefore the target density and accumulated beam charge cancels in the double-ratio.

Summary:

1. Extraction of the A(e,e'p)/C(e,e'p) and A(e,e'pp)/C(e,e'pp) cross-section ratios requires radiative corrections and normalization corrections, accounting for the target density and accumulated beam charge. The latter was measured by a Faraday Cup downstream of the beam line.
2. The extraction of the A(e,e'p)/C(e,e'p) / A(e,e'pp)/C(e,e'pp) cross-section double-ratio does not require any corrections as these cancel in the double ratio. Therefore the cross-section double ratio equals the measured yield double ratio.

Fig. S27 shows the *A* dependence of the measured A(e,e'p)/C(e,e'p) (*21*) and A(e,e'pp)/C(e,e'pp) cross section ratio. The inclusive A(e,e')/C(e,e') cross section ratio, measured at large-Q^2 and $x_B>1.5$ (*11*), is also shown for completeness. The latter was not measured for Fe/C and Pb/C but instead for Cu/C and Au/C. We also show absolute cross section ratios, instead of per-nucleon ratios reported in Ref. (*11*). The measured ratios are listed in Table S5. The uncertainty on the (e,e'p) cross-section ratio includes statistical uncertainty and cut sensitivity uncertainty as detailed in Ref. (*21*). The uncertainty on the (e,e'pp) cross-section ratio is dominated by statistics but also includes 4% systematical uncertainty mainly due to momentum corrections.

Fig. S28 (Table S6) shows (lists) the missing momentum dependence of the A/C (e,e'p)/(e,e'pp) cross section double ratio. We note that for both single- and double-proton final state the missing momentum is obtained from the (e,e'p) reaction using the leading proton of the event. The errors shown are statistical alone. The dashed red line shows the result of a fit to a constant. As can be seen, within statistical uncertainties, the cross section double ratio is independent of the missing momentum over the range of ~300 to 900 MeV/c. We note that a linear fit did not yield an improved agreement with the data and results in a slope parameter consistent with zero.

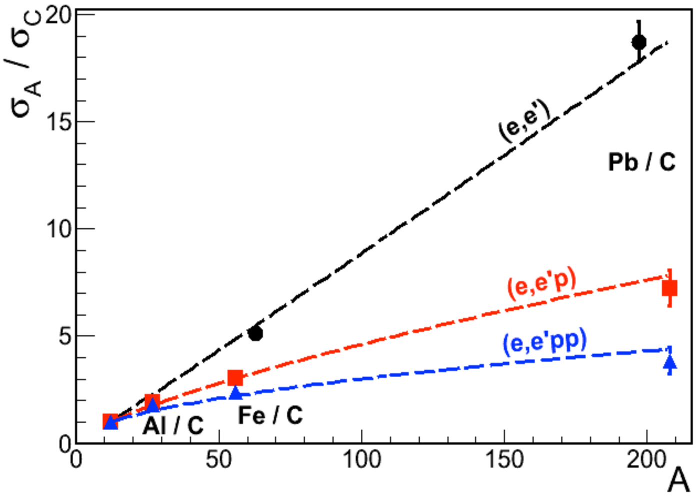

Fig. S27: The A dependence of the measured (e,e'), (e,e'p) and (e,e'pp) cross section ratios for nuclei relative to Carbon. The (e,e') ratios are taken from (*8*). The lines are fit to a power law in the form of $\sigma_A/\sigma_C \propto (A/12)^\alpha$ which result in $\alpha = 1.03\pm0.01$ for (e,e'), 0.72±0.02 for (e,e'p), and 0.52±0.03 for (e,e'pp).

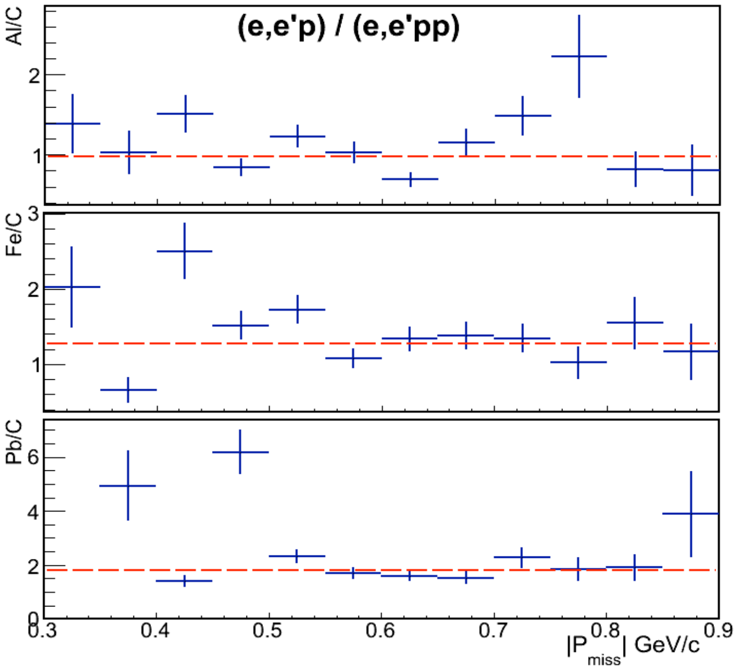

Fig. S28: The missing momentum dependence of the A/C (e,e'p)/(e,e'pp) double ratio. The dashed red lines are the result of a fit to a constant. Errors shown are statistical only.

Table S5: The measured (e,e'), (e,e'p) and (e,e'pp) cross section ratio for nuclei relative to Carbon. See text for details.

A	**C**	**Al**	**Fe**	**Pb**
A(e,e') / C(e,e') (*11*)	1	N/A	5.13 ± 0.25 [Cu/C]	17.7 ± 0.9 [Au/C]
A(e,e'p) / C(e,e'p)	1	1.9 ± 0.08	3.0 ± 0.2	7.2 ± 0.8
A(e,e'pp)/C(e,e'pp)	1	1.8 ± 0.2	2.4 ± 0.2	3.8 ± 0.6

Table S6: The missing momentum dependence of the A/C (e,e'p)/(e,e'pp) double ratio. Momentum values listed represent bin centers, which are each ±25 MeV/c wide. See text for details.

p_{miss}	Al/C	Fe/C	Pb/C
325	1.38 ± 0.37	2.02 ± 0.54	X
375	1.03 ± 0.27	0.65 ± 0.17	4.93 ± 1.30
425	1.51 ± 0.23	2.50 ± 0.38	1.40 ± 0.22
475	0.84 ± 0.11	1.51 ± 0.19	6.18 ± 0.82
525	1.23 ± 0.14	1.73 ± 0.19	2.32 ± 0.27
575	1.02 ± 0.13	1.07 ± 0.13	1.70 ± 0.22
625	0.69 ± 0.09	1.30 ± 0.17	1.61 ± 0.22
675	1.14 ± 0.17	1.37 ± 0.18	1.53 ± 0.22
725	1.48 ± 0.24	1.34 ± 0.19	2.28 ± 0.38
775	2.22 ± 0.51	1.02 ± 0.22	1.85 ± 0.44
825	0.82 ± 0.22	1.54 ± 0.35	1.91 ± 0.49
875	0.81 ± 0.32	1.16 ± 0.37	3.88 ± 1.58

6.2. Glauber Calculations

To extract information on the characteristics of SRCs in nuclei, the measured cross section must be corrected for Final-State Interaction (FSI) effects. These include Nuclear Transparency and Single Charge Exchange (SCX).

Nuclear Transparency (*T*) is the probability that a knocked out proton escapes the nucleus without further interaction.

Single-Charge Exchange is the probability that a struck neutron elastically scatters off a proton on its way out of the nucleus, leading to the detection of the proton in the final state.

These probabilities are calculated within a Glauber approximation according to (*22*), using effective cross-sections, as described below.

6.2.1. A(e,e'p)

Within the Glauber approximation the probability that a proton escapes the nucleus without further interaction is given by:
Eq. S5

$$T_p = \frac{1}{A}\int \rho(r)\exp\left\{-\sigma_{eff}\int \rho(r)\hat{z}\,dl\right\}d^3r,$$

where A is the nuclear mass number, $\rho(r)$ is the nuclear density distribution function, and σ_{eff} is the effective nucleon-nucleon cross section. We use the same procedure as in

Ref. (*50*), but following (*21,23*) we use world data on (e,e'p) nuclear transparency with no SRC corrections applied. Therefore, the resulting effective cross sections obtained for leading and recoil protons with final momenta in the range of 1 – 2 GeV/c and ~600 MeV/c are 37 ± 7 mb and 22 ± 5 mb respectively, slightly different from the values shown in Table III of Ref. (*50*). The uncertainty of the effective cross sections was chosen to equal 20%, which ensures full reproduction within uncertainties of the world-data transparency measurements on all measured nuclei. These uncertainties are larger than the 10-15% uncertainties quoted in Ref. (*50*).

The calculated nuclear transparencies for single-nucleon knockout from C, Al, Fe, and Pb are listed in Table S7. The uncertainty of the calculated transparency is due to the uncertainty in the effective nucleon-nucleon cross section used in the calculation (see above).

Table S7: The calculated nuclear transparency and SCX probabilities. The calculations were performed within a Glauber approximation using effective cross sections. The uncertainty of the calculations represents a 1σ uncertainty resulting from an assumed 20% uncertainty on the transparency cross-sections and 100% on the SCX cross-section.

A	**C**	**Al**	**Fe**	**Pb**
T_{p}	0.53 ± 0.05	0.43 ± 0.05	0.34 ± 0.04	0.22 ± 0.03
T_{recoil}	0.65 ± 0.05	0.56 ± 0.06	0.47 ± 0.06	0.33 ± 0.05
T_{pp}	0.44 ± 0.04	0.35 ± 0.04	0.26 ± 0.03	0.16 ± 0.02
P_{SCX}	0.02 ± 0.02	0.03 ± 0.03	0.04 ± 0.04	0.07 ± 0.06

6.2.2. A(e,e'pp)

Similarly to Eq. S5, the nuclear transparency for two-proton knockout reactions is given by:

Eq. S6

$$T_{pp} = \frac{1}{A}\int \rho(r)\exp\left\{-\sigma_{eff}^{leading}\int \rho(r)\hat{z}\,dl\right\}\exp\left\{-\sigma_{eff}^{recoil}\int \rho(r)\hat{n}\,dl\right\}d^3r,$$

where $\sigma_{eff}^{leading}$ and σ_{eff}^{recoil} are effective nucleon-nucleon cross sections for high and low momentum protons. This takes into account the spatial correlation of the two outgoing protons.

The combined nuclear transparencies for both the leading and recoil protons (T_{pp}) emerging from C, Al, Fe, and Pb are also listed in Table S7. As expected, the conditioned transparency for two-nucleon knockout is larger than that for the independent knockout of two nucleons, i.e. $T_{pp} < T_{p1} \times T_{p2}$. The uncertainty on the calculated transparency is due to the uncertainty in the effective nucleon-nucleon cross sections used in the calculation.

6.2.3. Single Charge Exchange

The SCX probability is defined as $P_{\mathrm{SCX}} = 1 - T_{\mathrm{SCX}}$ where T_{SCX} is defined by Eq. S5 and is calculated using a cross section of 1±1 mb (*24*). As there are no modern measurements of the SCX cross section available we apply a large uncertainty of 100% on its value.

The calculated SCX probabilities for neutron knockout from C, Al, Fe, and Pb are also listed in Table S7.

6.3. Extraction of np/pp SRC pairs ratio

6.3.1. Formalism

In the kinematics of this measurement, assuming scattering off 2N-SRC pairs (*9,48*) with no FSI, the A(e,e'p) and A(e,e'pp) cross sections can be expressed as a function of the number of NN-SRC pairs in the nucleus and the electron-proton cross section:

Eq. S7

$$
\begin{aligned}
A(e,e'pp) &\propto \# pp_A \cdot 2\sigma_p \\
A(e,e'p) &\propto \# pp_A \cdot 2\sigma_p + \# np_A \cdot \sigma_p
\end{aligned} ,
$$

where $\#pp_{\mathrm{A}}$ and $\#np_{\mathrm{A}}$ are the number of proton-proton and proton-neutron pairs in nucleus A and σ_p is the electron-proton cross section.

Taking FSI effects into account requires correcting Eq. S7 for the probability that the proton(s) in the reaction escape the nucleus (their nuclear transparency) and/or undergo Single-Charge Exchange (SCX). Written in terms of these quantities the cross sections are given by:

Eq. S8

$$
\begin{aligned}
A(e,e'pp) &\propto \# pp_A \cdot 2\sigma_p \cdot T_{pp}^A + \# np_A \cdot \sigma_n \cdot P_{SCX}^A T_{recoil}^A \\
&= \# pp_A \cdot 2\sigma_p \cdot \left(T_{pp}^A + \frac{1}{2} \frac{\# np_A}{\# pp_A} \cdot \frac{\sigma_n}{\sigma_p} \cdot P_{SCX}^A T_{recoil}^A \right) \\
A(e,e'p) &\propto \# pp_A \cdot 2\sigma_p \cdot T_p^A + \# np_A \cdot \left(\sigma_p \cdot T_p^A + \sigma_n \cdot P_{SCX}^A \right) + \# nn_A \cdot 2\sigma_n \cdot P_{SCX}^A \\
&= \# pp_A \cdot 2\sigma_p \cdot \left[T_p^A + \frac{1}{2} \frac{\# np_A}{\# pp_A} \cdot \left(T_p^A + \frac{\sigma_n}{\sigma_p} \cdot P_{SCX}^A \right) + \frac{\# nn_A}{pp_A} \cdot \frac{\sigma_n}{\sigma_p} \cdot P_{SCX}^A \right]
\end{aligned} ,
$$

where T_p (T_{recoil}) is the leading (recoil) proton transparency, T_{pp} is the joint two-proton transparency and P_{SCX} is the probability that a struck neutron undergo SCX and be detected as a proton (see Table S7). σ_n is the electron-neutron cross section.

Within the formalism of Eq. S8, the measured (e,e'p)/(e,e'pp) double cross section ratio for nucleus A relative to Carbon, *R*, is given by:

Eq. S9

$$\frac{\dfrac{A(e,e'p)}{A(e,e'pp)}}{\dfrac{C(e,e'p)}{C(e,e'pp)}}=\frac{\dfrac{A(e,e'p)}{C(e,e'p)}}{\dfrac{A(e,e'pp)}{C(e,e'pp)}}=\frac{\dfrac{T_p^A+\dfrac{1}{2}\dfrac{\#np_A}{\#pp_A}\cdot\left(T_p^A+\dfrac{\sigma_n}{\sigma_p}\cdot P_{SCX}^A\right)+\dfrac{\#nn_A}{pp_A}\cdot\dfrac{\sigma_n}{\sigma_p}\cdot P_{SCX}^A}{T_p^C+\dfrac{1}{2}\dfrac{\#np_C}{\#pp_C}\cdot\left(T_p^C+\dfrac{\sigma_n}{\sigma_p}\cdot P_{SCX}^C\right)+\dfrac{\#nn_C}{pp_C}\cdot\dfrac{\sigma_n}{\sigma_p}\cdot P_{SCX}^C}}{\dfrac{T_{pp}^A+\dfrac{1}{2}\dfrac{\#np_A}{\#pp_A}\cdot\dfrac{\sigma_n}{\sigma_p}\cdot P_{SCX}^A T_{recoil}^A}{T_{pp}^C+\dfrac{1}{2}\dfrac{\#np_C}{\#pp_C}\cdot\dfrac{\sigma_n}{\sigma_p}\cdot P_{SCX}^C T_{recoil}^C}}.$$

Using Eq. S9 one can express the double ratio of np/pp SRC pairs in nucleus A to Carbon as in terms of the measured cross section double ratio *R*:
Eq. S10

$$\frac{\#np_A}{\#pp_A}=2\frac{\left[\begin{array}{l}-R\cdot\dfrac{\#nn_C}{pp_C}\cdot\dfrac{\sigma_n}{\sigma_p}\cdot P_{SCX}^C\cdot T_{pp}^A-R\cdot T_p^C\cdot T_{pp}^A+\dfrac{\#nn_A}{pp_A}\cdot\dfrac{\sigma_n}{\sigma_p}\cdot P_{SCX}^A\cdot T_{pp}^C+T_p^A\cdot T_{pp}^C+\\ \dfrac{1}{2}\dfrac{\#np_C}{\#pp_C}\left[-R\cdot T_{pp}^A\cdot\left(\dfrac{\sigma_n}{\sigma_p}\cdot P_{SCX}^C+T_p^C\right)+\dfrac{\sigma_n}{\sigma_p}\cdot P_{SCX}^C\cdot T_{recoil}^C\cdot\left(\dfrac{\#nn_A}{pp_A}\cdot\dfrac{\sigma_n}{\sigma_p}\cdot P_{SCX}^A+T_p^A\right)\right]\end{array}\right]}{\left[\begin{array}{l}\dfrac{\sigma_n}{\sigma_p}\cdot P_{SCX}^A\left(\begin{array}{l}-T_{pp}^C+RT_{recoil}^A\left(\left(\dfrac{\#nn_C}{pp_C}+\dfrac{1}{2}\dfrac{\#np_C}{\#pp_C}\right)\dfrac{\sigma_n}{\sigma_p}\cdot P_{SCX}^C+T_p^C+\dfrac{1}{2}\dfrac{\#np_C}{\#pp_C}T_p^C\right)\\ -\dfrac{1}{2}\dfrac{\#np_C}{\#pp_C}\dfrac{\sigma_n}{\sigma_p}\cdot P_{SCX}^C\cdot T_{recoil}^C\end{array}\right)-\\ T_p^A\left(T_{pp}^C+\dfrac{1}{2}\dfrac{\#np_C}{\#pp_C}\dfrac{\sigma_n}{\sigma_p}\cdot P_{SCX}^C\cdot T_{recoil}^C\right)\end{array}\right]},$$

The np/pp SRC pair ratio in Carbon was previously measured as 18±5 (*9*). The nuclear transparencies and SCX probabilities were calculated within a Glauber approximation and are given in Table S7. Isospin symmetry implies that the nn/pp ratio equals unity in symmetric nuclei. However it is unknown for asymmetric nuclei. Because the final result is largely insensitive to the contribution from the nn pairs to the measured cross section, we will vary the nn/pp ratio in asymmetric nuclei from one to five times the combinatorial value of N(N-1)/Z(Z-1).

We extract the fraction of np- and pp-SRC pairs of the sum of pp- and np-SRC pairs :
Eq. S11

$$\frac{\#np}{\#np+\#pp}=\frac{1}{1+\#pp/\#np},$$
$$\frac{\#pp}{\#np+\#pp}=\frac{1}{1+\#np/\#pp},$$

for Al, Fe, and Pb. These are listed in Table S8. The extraction was done using the nuclear transparency and SCX correction factors listed in Table S7, the measured A/C

(e,e'pp)/(e,e'p) cross section double ratios listed in Table S5, an electron-proton to electron-neutron cross-section ratio of 2.5±0.5 (*51*) and a nn/pp ratio equal to its combinatorial value of N(N-1) / Z(Z-1).
The uncertainties listed in Table S5 represent a 68% confidence level resulting from uncertainties in the input parameters presented above (see next section for details). In the paper we also show the 95% confidence level of the extraction fractions. In the analysis presented above we assumed that $100 \pm 15\%$ of the A(e,e'p) strength originates from scattering off 2N-SRC pairs as measured in Ref. (*9*). This uncertainty was also taken into account and is included in the final results shown in Fig. 3 of the paper and Table S5.

6.3.2. Uncertainty estimate using Monte-Carlo calculations

To estimate the uncertainty on the extracted np- and pp- SRC pairs fractions resulting from the uncertainty on the input parameters, we calculate its Probability Density Function (PDF). The PDF results from repeated calculations of the np- and pp-SRC pair fractions using randomly generated input parameters. The latter are raffled from Gaussian distributions centered on the 'known' values of each input parameter, with a width equal to its uncertainty. These include all parameters used in Eq. S9 and S10 and the measured cross-section double ratio, see discussion after Eq. S10.

Fig. S29 and S30 show the resulting PDFs of the extracted np- and pp-SRC pairs fractions in Al, Fe, and Pb, respectively. The solid lines show the median values of the PDF distributions and the fine and coarse dashed lines show the 68% and 95% confidence regions around the median, respectively.

Table S8: The extracted fraction of np-SRC and pp-SRC pairs of the sum of pp and np pairs in different nuclei. See text for details.

Nuclei	**C**	**Al**	**Fe**	**Pb**
#np/(#np+#pp)	$0.947^{+0.014}_{-0.014}$	$0.949^{+0.022}_{-0.033}$	$0.959^{+0.023}_{-0.031}$	$0.984^{+0.036}_{-0.033}$
#pp/(#np+#pp)	$0.052^{+0.014}_{-0.014}$	$0.051^{+0.033}_{-0.022}$	$0.041^{+0.031}_{-0.023}$	$0.014^{+0.035}_{-0.034}$

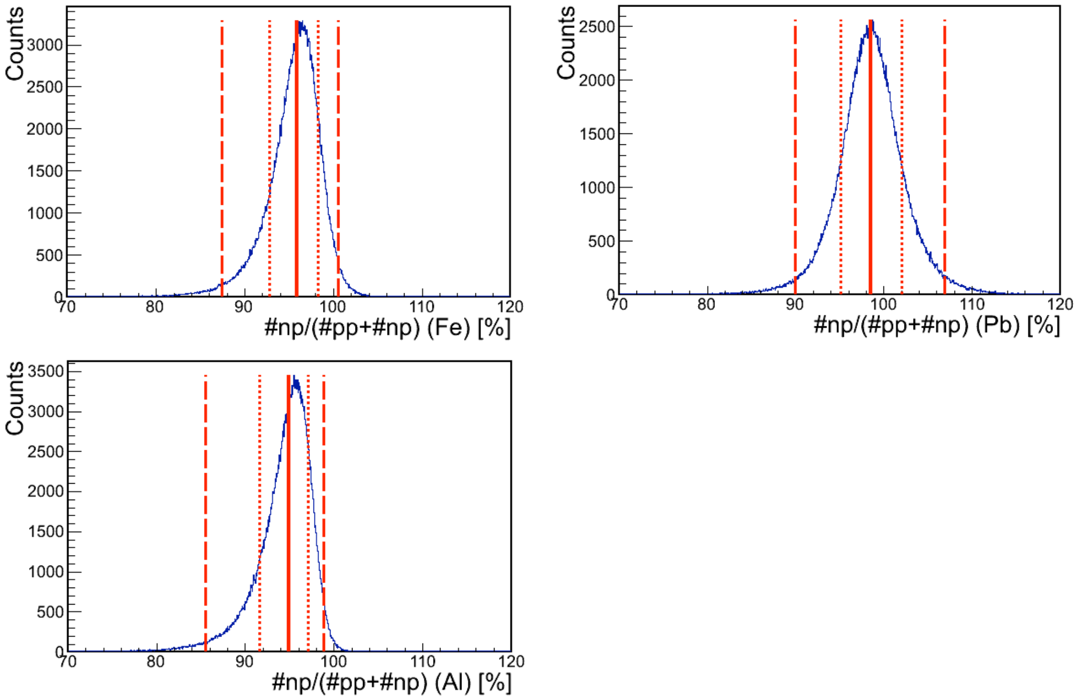

Fig. S29: The PDF distribution of the fraction of np-SRC pairs of the sum of pp and np pairs in Pb (top Right), Fe (top left), and Al (bottom left). The solid red line marks the median value while the fine and coarse dashed red lines mark the regions of 68% and 95% confidence level, respectively. See text for details.

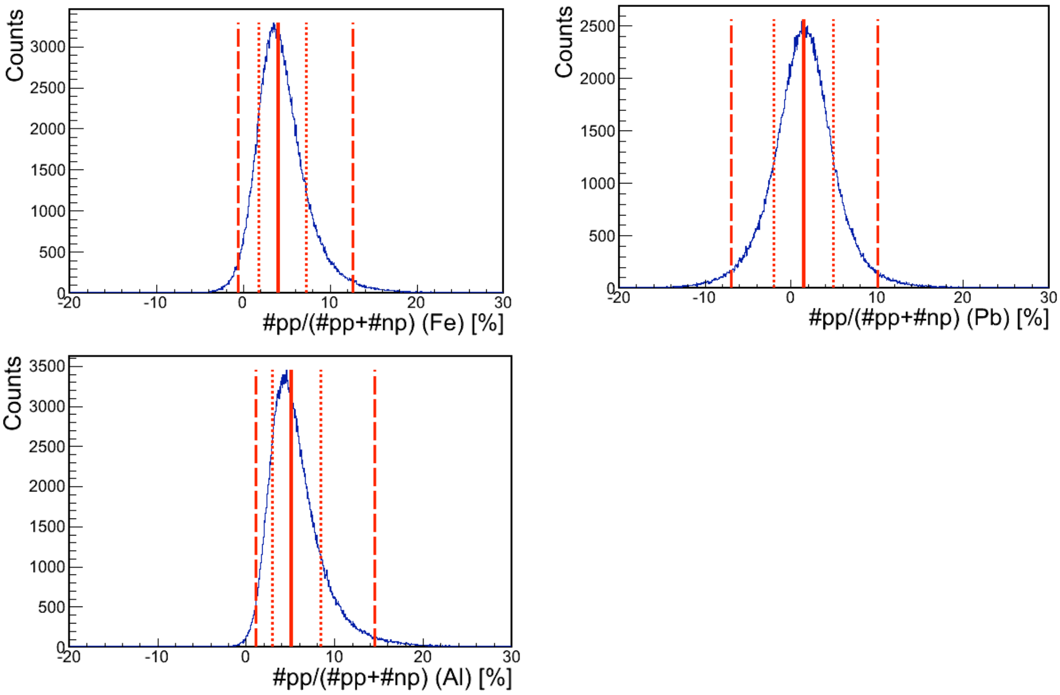

Fig. S30: Same as Fig S29, for the fraction of pp-SRC pairs.

References

[1] S. Tan, Annals of Physics 323, 2952 (2008).

[2] S. Tan, Annals of Physics 323, 2971 (2008).

[3] S. Tan, Annals of Physics 323, 2987 (2008).

[4] E. Braaten, Lect. Notes Phys. 836, 193 (2012).

[5] L. Lapikas, Nucl. Phys. A553, 297 (1993).

[6] K.I. Blomqvist et al., Phys. Lett. B421, 71 (1998).

[7] R. Starink et al., Phys. Lett. B474, 33 (2000).

[8] E. Piasetzky, M. Sargsian, L. Frankfurt, M. Strikman, J. Watson, Phys. Rev. Lett. 97, 162504 (2006).

[9] R. Subedi, et al., Science 320, 1426 (2008).

[10] K. Sh. Egiyan, et al. (CLAS Collaboration), Phys. Rev. Lett. 96, 082501 (2006).

[11] N. Fomin, et al., Phys. Rev. Lett. 108, 092502 (2012).

[12] V. R. Pandharipande, I. Sick, and P. K. A. deWitt Huberts, Rev. Mod. Phys. 69, 981 (1997).

[13] J. Arrington, D. W. Higinbotham, G. Rosner, M. Sargsian, Prog. Part. Nucl. Phys. 67 (2012) 898-938.

[14] J. T. Stewart, J. P. Gaebler, T. E. Drake, D. S. Jin, Phys. Rev. Lett. 104, 235301 (2010).

[15] E. D. Kuhnle, et al., Phys. Rev. Lett. 105, 070402 (2010).

[16] Materials and methods are available as supplementary material on Science Online.

[17] R. Schiavilla, R.B. Wiringa, S.C. Pieper, J. Carlson, Phys. Rev. Lett. 98, 132501 (2007).

[18] M.M. Sargsian, T.V. Abrahamyan, M.I. Strikman, L.L. Frankfurt, Phys. Rev. C 71, 044615 (2005).

[19] L. Frankfurt, M. Strikman, Phys. Rep. 160, 235 (1988).

[20] B. A. Mecking, et al. (CLAS Collaboration), Nucl. Inst Meth. A 503, 512 (2003).

[21] O. Hen, et al. (CLAS Collaboration), Phys. Lett. B 772, 63 (2013)

[22] I. Mardor, Y. Mardor, E. Piasetzky, J. Alster, M. M. Sargsian, Phys. Rev. C 46, 761 (1992). And references within.

[23] D. Dutta, K. Hafidi, M. Strikman, Prog. Part. Nucl. Phys. 69, 1 (2013).

[24] J. L. Friedes, et al., Phys. Rev. Lett. 15, 38 (1965).

[25] Misak M. Sargsian, Phys. Rev. C 89, 034305 (2014).

[26] R. B. Wiringa, R. Schiavilla, S. C. Pieper, J. Carlson, Phys. Rev. C 89, 024305 (2014).

[27] G. A. Fiorentini et al. (MINERvA Collaboration), Phys. Rev. Lett. 111, 022501 (2013).

[28] G. A. Fiorentini et al. (MINERvA Collaboration), Phys. Rev. Lett. 111, 022502 (2013).

[29] “Neutrino-Nucleus Interactions for Current and Next Generation Neutrino Oscillation Experiments”, Institute for Nuclear Theory (INT) workshop INT-13-54W, University of Washington, Seattle WA, USA, December 3-13 (2013).
[30] O. Hen, et al., Int. J. Mod. Phys. E 22, 133017 (2013).
[31] L.B. Weinstein, et al., Phys Rev. Lett. 106, 052301 (2011).
[32] G. P. Zeller, et al., Phys. Rev. Lett. 88, 091802 (2002).
[33] G. P. Zeller, et al., Phys. Rev. Lett. 90, 239902 (2003).
[34] I. C. Cloet, W. Bentz, A.W. Thomas, Phys Rev. Lett. 102, 252301 (2009).
[35] J. M. Lattimer and Y. Lim, Astro. Phys. J 771, 51 (2013).
[36] A. Carbone, A. Polls, A. Rios, Euro. Phys. Lett. 97, 22001 (2012).
[37] I. Vidana, A. Polls, C. Providencia, Phys. Rev. C 84, 062801(R) (2011).
[38] C. Xu, A. Li, B.A. Li, J. of Phys: Conference Series 420, 012190 (2013)
[39] Bao-An Li, Lie-Wen Chen and Che Ming Ko, Physics Reports 464, 113 (2008).
[40] C. Ciofi degli Atti, S. Simula, Phys. Rev. C 53, 1689 (1996)
[41] M. Vanhalst, J. Ryckebusch, Wim Cosyn, Phys. Rev. C 86, 044619 (2012).
[42] R. J. Furnstahl, B. D. Serot, H. B. Tang, Nucl. Phys. A 615, 441 (1997)
[43] O. Hen, E. Piasetzky, L.B. Weinstein, Phys. Rev. C 85, 047301 (2012).
[44] R.B. Wiringa, V. G. J. Stoks, R. Schiavilla, Phys. Rev. C 51, 38 (1995).
[45] E. Moniz et al., Phys. Rev. Lett. 26, 445 (1971).
[46] H. Hakobyan, et al., Nucl. Inst. and Meth. A 592, 218 (2008).
[47] R. Shneor, et al., Phys. Rev. Lett. 99, 072501 (2007).
[48] I. Korover et al., Phys. Rev. Lett. 113, 022501 (2014).
[49] C. Colle, W. Cosyn, M. Vanhalst, J. Ryckebusch, Phys. Rev. C 89, 024603 (2014).
[50] K. Garrow, et al., Phys. Rev. C 66, 044613 (2002).
[51] J. Lachniet, et al. (CLAS Collaboration), Phys. Rev. Lett. 102, 192001 (2009).

3. Results from A(e,e’p) and A(e,e’pp) measurements of ^{12}C, ^{27}Al, ^{56}Fe, and ^{208}Pb

3.1. Isospin structure of SRC pairs in medium and heavy nuclei

“Momentum Sharing in Imbalanced Fermi Systems”,
O. Hen et al. (CLAS Collaboration), Science ***346****, 614 (2014).*

REPORTS

NUCLEAR PHYSICS

Momentum sharing in imbalanced Fermi systems

O. Hen,[1]* M. Sargsian,[2] L. B. Weinstein,[3] E. Piasetzky,[1] H. Hakobyan,[4,5] D. W. Higinbotham,[6] M. Braverman,[1] W. K. Brooks,[4] S. Gilad,[7] K. P. Adhikari,[3] J. Arrington,[8] G. Asryan,[5] H. Avakian,[6] J. Ball,[9] N. A. Baltzell,[8] M. Battaglieri,[10] A. Beck,[1,11] S. May-Tal Beck,[1,11] I. Bedlinskiy,[12] W. Bertozzi,[7] A. Biselli,[13] V. D. Burkert,[6] T. Cao,[14] D. S. Carman,[6] A. Celentano,[10] S. Chandavar,[15] L. Colaneri,[16] P. L. Cole,[6,17,18] V. Crede,[19] A. D'Angelo,[16,20] R. De Vita,[10] A. Deur,[6] C. Djalali,[14,21] D. Doughty,[6,22] M. Dugger,[23] R. Dupre,[24] H. Egiyan,[6] A. El Alaoui,[8] L. El Fassi,[3] L. Elouadrhiri,[6] G. Fedotov,[14,25] S. Fegan,[10] T. Forest,[17] B. Garillon,[24] M. Garcon,[9] N. Gevorgyan,[5] Y. Ghandilyan,[5] G. P. Gilfoyle,[26] F. X. Girod,[6] J. T. Goetz,[15] R. W. Gothe,[14] K. A. Griffioen,[27] M. Guidal,[24] L. Guo,[2,6] K. Hafidi,[8] C. Hanretty,[28] M. Hattawy,[24] K. Hicks,[15] M. Holtrop,[29] C. E. Hyde,[3] Y. Ilieva,[14,30] D. G. Ireland,[31] B. I. Ishkanov,[25] E. L. Isupov,[25] H. Jiang,[14] H. S. Jo,[24] K. Joo,[32] D. Keller,[28] M. Khandaker,[17,33] A. Kim,[34] W. Kim,[34] F. J. Klein,[18] S. Koirala,[3] I. Korover,[1] S. E. Kuhn,[3] V. Kubarovsky,[6] P. Lenisa,[35] W. I. Levine,[36] K. Livingston,[31] M. Lowry,[6] H. Y. Lu,[14] I. J. D. MacGregor,[31] N. Markov,[32] M. Mayer,[3] B. McKinnon,[31] T. Mineeva,[32] V. Mokeev,[6,24,37] A. Movsisyan,[35] C. Munoz Camacho,[24] B. Mustapha,[8] P. Nadel-Turonski,[6] S. Niccolai,[24] G. Niculescu,[38] I. Niculescu,[38] M. Osipenko,[10] L. L. Pappalardo,[35,39] R. Paremuzyan,[5,29] K. Park,[6,34] E. Pasyuk,[6] W. Phelps,[2] S. Pisano,[40] O. Pogorelko,[12] J. W. Price,[41] S. Procureur,[9] Y. Prok,[3,28] D. Protopopescu,[31] A. J. R. Puckett,[32] D. Rimal,[2] M. Ripani,[10] B. G. Ritchie,[23] A. Rizzo,[16] G. Rosner,[31] P. Roy,[19] P. Rossi,[6] F. Sabatié,[9] D. Schott,[30] R. A. Schumacher,[36] Y. G. Sharabian,[6] G. D. Smith,[42] R. Shneor,[1] D. Sokhan,[31] S. S. Stepanyan,[34] S. Stepanyan,[6] P. Stoler,[43] S. Strauch,[14,30] V. Sytnik,[4] M. Taiuti,[44] S. Tkachenko,[28] M. Ungaro,[6] A. V. Vlassov,[12] E. Voutier,[45] N. K. Walford,[18] X. Wei,[6] M. H. Wood,[14,46] S. A. Wood,[6] N. Zachariou,[14] L. Zana,[29,42] Z. W. Zhao,[28] X. Zheng,[28] I. Zonta,[16] Jefferson Lab CLAS Collaboration†

The atomic nucleus is composed of two different kinds of fermions: protons and neutrons. If the protons and neutrons did not interact, the Pauli exclusion principle would force the majority of fermions (usually neutrons) to have a higher average momentum. Our high-energy electron-scattering measurements using ^{12}C, ^{27}Al, ^{56}Fe, and ^{208}Pb targets show that even in heavy, neutron-rich nuclei, short-range interactions between the fermions form correlated high-momentum neutron-proton pairs. Thus, in neutron-rich nuclei, protons have a greater probability than neutrons to have momentum greater than the Fermi momentum. This finding has implications ranging from nuclear few-body systems to neutron stars and may also be observable experimentally in two-spin–state, ultracold atomic gas systems.

Many-body systems composed of interacting fermions are common in nature, ranging from high-temperature superconductors and Fermi liquids to atomic nuclei, quark matter, and neutron stars. Particularly intriguing are systems that include a short-range interaction that is strong between unlike fermions and weak between the same type of fermions. Recent theoretical advances show that even though the underlying interaction can be very different, these systems share several universal features (*1–4*). In all of these systems, this interaction creates short-range–correlated (SRC) pairs of unlike fermions with a large relative momentum ($k_{\rm rel} > k_{\rm F}$) and a small center-of-mass momentum ($k_{\rm tot} < k_{\rm F}$), where $k_{\rm F}$ is the Fermi momentum of the system. This pushes fermions from low momenta ($k < k_{\rm F}$, where k is the fermion momentum) to high momenta ($k > k_{\rm F}$), creating a "high-momentum tail."

In atomic nuclei, SRC pairs have been studied using many different reactions, including pick-up, stripping, and electron and proton scattering. The results of these studies highlighted the importance of correlations in nuclei, which lead to a high-momentum tail and decreased occupancy of low-lying nuclear states (*5–13*).

Recent experimental studies of balanced (symmetric) interacting Fermi systems, with an equal number of fermions of the two kinds, confirmed these predictions of a high-momentum tail populated almost exclusively by pairs of unlike fermions (*8–11, 14–16*). These experiments were carried out using very different Fermi systems: protons and neutrons in atomic nuclei and two-spin–state, ultracold atomic gases. These systems span more than 15 orders of magnitude in Fermi energy from 10^6 to 10^{-9} eV and exhibit different short-range interactions [predominantly a strong tensor interaction in the nuclear systems (*8, 9, 17, 18*) and a tunable Feshbach resonance in the atomic system (*14, 15*)]. For cold atoms, Tan (*1–3*) showed that the momentum density decreases as C/k^4 for large k. The scale factor, C, is known as Tan's contact and describes many properties of the system (*4*). Similar pairing of nucleons in nuclei with $k > k_{\rm F}$ was also predicted in (*19*).

In this work, we extend these previous studies to imbalanced (asymmetric) nuclear systems, with unequal numbers of the different fermions. When there is no interaction, the Pauli exclusion principle pushes the majority fermions (usually neutrons) to a higher average momentum. Including a short-range interaction introduces a new universal feature: the probability for a fermion to have momentum $k > k_{\rm F}$ is greater for the minority than for the majority fermions. This is because the short-range interaction populates the high-momentum

---

[1]Tel Aviv University, Tel Aviv 69978, Israel. [2]Florida International University, Miami, FL 33199, USA. [3]Old Dominion University, Norfolk, VA 23529, USA. [4]Universidad Técnica Federico Santa María, Casilla 110-V Valparaíso, Chile. [5]Yerevan Physics Institute, 375036 Yerevan, Armenia. [6]Thomas Jefferson National Accelerator Facility, Newport News, VA 23606, USA. [7]Massachusetts Institute of Technology, Cambridge, MA 02139, USA. [8]Argonne National Laboratory, Argonne, IL 60439, USA. [9]Commissariat à l'Energie Atomique et aux Energies Alternatives, Centre de Saclay, Irfu/Service de Physique Nucléaire, 91191 Gif-sur-Yvette, France. [10]Istituto Nazionale di Fisica Nucleare (INFN), Sezione di Genova, 16146 Genova, Italy. [11]Nuclear Research Center Negev, P.O. Box 9001, Beer-Sheva 84190, Israel. [12]Institute of Theoretical and Experimental Physics, Moscow, 117259, Russia. [13]Fairfield University, Fairfield, CT 06824, USA. [14]University of South Carolina, Columbia, SC 29208, USA. [15]Ohio University, Athens, OH 45701, USA. [16]INFN, Sezione di Roma Tor Vergata, 00133 Rome, Italy. [17]Idaho State University, Pocatello, ID 83209, USA. [18]Catholic University of America, Washington, DC 20064, USA. [19]Florida State University, Tallahassee, FL 32306, USA. [20]Università di Roma Tor Vergata, 00133 Rome, Italy. [21]University of Iowa, Iowa City, IA 52242, USA. [22]Christopher Newport University, Newport News, VA 23606, USA. [23]Arizona State University, Tempe, AZ 85287-1504, USA. [24]Institut de Physique Nucléaire ORSAY, Orsay, France. [25]Skobeltsyn Institute of Nuclear Physics, Lomonosov, Russia. [26]University of Richmond, Richmond, VA 23173, USA. [27]College of William and Mary, Williamsburg, VA 23187-8795, USA. [28]University of Virginia, Charlottesville, VA 22901, USA. [29]University of New Hampshire, Durham, NH 03824-3568, USA. [30]The George Washington University, Washington, DC 20052, USA. [31]University of Glasgow, Glasgow G12 8QQ, UK. [32]University of Connecticut, Storrs, CT 06269, USA. [33]Norfolk State University, Norfolk, VA 23504, USA. [34]Kyungpook National University, Daegu 702-701, Republic of Korea. [35]INFN, Sezione di Ferrara, 44100 Ferrara, Italy. [36]Carnegie Mellon University, Pittsburgh, PA 15213, USA. [37]Moscow State University, Moscow, 119234, Russia. [38]James Madison University, Harrisonburg, VA 22807, USA. [39]Universitá di Ferrara, 44122 Ferrara, Italy. [40]INFN, Laboratori Nazionali di Frascati, 00044 Frascati, Italy. [41]California State University, Dominguez Hills, Carson, CA 90747, USA. [42]Edinburgh University, Edinburgh EH9 3JZ, UK. [43]Rensselaer Polytechnic Institute, Troy, NY 12180-3590, USA. [44]Università di Genova, 16146 Genova, Italy. [45]Laboratoire de Physique Subatomique et de Cosmologie, Universite Joseph Fourier, CNRS/IN2P3, Institut National Polytechnique, Grenoble, France. [46]Canisius College, Buffalo, NY 14208, USA.
***Corresponding author. E-mail: or.chen@mail.huji.ac.il** †The collaboration on this paper consists of all listed authors. There are no additional collaborators.

tail with equal numbers of majority and minority fermions, thereby leaving a larger fraction of majority fermions in low-momentum states ($k < k_F$) (see Fig. 1). In neutron-rich nuclei, this increases the average proton momentum and may even result in protons having higher average momentum than neutrons, inverting the momentum sharing in imbalanced nuclei from that in noninteracting systems. Theoretically, this can happen because of the tensor part of the nucleon-nucleon interaction, which creates predominantly spin-1, isospin-0 neutron-proton (np) SRC pairs (*17*, *18*).

Here we identify SRC pairs in the high-momentum tail of nuclei heavier than carbon with more neutrons (N) than protons (Z) (i.e., $N > Z$). The data show the universal nature of SRC pairs, which even in lead (N/Z = 126/82) are still predominantly np pairs. This np-pair dominance causes a greater fraction of protons than neutrons to have high momentum in neutron-rich nuclei.

The data presented here were collected in 2004 in Hall B of the Thomas Jefferson National Accelerator Facility using a 5.014-GeV electron beam incident on ^{12}C, ^{27}Al, ^{56}Fe, and ^{208}Pb targets. We measured electron-induced two-proton knockout reactions (Fig. 2). The CEBAF Large Acceptance Spectrometer (CLAS) (*20*) was used to detect the scattered electron and emitted protons. CLAS uses a toroidal magnetic field and six independent sets of drift chambers, time-of-flight scintillation counters, Cerenkov counters, and electromagnetic calorimeters for charged-particle identification and trajectory reconstruction (Fig. 2) (*16*).

We selected events in which the electron interacts with a single fast proton from an SRC pair in the nucleus (*9*, *16*) by requiring a large four-momentum transfer $Q^2 = \vec{q}^{\,2} - (\omega/c)^2 > 1.5$ GeV^2/c^2 [where $\vec{q}$ and ω are the three-momentum and energy, respectively, transferred to the nucleus and c is the speed of light] and Bjorken scaling parameter $x_B = Q^2/(2m_N \cdot \omega) > 1.2$ (where m_N is the nucleon mass). To ensure selection of events in which the knocked-out proton belonged to an SRC pair, we further required missing momentum $300 < |\vec{p}_{\text{miss}}| < 600$ MeV/c, where $\vec{p}_{\text{miss}} = \vec{p}_p - \vec{q}$ with $\vec{p}_p$ the measured proton momentum. We suppressed contributions from inelastic excitations of the struck nucleon by limiting the reconstructed missing mass of the two-nucleon system $m_{\text{miss}} < 1.1$ GeV/c^2. In each event, the leading proton that absorbed the transferred momentum was identified by requiring that its momentum $\vec{p}_p$ is within 25° of $\vec{q}$ and that $|\vec{p}_p|/|\vec{q}| \geq 0.6$ (*16*, *21*).

When a second proton was detected with momentum greater than 350 MeV/c, it was emitted almost diametrically opposite to $\vec{p}_{\text{miss}}$ (see fig. S19). The observed backward-peaked angular distributions are very similar for all four measured

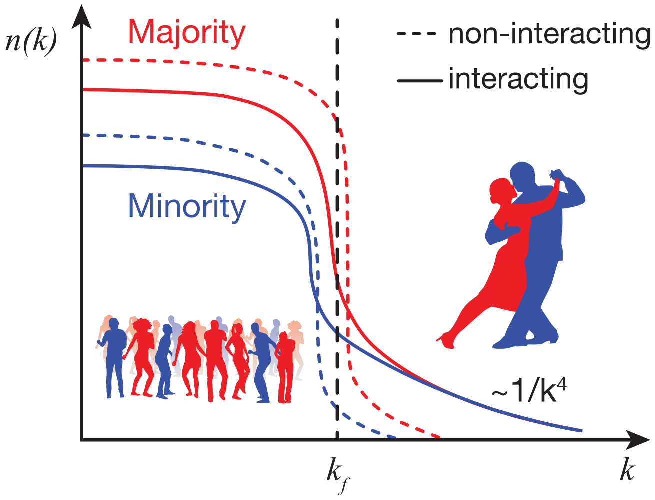

Fig. 1. Schematic representation of the momentum distribution, *n*(*k*), of two-component imbalanced Fermi systems. Red and blue dashed lines show the noninteracting system, whereas the solid lines show the effect of including a short-range interaction between different fermions. Such interactions create a high-momentum tail ($k > k_F$, where k_F is the Fermi momentum of the system). This is analogous to a dance party with a majority of girls, where boy-girl interactions will make the average boy dance more than the average girl.

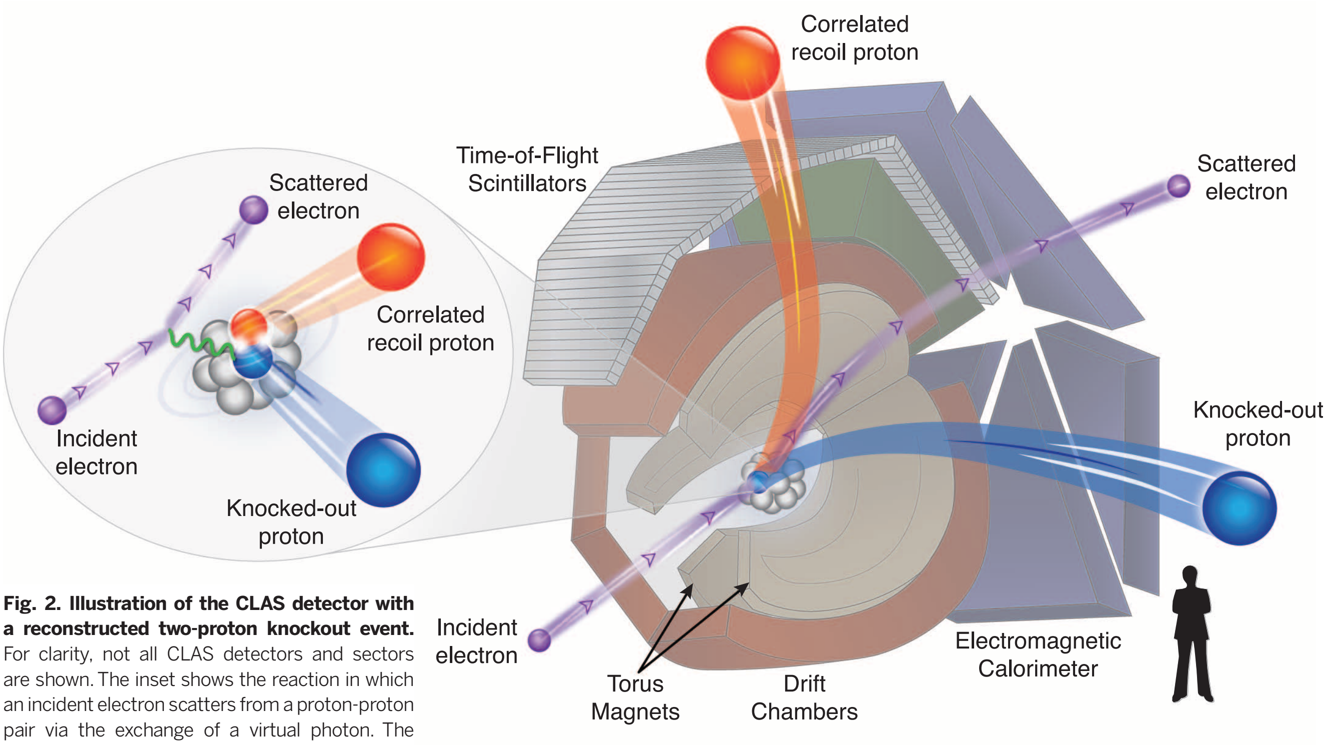

Fig. 2. Illustration of the CLAS detector with a reconstructed two-proton knockout event. For clarity, not all CLAS detectors and sectors are shown. The inset shows the reaction in which an incident electron scatters from a proton-proton pair via the exchange of a virtual photon. The human figure is shown for scale.

nuclei. This backward peak is a strong signature of SRC pairs, indicating that the two emitted protons were largely back-to-back in the initial state, having a large relative momentum and a small center-of-mass momentum (*8*, *9*). This is a direct observation of proton-proton (pp) SRC pairs in a nucleus heavier than ^{12}C.

Electron scattering from high–missing-momentum protons is dominated by scattering from protons in SRC pairs (*9*). The measured single-proton knockout (e,$e'p$) cross section (where e denotes the incoming electron, e' the measured scattered electron, and p the measured knocked-out proton) is sensitive to the number of pp and np SRC pairs in the nucleus, whereas the two-proton knockout (e,$e'pp$) cross section is only sensitive to the number of pp-SRC pairs. Very few of the single-proton knockout events also contained a second proton; therefore, there are very few pp pairs, and the knocked-out protons predominantly originated from np pairs.

To quantify this, we extracted the [$A(e,e'pp)/A(e,e'p)$]/[^{12}C(e,$e'pp$)/^{12}C(e,$e'p$)] cross-section double ratio for nucleus A relative to ^{12}C. The double ratio is sensitive to the ratio of np-to-pp SRC pairs in the two nuclei (*16*). Previous measurements have shown that in ^{12}C nearly every high-momentum proton ($k > 300$ MeV/$c > k_F$) has a correlated partner nucleon, with np pairs outnumbering pp pairs by a factor of ~20 (*8*, *9*).

To estimate the effects of final-state interactions (reinteraction of the outgoing nucleons in the nucleus), we calculated attenuation factors for the outgoing protons and the probability of the electron scattering from a neutron in an np pair, followed by a neutron-proton single-charge exchange (SCX) reaction leading to two outgoing protons. These correction factors are calculated as in (*9*) using the Glauber approximation (*22*) with effective cross sections that reproduce previously measured proton transparencies (*23*), and using the measured SCX cross section of (*24*). We extracted the cross-section ratios and deduced the relative pair fractions from the measured yields following (*21*); see (*16*) for details.

Figure 3 shows the extracted fractions of np and pp SRC pairs from the sum of pp and np pairs in nuclei, including all statistical, systematic, and model uncertainties. Our measurements are not sensitive to neutron-neutron SRC pairs. However, by a simple combinatoric argument, even in ^{208}Pb these would be only $(N/Z)^2$ ~ 2 times the number of pp pairs. Thus, np-SRC pairs dominate in all measured nuclei, including neutron-rich imbalanced ones.

The observed dominance of np-over-pp pairs implies that even in heavy nuclei, SRC pairs are dominantly in a spin-triplet state (spin 1, isospin 0), a consequence of the tensor part of the nucleon-nucleon interaction (*17*, *18*). It also implies that there are as many high-momentum protons as neutrons (Fig. 1) so that the fraction of protons above the Fermi momentum is greater than that of neutrons in neutron-rich nuclei (*25*).

In light imbalanced nuclei ($A \le 12$), variational Monte Carlo calculations (*26*) show that this results in a greater average momentum for the minority component (see table S1). The minority component can also have a greater average momentum in heavy nuclei if the Fermi momenta of protons and neutrons are not too dissimilar. For heavy nuclei, an np-dominance toy model that quantitatively describes the features of the momentum distribution shown in Fig. 1 shows that in imbalanced nuclei, the average proton kinetic energy is greater than that of the neutron, up to ~20% in ^{208}Pb (*16*).

The observed np-dominance of SRC pairs in heavy imbalanced nuclei may have wide-ranging implications. Neutrino scattering from two nucleon currents and SRC pairs is important for the analysis of neutrino-nucleus reactions, which are used to study the nature of the electro-weak interaction (*27*–*29*). In particle physics, the distribution of quarks in these high-momentum nucleons in SRC pairs might be modified from that of free nucleons (*30*, *31*). Because each proton has a greater probability to be in a SRC pair than a neutron and the proton has two u quarks for each d quark, the u-quark distribution modification could be greater than that of the d quarks (*19*, *30*). This could explain the difference between the weak mixing angle measured on an iron target by the NuTeV experiment and that of the Standard Model of particle physics (*32*–*34*).

In astrophysics, the nuclear symmetry energy is important for various systems, including neutron stars, the neutronization of matter in core-collapse supernovae, and r-process nucleosynthesis (*35*). The decomposition of the symmetry energy at saturation density ($\rho_0 \approx 0.17$ fm^{-3}, the maximum density of normal nuclei) into its kinetic and potential parts and its value at supranuclear densities ($\rho > \rho_0$) are not well constrained, largely because of the uncertainties in the tensor component of the nucleon-nucleon interaction (*36*–*39*). Although at supranuclear densities other effects are relevant, the inclusion of high-momentum tails, dominated by tensor-force–induced np-SRC pairs, can notably soften the nuclear symmetry energy (*36*–*39*). Our measurements of np-SRC pair dominance in heavy imbalanced nuclei can help constrain the nuclear aspects of these calculations at saturation density.

Based on our results in the nuclear system, we suggest extending the previous measurements of Tan's contact in balanced ultracold atomic gases to imbalanced systems in which the number of atoms in the two spin states is different. The large experimental flexibility of these systems will allow observing dependence of the momentum-sharing inversion on the asymmetry, density, and strength of the short-range interaction.

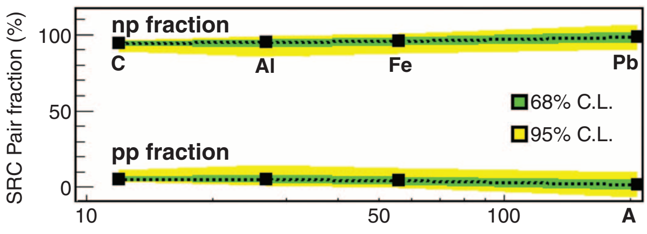

Fig. 3. The extracted fractions of np (top) and pp (bottom) SRC pairs from the sum of pp and np pairs in nuclei. The green and yellow bands reflect 68 and 95% confidence levels (CLs), respectively (*9*). np-SRC pairs dominate over pp-SRC pairs in all measured nuclei.

REFERENCES AND NOTES

1. S. Tan, *Ann. Phys.* **323**, 2952–2970 (2008).
2. S. Tan, *Ann. Phys.* **323**, 2971–2986 (2008).
3. S. Tan, *Ann. Phys.* **323**, 2987–2990 (2008).
4. E. Braaten, in *Lecture Notes in Physics* (Springer, Berlin, 2012), vol. 836, p. 193.
5. L. Lapikás, *Nucl. Phys. A.* **553**, 297–308 (1993).
6. K. I. Blomqvist *et al.*, *Phys. Lett. B* **421**, 71–78 (1998).
7. R. Starink *et al.*, *Phys. Lett. B* **474**, 33–40 (2000).
8. E. Piasetzky, M. Sargsian, L. Frankfurt, M. Strikman, J. W. Watson, *Phys. Rev. Lett.* **97**, 162504 (2006).
9. R. Subedi *et al.*, *Science* **320**, 1476–1478 (2008).
10. K. Sh. Egiyan *et al.*, *Phys. Rev. Lett.* **96**, 082501 (2006).
11. N. Fomin *et al.*, *Phys. Rev. Lett.* **108**, 092502 (2012).
12. V. R. Pandharipande, I. Sick, P. K. A. deWitt Huberts, *Rev. Mod. Phys.* **69**, 981–991 (1997).
13. J. Arrington, D. W. Higinbotham, G. Rosner, M. Sargsian, *Prog. Part. Nucl. Phys.* **67**, 898–938 (2012).
14. J. T. Stewart, J. P. Gaebler, T. E. Drake, D. S. Jin, *Phys. Rev. Lett.* **104**, 235301 (2010).
15. E. D. Kuhnle *et al.*, *Phys. Rev. Lett.* **105**, 070402 (2010).
16. Materials and methods are available as supplementary materials on *Science* Online.
17. R. Schiavilla, R. B. Wiringa, S. C. Pieper, J. Carlson, *Phys. Rev. Lett.* **98**, 132501 (2007).
18. M. M. Sargsian, T. V. Abrahamyan, M. I. Strikman, L. L. Frankfurt, *Phys. Rev. C* **71**, 044615 (2005).
19. L. Frankfurt, M. Strikman, *Phys. Rep.* **160**, 235–427 (1988).
20. B. A. Mecking *et al.*, *Nucl. Inst. Meth. A* **503**, 513–553 (2003).
21. O. Hen *et al.*, *Phys. Lett. B* **722**, 63–68 (2013).
22. I. Mardor, Y. Mardor, E. Piasetsky, J. Alster, M. M. Sargsyan, *Phys. Rev. C* **46**, 761–767 (1992).
23. D. Dutta, K. Hafidi, M. Strikman, *Prog. Part. Nucl. Phys.* **69**, 1–27 (2013).
24. J. L. Friedes, H. Palevsky, R. Stearns, R. Sutter, *Phys. Rev. Lett.* **15**, 38–41 (1965).
25. M. M. Sargsian, *Phys. Rev. C* **89**, 034305 (2014).
26. R. B. Wiringa, R. Schiavilla, S. C. Pieper, J. Carlson, *Phys. Rev. C* **89**, 024305 (2014).
27. L. Fields *et al.*, *Phys. Rev. Lett.* **111**, 022501 (2013).
28. G. A. Fiorentini *et al.*, *Phys. Rev. Lett.* **111**, 022502 (2013).
29. Neutrino-Nucleus Interactions for Current and Next Generation Neutrino Oscillation Experiments, Institute for Nuclear Theory (INT) workshop INT-13-54W, University of Washington, Seattle, WA, 3 to 13 December 2013.
30. O. Hen, D. W. Higinbotham, G. A. Miller, E. Piasetzky, L. B. Weinstein, *Int. J. Mod. Phys. E* **22**, 133017 (2013).
31. L. B. Weinstein *et al.*, *Phys. Rev. Lett.* **106**, 052301 (2011).
32. G. P. Zeller *et al.*, *Phys. Rev. Lett.* **88**, 091802 (2002).
33. G. P. Zeller *et al.*, *Phys. Rev. Lett.* **90**, 239902 (2003).
34. I. C. Cloët, W. Bentz, A. W. Thomas, *Phys. Rev. Lett.* **102**, 252301 (2009).
35. J. M. Lattimer, Y. Lim, *Astrophys. J.* **771**, 51 (2013).
36. A. Carbone, A. Polls, A. Rios, *Europhys. Lett.* **97**, 22001 (2012).
37. I. Vidana, A. Polls, C. Providencia, *Phys. Rev. C* **84**, 062801(R) (2011).
38. C. Xu, A. Li, B. A. Li, *J. Phys. Conf. Ser.* **420**, 012090 (2013).
39. B.-A. Li, L.-W. Chen, C. M. Ko, *Phys. Rep.* **464**, 113–281 (2008).

ACKNOWLEDGMENTS

This work was supported by the U.S. Department of Energy (DOE) and the National Science Foundation, the Israel Science Foundation, the Chilean Comisión Nacional de Investigación Científica y Tecnológica, the French Centre National de la

Recherche Scientifique and Commissariat a l'Energie Atomique, the French-American Cultural Exchange, the Italian Istituto Nazionale di Fisica Nucleare, the National Research Foundation of Korea, and the UK's Science and Technology Facilities Council. Jefferson Science Associates operates the Thomas Jefferson National Accelerator Facility for the DOE, Office of Science, Office of Nuclear Physics under contract DE-AC05-06OR23177. The raw data from this experiment are archived in Jefferson Lab's mass storage silo.

SUPPLEMENTARY MATERIALS

www.sciencemag.org/content/346/6209/614/suppl/DC1
Materials and Methods
Figs. S1 to S30
Tables S1 to S8
References (*40*–*51*)

2 June 2014; accepted 2 October 2014

10.1126/science.1256785

3.2. Nuclear Transparency Ratios

"Measurement of Transparency Ratios for Protons from Short-Range Correlated Pairs",
*O. Hen et al. (CLAS Collaboration), Phys. Lett. B **772**, 63 (2013).*

Physics Letters B 722 (2013) 63–68

Contents lists available at SciVerse ScienceDirect

Physics Letters B

www.elsevier.com/locate/physletb

Measurement of transparency ratios for protons from short-range correlated pairs

The CLAS Collaboration

O. Hen [a,*], H. Hakobyan [b,aq], R. Shneor [a], E. Piasetzky [a], L.B. Weinstein [c], W.K. Brooks [b,am], S. May-Tal Beck [a], S. Gilad [d], I. Korover [a], A. Beck [a], K.P. Adhikari [c], M. Aghasyan [v], M.J. Amaryan [c], S. Anefalos Pereira [v], J.R. Arrington [e], H. Baghdasaryan [ao,c], J. Ball [k], M. Battaglieri [w], V. Batourine [am,ab], I. Bedlinskiy [z], A.S. Biselli [o,i], J. Bono [p], S. Boiarinov [am], W.J. Briscoe [s], V.D. Burkert [am], D.S. Carman [am], A. Celentano [w], S. Chandavar [af], P.L. Cole [t,j,am], M. Contalbrigo [u], V. Crede [q], A. D'Angelo [x,ai], N. Dashyan [aq], R. De Vita [w], E. De Sanctis [v], A. Deur [am], C. Djalali [al], G.E. Dodge [c], D. Doughty [l,am], R. Dupre [y], H. Egiyan [am], A. El Alaoui [e], L. El Fassi [e], P. Eugenio [q], G. Fedotov [al,aj], S. Fegan [an,1], J.A. Fleming [n], M.Y. Gabrielyan [p], N. Gevorgyan [aq], G.P. Gilfoyle [ah], K.L. Giovanetti [aa], F.X. Girod [am], J.T. Goetz [af], W. Gohn [m], E. Golovatch [aj], R.W. Gothe [al], K.A. Griffioen [ap], L. Guo [p,am], K. Hafidi [e], N. Harrison [m], D. Heddle [l,am], K. Hicks [af], M. Holtrop [ad], C.E. Hyde [c], Y. Ilieva [al,s], D.G. Ireland [an], B.S. Ishkhanov [aj,ak], E.L. Isupov [aj], H.S. Jo [y], K. Joo [m], D. Keller [ao], M. Khandaker [ae], P. Khetarpal [p], A. Kim [ab], F.J. Klein [j], S. Koirala [c], A. Kubarovsky [ag,aj], V. Kubarovsky [am,ag], S.E. Kuhn [c], K. Livingston [an], H.Y. Lu [i], I.J.D. MacGregor [an], D. Martinez [t], M. Mayer [c], B. McKinnon [an], T. Mineeva [m], V. Mokeev [am,aj], R.A. Montgomery [an], H. Moutarde [k], E. Munevar [am], C. Munoz Camacho [y], B. Mustapha [e], P. Nadel-Turonski [am], R. Nasseripour [aa,p], S. Niccolai [y], G. Niculescu [aa], I. Niculescu [aa], M. Osipenko [w], A.I. Ostrovidov [q], L.L. Pappalardo [u], R. Paremuzyan [aq,2], K. Park [am,ab], S. Park [q], E. Pasyuk [am,f], E. Phelps [al], J.J. Phillips [an], S. Pisano [v], N. Pivnyuk [z], O. Pogorelko [z], S. Pozdniakov [z], J.W. Price [g], S. Procureur [k], D. Protopopescu [an], A.J.R. Puckett [am], B.A. Raue [p,am], D. Rimal [p], M. Ripani [w], B.G. Ritchie [f], G. Rosner [an], P. Rossi [v], F. Sabatié [k], M.S. Saini [q], D. Schott [s], R.A. Schumacher [i], H. Seraydaryan [c], Y.G. Sharabian [am], G.D. Smith [an], D.I. Sober [j], D. Sokhan [an], S.S. Stepanyan [ab], S. Stepanyan [am], S. Strauch [al,s], M. Taiuti [r,1], W. Tang [af], C.E. Taylor [t], Ye Tian [al], S. Tkachenko [ao], M. Ungaro [am,ag], B. Vernarsky [i], A. Vlassov [z], H. Voskanyan [aq], E. Voutier [ac], N.K. Walford [j], D.P. Watts [n], M.H. Wood [h,al], N. Zachariou [al], L. Zana [ad], J. Zhang [am], X. Zheng [e,3], I. Zonta [x,4]

[a] *Tel Aviv University, Tel Aviv 69978, Israel*
[b] *Universidad Técnica Federico Santa María, Casilla 110-V, Valparaíso, Chile*
[c] *Old Dominion University, Norfolk, VA 23529, United States*
[d] *Massachusetts Institute of Technology, Cambridge, MA 02139, United States*
[e] *Argonne National Laboratory, Argonne, IL 60439, United States*
[f] *Arizona State University, Tempe, AZ 85287-1504, United States*
[g] *California State University, Dominguez Hills, Carson, CA 90747, United States*
[h] *Canisius College, Buffalo, NY, United States*
[i] *Carnegie Mellon University, Pittsburgh, PA 15213, United States*
[j] *Catholic University of America, Washington, DC 20064, United States*
[k] *CEA, Centre de Saclay, Irfu/Service de Physique Nucléaire, 91191 Gif-sur-Yvette, France*
[l] *Christopher Newport University, Newport News, VA 23606, United States*
[m] *University of Connecticut, Storrs, CT 06269, United States*
[n] *Edinburgh University, Edinburgh EH9 3JZ, United Kingdom*
[o] *Fairfield University, Fairfield, CT 06824, United States*
[p] *Florida International University, Miami, FL 33199, United States*
[q] *Florida State University, Tallahassee, FL 32306, United States*
[r] *Università di Genova, 16146 Genova, Italy*
[s] *The George Washington University, Washington, DC 20052, United States*
[t] *Idaho State University, Pocatello, ID 83209, United States*
[u] *INFN, Sezione di Ferrara, 44100 Ferrara, Italy*
[v] *INFN, Laboratori Nazionali di Frascati, 00044 Frascati, Italy*
[w] *INFN, Sezione di Genova, 16146 Genova, Italy*
[x] *INFN, Sezione di Roma Tor Vergata, 00133 Rome, Italy*

http://dx.doi.org/10.1016/j.physletb.2013.04.011

[y] *Institut de Physique Nucléaire ORSAY, Orsay, France*
[z] *Institute of Theoretical and Experimental Physics, 117259 Moscow, Russia*
[aa] *James Madison University, Harrisonburg, VA 22807, United States*
[ab] *Kyungpook National University, Daegu 702-701, Republic of Korea*
[ac] *LPSC, Universite Joseph Fourier, CNRS/IN2P3, INPG, Grenoble, France*
[ad] *University of New Hampshire, Durham, NH 03824-3568, United States*
[ae] *Norfolk State University, Norfolk, VA 23504, United States*
[af] *Ohio University, Athens, OH 45701, United States*
[ag] *Rensselaer Polytechnic Institute, Troy, NY 12180-3590, United States*
[ah] *University of Richmond, Richmond, VA 23173, United States*
[ai] *Universita' di Roma Tor Vergata, 00133 Rome, Italy*
[aj] *Skobeltsyn Nuclear Physics Institute, 119899 Moscow, Russia*
[ak] *Physics Department, Moscow State University, 119899 Moscow, Russia*
[al] *University of South Carolina, Columbia, SC 29208, United States*
[am] *Thomas Jefferson National Accelerator Facility, Newport News, VA 23606, United States*
[an] *University of Glasgow, Glasgow G12 8QQ, United Kingdom*
[ao] *University of Virginia, Charlottesville, VA 22901, United States*
[ap] *College of William and Mary, Williamsburg, VA 23187-8795, United States*
[aq] *Yerevan Physics Institute, 375036 Yerevan, Armenia*

ARTICLE INFO

Article history:
Received 22 December 2012
Received in revised form 3 April 2013
Accepted 3 April 2013
Available online 6 April 2013
Editor: D.F. Geesaman

ABSTRACT

Nuclear transparency, $T_p(A)$, is a measure of the average probability for a struck proton to escape the nucleus without significant re-interaction. Previously, nuclear transparencies were extracted for quasi-elastic $A(e,e'p)$ knockout of protons with momentum below the Fermi momentum, where the spectral functions are well known. In this Letter we extract a novel observable, the transparency ratio, $T_p(A)/T_p(^{12}\mathrm{C})$, for knockout of high-missing-momentum protons from the breakup of short-range correlated pairs (2N-SRC) in Al, Fe and Pb nuclei relative to C. The ratios were measured at momentum transfer $Q^2 \geqslant 1.5$ (GeV/c)^2 and $x_B \geqslant 1.2$ where the reaction is expected to be dominated by electron scattering from 2N-SRC. The transparency ratios of the knocked-out protons coming from 2N-SRC breakup are 20–30% lower than those of previous results for low missing momentum. They agree with Glauber calculations and agree with renormalization of the previously published transparencies as proposed by recent theoretical investigations. The new transparencies scale as $A^{-1/3}$, which is consistent with dominance of scattering from nucleons at the nuclear surface.

Nuclear transparency, $T(A)$, is defined as the ratio of the cross section per nucleon for a process on a bound nucleon in the nucleus to that from a free nucleon. Conventionally, for protons, $T_p(A)$ has been extracted as the ratio of the measured $A(e,e'p)$ quasi-elastic (QE) cross section to the calculated Plane-Wave Impulse Approximation (PWIA) cross section, which does not include Final State Interactions (FSI). The experimental cross sections are typically integrated over proton missing momenta below the Fermi momentum ($|P_{miss}| \leqslant k_F \approx 250$ MeV/c), and missing energy, E_{miss}, below 80 MeV corresponding to knockout of mean-field protons [1–4]. ($\vec{P}_{miss} = \vec{q} - \vec{P}_p$ and $E_{miss} = \omega - T_p$, where $\vec{q}$ and ω are the momentum and energy transfer of the virtual photon and P_p and T_p are the momentum and kinetic energy of the outgoing proton, respectively.) For a recent review, see [5].

Two-nucleon short-range correlations (2N-SRC) are pairs of nucleons with high momentum ($\vec{p}_1$, $\vec{p}_2$) that balance each other. The pair has high relative momentum ($\vec{p}_{rel} = \frac{\vec{p}_1-\vec{p}_2}{2}$) and low center of mass momentum ($\vec{p}_{c.m.} = \vec{p}_1 + \vec{p}_2$), where high and low is relative to the Fermi momentum. 2N-SRC consist mainly of neutron–proton pairs and dominate the tail ($|P| \geqslant k_F$) of the nuclear momentum distribution for all nuclei [6–16].

For the extraction of nuclear transparency from the $A(e,e'p)$ quasi-elastic data, the 2N-SRC are an obstacle since they remove a fraction of the single-particle strength beyond the missing momentum and energy integration range. This removed strength is difficult to accurately ascertain and therefore introduces uncertainty to the absolute value of $T_p(A)$. Published experimental data, following [1], used large correction factors (1.11 ± 0.03, 1.22 ± 0.06, and 1.28 ± 0.10, for ^{12}C, ^{56}Fe, and ^{197}Au, respectively). These are larger than indicated by more recent calculations [17,18]. This is believed to be the main reason for the discrepancy between the measured $T_p(A)$ transparencies and calculations using the Glauber approximation to describe the FSI of the outgoing struck proton with the residual nucleus [17,18].

In this Letter we avoid the necessity of using hybrid measured-to-calculated ratios and bypass the uncertainty due to the 2N-SRC correction factors. We present the transparency ratios of $T_p(A)/T_p(^{12}\mathrm{C})$, where A stands for ^{27}Al, ^{56}Fe, and ^{208}Pb. These ratios are determined for high-missing-momentum protons knocked out from the breakup of two-nucleon short-range correlated pairs.

The data presented here were collected as part of the EG2 run period that took place in 2004 in Hall B of the Thomas Jefferson National Accelerator Facility (Jefferson Lab), using a 5.014 GeV unpolarized electron beam and the CEBAF Large Acceptance Spectrometer (CLAS) [19]. The analysis was carried out as part of the Jefferson Lab Hall B Data-Mining project [20].

CLAS uses a toroidal magnetic field (with electrons bending towards the beam line) and six independent sets of drift chambers, time-of-flight (TOF) scintillation counters, Cherenkov counters (CC), and electro–magnetic calorimeters (EC) for charged particle

---

* Corresponding author.
E-mail address: or.chen@mail.huji.ac.il (O. Hen).

[1] Current address: INFN, Sezione di Genova, 16146 Genova, Italy.

[2] Current address: Institut de Physique Nucléaire ORSAY, Orsay, France.

[3] Current address: University of Virginia, Charlottesville, VA 22901, United States.

[4] Current address: Universita' di Roma Tor Vergata, 00133 Rome, Italy.

identification and trajectory reconstruction. The polar angular acceptance is $8^\circ < \theta < 140^\circ$ and the azimuthal angular acceptance is 50% at small polar angles, increasing to 80% at larger polar angles.

We identified electrons and rejected pions by requiring that negative particles produced more than 2.5 photo-electrons in the Cherenkov counter. Additional electron/pion separation was achieved by demanding a correlation between the energy deposited in the inner and outer parts of the EC divided by the momentum of the particle [19]. The total energy deposited by electrons in the calorimeter was closely correlated with the electron momentum over the full momentum range. This indicates the electrons are identified cleanly. We applied fiducial cuts on the angle and momentum of the electrons to avoid regions with steeply varying acceptance close to the magnetic coils of CLAS.

Protons in CLAS were identified by requiring that the difference between the measured time-of-flight of positively charged particles and that calculated from their measured momentum and the proton mass be less than two standard deviations. This cut clearly separates protons from pions/kaons up to $p = 2.8$ GeV/c. Due to statistical limitations, we only show data for protons up to 2.4 GeV/c.

The kinetic energy of the incoming electron and emerging electron and proton were corrected event-by-event for coulomb distortions using the Effective Momentum Approximation (EMA) [21]. Following [13] we assume an effective electric potential equal to 75% of the potential produced by unscreened Z charges at the nucleus center. This amounts to a 3, 5, 10 and 20 MeV correction for ^{12}C, ^{27}Al, ^{56}Fe and ^{208}Pb, respectively.

The EG2 run period used a specially designed target setup, consisting of an approximately 2-cm LD_2 cryotarget followed by one of six independently-insertable solid targets ranging in thickness from 0.16 to 0.38 g/cm^2 (thin and thick Al, Sn, C, Fe, and Pb, all in natural isotopic abundance) [22]. The LD_2 target cell and the solid targets were separated by about 4 cm. We selected events with particles scattering from the solid targets by reconstructing the intersections of their trajectories with the beam line. The vertex reconstruction resolution for both electrons and protons was sufficient to unambiguously separate particles originating in the cryotarget and the solid target.

Cross section ratios for scattering off the solid targets are defined as the yield ratio, normalized according to the number of scatterers in the target and the integrated luminosity accumulated for each target during the experiment. Because all solid targets were located at the same location along the beam line and because the $A(e,e'p)$ missing energy and missing momentum distributions for the different targets were similar, the detector acceptance effects on the ratios of yields from different solid targets are negligible in comparison to our statistical and other systematic uncertainties.

To identify semi-exclusive $A(e,e'p)$ events dominated by scattering off 2N-SRC pairs, one must choose kinematics in which competing processes are suppressed. Table 1 lists the cuts applied and the ranges over which those cuts were varied to determine the systematic uncertainty. Q^2 and ω are the four-momentum and energy transfer of the virtual photon, $x_B = \frac{Q^2}{2m_N\omega}$ is the Bjorken scaling variable, and m_N is the nucleon mass. $\vec{P}_{miss} = \vec{q} - \vec{P}_p$ is the missing momentum which, in the Plane-Wave Impulse Approximation (PWIA), equals the initial momentum of the proton before it absorbed the virtual photon. m_{miss} is the reconstructed missing mass for the $(e,e'p)X$ reaction assuming scattering off a stationary nucleon pair. θ_{pq} is the angle between the outgoing proton and the virtual photon in the lab frame.

Table 1
The $(e,e'p)$ event selection cuts. Also shown is the sensitivity of the transparency ratios to variations in the cuts.

Cut	Cuts sensitivity			
	Range	Al/C	Fe/C	Pb/C
$x_B \geqslant 1.2$	± 0.05	1.4%	3.2%	0.4%
$300 \leqslant \lvert\vec{P}_{miss}\rvert \leqslant 600$ MeV/c	± 25 MeV/c*	2.0%	1.8%	2.6%
$\theta_{pq} \leqslant 25^\circ$	$\pm 5^\circ$**	0.6%	0.3%	0.2%
$\lvert\lvert\vec{P}_p\rvert/\lvert\vec{q}\rvert - 0.79\rvert \leqslant 0.17$	± 0.05**			
$m_{miss} \leqslant 1100$ MeV/c^2	± 50 MeV/c^2	0.5%	1.1%	3.3%

* The geometric mean of all combinations of 300+25 MeV/c and 600±25 MeV/c variations are presented.

** Both leading proton cuts were varied together as shown by the dashed squares in Fig. 1.

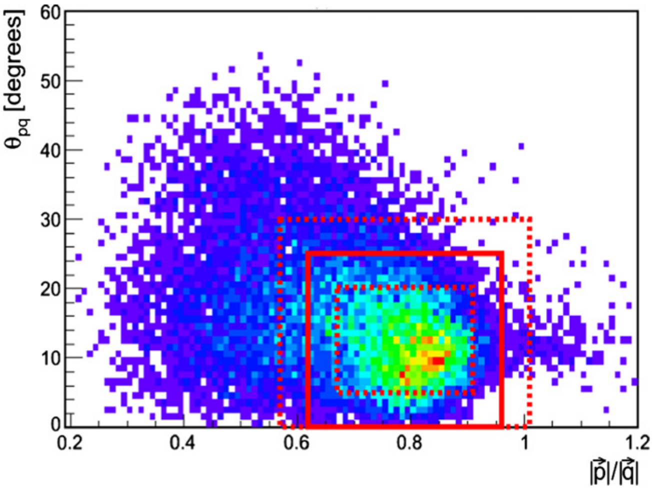

Fig. 1. (Color online) The relative angle between the detected proton and the momentum transfer vector $\vec{q}$ versus the ratio of the detected proton momentum and the momentum transfer ($|\vec{p}_p|/|\vec{q}|$). Only ^{12}C$(e,e'p)$ events with $x_B \geqslant 1.2$ and $300 \leqslant |P_{miss}| \leqslant 1000$ MeV/c are shown. The solid/dashed boxes (red online) show the cuts applied to select leading protons. See Table 1 for details.

The cut on x_B is lower than used in inclusive scattering, but the additional cut on P_{miss} ensures the selection of events dominated by scattering off 2N-SRC pairs, as shown by previous experiments [6,7]. The cut on m_{miss} suppresses the contribution of Δ excitations and meson production. The cuts on $|\vec{P}_p|/|\vec{q}|$ and θ_{pq} select the struck leading proton (see Fig. 1). At most one proton per event passed these cuts, even for events with more than one detected proton. These cuts combined with the CLAS acceptance result in a momentum transfer distribution that ranges from approximately 1.5 to 3.5 (GeV/c)^2 (see Fig. 2).

At these kinematics ($Q^2 > 1.5$ (GeV/c)^2, $x_B > 1.2$, and missing momentum $300 \leqslant P_{miss} \leqslant 600$ MeV/c) the nucleon momentum distribution for any given nucleus scales as the number of 2N-SRC pairs in that nucleus times a common momentum distribution. This interpretation is strongly supported by both experimental [6–13] and theoretical investigations [14–16]. The $A(e,e'p)$ cross section in the Plane-Wave Impulse Approximation (PWIA) equals a kinematic factor times the elementary electron–proton elastic cross section times the probability of finding a proton at that missing energy and missing momentum. Under these assumptions, the PWIA cross section ratio for scattering off high-momentum protons from two different nuclei will equal the ratio of the number of pN-SRC pairs in the two nuclei (since the other factors all cancel in the ratio). Since the PWIA cross section does not include the effects of nucleon rescattering as they exit the nucleus, we therefore define the proton transparency ratio of any two nuclei in this kinematical regime as the ratio of their measured cross sections scaled by the product of the number of pN-SRC pairs:

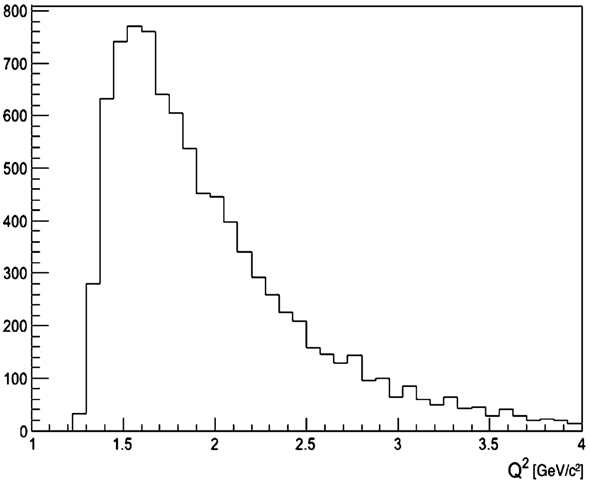

Fig. 2. Q^2 distribution for the selected $(e, e'p)$ event sample.

$$\frac{T_p(A_1)}{T_p(A_2)} = \frac{\sigma_{A_1(e,e'p)}/(N_{np}^{A_1} + 2N_{pp}^{A_1})}{\sigma_{A_2(e,e'p)}/(N_{np}^{A_2} + 2N_{pp}^{A_2})}, \tag{1}$$

where $\sigma_{A(e,e'p)}$ is the measured quasi-elastic scattering cross section for nucleus A, and N_{np}^A and N_{pp}^A are the average number of np and pp SRC pairs in nucleus A. (The factor of 2 multiplying N_{pp}^A reflects the fact that the electron can scatter from either proton in a pp pair.)

Under minimal assumptions (see Appendix A for details), this simplifies to

$$\frac{T_p(A_1)}{T_p(A_2)} = \frac{1}{a_2(A_1/A_2)} \cdot \frac{\sigma_{A_1(e,e'p)}/A_1}{\sigma_{A_2(e,e'p)}/A_2}, \tag{2}$$

where $a_2(A_1/A_2)$ is the relative number of $2N$-SRC pairs per nucleon in nuclei A_1 and A_2. This is exact for isospin symmetric nuclei and should be valid to better than 5% even for asymmetric nuclei such as lead. The ratios $a_2(A_1/A_2)$ are taken from a compilation of world data on (e, e') cross section ratios at large Q^2 and $x_B > 1$ including different theoretical corrections [24]. The values used are: $a_2(^{27}\text{Al}/^{12}\text{C}) = a_2(^{56}\text{Fe}/^{12}\text{C}) = 1.100 \pm 0.055$ and $a_2(^{208}\text{Pb}/^{12}\text{C}) = 1.080 \pm 0.054$. These values are the average of the high precision data of [13], with three different sets of theoretical corrections as presented in Table I, columns 4–6 of Ref. [24]. Notice that the corrections due to the center-of-mass motion of the pair, and their uncertainties, are relevant for the ratios to deuterium and are negligible in the ratio of $A/^{12}\text{C}$. To be conservative, the uncertainty of $a_2(A_1/A_2)$ was taken to be that of column 6 of Ref. [24]. Notice that for all nuclei with $A \geqslant 12$, $a_2(A_1/A_2)$ is close to unity. This means that all of these nuclei have about the same number of $2N$-SRC pairs per nucleon. From the measured inclusive data we know this probability is about 20% to 25% for $A \geqslant 12$ [11,12].

The transparency ratios of protons from $2N$-SRC pairs for ^{27}Al, ^{56}Fe, and ^{208}Pb relative to ^{12}C, as extracted from the semi-inclusive $A(e, e'p)$ cross sections in SRC-dominated kinematics ($x_B \geqslant 1.2$, $Q^2 \geqslant 1.5$ (GeV/c)^2, and $P_{miss} \geqslant 0.3$ GeV/c), using Eq. (2), are shown in Fig. 3 as a function of the outgoing proton momentum

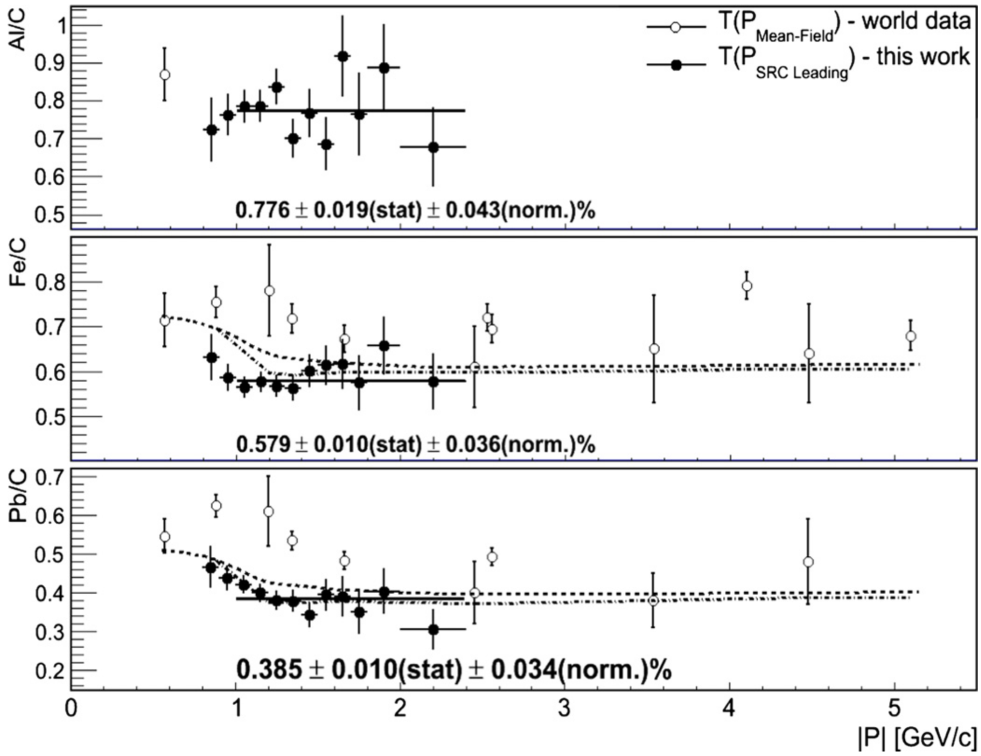

Fig. 3. The measured transparency ratios for various nuclei with respect to carbon of protons from $2N$-SRC pairs (full circles), extracted using Eq. (2), shown as a function of the outgoing proton momentum. The horizontal error bars represent the integration region (bin widths). The solid line is the average transparency and the values are shown. The normalization uncertainty is dominated by the uncertainties in the SRC scaling factors (see text for details). Also shown for comparison are the world data for transparency ratios for mean-field proton knockout from Refs. [1–4] (empty circles), extending up to a proton momenta of 5 GeV/c. Note that Ref. [2] did not report results for Fe and Pb; we show their results for Ni and Ta instead. The results from Refs. [1,3] and also [4] in the bottom panel are for Au rather than Pb. Over the momentum range covered by this experiment, the transparency ratios of protons from $2N$-SRC are lower than those of mean-field protons by 20–30%. Glauber calculations are shown as dashed lines [23] and dash-dotted lines [5,18]. For figure clarity we omitted the world data for mean-field transparencies without the SRC renormalization which can be found in [5].

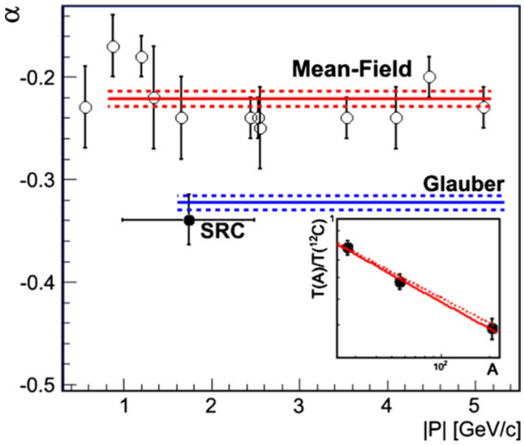

Fig. 4. (Color online) The A-dependence of the nuclear transparency extracted by fitting the SRC transparency ratios (filled circles) and the mean-field transparency ratios [4] (open circles) to A^α. The solid line is a constant fit to the world data (red online) and the dashed lines show the $\pm 1\sigma$ limits. The dashed-dot line is the Glauber result (blue online) of [23]. The insert shows the A-dependence of the SRC transparency ratio with the fits to the data (solid line) and to the Glauber result (dashed line) on a log–log scale. The transparency ratios used are average values shown in Fig. 3, where the statistical and normalization uncertainties were added linearly. The horizontal error bars indicate the bin width.

(which should determine the probability for re-interacting). The errors shown are statistical only. The $A(e,e'p)$ cross section ratios were corrected for radiative effects [25] in the same way as was done in [11,12]. The radiative correction to the transparency ratios was found to equal $\approx 7\%$ for all ratios, with a negligible contribution to the total systematic uncertainty. The extracted transparency ratios are independent of the proton momentum for $1.0 \leqslant P_p \leqslant 2.4$ GeV/c for each of the three nuclei. The average proton transparency, $T_p(A/\mathrm{C})$, equals $0.776 \pm 0.019 \pm 0.043$ for Al, $0.579 \pm 0.010 \pm 0.036$ for Fe and $0.385 \pm 0.010 \pm 0.034$ for Pb. The first uncertainty is statistical and the second is systematic. The systematic uncertainty includes the uncertainty in $a_2(A_1/A_2)$ (5%), the sensitivity to cuts (see Table 1), and the uncertainty of 5% in the np-dominance assumption for the $^{208}\mathrm{Pb}/^{12}\mathrm{C}$ case. The uncertainty on the integrated luminosity is negligible. The systematic uncertainty is independent of the proton momentum.

These transparency ratios indicate that a high-momentum proton from an SRC pair in iron is only about 60% as likely to escape the nucleus as a similar proton in carbon. This probability ratio for lead is 40%. These ratios are 20–30% lower than the corresponding published ratios for mean-field protons [1–4]. Recent theoretical studies [17,18] claim that the published mean-field proton transparencies are too high because the PWIA calculations incorrectly included a correction factor that overestimated the effect of 2N-SRC and therefore underestimated the number of available mean-field protons. This same conclusion was reached from transport calculations [26]. Our measured proton transparency ratios support this claim.

Following [1–4], the A-dependence of the measured transparency ratios was studied by fitting it to $(\frac{A}{12})^\alpha$ (see Fig. 4). Our extracted value of $\alpha = -0.34 \pm 0.02$ is considerably lower than the average mean-field value of $\alpha = -0.22 \pm 0.01$ [4] and is consistent with the Glauber result of $\alpha = -0.322 \pm 0.007$. The observation of $\alpha \approx -1/3$ is consistent with the $T(A) \propto 1/r$ attenuation expectation of Ref. [17], where r is the nuclear radius, indicating that the reaction is dominated by scattering off the nuclear surface.

In summary, we measured semi-inclusive $A(e,e'p)$ cross section ratios for $^{27}\mathrm{Al}$, $^{56}\mathrm{Fe}$ and $^{208}\mathrm{Pb}$ nuclei relative to $^{12}\mathrm{C}$ at $Q^2 \geqslant 1.5$ GeV/c^2, $x_B \geqslant 1.2$ and $300 \leqslant P_{miss} \leqslant 600$ MeV/c where knockout of protons from 2N-SRC should dominate. We used these cross section ratios to extract the transparency ratios for protons from the 2N-SRC breakup. The proton transparency ratios are independent of proton momentum and are 20–30% lower than the transparency ratios of mean-field proton knockout. This difference is consistent with the proposed renormalization of the mean-field transparencies to properly account for the effects of correlated nucleons [17,18]. See Ref. [5] for a comparison of the Glauber calculations to the data, with and without the SRC correction factors.

The A-dependence of our measured transparency ratios are steeper than that of mean-field protons [4] and consistent with Glauber calculations. This A-dependence is consistent with a simple picture of proton knockout from the nuclear surface, i.e., that protons knocked out from the nuclear volume rescatter.

Acknowledgements

We acknowledge the efforts of the staff of the Accelerator and Physics Divisions at Jefferson Lab that made this experiment possible. We are also grateful for many fruitful discussions with L.L. Frankfurt, M. Strikman, J. Ryckebusch, W. Cosyn, M. Sargsyan, and C. Ciofi degli Atti on the formalism and implications of the results. This work was supported by the US Department of Energy and National Science Foundation, the Israel Science Foundation, the US–Israeli Bi-National Science Foundation, the Chilean Comisión Nacional de Investigación Científica y Tecnológica (CONICYT) grants FB0821, ACT-119, 1120953, 11121448, and 791100017, the French Centre National de la Recherche Scientifique and Commissariat a l'Energie Atomique, the French-American Cultural Exchange (FACE), the Italian Istituto Nazionale di Fisica Nucleare, the National Research Foundation of Korea, and the United Kingdom's Science and Technology Facilities Council (STFC). The Jefferson Science Associates (JSA) operates the Thomas Jefferson National Accelerator Facility for the United States Department of Energy under contract DE-AC05-06OR23177.

Appendix A

Inclusive $A(e,e')$ scattering cross section ratios for nuclei A relative to deuterium at $Q^2 > 1.5$ (GeV/c)^2 are independent of x_B (scale) for $1.5 \leqslant x_B \leqslant 1.9$ [10–13]. The scaling factor (the value of this cross section ratio), denoted as $a_2(A/d)$, is typically interpreted as a measure of the number of 2N-SRC pairs per nucleon in nucleus A relative to d [14–16]. When we take the ratio of $a_2(A_1/d)$ and $a_2(A_2/d)$, this gives us $a_2(A_1/A_2)$, the relative number of 2N-SRC pairs per nucleon in nuclei A_1 and A_2. In this appendix we will relate this measured quantity to the values $N_{Np}^{A_1}$ used in Eq. (1).

In this kinematic region we can assume that the electron scattering cross section from the nucleus is approximately equal to the incoherent sum of electron scattering from the constituent nucleons and therefore is proportional to the number of nucleons times the electron–nucleon cross section. Since at $x_B \geqslant 1.5$, inclusive electron scattering from nuclei is only sensitive to high-momentum nucleons, this gives

$$a_2(A_1/A_2) = \frac{(N_{np}^{A_1} \cdot (\sigma_{ep} + \sigma_{en}) + 2N_{pp}^{A_1} \cdot \sigma_{ep} + 2N_{nn}^{A_1} \cdot \sigma_{en})/A_1}{(N_{np}^{A_2} \cdot (\sigma_{ep} + \sigma_{en}) + 2N_{pp}^{A_2} \cdot \sigma_{ep} + 2N_{nn}^{A_2} \cdot \sigma_{en})/A_2}, \tag{3}$$

where σ_{eN} is the off-shell electron–nucleon elastic scattering cross section and N_{nn}^{A} is the number of neutron–neutron SRC pairs in nucleus A. (For np pairs, the electron can scatter from either the proton or the neutron, so the relevant cross section is $\sigma_{ep} + \sigma_{en}$ and similarly for nn and pp pairs.)

For isospin symmetric nuclei, we can assume that $N_{nn} = N_{pp}$ and therefore Eq. (3) simplifies to

$$a_2(A_1/A_2) = \frac{(\sigma_{ep} + \sigma_{en}) \cdot (N_{np}^{A_1} + 2N_{pp}^{A_1})/A_1}{(\sigma_{ep} + \sigma_{en}) \cdot (N_{np}^{A_2} + 2N_{pp}^{A_2})/A_2} = \frac{1/A_1}{1/A_2} \cdot \frac{(N_{np}^{A_1} + 2N_{pp}^{A_1})}{(N_{np}^{A_2} + 2N_{pp}^{A_2})}, \tag{4}$$

which can be inserted directly in Eq. (1).

Even for non-isospin symmetric nuclei Eq. (4) is reasonably accurate because there are about 20 times more np-SRC than pp- or nn-SRC pairs ($N_{np} \approx 20 \times N_{pp}, N_{nn}$) [6–9]. If we use the measured value of $N_{np}/N_{pp} = 18 \pm 3$ [7] and assume that $N_{nn}^{\mathrm{Pb}}/N_{pp}^{\mathrm{Pb}} = 126^2/82^2 = 2.5$, then Eq. (4) is valid to about 5%.

Therefore we can rewrite Eq. (1) as

$$\frac{T_p(A_1)}{T_p(A_2)} = \frac{1}{a_2(A_1/A_2)} \cdot \frac{\sigma_{A_1(e,e'p)}/A_1}{\sigma_{A_2(e,e'p)}/A_2}. \tag{5}$$

This is exact for isospin symmetric nuclei and should be valid to better than 5% even for asymmetric nuclei such as lead.

References

[1] T.G. O'Neill, et al., Phys. Lett. B 351 (1995) 87.
[2] G. Garino, et al., Phys. Rev. C 45 (1992) 780.
[3] D. Abbott, et al., Phys. Rev. Lett. 80 (1998) 5072.
[4] K. Garrow, et al., Phys. Rev. C 66 (2002) 044613.
[5] D. Dutta, K. Hafidi, M. Strikman, arXiv:1211.2826, 2012.
[6] R. Shneor, et al., Phys. Rev. Lett. 99 (2007) 072501.
[7] R. Subedi, et al., Science 320 (2008) 1476.
[8] A. Tang, et al., Phys. Rev. Lett. 90 (2003) 042301.
[9] E. Piasetzky, et al., Phys. Rev. Lett. 97 (2006) 162504.
[10] D. Day, et al., Phys. Rev. Lett. 59 (1987) 427.
[11] K. Egiyan, et al., CLAS Collaboration, Phys. Rev. C 68 (2003) 014313.
[12] K. Egiyan, et al., CLAS Collaboration, Phys. Rev. Lett. 96 (2006) 082501.
[13] N. Fomin, et al., Phys. Rev. Lett. 108 (2012) 092502.
[14] L.L. Frankfurt, M.I. Strikman, Phys. Rep. 76 (1981) 215;
L.L. Frankfurt, M.I. Strikman, Phys. Rep. 160 (1988) 235.
[15] L.L. Frankfurt, M.I. Strikman, D.B. Day, M. Sargsyan, Phys. Rev. C 48 (1993) 2451.
[16] C. Ciofi degli Atti, S. Simula, Phys. Lett. B 325 (1994) 276;
C. Ciofi degli Atti, S. Simula, Phys. Rev. C 53 (1996) 1689.
[17] P. Lava, M.C. Martinez, J. Ryckebsch, J.A. Caballero, J.M. Udias, Phys. Lett. B 595 (2004) 177.
[18] L.L. Frankfurt, M.I. Strikman, M. Zhalov, Phys. Lett. B 503 (2001) 73.
[19] B.A. Mecking, et al., Nucl. Instrum. Methods A 503 (2003) 512.
[20] L.B. Weinstein, S.E. Kuhn, Short distance structure of nuclei: Mining the wealth of existing jefferson lab data, DOE Grant DE-SC0006801.
[21] A. Aste, C. von Arx, D. Trautmann, Eur. Phys. J. A 26 (2005) 167, nucl-th/0502074.
[22] H. Hakobyan, et al., Nucl. Instrum. Methods A 592 (2008) 218.
[23] V.J. Pandharipande, S.C. Pieper, Phys. Rev. C 45 (1992) 791.
[24] O. Hen, E. Piasetzky, L.B. Weinstein, Phys. Rev. C 85 (2012) 047301.
[25] M.M. Sargsyan, Report No. YERPHI-1331-26-91, 1991, unpublished.
[26] J. Lehr, U. Mosel, Nucl. Phys. A 699 (2002) 324.

4. Implications of High-Momentum Nucleons in Nuclei

4.1. Deep Inelastic Scattering

"Short-Range Correlations and the EMC Effect",
L.B. Weinstein et al., Phys. Rev. Lett. ***106****, 052301 (2011).*

"New data strengthen the connection between Short Range Correlations and the EMC effect",
O. Hen et al., Phys. Rev. C ***85****, 047301 (2012).*

"Constraints on the Large-x d/u Ratio from Electron-Nucleus Scattering at x→1",
O. Hen et al., Phys. Rev. D. ***84****, 117501 (2011).*

Short Range Correlations and the EMC Effect

L. B. Weinstein,[1,*] E. Piasetzky,[2] D. W. Higinbotham,[3] J. Gomez,[3] O. Hen,[2] and R. Shneor[2]
[1]*Old Dominion University, Norfolk, Virginia 23529, USA*
[2]*Tel Aviv University, Tel Aviv 69978, Israel*
[3]*Thomas Jefferson National Accelerator Facility, Newport News, Virginia 23606, USA*

(Received 29 September 2010; published 4 February 2011)

This Letter shows quantitatively that the magnitude of the EMC effect measured in electron deep inelastic scattering at intermediate x_B, $0.35 \leq x_B \leq 0.7$, is linearly related to the short range correlation (SRC) scale factor obtained from electron inclusive scattering at $x_B \geq 1$. The observed phenomenological relationship is used to extract the ratio of the deuteron to the free pn pair cross sections and F_2^n/F_2^p, the ratio of the free neutron to free proton structure functions. We speculate that the observed correlation is because both the EMC effect and SRC are dominated by the high virtuality (high momentum) nucleons in the nucleus.

DOI: 10.1103/PhysRevLett.106.052301 PACS numbers: 25.30.Fj, 13.60.Hb, 21.30.−x

Inclusive electron scattering, $A(e, e')$, is a valuable tool for studying nuclei. By selecting specific kinematic conditions, especially the four-momentum and energy transfers, Q^2 and ω, one can focus on different aspects of the nucleus. Elastic scattering has been used to measure the nuclear charge distribution. Deep inelastic scattering at $Q^2 > 2\ \mathrm{GeV}^2$, and $0.35 \leq x_B \leq 0.7$ ($x_B = Q^2/2m\omega$, where m is the nucleon mass) is sensitive to the nuclear quark distributions. Inelastic scattering at $Q^2 > 1.4\ \mathrm{GeV}^2$ and $x_B > 1.5$ is sensitive to nucleon-nucleon short range correlations (SRCs) in the nucleus. This Letter will explore the relationship between deep inelastic and large-x_B inelastic scattering.

The per-nucleon electron deep inelastic scattering (DIS) cross sections of nuclei with $A \geq 3$ are smaller than those of deuterium at $Q^2 \geq 2\ \mathrm{GeV}^2$, and moderate x_B, $0.35 \leq x_B \leq 0.7$. This effect, known as the EMC effect, has been measured for a wide range of nuclei [1–7]. There is no generally accepted explanation of the EMC effect. In general, proposed explanations need to include both nuclear structure effects (momentum distributions and binding energy) and modification of the bound nucleon structure due to the nuclear medium. Comprehensive reviews of the EMC effect can be found in [8–11] and references therein. Recent high-precision data on light nuclei [7] suggest that it is a local density effect and not a bulk property of the nuclear medium.

The per-nucleon electron inelastic scattering cross sections of nuclei with $A \geq 3$ are greater than those of deuterium for $Q^2 > 1.4\ \mathrm{GeV}^2$ and large x_B, $1.5 \leq x_B \leq 2$. The cross section ratio for two different nuclei (e.g., carbon and helium) shows a plateau when plotted as a function of x_B (i.e., it is independent of x_B). This was first observed at SLAC [12] and subsequently at Jefferson Laboratory [13,14]. The plateau indicates that the nucleon momentum distributions of different nuclei for high momentum, $p \geq p_{\mathrm{thresh}} = 0.275\ \mathrm{GeV}/c$, are similar in shape and differ only in magnitude. The ratio (in the plateau region) of the per-nucleon inclusive (e, e') cross sections for two nuclei is then the ratio of the probabilities to find high-momentum nucleons in those two nuclei [15,16].

These high-momentum nucleons were shown recently in hadronic [17,18] and leptonic [19,20] two-nucleon knockout experiments to be almost entirely due to central and tensor nucleon-nucleon short range correlations (SRCs) [21–24]. SRCs occur between pairs of nucleons with high relative momentum and low center of mass momentum, where low and high are relative to the Fermi momentum in heavy nuclei. Thus, we will call the ratio of cross sections in the plateau region the "SRC scale factor."

This Letter will show quantitatively that the magnitude of the EMC effect in nucleus A is linearly related to the SRC scale factor of that nucleus relative to deuterium. This idea was suggested by Higinbotham *et al.* [25].

We characterize the strength of the EMC effect for nucleus A following Ref. [7], as the slope of the ratio of the per-nucleon deep inelastic electron scattering cross sections of nucleus A relative to deuterium, dR_{EMC}/dx, in the region $0.35 \leq x_B \leq 0.7$. This slope is proportional to the value of the cross section ratio at $x \approx 0.5$, but is unaffected by overall normalization uncertainties that merely raise or lower all of the data points together. For ^{3}He, ^{4}He, ^{9}Be and ^{12}C we use the published slopes from [7] measured at $3 \leq Q^2 \leq 6\ \mathrm{GeV}^2$. We also fit the ratios, measured in Ref. [3], as a function of x_B for $0.36 \leq x_B \leq 0.68$. The results are averages over all measured Q^2 (i.e., $Q^2 = 2$, 5 and 10 GeV^2 for $x_B < 0.6$ and $Q^2 = 5$ and 10 GeV^2 for larger x_B). The results from the two measurements for ^{4}He and ^{12}C are consistent and we use the weighted average of the two. See Table I. The uncertainties are not meant to take into account possible effects of the antishadowing region at $x_B \approx 0.15$ and the Fermi motion region at $x_B > 0.75$ extending into the region of interest.

TABLE I. The measured EMC slopes dR_{EMC}/dx for $0.35 \leq x_B \leq 0.7$.

Nucleus	dR_{EMC}/dx (Ref. [7])	dR_{EMC}/dx (Ref. [3])	dR_{EMC}/dx (combined)
Deuteron			0
^{3}He	-0.070 ± 0.029		-0.070 ± 0.029
^{4}He	-0.199 ± 0.029	-0.191 ± 0.061	-0.197 ± 0.026
^{9}Be	-0.271 ± 0.029	-0.207 ± 0.037	-0.243 ± 0.023
^{12}C	-0.280 ± 0.029	-0.318 ± 0.040	-0.292 ± 0.023
^{27}Al		-0.325 ± 0.034	-0.325 ± 0.034
^{40}Ca		-0.350 ± 0.047	-0.350 ± 0.047
^{56}Fe		-0.388 ± 0.032	-0.388 ± 0.032
^{108}Ag		-0.496 ± 0.051	-0.496 ± 0.051
^{197}Au		-0.409 ± 0.039	-0.409 ± 0.039

The SRC scale factors determined from the isospin-corrected per-nucleon ratio of the inclusive (e, e') cross sections on nucleus A and ^{3}He, $a_2(A/^3\mathrm{He}) = (3/A)[\sigma_A(Q^2, x_B)/\sigma_{^3\mathrm{He}}(Q^2, x_B)]$ are listed in Table II using data from [14]. We used the ratio of deuterium to ^{3}He determined in Ref. [14] primarily from the calculated ratio of their momentum distributions above the scaling threshold ($p_{\mathrm{thresh}} = 0.275 \pm 0.025$ GeV/c). We combined the statistical and systematic uncertainties in quadrature to give the total uncertainties shown in the table. The SRC scale factors for nucleus A relative to deuterium, $a_2(A/d)$, are calculated from the second column.

The value of the SRC scale factors was shown to be Q^2 independent for $1.5 \leq Q^2 \leq 2.5$ GeV^2 [13] and more recently for $1.5 \leq Q^2 \leq 5$ GeV^2 [26]. Similarly, the EMC effect was shown to be Q^2 independent for SLAC, BCDMS and NMC data for $2 \leq Q^2 \leq 40$ GeV^2 [3]. This Q^2 independence allows us to compare these quantities in their different measured ranges.

Figure 1 shows the EMC slopes versus the SRC scale factors. The two values are strongly linearly correlated,

$$- dR_{\mathrm{EMC}}/dx = [a_2(A/d) - 1] \times (0.079 \pm 0.006). \quad (1)$$

This implies that both stem from the same underlying nuclear physics, such as high local density or large nucleon virtuality ($v = P^2 - m^2$ where P is the four-momentum).

This striking correlation means that we can predict the SRC scale factors for a wide range of nuclei from Be to Au using the linear relationship from Eq. (1) and the measured EMC slopes (see Table II). Note that ^{9}Be is a particularly interesting nucleus because of its cluster structure and because its EMC slope is much larger than that expected from a simple dependence on average nuclear density [7]. The EMC slopes and hence the predicted SRC scale factors may saturate for heavy nuclei but better data are needed to establish the exact A dependence.

This correlation between the EMC slopes and the SRC scale factors also allows us to extract significant information about the deuteron itself. Because of the lack of a free neutron target, the EMC measurements used the deuteron as an approximation to a free proton and neutron system and measured the ratio of inclusive DIS on nuclei to that of

TABLE II. The SRC scale factors for nucleus A with respect to ^{3}He and to deuterium. The third column is calculated from the second. The resulting uncertainties are slightly overestimated since the uncertainty in the $d/^3$He ratio of about 5% is added to all of the other ratios. The predicted values (fourth column) are calculated from the values in Table I and Eq. (1).

Nucleus	Measured $a_2(A/^3\mathrm{He})$	Measured $a_2(A/d)$	Predicted $a_2(A/d)$
Deuteron	0.508 ± 0.025	1	
^{3}He	1	1.97 ± 0.10	
^{4}He	1.93 ± 0.14	3.80 ± 0.34	
^{12}C	2.41 ± 0.17	4.75 ± 0.41	
^{56}Fe	2.83 ± 0.18	5.58 ± 0.45	
^{9}Be			4.08 ± 0.60
^{27}Al			5.13 ± 0.55
^{40}Ca			5.44 ± 0.70
^{108}Ag			7.29 ± 0.83
^{197}Au			6.19 ± 0.65

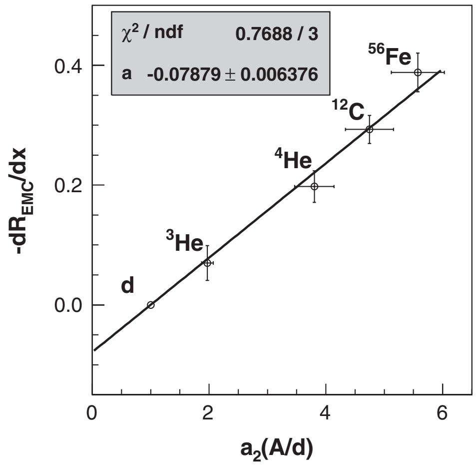

FIG. 1. The EMC slopes versus the SRC scale factors. The uncertainties include both statistical and systematic errors added in quadrature. The fit parameter is the intercept of the line and also the negative of the slope of the line.

the deuteron. This seems like a reasonable approximation since the deuteron is loosely bound (≈ 2 MeV) and the average distance between the nucleons is large (≈ 2 fm). But the deuteron is not a free system; the pion tensor force binds the two nucleons even if weakly.

To quantify the effects of the binding of nucleons in deuterium, we define the in-medium correction (IMC) effect as the ratio of the DIS cross section per nucleon bound in a nucleus relative to the free (unbound) *pn* pair cross section (as opposed to the EMC effect which uses the ratio to deuterium).

The deuteron IMC effect can be extracted from the data in Fig. 1. If the IMC effect and the SRC scale factor both stem from the same cause, then the IMC effect and the SRC scale factor will both vanish at the same point. The value $a_2(A/d) = 0$ is the limit of free nucleons with no SRC. Extrapolating the best fit line in Fig. 1 to $a_2(A/d) = 0$ gives an intercept of $dR_{\mathrm{EMC}}/dx = -0.079 \pm 0.006$. The difference between this value and the deuteron EMC slope of 0 is the deuteron IMC slope:

$$\left|\frac{dR_{\mathrm{IMC}}(d)}{dx}\right| = 0.079 \pm 0.006. \tag{2}$$

This slope is the same size as the EMC slope measured for the ratio of ^{3}He to deuterium [7]. It is slightly smaller than the deuterium IMC slope of ≈ 0.10 derived in [3] assuming that the EMC effect is proportional to the average nuclear density and the slope of 0.098 deduced by Frankfurt and Strikman based on the relative virtuality of nucleons in iron and deuterium [16] and the iron EMC slope [3].

The IMC effect for nucleus *A* is then just the difference between the measured EMC effect and the value $dR_{\mathrm{EMC}}/dx = -0.079 \pm 0.006$. Thus

$$\left|\frac{dR_{\mathrm{IMC}}(A)}{dx}\right| = \left|\frac{dR_{\mathrm{EMC}}(A)}{dx}\right|_{\mathrm{meas}} + 0.079 \pm 0.006. \tag{3}$$

This is true when the slopes are small compared to one.

The free neutron cross section can be obtained from the measured deuteron and proton cross sections using the observed phenomenological relationship presented in Fig. 1 to determine the nuclear corrections. Since the EMC effect is linear for $0.3 \le x_B \le 0.7$, we have

$$\frac{\sigma_d}{\sigma_p + \sigma_n} = 1 - a(x_B - b) \quad \text{for}\; 0.3 \le x_B \le 0.7, \tag{4}$$

where σ_d and σ_p are the measured DIS cross sections for the deuteron and free proton, σ_n is the free neutron DIS cross section that we want to extract, $a = |dR_{\mathrm{IMC}}(d)/dx| = 0.079 \pm 0.006$ and $b = 0.31 \pm 0.04$ is the average value of x_B where the EMC ratio is unity [i.e., where the per-nucleon cross sections are equal $\sigma_A(x_B)/A = \sigma_d(x_B)/2$] as determined in Refs. [3,7] and taking into account the quoted normalization uncertainties.

Our results imply that $\sigma_d/(\sigma_p + \sigma_n)$ decreases linearly from 1 to 0.97 over the range $0.3 \le x_B \le 0.7$. [More precisely, that it decreases by 0.031 ± 0.004 where the uncertainty is due to the fit uncertainties in Eq. (3).] This depletion [see Eq. (4)] is similar in size to the depletion calculated by Melnitchouk using the weak binding approximation smearing function with target mass corrections and an off-shell correction [27]. However, the distribution in x_B is very different. Melnitchouk's calculated ratio reaches its minimum of 0.97 at $x_B \approx 0.5$ and increases rapidly, crossing 1 at $x_B \approx 0.7$.

If the structure function F_2 is proportional to the DIS cross section [i.e., if the ratio of the longitudinal to transverse cross sections is the same for *n*, *p* and *d* (see discussion in [8])], then the free neutron structure function, $F_2^n(x_B, Q^2)$, can also be deduced from the measured deuteron and proton structure functions:

$$F_2^n(x_B, Q^2) = \frac{2F_2^d(x_B, Q^2) - [1 - a(x_B - b)]F_2^p(x_B, Q^2)}{[1 - a(x_B - b)]} \tag{5}$$

which leads to

$$\frac{F_2^n(x_B, Q^2)}{F_2^p(x_B, Q^2)} = \frac{2\frac{F_2^d(x_B,Q^2)}{F_2^p(x_B,Q^2)} - [1 - a(x_B - b)]}{[1 - a(x_B - b)]}. \tag{6}$$

This is only valid for $0.35 \le x_B \le 0.7$.

Figure 2 shows the ratio of F_2^n/F_2^p extracted in this work using the IMC-based correction and the $Q^2 = 12\ \mathrm{GeV}^2$ ratio F_2^d/F_2^p from Ref. [28]. Note that the ratio F_2^d/F_2^p is Q^2 independent from $6 \le Q^2 \le 20\ \mathrm{GeV}^2$ for $0.4 \le x_B \le 0.7$ [28]. The dominant uncertainty in this extraction is the uncertainty in the measured F_2^p/F_2^d. The IMC-based correction increases the extracted free neutron structure function (relative to that extracted using the deuteron

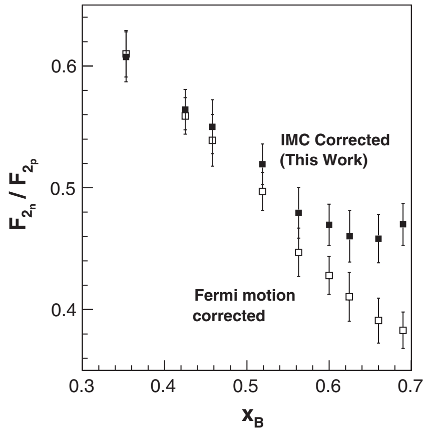

FIG. 2. The ratio of neutron to proton structure functions, $F_2^n(x_B, Q^2)/F_2^p(x_B, Q^2)$ as extracted from the measured deuteron and proton structure functions, F_2^d and F_2^p. The filled symbols show F_2^n/F_2^p extracted in this work from the deuteron in-medium correction (IMC) ratio and the world data for F_2^d/F_2^p at $Q^2 = 12\ \mathrm{GeV}^2$ [28]. The open symbols show F_2^n/F_2^p extracted from the same data correcting only for nucleon motion in deuterium using a relativistic deuteron momentum density [28].

momentum density [28]) by an amount that increases with x_B. Thus, the IMC-based F_2^n strongly favors model-based extractions of F_2^n that include nucleon modification in the deuteron [29].

The IMC-based F_2^n appears to be constant or slightly increasing in the range from $0.6 \leq x_B \leq 0.7$. The d/u ratio is simply related to the ratio of F_2^n/F_2^p in the deep inelastic limit, $x^2 \ll Q^2/4m^2$ [28], $d/u = (4F_2^n/F_2^p - 1)/(4 - F_2^n/F_n^p)$. While it is quite hazardous to extrapolate from our limited x_B range all the way to $x_B = 1$, these results appear to disfavor models of the proton with d/u ratios of 0 at $x_B = 1$ (see [29] and references therein).

By using the deuteron IMC slope, these results take into account both the nuclear corrections as well as any possible changes to the internal structure of the neutron in the deuteron. Note that this assumes either that the EMC and F_2 data are taken at the same Q^2 or that they are Q^2 independent for $6 \leq Q^2 \leq 12$ GeV^2. The fact that the measured EMC ratios for nuclei with $A \geq 3$ decrease linearly with increasing x_B for $0.35 \leq x_B \leq 0.7$ indicates that Fermi smearing is not significant in this range.

We now speculate as to the physical reason for the EMC-SRC relation presented above. Assuming that the IMC/EMC effect is due to a difference in the quark distributions in bound and free nucleons, these differences could occur predominantly in either mean field nucleons or in nucleons affected by SRC.

According to Ref. [30], the IMC/EMC effect is mainly associated with nucleons at high virtuality. These nucleons, like the nucleons affected by SRC, have larger momenta and a denser local environment than that of the other nucleons in the nucleus. Therefore, they should exhibit the largest changes in their internal structure.

The linear correlation between the strength of the EMC and the SRC in nuclei, shown in Fig. 1, indicates that possible modifications of the quark distributions occur in nucleons affected by SRC. This also predicts a larger EMC effect in higher density nuclear systems such as neutron stars. This correlation may also help us to understand the difficult to quantify nucleon modification (off-shell effects) that must occur when two nucleons are close together.

To summarize, we have found a striking linear correlation between the EMC slope measured in deep inelastic electron scattering and the short range correlations scale factor measured in inelastic scattering. The SRC are associated with large nucleon momenta and the EMC effect is associated with modified nucleon structure. This correlation allows us to extract the free neutron structure function model-independently and to place constraints on large x_B parton distribution functions. Knowledge of these parton distribution functions is important for searches for new physics in collider experiments [31] and for neutrino oscillation experiments.

We are grateful for many fruitful discussions with John Arrington, Sebastian Kuhn, Mark Strikman, Franz Gross, Jerry Miller, and Wally Melnitchouk. This work was supported by the U.S. Department of Energy, the U.S. National Science Foundation, the Israel Science Foundation, and the US-Israeli Bi-National Science Foundation. Jefferson Science Associates operates the Thomas Jefferson National Accelerator Facility under DOE Contract No. DE-AC05-06OR23177.

---

*Corresponding author; weinstein@odu.edu

[1] J. Aubert *et al.*, Phys. Lett. B **123**, 275 (1983).
[2] J. Ashman *et al.*, Phys. Lett. B **202**, 603 (1988).
[3] J. Gomez *et al.*, Phys. Rev. D **49**, 4348 (1994).
[4] M. Arneodo *et al.*, Phys. Lett. B **211**, 493 (1988).
[5] M. Arneodo *et al.*, Nucl. Phys. B **333**, 1 (1990).
[6] D. Allasia *et al.*, Phys. Lett. B **249**, 366 (1990).
[7] J. Seely *et al.*, Phys. Rev. Lett. **103**, 202301 (2009).
[8] D. Geesaman, K. Saito, and A. Thomas, Annu. Rev. Nucl. Part. Sci. **45**, 337 (1995).
[9] P. R. Norton, Rep. Prog. Phys. **66**, 1253 (2003).
[10] M. M. Sargsian *et al.*, J. Phys. G **29**, R1 (2003).
[11] J. R. Smith and G. A. Miller, Phys. Rev. C **65**, 055206 (2002).
[12] L. L. Frankfurt and M. I. Strikman, D. B. Day, and M. Sargsyan, Phys. Rev. C **48**, 2451 (1993).
[13] K. Egiyan *et al.*, Phys. Rev. C **68**, 014313 (2003).
[14] K. Egiyan *et al.*, Phys. Rev. Lett. **96**, 082501 (2006).
[15] L. L. Frankfurt and M. I. Strikman, Phys. Rep. **76**, 215 (1981).
[16] L. Frankfurt and M. Strikman, Phys. Rep. **160**, 235 (1988).
[17] A. Tang *et al.*, Phys. Rev. Lett. **90**, 042301 (2003).
[18] E. Piasetzky, M. Sargsian, L. Frankfurt, M. Strikman, and J. W. Watson, Phys. Rev. Lett. **97**, 162504 (2006).
[19] R. Shneor *et al.*, Phys. Rev. Lett. **99**, 072501 (2007).
[20] R. Subedi *et al.*, Science **320**, 1476 (2008).
[21] M. M. Sargsian, T. V. Abrahamyan, M. I. Strikman, and L. L. Frankfurt, Phys. Rev. C **71**, 044615 (2005).
[22] R. Schiavilla, R. B. Wiringa, S. C. Pieper, and J. Carlson, Phys. Rev. Lett. **98**, 132501 (2007).
[23] M. Alvioli, C. Ciofi degli Atti, and H. Morita, Phys. Rev. Lett. **100**, 162503 (2008).
[24] H. Baghdasaryan *et al.*, Phys. Rev. Lett. **105**, 222501 (2010).
[25] D. W. Higinbotham, J. Gomez, and E. Piasetzky, arXiv:1003.4497.
[26] N. Fomin, Ph.D. thesis, University of Virginia, 2007.
[27] W. Melnitchouk, AIP Conf. Proc. **1261**, 85 (2010).
[28] J. Arrington, F. Coester, R. Holt, and T.-S. H. Lee, J. Phys. G **36**, 025005 (2009).
[29] W. Melnitchouk and A. W. Thomas, Phys. Lett. B **377**, 11 (1996).
[30] C. Ciofi degli Atti, L. L. Frankfurt, L. P. Kaptari, and M. I. Strikman, Phys. Rev. C **76**, 055206 (2007).
[31] S. Kuhlmann *et al.*, Phys. Lett. B **476**, 291 (2000).

PHYSICAL REVIEW C **85**, 047301 (2012)

New data strengthen the connection between short range correlations and the EMC effect

O. Hen,[1] E. Piasetzky,[1] and L. B. Weinstein[2]
[1] *Tel Aviv University, Tel Aviv 69978, Israel*
[2] *Old Dominion University, Norfolk, Virginia 23529, USA*

(Received 15 February 2012; revised manuscript received 10 April 2012; published 26 April 2012)

Recently published measurements of the two-nucleon short range correlation (NN-SRC) scaling factors, $a_2(A/d)$, strengthen the previously observed correlation between the magnitude of the EMC effect measured in electron deep inelastic scattering at $0.35 \leqslant x_B \leqslant 0.7$ and the SRC scaling factor measured at $x_B \geqslant 1$. The new results improve precision and include previously unmeasured nuclei. The measurements of $a_2(A/d)$ for ^{9}Be and ^{197}Au agree with published predictions based on the EMC-SRC correlation. This Brief Report examines the effects of the new data and of different corrections to the data on the slope and quality of the EMC-SRC correlation, the size of the extracted deuteron in-medium correction effect, and the free-neutron structure function. The results show that the linear EMC-SRC correlation is robust and that the slope of the correlation is insensitive to most combinations of corrections examined in this work. This strengthens the interpretation that both NN-SRC and the EMC effect are related to high-momentum nucleons in the nucleus.

DOI: 10.1103/PhysRevC.85.047301 PACS number(s): 25.30.Fj, 13.60.Hb, 21.30.−x

Introduction. The per-nucleon lepton deep inelastic scattering (DIS) cross sections of heavy nuclei are less than those of deuterium at moderate to large four-momentum transfer, $Q^2 \geqslant 2$ (GeV/c)^2, and $0.35 \leqslant x_B \leqslant 0.7$ ($x_B = Q^2/2m\nu$, where ν is the energy transfer and m is the proton mass). This "EMC effect" was discovered in 1982 by the European Muon Collaboration in the cross-section ratios of iron to deuterium [1] and confirmed by many measurements on a range of nuclei [2–7]. The latest data [7] show that for light nuclei the EMC effect does not increase monotonically with increasing average nuclear density. Although there is no generally accepted explanation of the EMC effect, proposed explanations generally need to include both nuclear structure effects (momentum distributions and binding energy) and modification of the bound nucleon structure.

A recent paper showed a strong correlation between the magnitude of the EMC effect and the short range correlation (SRC) scaling factor [8]. Because the per-nucleon cross-section ratios of nuclei to deuterium for $0.35 \leqslant x_B \leqslant 0.7$ decrease approximately linearly with x_B, in this range of x_B the EMC effect can be quantified by the slope of this ratio, dR_{EMC}/dx_B [7]. The SRC scaling factor, $a_2(A/d)$, equals the ratio of the per-nucleon inclusive electron scattering cross section for nucleus A to deuterium at $Q^2 > 1.4$ (GeV/c)^2 and $1.5 \leqslant x_B < 2$. In this range of x_B, the cross-section ratio is constant [9–12]. The constancy of the ratio in this range of x_B is attributed to high-momentum components of the nuclear wave function. These high-momentum components have been shown to be almost entirely due to central and tensor nucleon-nucleon short range correlations [13–17].

This correlation between the magnitude of the EMC effect measured at $0.35 \leqslant x_B \leqslant 0.7$ and the SRC scale factor measured at $1.5 \leqslant x_B < 2$ was used to phenomenologically determine the ratio of the DIS cross section for a proton and neutron bound in deuterium to the DIS cross section for free (unbound) pn pair and thus to determine the free-neutron cross section for $0.35 \leqslant x_B \leqslant 0.7$. The free-neutron cross section was then used to determine the ratio of the neutron to proton structure function, F_2^n/F_2^p, and hence the ratio of d/u in this range of x_B.

Recently, high-precision measurements of the per-nucleon inclusive electron scattering cross-section ratio for different nuclei relative to deuterium at $Q^2 \sim 2.7$ (GeV/c)^2 and $1 < x_B < 2$ were published [18], covering more nuclei at greater precision than previous measurements. These ratios also show scaling behavior for $x_B > 1.5$. These new data allow us to reexamine the observed linear correlation between the strength of the EMC effect and the SRC scaling factor [8]. The analysis of the new data also includes various corrections to the measured cross-section ratios that were not included in previous analyses [11,12].

In this Brief Report we examine the consistency of the old and new data and the effects of different corrections to the cross-section ratios and therefore on the slope of the EMC-SRC correlation. We also examine the effects of these on the ratio of the bound to free pn DIS cross sections and on the free-neutron structure function [19].

The new data. New measurements by Fomin *et al.* [18] of the SRC scaling factor $a_2(A/d)$ have about four times smaller uncertainties than previous ones by Egiyan *et al.* [11,12]. They also include two nuclei, ^{9}Be and ^{197}Au, for which the SRC scaling factors were previously predicted based on their measured EMC effect [3,7] and the linear EMC-SRC correlation [8]. ^{9}Be is of particular interest due to the anomalous density dependence of its EMC effect (its EMC effect is larger than that of ^{4}He although its average density is much smaller) [7]. It therefore presents a challenging test for the prediction made in Ref. [8] and for the validity of the EMC-SRC correlation in general.

The different measurements have different corrections applied to their results. Both sets of measurements applied radiative corrections to their measured cross-section ratios. Egiyan *et al.* [11,12] also applied isoscalar corrections to correct for differences in the per-nucleon cross-section ratio for asymmetric nuclei due to the difference between the elementary electron-proton and electron-neutron cross

TABLE I. A comparison of SRC scaling factors, $a_2(A/d)$, extracted from different data sets with different corrections. Column 2 shows the scaling factors from Egiyan *et al.* [12]. Column 3 shows the prediction of Ref. [8] based on the EMC data of Refs. [3,7]. Columns 4 through 6 show the data of Fomin *et al.* [18] with different corrections. Column 4 shows the data with the same corrections used by Egiyan *et al.*, column 5 shows the data as published, and column 6 shows the data excluding their correction for the c.m. motion of the SRC pair. Column 7 shows the results from SLAC [10]. Column 8 shows the slopes of the EMC effect from Refs. [3,7] as cited in Ref. [8]. See the text for more details.

Nucleus	Egiyan *et al.* [12]	EMC-SRC prediction [8]	Fomin *et al.* [18] (analysis as in Ref. [12])	Fomin *et al.* [18]	Fomin *et al.* [18] (excluding the c.m. motion correction)	SLAC [10][a]	EMC slope [8] dR_{EMC}/dx
^{3}He	1.97 ± 0.10[b]		1.87 ± 0.06	1.93 ± 0.10	2.13 ± 0.04	1.7 ± 0.3	-0.070 ± 0.029
^{4}He	3.80 ± 0.34		3.64 ± 0.07	3.02 ± 0.17	3.60 ± 0.10	3.3 ± 0.5	-0.197 ± 0.026
^{9}Be		4.08 ± 0.60	4.15 ± 0.09	3.37 ± 0.17	3.91 ± 0.12		-0.243 ± 0.023
^{12}C	4.75 ± 0.41		4.81 ± 0.10	4.00 ± 0.24	4.75 ± 0.16	5.0 ± 0.5	-0.292 ± 0.023
^{56}Fe(^{63}Cu)	5.58 ± 0.45		5.29 ± 0.12	4.33 ± 0.28	5.21 ± 0.20	5.2 ± 0.9	-0.388 ± 0.032
^{197}Au		6.19 ± 0.65	5.29 ± 0.16	4.26 ± 0.29	5.16 ± 0.22	4.8 ± 0.7	-0.409 ± 0.039
EMC-SRC slope a	0.079 ± 0.006		0.082 ± 0.004	0.106 ± 0.006	0.084 ± 0.004		
$\frac{\sigma(n+p)}{\sigma_d}\vert_{x_B=0.7}$	1.032 ± 0.004		1.033 ± 0.004	1.043 ± 0.005	1.034 ± 0.004		
χ^2/ndf	0.7688/3		4.742/5	4.078/5	4.895/5		

[a] The SLAC ratios [10] used cross sections from different experiments at different kinematics. They interpolated the deuterium cross sections to the kinematics of the cross sections measured for heavier nuclei and have larger uncertainties than the later measurements. They are included here for completeness.

[b] The ^{3}He SRC scaling factor in column 2 from Ref. [12] was determined primarily from the calculated ratio of the ^{3}He and d momentum distribution above the scaling threshold ($p_{\mathrm{thresh}} = 0.275 \pm 0.025$ GeV/c).

sections. Fomin *et al.* [18] did not apply the isoscalar correction but did apply corrections for the nuclear Coulomb field, inelastic contributions, and SRC-pair center-of-mass motion. Inspired by results of exclusive ^{12}C(p, ppn) and ^{12}C$(e, e'pN)$ measurements, which showed that two-nucleon (NN)-SRC pairs are dominated by neutron-proton pairs (~18 times more neutron-proton than proton-proton pairs were observed) [13–17], Fomin *et al.* assumed that at $x_B > 1.4$, electrons scatter mainly off neutron-proton pairs and therefore isoscalar corrections are unnecessary. The largest correction made by Fomin *et al.* is a correction for enhancement of the cross-section ratio (and therefore of the SRC scaling factors) due to the SRC-pair center of mass (c.m.) motion for $A > 2$. The c.m. correction is defined as the ratio of the convolution of the pair c.m. motion and deuteron momentum distributions to the deuteron momentum distribution. This ratio was calculated in Ref. [18] for ^{56}Fe using the SRC-pair momentum distributions of Ciofi degli Atti and Simula [20]. It was then scaled to other nuclei based on the A dependence of the pair motion. Because of the uncertainties in the calculation, including its x_B and A dependence, they applied an uncertainty equal to 30–50 % of the calculated correction.

Table I lists the per-nucleon cross-section ratios for all nuclei measured by Fomin *et al.* The second column shows the ratios measured by Egiyan *et al.* that were used in the original EMC-SRC analysis [8]. Fomin *et al.* measured ^{63}Cu, which was not measured by Egiyan *et al.*; we assume the SRC scaling factor of ^{63}Cu to be the same as that of ^{56}Fe. The values of ^{9}Be and ^{197}Au in the third column are those predicted by Ref. [8] based on their measured EMC effect and the linear EMC-SRC correlation. The fourth column shows the Fomin *et al.* results, analyzed in the same manner as the Egiyan *et al.* data (i.e., including radiative and isoscalar corrections only). The fifth column shows the Fomin *et al.* results as published (i.e., including inelastic, radiative, Coulomb, and center of mass motion corrections). The sixth column shows the as-published Fomin *et al.* results with the center of mass motion correction removed (i.e., including inelastic, radiative, and Coulomb corrections). Comparing the second and fourth columns, one can see that the measured values of $a_2(A/d)$ from the two measurements agree within uncertainty when analyzed with the same corrections (radiative and isoscalar corrections only). Applying the radiative, Coulomb field, and inelastic (but not the isoscalar) corrections changes the measured scale factors by about 10%. Applying the SRC-pair center-of-mass motion correction decreases the ratios by 10–20 %. The last column of Table I shows the magnitude of the EMC effect for the different nuclei as measured by Refs. [3,7] and averaged by Ref. [8].

The EMC-SRC correlation. The quality of the correlation between the magnitude of the EMC effect and the newly measured SRC scaling factors, $a_2(A/d)$, is shown in Fig. 1. Because of the large uncertainties of the SRC-pair center-of-mass motion correction, Fig. 1 shows the data of Fomin *et al.* as published but without that correction. Figure 1 also shows the results of a one-parameter fit to the EMC slopes as a function of the SRC scaling factors. Because the point for the deuteron is fixed at $dR_{\mathrm{EMC}}/dx = 0$ and $a_2(A/d) = 1$, the fitted slope is also the negative of the intercept of the line.

To test the robustness of the EMC-SRC correlation, we made a series of one-parameter linear fits to the EMC slopes (Table I, column 8) as a function of the different SRC scaling factors shown in Table I. The χ^2 per degree of freedom for each of these fits was approximately 1, indicating an excellent fit. In addition, the values of $a_2(A/d)$ predicted for ^{9}Be and ^{197}Au by Ref. [8] agree within uncertainties with the new values measured by Fomin *et al.* with the radiative and isoscalar corrections from Ref. [12].

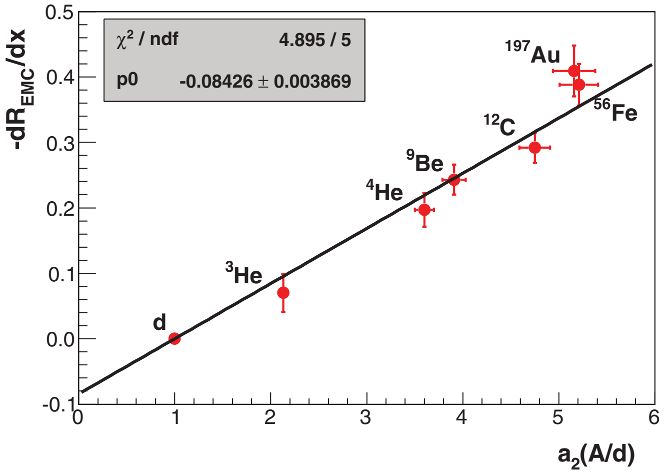

FIG. 1. (Color online) The slope of the EMC effect for $0.35 \leqslant x_B \leqslant 0.7$ plotted vs $a_2(A/d)$, the SRC scaling factor (the relative amount of NN-SRC pairs), in a variety of nuclei. The uncertainties include both statistical and systematic uncertainties added in quadrature. The values of $a_2(A/d)$ are taken from Fomin *et al.* [18] as published except for the SRC-pair center-of-mass motion corrections. The fit parameter, $a = -0.084 \pm 0.004$, is the intercept of the line and also the negative of the slope of the line.

Following Ref. [8], the value $a_2(A/d) = 0$ corresponds to the limit of free nucleons with no SRC. If we extrapolate the linear fit to this point, this should give us the EMC ratio for a free (unbound) pn pair to the deuteron, the so-called in-medium correction (IMC) effect. The IMC effect then equals the negative of the fitted EMC-SRC slope. This value ranges from $|dR_{\mathrm{IMC}}/dx| = 0.079 \pm 0.006$ to 0.084 ± 0.004 for the different data sets with the different corrections (excluding the c.m. motion correction). If we include the SRC-pair center-of-mass motion correction, then the linear fit is still excellent. However, the slope and hence the intercept increases by about 20% to 0.106 ± 0.006.

Since the EMC effect is linear for $0.3 \leqslant x_B \leqslant 0.7$, we have (also following Ref. [8])

$$\frac{\sigma_d}{\sigma_p + \sigma_n} = 1 - a(x_B - b),$$

where σ_d and σ_p are the measured DIS deuteron and proton cross sections, σ_n is the unmeasured free-neutron cross section, $a = |dR_{\mathrm{IMC}}/dx| \approx 0.08$, and $b = 0.31 \pm 0.04$ is the average value of x_B where the EMC effect is unity (i.e., where the per-nucleon cross sections are equal). Evaluating this at $x_B = 0.7$ gives the ratio of the free pn cross section to the bound pn (deuteron) cross section, which ranges from 1.032 ± 0.004 to 1.034 ± 0.004 for the different data sets and corrections (again excluding the c.m. motion correction). If we include the c.m. motion correction, then this ratio changes to 1.043 ± 0.005.

The agreement of the slope of the EMC-SRC correlation, and therefore of the deuteron IMC effect at $x_B = 0.7$, among all combinations of data sets and corrections is a clear indication of the robustness of the EMC-SRC correlation. This also indicates that the deuteron IMC effect and the free-neutron structure function extracted in Ref. [8] and used in Ref. [19] do not change due to the new data and/or analysis. If the center-of-mass motion correction is included, then the linearity of the EMC-SRC relation improves slightly and the deuteron IMC effect increases by about 20% to $dR_{\mathrm{IMC}}/dx = 0.106 \pm 0.006$.

Conclusions and outlook. New higher-precision data [18] strengthen the phenomenological correlation between the strength of the EMC effect and the relative amount of SRC-correlated NN pairs in a nucleus [8]. The new measurements are consistent with the SRC scaling factors for ^{9}Be and ^{197}Au that were predicted based on this EMC-SRC correlation. Different corrections for the SRC cross-section ratio were examined and all were shown to be consistent with a linear correlation between the strength of the EMC effect and the relative amount of SRC-correlated NN pairs in nuclei. The linearity of the EMC-SRC correlation, regardless of the exact corrections considered, is a clear indication of the robustness of the EMC-SRC correlation. This strengthens the speculation presented in Ref. [8] that both the EMC effect and the NN-SRC originate from high-momentum nucleons in the nucleus.

More data are required to further map out and understand this correlation. Several experiments approved to run as part of the 12 GeV program at Jefferson Lab will measure both the SRC scaling factors and the EMC effect at high precision over a wide range of light and heavy nuclei [21–23]. Another experiment [24] will search for medium modification of the structure function of deeply bound, high-momentum nucleons. This will be done by performing DIS scattering off high-momentum nucleons in deuterium and tagging the partner (high-momentum) recoil nucleon. The results of this experiment will allow comparison of the structure function of free and bound nucleons and gain insight on the connection of the EMC effect to high-momentum nucleons in the nucleus.

Acknowledgements. We are grateful for many fruitful discussions with John Arrington, Nadia Fomin, Leonid Frankfurt, Doug Higinbotham, Sebastian Kuhn, Jerry Miller, and Mark Strikman. This work was supported by the U.S. Department of Energy, the Israel Science Foundation, and the US-Israeli Bi-National Science Foundation.

---

[1] J. Aubert *et al.*, Phys. Lett. B **123**, 275 (1983).
[2] J. Ashman *et al.*, Phys. Lett. B **202**, 603 (1988).
[3] J. Gomez *et al.*, Phys. Rev. D **49**, 4348 (1994).
[4] M. Arneodo *et al.*, Phys. Lett. B **211**, 493 (1988).
[5] M. Arneodo *et al.*, Nucl. Phys. B **333**, 1 (1990).
[6] D. Allasia *et al.*, Phys. Lett. B **249**, 366 (1990).
[7] J. Seely *et al.*, Phys. Rev. Lett. **103**, 202301 (2009).
[8] L. B. Weinstein, E. Piasetzky, D. W. Higinbotham, J. Gomez, O. Hen, and R. Shneor, Phys. Rev. Lett. **106**, 052301 (2011).
[9] D. B. Day *et al.*, Phys. Rev. Lett. **59**, 427 (1987).
[10] L. L. Frankfurt, M. I. Strikman, D. B. Day, and M. Sargsyan, Phys. Rev. C **48**, 2451 (1993).
[11] K. Egiyan *et al.* (CLAS Collaboration), Phys. Rev. C **68**, 014313 (2003).

[12] K. Egiyan *et al.* (CLAS Collaboration), Phys. Rev. Lett. **96**, 082501 (2006).
[13] A. Tang *et al.*, Phys. Rev. Lett. **90**, 042301 (2003).
[14] E. Piasetzky, M. Sargsian, L. Frankfurt, M. Strikman, and J. W. Watson, Phys. Rev. Lett. **97**, 162504 (2006).
[15] R. Shneor *et al.*, Phys. Rev. Lett. **99**, 072501 (2007).
[16] R. Subedi *et al.*, Science **320**, 1476 (2008).
[17] H. Baghdasaryan *et al.* (CLAS Collaboration), Phys. Rev. Lett. **105**, 222501 (2010).
[18] N. Fomin *et al.*, Phys. Rev. Lett. **108**, 092502 (2012).
[19] O. Hen, A. Accardi, W. Melnitchouk, and E. Piasetzky, Phys. Rev. D **84**, 117501 (2011).
[20] C. Ciofi degli Atti and S. Simula, Phys. Rev. C **53**, 1689 (1996).
[21] J. Arrington and D. Day, Inclusive scattering from nuclei at $x > 1$ in the quasielastic and deeply inelastic regimes, Jefferson Lab Experiment No. E12-06-105, 2006 (unpublished).
[22] P. Solvignon-Slifer and J. Arrington, Precision measurement of the isospin dependence in the 2N and 3N short range correlation region, Jefferson Lab Experiment No. E12-11-112, 2011, (unpublished).
[23] J. Arrington, D. Gaskell, and A. Daniel, Detailed studies of the nuclear dependence of F_2 in light nuclei, Jefferson Lab Experiment No. E12-10-008, 2010 (unpublished).
[24] O. Hen, L. Weinstein, S. Wood, and S. Gilad, In medium nucleon structure functions, SRC, and the EMC effect, Jefferson Lab Experiment No. E12-11-107, 2011 (unpublished).

PHYSICAL REVIEW D **84,** 117501 (2011)

Constraints on the large-x d/u ratio from electron-nucleus scattering at $x > 1$

O. Hen,[1] A. Accardi,[2,3] W. Melnitchouk,[3] and E. Piasetzky[1]

[1] *Tel Aviv University, Tel Aviv 69978, Israel*
[2] *Hampton University, Hampton, Virginia 23668, USA*
[3] *Jefferson Lab, Newport News, Virginia 23606, USA*

(Received 18 October 2011; published 23 December 2011)

Recently the ratio of neutron to proton structure functions F_2^n/F_2^p was extracted from a phenomenological correlation between the strength of the nuclear EMC effect and inclusive electron–nucleus cross section ratios at $x > 1$. Within conventional models of nuclear smearing, this ''in-medium correction'' (IMC) extraction constrains the size of nuclear effects in the deuteron structure functions, from which the neutron structure function F_2^n is usually extracted. The IMC data determine the resulting proton d/u quark distribution ratio, extrapolated to $x = 1$, to be 0.23 ± 0.09 with a 90% confidence level. This is well below the SU(6) symmetry limit of $1/2$ and significantly above the scalar diquark dominance limit of 0.

DOI: 10.1103/PhysRevD.84.117501 PACS numbers: 12.38.−t, 13.60.−r, 24.85.+p

I. INTRODUCTION

Currently, uncertainties in parton distribution functions (PDFs) at large parton momentum fractions x represent one of the main impediments to the determination of the longitudinal structure of the nucleon in terms of its fundamental constituents. The large-x region provides a unique opportunity for studying the flavor and spin dynamics of quarks in the nucleon, with the d/u quark distribution ratio, in particular, being very sensitive to different mechanisms of spin-flavor symmetry breaking [1,2]. Knowledge of PDFs at large x is also important for several other reasons, such as the reliable calculation of QCD backgrounds in new physics searches at hadron colliders especially at large rapidities, as well as in neutrino oscillation experiments.

The systematics of uncertainties in parton distributions at large x has been the focus of recent dedicated global QCD analyses by the CTEQ-Jefferson Lab (CJ) Collaboration [3,4], which investigated the sensitivity of PDFs to different treatments of nuclear corrections in deep-inelastic scattering (DIS) from deuterium. While proton DIS data place strong constraints on the u-quark distribution, neutron structure functions are needed in order to also determine the d-quark PDF. The absence of free neutron targets, however, means that deuterium DIS data must be used to infer information about the structure of the free neutron.

Uncertainties in the nuclear corrections in the deuteron, such as those associated with nucleon off-shell effects and the large-momentum components of the deuteron wave function, give rise to significant uncertainties in the resulting d/u ratio for $x \gtrsim 0.5$ [4]. This prevents drawing any firm conclusions about the $x \to 1$ behavior of d/u predicted in various nonperturbative and perturbative models, which range from 0 in models with scalar diquark dominance [5–7] to ≈ 0.2 in models with admixtures of axial-vector diquarks [8] or those based on helicity conservation [9], and up to 0.5 in models with SU(6) spin-flavor symmetry [10].

A recent analysis of the strength of the EMC effect in nuclei and data on inclusive electron-nucleus scattering at $x > 1$ proposed a phenomenological, theory-independent, determination of the neutron to proton structure function ratio F_2^n/F_2^p, known as the ''in-medium correction'' (IMC) extraction [11]. The IMC analysis is based on the observed correlation between the strength of the nuclear EMC effect at intermediate x ($x \approx 0.3$–0.7) and the number of short range correlated nucleon-nucleon pairs in light, medium, and heavy nuclei, which is then extrapolated to a free nucleon.

In this report we combine the phenomenology of these two approaches and illustrate how the IMC-extracted neutron structure function can, in principle, limit the range of parameters describing nuclear corrections in the deuteron, thereby significantly reducing the uncertainties in the resulting d/u ratio at large x. As we shall see, the IMC analysis favors values of d/u at the upper end of the uncertainty band obtained in the CJ global QCD fit [4], indicating the presence of significant nucleon off-shell corrections in the deuteron structure function.

II. NUCLEAR EFFECTS IN THE DEUTERON

In the conventional description of DIS from the deuteron at $x \gg 0$, the scattering is assumed to take place incoherently from individual nucleons in the deuterium nucleus [12]. In the weak binding approximation (WBA), the deuteron structure function can be written as a convolution of the bound nucleon structure functions F_2^N and a momentum distribution function of nucleons in the deuteron (also known as the ''smearing function'') [13–15].

In Ref. [14], Kulagin and Petti used a simple quark spectral model to obtain a physically motivated parametrization of the nucleon off-shell corrections (see also Refs. [13,16–18]). The off-shell corrections were estimated by integrating the quark-nucleon spectral function over quark virtualities up to some high-momentum scale Λ that depends on the nucleon off-shell mass $p^2 = p_0^2 - \boldsymbol{p}^2 \neq M^2$, where $p_0 = M_d - \sqrt{M^2 + \boldsymbol{p}^2}$ is the nucleon energy and $\boldsymbol{p}$ its momentum, with M and M_d the nucleon and deuteron masses. Taking Λ to be inversely proportional to the quark confinement radius R in the nucleon, its dependence on p^2 can be related to the change in the size of the nucleon in the nuclear medium (“nucleon swelling”). The change of scale δR and nucleon virtuality can be conveniently parametrized in terms of a single parameter λ, given by [14]

$$\lambda = \frac{\partial \Lambda^2}{\partial \log p^2}\bigg|_{p^2=M^2} = -2\frac{\delta R}{R}\frac{\delta p^2}{M^2}, \tag{1}$$

where δp^2 is the average nucleon virtuality $(p^2 - M^2)$ in the deuteron.

The parameter λ was chosen in Ref. [4] to reproduce the phenomenological values of the change of confinement radius from the study of the nuclear EMC effect in the Q^2-rescaling model [19], $\delta R/R = 1.5\%–1.8\%$. This was somewhat smaller than the nuclear-averaged value of $\delta R/R \approx 9\%$ obtained by fitting the off-shell correction to ratios of nuclear structure functions for a range of nuclei [14]. While it is generally accepted that some off-shell corrections to the convolution approximation are needed in order to describe nuclear structure functions at large x [20], their magnitude varies considerably between different models [14,17,18,21–23], and on the definition of the smearing function. (In fact, in some approaches such as the light-front [24–26] explicit off-mass-shell corrections do not appear at all, their effects instead being subsumed by higher Fock state components or contact interactions).

In the present analysis we treat λ as a free parameter, allowing it to be determined by the IMC extraction data for a given virtuality δp^2. The latter is computed from several modern deuteron wave functions which give high-precision fits to nucleon-nucleon scattering data, namely, the CD-Bonn [27], AV18 [28], and the relativistic WJC-1 and WJC-2 wave functions [29], yielding values of the nucleon virtuality of $\delta p^2/M^2 = -3.7\%$, -4.5%, -6.2%, and -4.9%, respectively. (The older Paris deuteron wave function [30] gives a value $\delta p^2/M^2 = -4.3\%$, similar to the AV18 model). This “modified Kulagin-Petti” (mKP) parametrization of the off-shell corrections (1) allows a wide range of models to be assessed in terms of a single parameter, the nucleon swelling $\delta R/R$, for a given deuteron wave function.

III. IMC CONSTRAINTS ON THE d/u RATIO

In Fig. 1 the ratio of neutron to proton structure functions F_2^n/F_2^p at $Q^2 = 12$ GeV^2 is shown for various deuteron wave functions and swelling levels $\delta R/R$, ranging from 0% to 3%, in increments of 0.3%, using the WBA smearing function and the mKP off-shell model. For each combination of wave function and swelling parameters, the structure functions are computed from the CJ global next-to-leading order QCD fit of PDFs as described in Ref. [4], using a flexible parametrization for the d-quark PDF, which allows finite d/u values as $x \to 1$. Each of the fitted PDF sets represented by the curves in Fig. 1 give a similar quality fit to the global data base used in Ref. [4] by allowing the changes in the nuclear corrections to the deuteron F_2^d structure function to be compensated by corresponding changes in the d-quark PDF (inducing a similar change in the calculated neutron F_2^n). The curves are compared with the F_2^n/F_2^p ratios obtained from the IMC extraction over the range $0.35 \lesssim x \lesssim 0.7$.

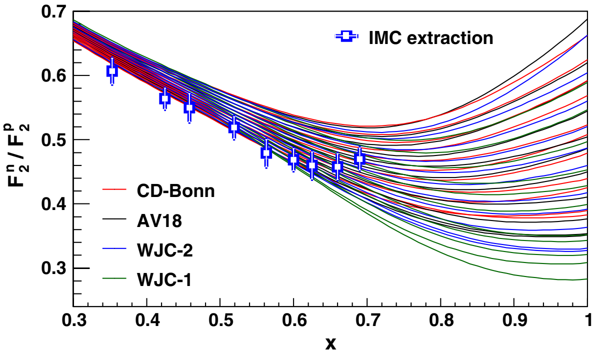

FIG. 1 (color online). Neutron to proton structure function ratio F_2^n/F_2^p from the CJ global QCD fit [4] assuming different deuteron wave functions: CD-Bonn (red), AV18 (black), WJC-1 (green) and WJC-2 (blue). The curves correspond to different nucleon swelling levels, $\delta R/R$, ranging from 0% (lowest curves) to 3% (highest curves) in steps of 0.3%. The IMC data (squares) [11] and the fits are at a fixed $Q^2 = 12$ GeV^2.

To constrain the nuclear correction uncertainty in F_2^n/F_2^p, we calculate the χ^2 of the IMC data for each deuteron wave function and swelling combination. This is shown in Fig. 2 as a function of the nucleon swelling $\delta R/R$ for the different deuteron wave functions. Note that the wave function determines not only the average nucleon virtuality δp^2 in the deuteron, but also the amount of binding and Fermi motion in the smearing function [4,15]. For the choice of confidence level (C. L.), we treat the deuteron wave function as a (discrete) parameter and consider a 90% C. L. for two free parameters, corresponding to an increase in χ^2 of 4.61 above the minimum [31]. With this C. L. the IMC extraction constrains the swelling levels to the range $\delta R/R = 0.2\%–1.4\%$, with a preference for the CD-Bonn, AV18, and WJC-2 wave functions. The minimum χ^2 occurs for the CD-Bonn model at $\delta R/R = 0.9\%$. The minimum χ^2 for the WJC-1 wave function at $\delta R/R \approx 1.5\%$ lies outside of the 90% C. L. and is disfavored by the IMC data.

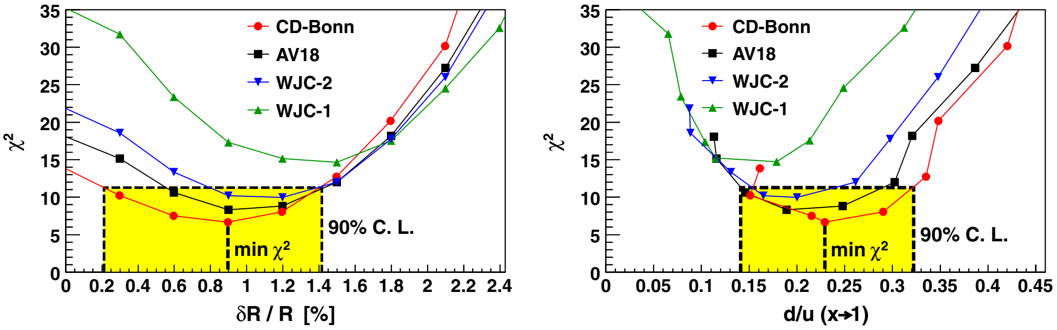

FIG. 2 (color online). Total χ^2 for fits of the calculated F_2^n/F_2^p ratios in Fig. 1 to the IMC extraction data [11] for various deuteron wave functions (CD-Bonn-circles, AV18-squares, WJC-2-inverted triangles, WJC-1-triangles), as a function of the swelling level $\delta R/R$ (*left*) and the d/u ratio in the $x \rightarrow 1$ limit (*right*). The 90% confidence levels are indicated by the shaded (yellow) box, and the minimum χ^2 values by the vertical dashed line.

The implications of these constraints for the d/u ratio in the limit $x \rightarrow 1$ are illustrated in Fig. 2 , where the χ^2 is shown as a function of the limiting d/u value of each PDF fit. The IMC extraction yields a d/u limiting value of 0.23 ± 0.09 at the 90% C. L. (at the 99% C. L., using a χ^2 increase of 9.21, the uncertainty would increase to ± 0.13). These results strongly disfavor the SU(6) value $d/u = 1/2$ as well as the $d/u \rightarrow 0$ limit predicted in models with scalar diquark dominance. Furthermore, global PDF analyses often assume the same functional x dependence for both u and d quark distributions, forcing the d/u ratio to approach either zero or infinity in the $x \rightarrow 1$ limit. The results shown in Fig. 2, however, suggest that a more flexible parametrization for the d/u ratio, which allows finite $x \rightarrow 1$ limits, may be more realistic [4].

The resulting uncertainty bands on the d/u ratio are shown in Fig. 3, including the full theoretical uncertainty from the CJ global fit [4] and the 90% C. L. extracted from the IMC constraints. Even though the IMC extraction only covers an x range of ≈ 0.35–0.7, it nevertheless imposes a tight constraint on the d/u parton distributions ratio for $x \rightarrow 1$.

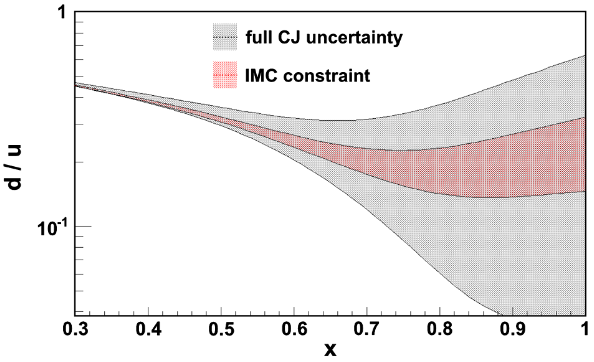

FIG. 3 (color online). d/u ratio at $Q^2 = 12\ \text{GeV}^2$ with the full theoretical uncertainty from Ref. [4] (black) and with the IMC constraint at the 90% C. L. (red).

IV. SUMMARY

Within a global PDF analysis we have studied the constraints imposed by the theory-independent IMC-extracted F_2^n structure function data on nuclear corrections in deuterium. These phenomenologically extracted data strongly support the presence of off-shell modifications of nucleons in the deuteron, and constrain their magnitude to a more limited range than in the recent CJ global QCD analysis without the IMC data [4]. The IMC data also disfavor deuterium wave functions with very "hard" momentum distributions, such as for the WJC-1 nucleon-nucleon potential [29], which produce a shallow EMC ratio F_2^d/F_2^N at intermediate and large x [4,15].

While the u-quark PDF is well constrained by the proton DIS data, the lack of a free neutron target makes the d-quark distribution very sensitive to the assumptions used to calculate the nuclear correction in the deuteron. The use of the IMC-extracted neutron structure function directly constrains the d-quark PDF for $x \lesssim 0.7$ and indirectly for $x \rightarrow 1$. We find the d/u ratio in the limit $x \rightarrow 1$ to be 0.23 ± 0.09 at the 90% confidence level, in agreement with models predicting intermediate values of d/u between the SU(6) symmetry and scalar diquark dominance limits [8,9].

Of course, these conclusions strongly depend on the assumptions underlying the IMC extraction of F_2^n [11]. Some of these are being tested through the study of DIS events with a tagged high-momentum proton recoil at Jefferson Lab [32] and will be the subject of a similar experiment at the future 12 GeV upgraded facility [33]. The ultimate arbiter, however, will be data on free or nearly free neutron targets, such as from the BoNuS experiment [34] at Jefferson Lab that collected DIS data up to $x \approx 0.6$, or its future 12 GeV extension [35] that will reach $x \approx 0.8$. Further avenues to direct experimental constraints on d/u at large x include the 12 GeV MARATHON experiment [36] at Jefferson Lab on DIS from the ${}^3\text{He}{}^3\text{H}$ mirror nuclei and the parity-violating DIS program on a hydrogen target [37], as well as the measurement of W boson asymmetries at large rapidities in $p\bar{p}$ collisions at the Tevatron or in pp scattering at RHIC and the LHC [4,38].

ACKNOWLEDGMENTS

We are grateful for collaboration and many fruitful discussions with D. W. Higinbotham, J. F. Owens, and L. B. Weinstein. This work was supported by the Israel Science Foundation, the U.S.-Israeli Bi-National Science Foundation, the U.S. DOE Contract No. DE-AC05-06OR23177, under which Jefferson Science Associates, LLC operates Jefferson Lab, and the U.S. National Science Foundation under NSF Grant No. 1002644.

---

[1] W. Melnitchouk and A. W. Thomas, Phys. Lett. B **377**, 11 (1996).
[2] R. J. Holt and C. D. Roberts, Rev. Mod. Phys. **82**, 2991 (2010).
[3] A. Accardi *et al.*, Phys. Rev. D **81**, 034016 (2010).
[4] A. Accardi *et al.*, Phys. Rev. D **84**, 014008 (2011).
[5] R. P. Feynman, *Photon Hadron Interactions* (Benjamin, New York, 1972).
[6] F. E. Close, Phys. Lett. B **43**, 422 (1973).
[7] R. D. Carlitz, Phys. Lett. B **58**, 345 (1975).
[8] I. C. Cloët, W. Bentz, and A. W. Thomas, Phys. Lett. B **621**, 246 (2005).
[9] G. R. Farrar and D. R. Jackson, Phys. Rev. Lett. **35**, 1416 (1975).
[10] F. E. Close, *An Introduction to Quarks and Partons* (Academic Press, London, 1979).
[11] L. B. Weinstein *et al.*, Phys. Rev. Lett. **106**, 052301 (2011).
[12] R. L. Jaffe, in *Relativistic Dynamics and Quark-Nuclear Physics*, edited by M. B. Johnson and A. Pickleseimer (Wiley, New York, 1985).
[13] S. A. Kulagin, G. Piller, and W. Weise, Phys. Rev. C **50**, 1154 (1994).
[14] S. A. Kulagin and R. Petti, Nucl. Phys. A **765**, 126 (2006).
[15] W. Melnitchouk, AIP Conf. Proc. **1261**, 85 (2010).
[16] S. A. Kulagin, W. Melnitchouk, G. Piller, and W. Weise, Phys. Rev. C **52**, 932 (1995).
[17] F. Gross and S. Liuti, Phys. Rev. C **45**, 1374 (1992).
[18] W. Melnitchouk, A. W. Schreiber, and A. W. Thomas, Phys. Rev. D **49**, 1183 (1994).
[19] F. E. Close, R. L. Jaffe, R. G. Roberts, and G. G. Ross, Phys. Rev. D **31**, 1004 (1985).
[20] D. F. Geesaman, K. Saito, and A. W. Thomas, Annu. Rev. Nucl. Part. Sci. **45**, 337 (1995); P. R. Norton, Rep. Prog. Phys. **66**, 1253 (2003).
[21] L. L. Frankfurt and M. I. Strikman, Nucl. Phys. B **250**, 143 (1985).
[22] W. Melnitchouk, A. W. Schreiber, and A. W. Thomas, Phys. Lett. B **335**, 11 (1994).
[23] W. Melnitchouk, M. Sargsian, and M. I. Strikman, Z. Phys. A **359**, 99 (1997).
[24] L. L. Frankfurt and M. I. Strikman, Phys. Rep. **76**, 215 (1981).
[25] B.-Q. Ma, Int. J. Mod. Phys. E **1**, 809 (1992).
[26] J. Arrington, F. Coester, R. J. Holt, and T. S. Lee, J. Phys. G **36**, 025005 (2009).
[27] R. Machleidt, Phys. Rev. C **63**, 024001 (2001).
[28] R. B. Wiringa, V. G. J. Stoks, and R. Schiavilla, Phys. Rev. C **51**, 38 (1995).
[29] F. Gross and A. Stadler, Phys. Rev. C **78**, 014005 (2008); , **82**, 034004 (2010).
[30] M. Lacombe *et al.*, Phys. Rev. C **21**, 861 (1980).
[31] W. H. Press *et al.*, *Numerical Recipes in FORTRAN: The Art of Scientific Computing* (Cambridge University Press, Cambridge, England, 2007).
[32] A. V. Klimenko *et al.*, Phys. Rev. C **73**, 035212 (2006).
[33] O. Hen *et al.*, Jefferson Lab Experiment, Proposal No. E12-11-107.
[34] N. Baillie *et al.*, arXiv:1110.2770 (BoNuS Collaboration), [Phys. Rev. Lett. (to be published)].
[35] S. Bültmann *et al.* (BoNuS12 Collaboration), Jefferson Lab Experiment, Proposal No. E12-10-102.
[36] G. G. Petratos, J. Gomez, R. J.Holt, and R. D. Ransome (MARATHON Collaboration), Jefferson Lab Experiment, Proposal No. C12-10-103.
[37] P. Souder (SoLID Collaboration), Jefferson Lab Experiment, Proposal No. E12-10-007.
[38] L. T. Brady, A. Accardi, W. Melnitchouk, and J. F. Owens, arXiv:1110.5398 .

4.2. Nuclei, Nuclear Matter and Neutron Stars

“Extracting the Mass Dependence and Quantum Numbers of Short-Range Correlated Pairs from A(e,e’p) and A(e,e’pp) Scattering”,
C. Colle and O. Hen et al., Phys. Rev. C ***92****, 024604 (2015).*

“Symmetry Energy of Nucleonic Matter with Tensor Correlations”,
O. Hen et al., Phys. Rev. C ***91****, 025803 (2015).*

”Effect of the Correlated Fermi-Gas Model on Analysis of Neutron Starts Observations”, *O. Hen and A.W. Steiner et al., In-preparation.*

PHYSICAL REVIEW C **92**, 024604 (2015)

Extracting the mass dependence and quantum numbers of short-range correlated pairs from $A(e,e'p)$ and $A(e,e'pp)$ scattering

C. Colle,[1] O. Hen,[2] W. Cosyn,[1] I. Korover,[2] E. Piasetzky,[2] J. Ryckebusch,[1] and L. B. Weinstein[3]
[1]*Ghent University, Ghent, Belgium*
[2]*School of Physics and Astronomy, Tel Aviv University, Tel Aviv 69978, Israel*
[3]*Old Dominion University, Norfolk, Virginia, USA*

(Received 3 April 2015; published 6 August 2015)

The nuclear mass dependence of the number of short-range correlated (SRC) proton-proton (pp) and proton-neutron (pn) pairs in nuclei is a sensitive probe of the dynamics of short-range pairs in the ground state of atomic nuclei. This work presents an analysis of electroinduced single-proton and two-proton knockout measurements off ^{12}C, ^{27}Al, ^{56}Fe, and ^{208}Pb in kinematics dominated by scattering off SRC pairs. The nuclear mass dependence of the observed $A(e,e'pp)/^{12}\text{C}(e,e'pp)$ cross-section ratios and the extracted number of pp- and pn-SRC pairs are much softer than the mass dependence of the total number of possible pairs. This is in agreement with a physical picture of SRC affecting predominantly nucleon-nucleon pairs in a nodeless relative-S state of the mean-field basis.

DOI: 10.1103/PhysRevC.92.024604 PACS number(s): 25.30.Rw, 25.30.Fj, 24.10.−i

I. INTRODUCTION

The nuclear momentum distribution (NMD) is often quoted as being composed of two separate parts [1–3]. Below the Fermi momentum ($k_F \approx 250$ MeV/c) single nucleons move as independent particles in a mean field created by their mutual interactions. Above the Fermi momentum ($k > k_F$) nucleons predominantly belong to short-range correlated (SRC) pairs with high relative and low center-of-mass (c.m.) momenta, where high and low are relative to the Fermi momentum [4–8]. In addition to its intrinsic interest, the NMD and its division into mean-field and correlated parts is relevant to two-component Fermi systems [9], neutrino physics [10,11], and the symmetry energy of nuclear matter [12].

The mean-field and long-range aspects of nuclear dynamics have been studied extensively since the dawn of nuclear physics. The effect of long-range correlations on the NMDs is limited to momenta which do not extend far beyond k_F [13]. Study of the short-range aspects of nuclear dynamics has blossomed with the growing availability of high-energy high-intensity electron and proton accelerators. Recent experiments confirm the predictions that SRC pairs dominate the high-momentum tails ($k > k_F$) of the NMDs [4–7], accounting for 20–25 % of the NMD probability density [14–17]. These high-momentum tails have approximately the same shape for all nuclei [2,3,9,14–18], differing only by scale factors which can be interpreted as a measure of the relative number of SRC pairs in the different nuclei. In this work, we aim at understanding the underlying dynamics which give rise to this universal behavior of the high-momentum tail.

An intuitive picture describing the dynamics of nuclei including SRCs is that of independent bound nucleons moving in the nucleus, occasionally getting sufficiently close to each other to temporarily fluctuate into SRC-induced nucleon-nucleon pairs. This picture can be formally implemented in a framework in which one shifts the complexity of the nuclear SRC from the wave functions to the operators by calculating independent-particle model (IPM) Slater determinant wave functions and acting on them with correlation operators to include the effect of SRCs [18–20]. The observed number of proton-proton (pp) and proton-neutron (pn) SRC pairs in various nuclei can then be used to constrain the amount and the quantum numbers of the initial-state IPM nucleon-nucleon (SRC-prone) pairs that can fluctuate dynamically into SRC pairs through the action of correlation operators.

In this paper, we will extract the relative number of pp-SRC and pn-SRC pairs in different nuclei from measurements of electroinduced two-proton and one-proton knockout cross-section ratios for medium and heavy nuclei (^{27}Al, ^{56}Fe, and ^{208}Pb) relative to ^{12}C in kinematics dominated by scattering off SRC pairs [8,21]. In these kinematics in the plane-wave approximation $A(e,e'pp)$ cross sections are proportional to the number of pp pairs in the nucleus and $A(e,e'p)$ cross sections are proportional to twice the number of pp pairs plus the number of pn pairs ($2pp + pn$). Therefore, after correcting the measured cross sections for rescattering of the outgoing nucleons from the residual nucleus (final state interactions or FSIs), the relative number of pp and pn pairs will be extracted from measurements of $A(e,e'pp)/^{12}\text{C}(e,e'pp)$ and $A(e,e'p)/^{12}\text{C}(e,e'p)$ cross-section ratios [8].

We will then compare the $A(e,e'pp)/^{12}\text{C}(e,e'pp)$ cross-section ratios and the extracted number of pp and pn pairs to factorized calculations using different models of nucleon pairs in order to deduce the quantum numbers of the IPM SRC-prone pairs. We will provide strong evidence that the relative quantum numbers of the majority of the SRC-susceptible pairs are $^1S_0(1)$ for pp and $^3S_1(0)$ for pn. Hereby, we used the notation $^{2J+1}L_S(T)$ to identify the pair's quantum state (T is the total isospin).

This paper is structured as follows. The one- and two-proton knockout experiments analyzed in this paper are described in Sec. II. In Sec. III we introduce the model to calculate the FSI-corrected two-nucleon knockout cross-section ratios. Results and discussions are presented in Sec. IV. Section V contains the concluding remarks.

II. EXPERIMENT

The one- and two-proton knockout measurements analyzed in this paper were described in [8] and its supplemental information. They were carried out using the CEBAF Large Acceptance Spectrometer (CLAS) [22], located in Hall-B of the Thomas Jefferson National Accelerator Facility (Jefferson Lab) in Newport News, Virginia. The data were collected in 2004 using a 5.014 GeV electron beam incident on ^{12}C, ^{27}Al, ^{56}Fe, and ^{208}Pb targets. The scattered electron and knocked out proton(s) were measured with CLAS. We selected $A(e,e'p)$ events in which the electron interacts with a single fast proton from a SRC nucleon-nucleon pair in the nucleus by requiring large four-momentum transfer ($Q^2 > 1.5$ GeV^2), Bjorken scaling parameter $x_B = \frac{Q^2}{2m_N\omega} > 1.2$, and missing momentum $300 < |\vec{p}_{\rm miss}| < 600$ MeV/c. The four-momentum transfer $Q^2 = \vec{q}\cdot\vec{q} - (\frac{\omega}{c})^2$ where $\vec{q}$ and ω are the three-momentum and energy transferred to the nucleus respectively; m_N is the nucleon mass; the missing momentum $\vec{p}_{\rm miss} = \vec{p}_p - \vec{q}$, and $\vec{p}_p$ is the knockout proton three-momentum. We also required that the knockout proton was detected within a cone of 25° of the momentum transfer $\vec{q}$ and that it carried at least 60% of its momentum (i.e., $\frac{|\vec{p}_p|}{|\vec{q}|} \geqslant 0.6$). To suppress contributions from inelastic excitations of the struck nucleon we limited the reconstructed missing mass of the two-nucleon system $m_{\rm miss} < 1.1$ GeV/c^2.

The $A(e,e'pp)$ event sample contains all $A(e,e'p)$ events in which a second, recoil, proton was detected with momentum greater than 350 MeV/c. Figure 1 shows the distribution of the cosine of the angle between the initial momentum of the knockout proton and the recoil proton for these events [8]. The recoil proton is emitted almost diametrically opposite to the missing-momentum direction. The observed backward-peaked angular distributions are very similar for all nuclei and are not due to acceptance effects as shown by the angular distribution of mixed events. These distributions are a signature of scattering on a nucleon in a SRC pair, indicating that the two emitted protons were largely back-to-back in the initial state, having large relative momentum and small c.m. momentum [6,23]. Further evidence of scattering on a SRC nucleon pair is that the recoil proton was emitted at forward angles (i.e., angles in the range 20°–60° with respect to $\vec{q}$).

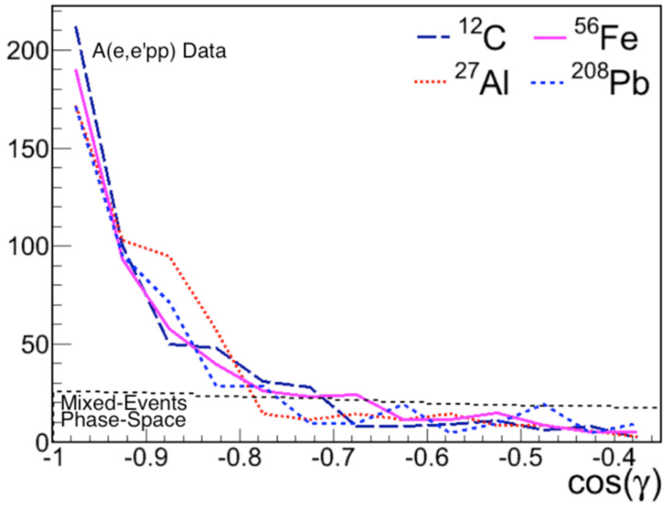

FIG. 1. (Color online) Distribution (in arbitrary units) of the cosine of the angle γ between the missing momentum of the leading proton and the recoil proton for ^{12}C (dark blue long-dashed line), ^{27}Al (red dotted line), ^{56}Fe (purple solid line), and ^{208}Pb (blue dashed line). The black dashed line shows the distribution of the random phase-space extracted from mixed events.

The $A(e,e'p)/^{12}$C$(e,e'p)$ and $A(e,e'pp)/^{12}$C$(e,e'pp)$ cross-section ratios are obtained from the ratio of the measured number of events, normalized by the incident integrated electron flux and the nuclear density of each target. During the experiment all solid targets were held in the same location, the detector instantaneous rate was kept constant, and the kinematics of the measured events from all target nuclei were almost identical [8,21]. Therefore detector acceptance effects cancel almost entirely in the $A(e,e'pp)$/C$(e,e'pp)$ cross-section ratios. Due to the large acceptance of CLAS, radiative effects affect mainly the electron kinematics. These corrections were calculated in Ref. [21] for the extraction of the $A(e,e'p)$/C$(e,e'p)$ cross-section ratio. As the electron kinematics is the same for the $A(e,e'p)$ and $A(e,e'pp)$ reactions, the same corrections are used here to extract the $A(e,e'pp)$/C$(e,e'pp)$ cross-section ratios. See Ref. [8] for additional details.

III. FSI AND CROSS-SECTION MODEL

To extract the underlying relative number of *pp* and *pn* SRC pairs in nuclei from the measured cross-section ratios, we must correct the data for FSI effects [8]. Alternatively, in order to compare the measured ratios to calculations, we must correct either the data or the calculation for FSI effects. The two dominant contributions are (1) attenuation of the outgoing nucleon(s) upon traversing the residual $A-1$ or $A-2$ nucleus, and (2) rescattering of a neutron into a proton [i.e., single charge-exchange (SCX)]. SCX can lead to a *pp* final state which originates from a *pn* pair.

The effect of FSIs of the ejected pair with the remaining $A-2$ spectators was computed in a relativistic multiple-scattering Glauber approximation (RMSGA) [24,25]. The RMSGA is a multiple-scattering formalism based on the eikonal approximation with spin-independent *NN* interactions. We have included both the elastic and the SCX rescattering of the outgoing nucleons with the $A-2$ spectators. The three parameters entering in the RMSGA model are taken from *NN* scattering data and yield an excellent description of the world's $A(e,e'p)$ transparency data [25]. In this work no free parameters are tuned to model the FSI effects in the $A(e,e'p)$ and $A(e,e'pp)$ data under study. The RMSGA yields attenuation coefficients that are similar to the power-law results obtained in nuclear transparency measurements [21]. For those reasons, we estimate the systematic uncertainty related to the FSI calculation as small.

The SCX probabilities are calculated in a semiclassical approximation. The probability of charge-exchange re-scattering for a nucleon with initial IPM quantum numbers α which is brought in a continuum state at the coordinate $\vec{r}$ is modeled by

$$P_{\mathrm{CX}}^{\alpha(\beta)}(\vec{r}\,) = 1 - \exp\left[-\sigma_{\mathrm{CX}}(s)\int_{z}^{+\infty} dz'\rho^{\alpha\beta}(z')\right]. \tag{1}$$

The z axis is chosen along the direction of propagation of the nucleon with initial quantum numbers α. The quantum numbers of the correlated partner in the SRC pair are denoted with β. The $\rho^{\alpha\beta}$ is the IPM one-body density of the residual nucleus available for SCX reactions. The $\rho^{\alpha\beta}$ is determined as the IPM density of the target nucleus, minus the contribution from the single-particle orbitals α and β. Obviously, for an ejected proton (neutron) only the neutron (proton) density of the residual nucleus affects SCX reactions. $\sigma_{\mathrm{CX}}(s)$ in Eq. (1), with s the total c.m. energy squared of the two nucleons involved in the SCX [26], can be extracted from elastic proton-neutron scattering data [27].

As outlined in Refs. [23,28], in the spectator approximation it is possible to factorize the $A(e,e'pN)$ cross section in kinematics probing short-range correlated pairs as

$$\frac{d^8\sigma[A(e,e'pN)]}{d^2\Omega_{e'}\,d^3\vec{P}_{12}\,d^3\vec{k}_{12}} = K_{epN}\,\sigma_{epN}(\vec{k}_{12})F_A^{pN(D)}(\vec{P}_{12}), \tag{2}$$

where $\Omega_{e'}$ is the solid angle of the scattered electron, and $\vec{k}_{12}$ and $\vec{P}_{12}$ are the relative and c.m. momenta of the nucleon pair that absorbed the virtual photon. The K_{epN} is a kinematic factor and $\sigma_{epN}(\vec{k}_{12})$ is the cross section for virtual-photon absorption on a correlated pN pair. The $F_A^{pN(D)}(\vec{P}_{12})$ is the distorted two-body c.m. momentum distribution of the correlated pN pair. In the limit of vanishing FSIs, it is the conditional c.m. momentum distribution of a pN pair with relative $S_{n=0}$ quantum numbers. Distortions of $F_A^{pN(D)}(\vec{P}_{12})$ due to FSI are calculated in the RMSGA. The factorized cross-section expression of Eq. (2) hinges on the validity of the zero-range approximation (ZRA), which amounts to putting the relative pair coordinate $\vec{r}_{12}$ to zero. The ZRA works as a projection operator for selecting the very-short-range components of the IPM relative pair wave functions.

The probability for charge-exchange reactions in pN knockout is calculated on an event per event basis, using the SRC pair probability density $F_A^{pN(D)}(\vec{R}_{12})$ in the ZRA corrected for FSI. With the aid of the factorized cross-section expression of Eq. (2), the phase-space integrated $A(e,e'pN)$ to ^{12}C$(e,e'pN)$ cross-section ratios can be approximately expressed as integrals over distorted c.m. momentum distributions,

$$\begin{aligned}
&\frac{\sigma[A(e,e'pN)]}{\sigma[{}^{12}\mathrm{C}(e,e'pN)]}\\
&\quad\approx \frac{\int d^2\Omega_{e'}\,d^3\vec{k}_{12}K_{epN}\,\sigma_{epN}(\vec{k}_{12})\int d^3\vec{P}_{12}F_A^{pN(D)}(\vec{P}_{12})}{\int d^2\Omega_{e'}\,d^3\vec{k}_{12}K_{epN}\,\sigma_{epN}(\vec{k}_{12})\int d^3\vec{P}_{12}F_C^{pN(D)}(\vec{P}_{12})}\\
&\quad= \frac{\int d^3\vec{P}_{12}F_A^{pN(D)}(\vec{P}_{12})}{\int d^3\vec{P}_{12}F_C^{pN(D)}(\vec{P}_{12})}.
\end{aligned} \tag{3}$$

In the absence of FSI, the integrated c.m. momentum distributions $\int d^3\vec{P}_{12}F_A^{pN(D)}(\vec{P}_{12})$ equal the total number of SRC-prone pN pairs in the nucleus A. Hence, the cross-section ratios of Eq. (3) provide access to the relative number of SRC pN pairs up to corrections stemming from FSI. We have evaluated the ratios of the distorted c.m. momentum distributions of Eq. (3) over the phase space covered in the experiment. Given the almost 4π phase space and the high computational requirement of multidimensional FSI calculations, we use an importance-sampling approach. The major effect on the c.m. momentum distribution $F_A^{pN(D)}(\vec{P}_{12})$ when including FSIs is an overall attenuation; the shape is almost unaffected [23]. Motivated by this, we used the c.m. momentum distributions without FSI as the sampling distribution for the importance sampling in the FSI calculations. When convergence is reached, the computed impact of FSI is extrapolated to the whole phase space.

IV. RESULTS AND DISCUSSIONS

Figure 2 shows the measured uncorrected $\frac{\sigma[A(e,e'pp)]}{\sigma[{}^{12}\mathrm{C}(e,e'pp)]}$ cross-section ratios compared with the ZRA reaction-model calculation with and without RMSGA FSI corrections. The first striking observation is that the measured cross-section ratios increase very slowly with A (e.g., the Pb/C ratio is only 3.8 ± 0.5). For contrast, combinatorial scaling based on the number of pp pairs leads to a ratio of over 200. The ZRA-RMSGA calculations agree well with the measured data, yielding a Pb/C ratio of $4.96^{+0.11}_{-0.14}$. The ZRA and ZRA-RMSGA calculations assume that only pairs with a finite probability density at relative coordinate zero contribute to the cross section. This is consistent with assuming that only IPM pairs in a nodeless relative-S state (i.e., $S_{n=0}$) contribute.

Figure 3 shows the number of pp- and pn-SRC pairs in various nuclei relative to carbon extracted from the measured $A(e,e'pp)/\mathrm{C}(e,e'pp)$ and $A(e,e'p)/\mathrm{C}(e,e'p)$ cross-section ratios following the method outlined in Ref. [8] with RMSGA corrections for FSI and SCX. The extracted number of pp pairs are very sensitive to SCX. If the virtual photon is absorbed on a pn pair and the neutron subsequently undergoes a single

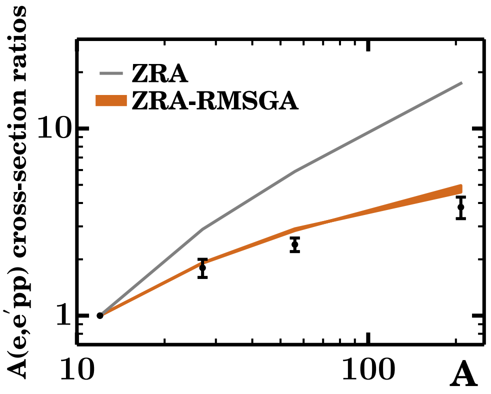

FIG. 2. (Color online) The mass dependence of the $A(e,e'pp)/{}^{12}\mathrm{C}(e,e'pp)$ cross-section ratios. The points show the measured, FSI-uncorrected, cross-section ratios. The lower orange band and upper grey line denote ZRA reaction-model calculations for ^{12}C, ^{27}Al, ^{56}Fe, and ^{208}Pb based on Eq. (3) with and without FSI corrections respectively. The width of the ZRA-RMSGA band reflects the maximum possible effect of SCX.

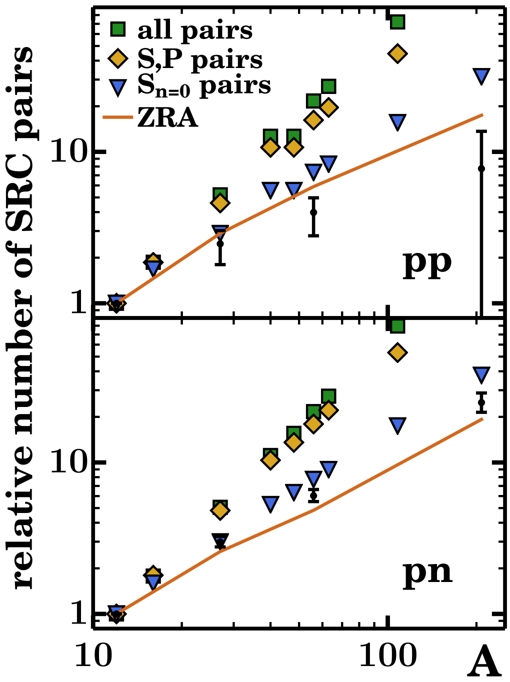

FIG. 3. (Color online) Mass dependence of the number of *pp* (top panel) and *pn* (bottom panel) SRC pairs of nucleus *A* relative to ^{12}C. Data (small black circles with error bars) are extracted from the measured CLAS $A(e,e'p)$ and $A(e,e'pp)$ cross-section ratios [8,21] after correcting for FSI. Error bars include the estimated uncertainty on the cross-section ratios and the FSI corrections. The green squares correspond with unconditional counting of the *pp* pairs, i.e., $[Z(Z-1)/30$ in the upper panel] and *pn* pairs ($ZN/36$ in the bottom panel) for the nuclei ^{12}C, ^{16}O, ^{27}Al, ^{40}Ca, ^{48}Ca, ^{56}Fe, ^{63}Cu, ^{108}Ag, and ^{208}Pb. The yellow diamonds are the ratios obtained by counting IPM pairs in a relative *S* and *P* state. The blue triangles count IPM $S_{n=0}$ pairs. The solid line denotes the result of a reaction-model calculation for scattering from close-proximity pairs [Eq. (3)] which takes full account of the experimental phase space. This calculation does not include FSI corrections because these are applied to the data, see text for details.

charge-exchange reaction with a proton, two protons will be detected in the final state. These events must be subtracted in order to extract the number of *pp*-SRC pairs. Since the contribution from these *pn* pairs to the *pp* final state is comparable to the number of initial *pp* pairs, this leads to a large uncertainty in the number of *pp* pairs, especially for heavy nuclei.

Figure 3 also shows the expected number of *pp* and *pn* SRC pairs relative to carbon for different quantum numbers of the IPM pairs that can dynamically form SRC pairs through the action of correlation operators. These include (a) all possible *NN* pairs (i.e., $Z(Z-1)/(6\times 5)$ and $ZN/(6\times 6)$ for *pp* and *pn* pairs respectively), (b) pairs in a nodeless relative-*S* state (i.e., $S_{n=0}$), and (c) $L \leqslant 1$ pairs (i.e., both *S* and *P* state pairs). Those $S_{n=0}$ pairs are characterized by the $(n=0, L=0)$ quantum numbers for their relative orbital motion. Of all possible states for the pairs, the $S_{n=0}$ pairs have the highest probability for the two nucleons in the pair to approach each other closely. Close-proximity IPM *pn* pairs in a $^3S_1(0)$ state are highly susceptible to the tensor correlation operator that creates SRC pairs in a spin-triplet state with predominantly deuteron-like quantum numbers ($L=0,2; T=0; S=1$).

TABLE I. Relative number of SRC *pp* and *pn* pairs calculated using $S_{n=0}$ counting and the ZRA reaction model compared to the extracted values from the measured $A(e,e'p)$ and $A(e,e'pp)$ ratios after correcting for FSI effects. The error includes the uncertainties in the cross-section ratios and FSI calculations.

	pp			*pn*		
	$S_{n=0}$	ZRA	Expt.	$S_{n=0}$	ZRA	Expt.
^{27}Al / ^{12}C	3.10	2.89	$2.47^{+0.55}_{-0.67}$	2.99	2.52	$2.99^{+0.26}_{-0.22}$
^{56}Fe / ^{12}C	8.60	5.89	$3.98^{+0.99}_{-1.19}$	7.72	4.82	$6.03^{+0.60}_{-0.51}$
^{208}Pb / ^{12}C	45.29	17.44	$7.73^{+5.92}_{-7.23}$	37.62	18.80	$24.87^{+3.89}_{-3.42}$

We determine the number of pairs in each case using an IPM harmonic-oscillator basis and performing a standard transformation to relative and center-of-mass coordinates as detailed in Ref. [29]. The relative number of pairs are displayed in Fig. 3 and listed in Table I. As can be seen, both (a) the naive combinatorial assumption and (c) the calculations that include IPM *S* and *P* pair contributions both drastically overestimate the increase in the number of pairs with *A*. The ZRA and $S_{n=0}$ pair counting calculations are in fair agreement with the extracted number of *pp* and *pn* pairs.

As both the ZRA and the $S_{n=0}$ pair counting methods project IPM states onto close-range pairs, we expect the two methods to produce a similar mass dependence of the number of SRC pairs. The ZRA predicts a somewhat softer mass dependence ($\propto A^{1.01\pm0.02}$ vs $A^{1.12\pm0.02}$). This can be explained by the fact that the ZRA is a more restrictive projection on close-proximity pairs than the $S_{n=0}$ counting which accounts also for $\vec{r}_{12} \neq 0$ contributions.

The observed agreement with the experimental data indicates that correlation operators acting on IPM $S_{n=0}$ pairs are responsible for the largest fraction of the high-momentum nucleons in nuclei. This gives further support to the assumption that the number of IPM pairs with quantum numbers $S_{n=0}$ is a good proxy for the number of correlated pairs in any nucleus *A* [18,29,30]. This is also consistent with an analysis of the cross section of the ground-state to ground-state transition in high-resolution $^{16}\text{O}(e,e'pp)^{14}\text{C}$ measurements [31,32] which provided evidence for the $^1S_0(1)$ dominance in SRC-prone *pp* pairs.

V. CONCLUSIONS

We have extracted the relative number of *pn* and *pp* SRC correlated pairs in nucleus *A* relative to carbon from previously published measured $A(e,e'pp)/\text{C}(e,e'pp)$ and $A(e,e'p)/\text{C}(e,e'p)$ cross-section ratios corrected for final state interactions. The relative number of *pn* and *pp* pairs increases much more slowly with *A* than expected from simple combinatorics.

We calculated the cross section in a framework which shifts the complexity of the nuclear SRC from the wave functions to the operators by calculating independent-particle model (IPM)

Slater determinant wave functions and acting on them with correlation operators to include the effect of SRCs [18–20]. The uncorrected $A(e,e'pp)/\mathrm{C}(e,e'pp)$ cross-section ratios are consistent with a zero range approximation (ZRA) calculation that includes the effects of FSI.

Due to factorization, the ratio of calculated cross sections is approximately equal to the ratio of the distorted c.m. momentum distributions. In the absence of FSI, the integrated c.m. momentum distribution equals the total number of SRC-prone pairs in that nucleus. We compared three choices of SRC-prone pairs to the data: (a) all pairs, (b) pairs in a nodeless relative-S state ($S_{n=0}$), and (c) $L \leqslant 1$ pairs (i.e., both S and P).

We found that the soft mass dependence of the measured $A(e,e'pp)$ cross-section ratios agrees with scattering from highly selective close-proximity pairs (i.e., only IPM relative $S_{n=0}$ pairs). The mass dependence of the extracted ratios of the number of short-range correlated pp and pn pairs provides additional support for this conclusion. All these results consistently hint at a physical picture whereby the aggregated effect of SRC in the nuclear wave function is determined to a large extent by mass-independent correlation operators on $S_{n=0}$ pairs. This provides additional evidence for the scale separation between the mean-field and SRC dynamics that has, for example, been used in calculations of NMD of Refs. [18–20]. Among other things, these conclusions are likely to affect the models used to estimate the effect of correlated pairs on neutrino-nucleus cross sections [33] and studies of the nuclear equation-of-state in conditions of increased density, i.e., enhanced sensitivity of SRC [34].

ACKNOWLEDGMENTS

We acknowledge the efforts of the Jefferson Lab staff that made this experiment possible and the EG2 group and CLAS Collaboration. The Ghent group is supported by the Research Foundation Flanders (FWO-Flanders) and by the Interuniversity Attraction Poles Programme P7/12 initiated by the Belgian Science Policy Office. For the theoretical calculations, the computational resources (Stevin Supercomputer Infrastructure) and services used in this work were provided by Ghent University, the Hercules Foundation, and the Flemish Government. O. Hen and E. Piasetzky are supported by the Israeli Science Foundation. L. B. Weinstein is supported by the US Department of Energy under Grants No. de-SC00006801 and No. DOE-FG02-96ER40960.

[1] O. Benhar, A. Fabrocini, S. Fantoni, and I. Sick, Nucl. Phys. A **579**, 493 (1994).

[2] M. Alvioli, C. Ciofi degli Atti, L. P. Kaptari, C. B. Mezzetti, and H. Morita, Phys. Rev. C **87**, 034603 (2013).

[3] R. B. Wiringa, R. Schiavilla, S. C. Pieper, and J. Carlson, Phys. Rev. C **89**, 024305 (2014).

[4] A. Tang, J. W. Watson, J. Aclander, J. Alster, G. Asryan, Y. Averichev, D. Barton, V. Baturin, N. Bukhtoyarova, A. Carroll *et al.*, Phys. Rev. Lett. **90**, 042301 (2003).

[5] E. Piasetzky, M. Sargsian, L. Frankfurt, M. Strikman, and J. W. Watson, Phys. Rev. Lett. **97**, 162504 (2006).

[6] R. Subedi, R. Shneor, P. Monaghan, B. Anderson, K. Aniol, J. Annand, J. Arrington, H. Benaoum, F. Benmokhtar, W. Boeglin *et al.*, Science **320**, 1476 (2008).

[7] I. Korover, N. Muangma, O. Hen, R. Shneor, V. Sulkosky, A. Kelleher, S. Gilad, D. W. Higinbotham, E. Piasetzky, J. W. Watson *et al.* (Jefferson Lab Hall A Collaboration), Phys. Rev. Lett. **113**, 022501 (2014).

[8] O. Hen, M. Sargsian, L. B. Weinstein, E. Piasetzky, H. Hakobyan, D. W. Higinbotham, M. Braverman, W. K. Brooks, S. Gilad, K. P. Adhikari *et al.*, Science **346**, 614 (2014).

[9] O. Hen, L. Weinstein, E. Piasetzky, G. A. Miller, M. M. Sargsian, and Y. Sagi, arXiv:1407.8175.

[10] L. Fields *et al.*, Phys. Rev. Lett. **111**, 022501 (2013).

[11] G. A. Fiorentini *et al.*, Phys. Rev. Lett. **111**, 022502 (2013).

[12] O. Hen, B.-A. Li, W.-J. Guo, L. B. Weinstein, and E. Piasetzky, Phys. Rev. C **91**, 025803 (2015).

[13] W. Dickhoff and C. Barbieri, Prog. Part. Nucl. Phys. **52**, 377 (2004).

[14] L. L. Frankfurt, M. I. Strikman, D. B. Day, and M. Sargsyan, Phys. Rev. C **48**, 2451 (1993).

[15] K. S. Egiyan, N. Dashyan, M. Sargsian, S. Stepanyan, L. B. Weinstein, G. Adams, P. Ambrozewicz, E. Anciant, M. Anghinolfi, B. Asavapibhop *et al.* (CLAS Collaboration), Phys. Rev. C **68**, 014313 (2003).

[16] K. S. Egiyan, N. B. Dashyan, M. M. Sargsian, M. I. Strikman, L. B. Weinstein, G. Adams, P. Ambrozewicz, M. Anghinolfi, B. Asavapibhop, G. Asryan *et al.* (CLAS Collaboration), Phys. Rev. Lett. **96**, 082501 (2006).

[17] N. Fomin, J. Arrington, R. Asaturyan, F. Benmokhtar, W. Boeglin, P. Bosted, A. Bruell, M. H. S. Bukhari, M. E. Christy, E. Chudakov *et al.*, Phys. Rev. Lett. **108**, 092502 (2012).

[18] J. Ryckebusch, M. Vanhalst, and W. Cosyn, J. Phys. G **42**, 055104 (2015).

[19] R. Roth, T. Neff, and H. Feldmeier, Prog. Part. Nucl. Phys. **65**, 50 (2010).

[20] S. K. Bogner and D. Roscher, Phys. Rev. C **86**, 064304 (2012).

[21] O. Hen *et al.* (CLAS Collaboration), Phys. Lett. B **722**, 63 (2013).

[22] B. Mecking *et al.* (CLAS Collaboration), Nucl. Instrum. Methods Phys. Res., Sect. A **503**, 513 (2003).

[23] C. Colle, W. Cosyn, J. Ryckebusch, and M. Vanhalst, Phys. Rev. C **89**, 024603 (2014).

[24] J. Ryckebusch, D. Debruyne, P. Lava, S. Janssen, B. Van Overmeire, and T. Van Cauteren, Nucl. Phys. A **728**, 226 (2003).

[25] W. Cosyn and J. Ryckebusch, Phys. Rev. C **87**, 064608 (2013).

[26] W. R. Gibbs and B. Loiseau, Phys. Rev. C **50**, 2742 (1994).

[27] M. Jain, M. L. Evans, G. Glass, J. C. Hiebert, R. A. Kenefick, L. C. Northcliffe, B. E. Bonner, J. E. Simmons, C. W. Bjork, P. J. Riley *et al.*, Phys. Rev. C **30**, 566 (1984).

[28] J. Ryckebusch, Phys. Lett. B **383**, 1 (1996).

[29] M. Vanhalst, W. Cosyn, and J. Ryckebusch, Phys. Rev. C **84**, 031302 (2011).

[30] M. Vanhalst, J. Ryckebusch, and W. Cosyn, Phys. Rev. C **86**, 044619 (2012).

[31] C. J. G. Onderwater *et al.*, Phys. Rev. Lett. **78**, 4893 (1997).

[32] R. Starink, M. van Batenburg, E. Cisbani, W. Dickhoff, S. Frullani, F. Garibaldi, C. Giusti, D. Groep, P. Heimberg, W. Hesselink *et al.*, Phys. Lett. B **474**, 33 (2000).

[33] R. Acciarri, C. Adams, J. Asaadi, B. Baller, T. Bolton, C. Bromberg, F. Cavanna, E. Church, D. Edmunds, A. Ereditato *et al.*, Phys. Rev. D **90**, 012008 (2014).

[34] Xin Zhang, Chang Xu, Zhongzhou Ren, Eur. Phys. J. A **50**, 113 (2014).

PHYSICAL REVIEW C **91**, 025803 (2015)

Symmetry energy of nucleonic matter with tensor correlations

Or Hen,[1,*] Bao-An Li,[2] Wen-Jun Guo,[2,3] L. B. Weinstein,[4] and Eli Piasetzky[1]
[1]*School of Physics and Astronomy, Tel Aviv University, Tel Aviv 69978, Israel*
[2]*Department of Physics and Astronomy, Texas A&M University–Commerce, Commerce, Texas 75429-3011, USA*
[3]*College of Science, University of Shanghai for Science and Technology, Shanghai, 200093, China*
[4]*Old Dominion University, Norfolk, Virginia 23529, USA*

(Received 18 August 2014; published 5 February 2015)

The nuclear symmetry energy ($E_{\rm sym}(\rho)$) is a vital ingredient of our understanding of many processes, from heavy-ion collisions to neutron stars structure. While the total nuclear symmetry energy at nuclear saturation density (ρ_0) is relatively well determined, its value at supranuclear densities is not. The latter can be better constrained by separately examining its kinetic and potential terms and their density dependencies. The kinetic term of the symmetry energy, $E_{\rm sym}^{\rm kin}(\rho_0)$, equals the difference in the per-nucleon kinetic energy between pure neutron matter (PNM) and symmetric nuclear matter (SNM), often calculated using a simple Fermi gas model. However, experiments show that tensor force induced short-range correlations (SRC) between proton-neutron pairs shift nucleons to high momentum in SNM, where there are equal numbers of neutrons and protons, but have almost no effect in PNM. We present an approximate analytical expression for $E_{\rm sym}^{\rm kin}(\rho_0)$ of correlated nucleonic matter. In our model, $E_{\rm sym}^{\rm kin}(\rho_0) = -10$ MeV, which differs significantly from $+12.5$ MeV for the widely-used free Fermi gas model. This result is consistent with our analysis of recent data on the free proton-to-neutron ratios measured in intermediate energy nucleus-nucleus collisions as well as with microscopic many-body calculations, and previous phenomenological extractions. We then use our calculated $E_{\rm sym}^{\rm kin}(\rho)$ in combination with the known total symmetry energy and its density dependence at saturation density to constrain the value and density dependence of the potential part and to extrapolate the total symmetry energy to supranuclear densities.

DOI: 10.1103/PhysRevC.91.025803 PACS number(s): 21.65.Ef, 21.30.Fe, 24.10.Lx, 25.60.−t

The nuclear symmetry energy $E_{\rm sym}(\rho)$, where ρ is the nuclear density, is related to the difference in the energy per nucleon of pure neutron matter (PNM) and symmetric nuclear matter (SNM). It determines many nuclear and astrophysical properties, such as the cooling of proto-neutron stars [1], the mass-radius relations of neutron stars [2], properties of nuclei involved in r-process nucleosynthesis [3], and heavy-ion collisions [4–6].

Much effort is being invested in improving our knowledge of $E_{\rm sym}(\rho)$. In particular, several major radioactive beam facilities being built around the world have all listed constraining the symmetry energy as one of their major science drivers; see, e.g., Ref. [7]. Moreover, observations of neutron stars from current missions such as the Chandra X-ray and XMM-Newton observatories and upcoming missions such as the Neutron Star Interior Composition Explorer (NICER) [8] will provide high-precision data to allow us to infer more accurately neutron star radii, which are very sensitive to the symmetry energy [9–12].

Significant progress has been made in recent years in constraining $E_{\rm sym}(\rho)$, especially around $\rho \approx \rho_0$, the saturation density, using data from both terrestrial laboratory experiments and astrophysical observations [13–18]. Recent surveys of model analyses of world data found that the mean values of the symmetry energy and its density dependence at ρ_0 are consistent with $29 \leqslant E_{\rm sym}(\rho_0) \leqslant 33$ MeV and $40 \leqslant L = 3\rho \frac{\partial E_{\rm sym}(\rho)}{\partial \rho}|_{\rho_0} \leqslant 60$ MeV [19,20]. However, the decomposition of the symmetry energy into its kinetic and potential parts and its behavior at both subsaturation ($\rho < \rho_0$) and suprasaturation ($\rho > \rho_0$) densities are still poorly known.

A common method to improving our knowledge of the total symmetry energy, $E_{\rm sym}(\rho)$, is to separate it into its potential ($E_{\rm sym}^{\rm pot}(\rho)$) and kinetic ($E_{\rm sym}^{\rm kin}(\rho)$) parts,

$$E_{\rm sym}(\rho) = E_{\rm sym}^{\rm kin}(\rho) + E_{\rm sym}^{\rm pot}(\rho) \tag{1}$$

and probing them separately [6,12,18]. The kinetic part of the symmetry energy, $E_{\rm sym}^{\rm kin}(\rho)$, can be readily calculated from the nuclear momentum distribution. The much less understood potential part can then be calculated as $E_{\rm sym}^{\rm pot}(\rho) = E_{\rm sym}(\rho) - E_{\rm sym}^{\rm kin}(\rho)$.

This separation is valuable for several reasons. As $E_{\rm sym}^{\rm kin}(\rho)$ and $E_{\rm sym}^{\rm pot}(\rho)$ have different density dependencies (typically parameterized as $E_{\rm sym}^{\rm kin}(\rho_0)(\frac{\rho}{\rho_0})^\alpha$ and $E_{\rm sym}^{\rm pot}(\rho)(\frac{\rho}{\rho_0})^\gamma$) the total symmetry energy can be more reliably extrapolated to higher densities by extrapolating its kinetic and potential parts separately. Second, knowledge of $E_{\rm sym}^{\rm pot}(\rho)$ is important for constraining key parameters in calculations of the symmetry energy, such as three-body forces [21] and high-order chiral effective interactions [22]. These improved models then allow extrapolation of $E_{\rm sym}^{\rm pot}(\rho)$ to suprasaturation densities with improved accuracy [18,23–25]. Third, knowing $E_{\rm sym}^{\rm kin}(\rho)$ and $E_{\rm sym}^{\rm pot}(\rho)$ separately is required to describe heavy-ion reactions and describe the isovector dynamical observables. For example, the density dependence of $E_{\rm sym}(\rho)$ as extracted from heavy-ion collisions depends on models of $E_{\rm sym}^{\rm kin}(\rho)$ [26].

The kinetic part is often approximated in a nonrelativistic free Fermi gas model [6,12] as the per-nucleon difference

---

[*] or.chen@mail.huji.ac.il

between the kinetic energy of pure neutron matter at a density ρ and the kinetic energy of symmetric nuclear matter where the protons and neutrons each have density $\rho/2$:

$$E^{\rm kin}_{\rm sym}(\rho)|_{\rm FG} = (2^{\frac{2}{3}} - 1)\tfrac{3}{5}E_F(\rho) \approx 12.5{\rm MeV}(\rho/\rho_0)^{2/3}, \quad (2)$$

where $E_F(\rho)$ is the Fermi energy at density ρ.

However, short-range correlations (SRC) due to the tensor force acting predominantly between neutron-proton pairs significantly increase the average momentum and hence the kinetic energy in SNM but have almost no effect in PNM. They thus reduce significantly the kinetic symmetry energy, possibly even to negative values. This has been shown recently in both phenomenological models [27] and microscopic many-body theories [28–31]. For a given symmetry energy, $E_{\rm sym}(\rho)$, the SRC-induced decrease of $E^{\rm kin}_{\rm sym}(\rho)$ increases $E^{\rm pot}_{\rm sym}(\rho)$ beyond its Fermi gas model limit of $E^{\rm pot}_{\rm sym}(\rho_0) = E_{\rm sym}(\rho_0) - E^{\rm kin}_{\rm sym}(\rho_0)|_{FG} \approx 19.1$ MeV at saturation density. This is important for transport model simulations of heavy-ion collisions [4–6,32,33].

In this paper we provide a phenomenological analytical expression for the kinetic symmetry energy of correlated nucleonic matter based on calculations of nuclear momentum distributions and on data at saturation density (ρ_0) from inclusive (e,e') and exclusive $(e,e'pN)$ scattering experiments at the Thomas Jefferson National Accelerator Facility (JLab) [34–38]. We give credence to our model by comparing to a transport model analysis of nucleon emission data in intermediate energy heavy-ion collisions [40,41] and to many-body theoretical calculations of nuclei and nuclear matter [28–31,41,42]. Last we use the known values of the total symmetry energy, $E_{\rm sym}(\rho_0)$, and its density dependence, L, at saturation density to extract the total symmetry energy at supranuclear densities and to constrain the value and density dependence of the potential part of the symmetry energy.

It has long been known that the tensor-force-induced SRC leads to a high-momentum tail in the single-nucleon momentum distribution around 300–600 MeV/c [43,44]. This high-momentum tail scales; i.e., its shape is almost identical for all nuclei from deuteron to infinite nuclear matter. See, e.g. Refs. [42,45,46]. This is shown by the constancy of the ratio of the per-nucleon inclusive (e,e') cross sections for nucleus A to the deuteron, $a_2(A)$, for Bjorken scaling parameter x_B between about 1.5 and 1.9 [34–36,47]. The ratio of the momentum distribution in nucleus A to the deuteron for $300 \leqslant k \leqslant 600$ MeV/c is just the cross-sectional ratio $a_2(A)$. Extrapolation of the measured $a_2(A)$ to infinite SNM using three different techniques [48–50] yields an average value of $a_2(\infty) = 7 \pm 1$. The uncertainty in the extrapolation represents about 50% of the difference between $a_2(A) \approx 5$ for heavy nuclei and $a_2(\infty) = 7$ for SNM.

Exclusive two-nucleon knockout experiments [37,38,51–53] show that, for $300 \leqslant k \leqslant 600$ MeV/c, proton knockout is accompanied by a recoil second nucleon and that second nucleon is predominantly a neutron, i.e., that np-SRC pairs dominate over pp pairs by a factor of about 20. For recent reviews, see Refs. [54,55]. This implies that correlations are about 20 times smaller in PNM than in SNM. Since the integral of the deuteron momentum distribution from 300 to 600 MeV/c is about 4% [56] and $a_2(\infty) = 7 \pm 1$, the probability of finding a high-momentum nucleon in SNM is about 25% and in PNM is about 1–2%.

The deuteron momentum distribution, $n_d(k)$, decreases as $1/k^4$ for $300 \leqslant k \leqslant 600$ MeV/c [57]. Since the nuclear momentum distribution, $n_A(k)$, in that range is predominantly due to np-SRC pairs and since it is proportional to the deuteron distribution, we can write that $n_A(k/k_F)(k/k_F)^4 = R_d a_2(A)$, where $R_d = 0.64 \pm 0.10$ is extracted from the deuteron momentum distribution and k_F is the Fermi momentum [57]. At higher momenta, the momentum distribution $n(k)$ drops much more rapidly.

This is supported by "exact" variational Monte Carlo (VMC) momentum distributions calculated [41] for ^{4}He and ^{10}B, which decrease as k^{-4} for np pairs with small-pair center-of-mass momentum for nucleon momenta $1.2 < k/k_F < 3$ to within about 10%.

We therefore model $n(k)$ for SNM with a depleted Fermi gas region and a correlated high-momentum tail:

$$n^{\rm SRC}_{\rm SNM}(k) = \begin{cases} A_0 & k < k_F \\ C_\infty/k^4 & k_F < k < \lambda k^0_F \\ 0 & k > \lambda k^0_F \end{cases}, \quad (3)$$

where $C_\infty = R_d a_2(\infty) k_F \equiv c_0 k_F$ is the phenomenological height factor [57], $c_0 = 4.16 \pm 0.95$, k^0_F is the Fermi momentum at ρ_0, and $\lambda \approx 2.75 \pm 0.25$ is the high-momentum cutoff obtained from the momentum distribution of the deuteron [57]. A_0 is a constant given by

$$A_0 = \frac{3\pi^2}{(k^0_F)^3}\frac{\rho_0}{\rho}\left\{1 - \left[1 - \frac{1}{\lambda}\left(\frac{\rho}{\rho_0}\right)^{1/3}\right]\frac{c_0}{\pi^2}\right\}, \quad (4)$$

determined by the normalization

$$\frac{4\pi}{(2\pi)^3}\int_0^{\lambda k^0_F} n^{\rm SRC}_{\rm SNM}(k)k^2 dk \equiv 0.5. \quad (5)$$

Based on the JLab data [38], fewer than 2% of neutrons belong to nn-SRC pairs. We thus use the free Fermi gas model for PNM and include the 2% upper limit for correlated neutrons in our estimate of the uncertainty band. In what follows we refer to this as the correlated Fermi gas (CFG) model.

The per-nucleon kinetic energy of nuclei and of symmetric nuclear matter can then be calculated from the momentum distribution using

$$E_{\rm kin} = \frac{4\pi}{(2\pi)^3}\int_0^\infty \frac{\hbar^2 k^2}{2m} n(k) k^2 dk. \quad (6)$$

Figure 1 shows the resulting kinetic energy for finite nuclei, calculated within the CFG model using $a_2(A) = 5 \pm 0.3$ and shown as a function of λ. The CFG kinetic energy is much larger than that of the uncorrelated Fermi gas. It agrees with the kinetic energies from many-body nuclear calculations for ^{12}C, ^{16}O, ^{40}Ca, ^{56}Fe, and ^{208}Pb [42] and from VMC calculations for ^{12}C [41].

Figure 2 shows the average nucleon kinetic energy for SNM, $E^{\rm kin}_{\rm SNM}(\rho_0)$ calculated at saturation density and shown as a function of λ. The CFG calculation is done using

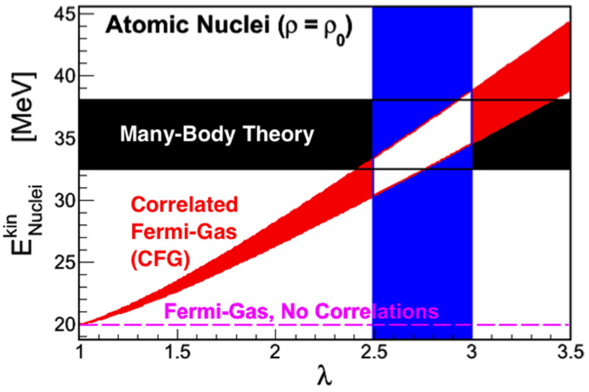

FIG. 1. (Color online) The per-nucleon kinetic energy calculated using the correlated Fermi gas (CFG) model (diagonal red [gray] band) for atomic nuclei from ^{12}C to ^{208}Pb. The calculated kinetic energy is shown as a function of λ, the high-momentum tail cutoff parameter. The vertical blue (gray) band shows the constraints on λ from the deuteron momentum distribution. The red band reflects the model uncertainties. Also shown are the results from the uncorrelated Fermi gas model (dashed purple [gray] line) and a horizontal black band spanning the results from many-body nuclear calculations for various nuclei from ^{12}C to ^{208}Pb [42] and from exact variational Monte Carlo (VMC) calculations for ^{12}C [41].

$a_2(\infty) = 7 \pm 1$ and $R_d = 0.64 \pm 0.10$ and is compared with the free Fermi gas model and the predictions of several microscopic models [28,30,31]. The error band on the CFG results combines estimated uncertainties in R_d and $a_2(\infty)$. The self-consistent Green's function (SCGF) calculations of the kinetic energy of symmetric nuclear matter, $E^{kin}_{SNM}(\rho_0)$ [30,31], agree with our CFG calculation (Fig. 2).

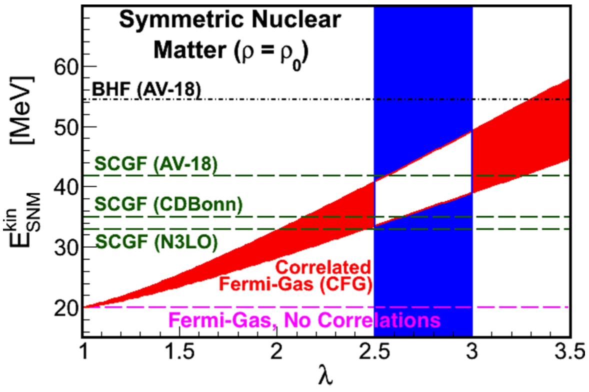

FIG. 2. (Color online) The per-nucleon kinetic energy for symmetric nuclear matter calculated using the correlated Fermi gas (CFG) model (diagonal red [gray] band). The calculated kinetic energy is shown as a function of λ, the high-momentum tail cutoff parameter. The vertical blue (gray) band shows the constraints on λ from the deuteron momentum distribution. The red band reflects the model uncertainties. Also shown are the results from the uncorrelated Fermi gas model (dashed purple [gray, bottom] line), the Brueckner-Hartree-Fock (BHF) model using the AV-18 interaction [28], and the self-consistent Green's function (SCGF) approach using the CDBonn, N3LO, and AV18 nucleon-nucleon interactions [30,31].

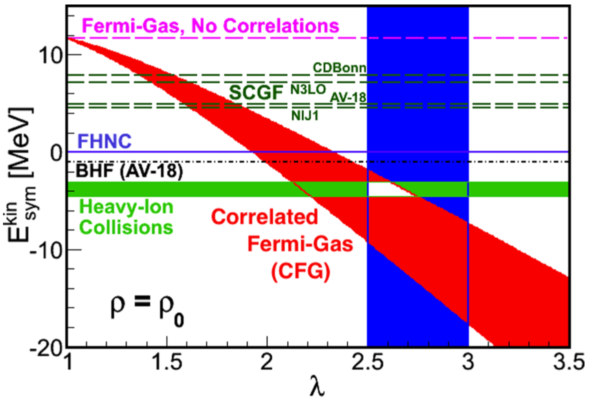

FIG. 3. (Color online) The per-nucleon kinetic symmetry energy at saturation density, $E^{kin}_{sym}(\rho_0)$, calculated using the correlated Fermi gas model (diagonal red [gray] band) as a function of λ, the high-momentum tail cutoff parameter. The dashed purple (gray, top) line shows the results of the uncorrelated Fermi gas model. The horizontal green (gray) band shows the results from transport model analyses of Sn+Sn collisions described in the text. Also shown for comparison are the results from microscopic calculations: Brueckner-Hartree-Fock (BHF) [28], Fermi hypernetted chain (FHNC) [29], and the self-consistent Green's gunction (SCGF) using the CDBonn, N3LO, Nij1, and AV18 nucleon-nucleon interactions [30,31].

Almost all phenomenological and microscopic many-body theories lead to equations of state (EOS) of asymmetric nucleonic matter that vary quadratically with the isospin-asymmetry $\delta = (\rho_n - \rho_p)/(\rho_n + \rho_p)$ according to the so-called empirical parabolic law $E(\rho,\delta) = E(\rho,\delta = 0) + E_{sym}(\rho)\delta^2 + O(\delta^4)$. The coefficient of the δ^4 term at ρ_0 has been found to be less than 1 MeV [33]. The symmetry energy can thus be calculated equally accurately from either the energy difference between PNM and SNM, i.e., $E_{sym}(\rho) = E(\rho,1) - E(\rho,0)$, or the curvature $E_{sym}(\rho) = \frac{1}{2}\frac{\partial^2 E(\rho,\delta)}{\partial \delta^2}$ at any δ.

However, it has never been tested whether the empirical parabolic law is valid separately for the kinetic and potential parts of the EOS. While the free Fermi gas kinetic energy satisfies the parabolic law, models that include SRC may not [58]. To be consistent and compare with the free Fermi gas model and microscopic many-body theories, we will define the kinetic symmetry energy of correlated nucleonic matter as $E^{kin}_{sym}(\rho) = E^{kin}_{PNM}(\rho) - E^{kin}_{SNM}(\rho)$. We add a SRC correction term to the Fermi gas symmetry energy to get the full kinetic symmetry energy:

$$E^{kin}_{sym}(\rho) = E^{kin}_{sym}(\rho)|_{FG} - \Delta E^{kin}_{sym}(\rho), \tag{7}$$

where the SRC correction term is

$$\Delta E^{kin}_{sym} \equiv \frac{E^0_F}{\pi^2} c_0 \left[\lambda \left(\frac{\rho}{\rho_0}\right)^{1/3} - \frac{8}{5}\left(\frac{\rho}{\rho_0}\right)^{2/3} + \frac{3}{5}\frac{1}{\lambda}\left(\frac{\rho}{\rho_0}\right)\right]. \tag{8}$$

As one expects, the SRC correction increases with both the height ($c_0 = C_\infty/k_F = R_d a_2(\infty)$) and width (λ) of the high-momentum tail in SNM.

Figure 3 shows the kinetic symmetry energy, $E^{kin}_{sym}(\rho_0)$, calculated at saturation density assuming a free Fermi gas model for PNM and shown as a function of λ. The error band on the CFG results combines estimated uncertainties in $R_d, a_2(\infty)$ and the amount of SRC in PNM ($<2\%$). Within the uncertainty range of the parameter $\lambda = 2.75 \pm 0.25$, $E^{\rm kin}_{\rm sym}(\rho_0)$ is found to be -10 ± 7.5 MeV, much less than the free Fermi gas result of $\approx +12.5$ MeV. The microscopic many-body theories yield results that are significantly smaller than the free Fermi gas prediction but significantly larger than our CFG model. Despite the agreement between our CFG model and the SCGF calculations of the kinetic energy of symmetric nuclear matter, $E^{\rm kin}_{\rm SNM}(\rho_0)$ [30,31], the SCGF symmetry energy, $E^{\rm kin}_{\rm sym}(\rho_0) = E^{\rm kin}_{\rm PNM}(\rho_0) - E^{\rm kin}_{\rm SNM}(\rho_0)$, is significantly larger than our model's. This is because the SCGF calculations include about 10% correlations in PNM.

To further validate our CFG model, we perform a transport model analysis of nucleon emission data in intermediate energy heavy-ion collisions. The dynamics of heavy-ion collisions around the Fermi energy are sensitive to the density dependence of the nuclear symmetry energy around ρ_0 [32,33]. Specifically, the ratio of free neutrons to protons emitted in heavy-ion collisions was found to be sensitive to the symmetry energy [4]. This ratio has been measured recently in $^{124}{\rm Sn} + {}^{124}{\rm Sn}$ and $^{112}{\rm Sn} + {}^{112}{\rm Sn}$ reactions at $E_{\rm beam}/A = 50$ and 120 MeV at MSU [40] with improved precision as compared to earlier measurements [39]. The data are given for the double ratio of neutrons to protons in $^{124}{\rm Sn} + {}^{124}{\rm Sn}$ to $^{112}{\rm Sn} + {}^{112}{\rm Sn}$ reactions to reduce systematic errors associated with neutron detection.

Using the Isospin-dependent Boltzmann-Uehling-Uhlenbeck (IBUU) transport model [33], analysis of this double ratio was done by introducing two parameters, η and γ, to describe the potential symmetry energy:

$$E^{\rm pot}_{\rm sym}(\rho) = \left[E_{\rm sym}(\rho_0) - \eta E^{\rm kin}_{\rm sym}(\rho_0)\big|_{\rm FG}\right](\rho/\rho_0)^{\gamma}. \qquad (9)$$

Without considering the momentum dependence of nuclear potentials, the corresponding symmetry potential is then

$$V^{n/p}_{\rm sym}(\rho,\delta) = \left[E_{\rm sym}(\rho_0) - \eta E^{\rm kin}_{\rm sym}(\rho_0)\big|_{\rm FG}\right](\rho/\rho_0)^{\gamma} \times [\pm 2\delta + (\gamma - 1)\delta^2]. \qquad (10)$$

The 2δ term dominates. The $\pm$ sign is due to the fact that neutrons and protons feel repulsive and attractive symmetry potentials respectively.

We varied η and γ on a large two-dimensional (2D) fine lattice to minimize the χ^2 between the model calculations and the MSU data at both beam energies. We then performed a covariance analysis to find the uncertainties of η and γ corresponding to a $\pm 1\sigma$ error band using the method reviewed recently in Refs. [59,60]. We used an impact parameter of 3 fm, consistent with that estimated for the data [61]. Free nucleons are identified as those with local densities less than $\rho_0/8$ at the time of their final freeze-out from the reaction. Calculations using a phase-space coalescence model lead to similar results within the error band [26].

Figure 4 shows the double free neutron-proton ratios in the two 124 and 112 Sn+Sn reactions at $E_{\rm beam}/A =$ 50 MeV/nucleon [40]. The calculations (red band) shown used the optimized parameters $\eta_0 = -0.30\,(1 \pm 18.53\%)$ that corresponds to $E^{\rm kin}_{\rm sym}(\rho_0) = -(3.8 \pm 0.7)$ MeV and $\gamma_0 = 0.80\,(1 \pm 5.98\%)$ with a $\chi^2_0 = 8$. This value of $E^{\rm kin}_{\rm sym}(\rho_0)$ was determined without considering the momentum dependence of the symmetry potential known to decrease somewhat the free neutron-proton ratio [62]. It thus represents an upper bound on the kinetic symmetry energy used to reproduce the MSU data within the IBUU model. For comparison, results with a $\chi^2 = 21$ using $E^{\rm kin}_{\rm sym}(\rho_0)|_{\rm FG} = 12.5$ MeV and $\gamma = 0.8$ are also shown. Calculations with $E^{\rm kin}_{\rm sym}(\rho_0)|_{\rm FG}$ and other values of γ between 0.4 and 1 leads to even higher χ^2 values.

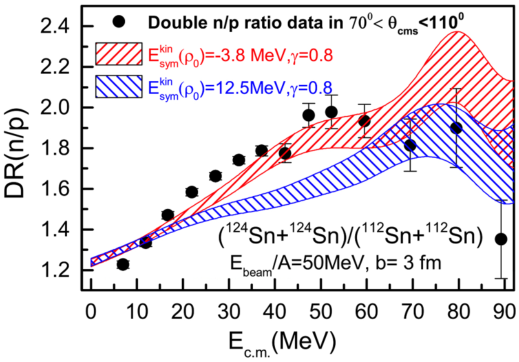

FIG. 4. (Color online) The calculated double ratio of free neutron-protons in the two reactions in comparison with the MSU data for transversely emitted nucleons in the angular range of $70^\circ \leqslant \theta_{\rm cms} \leqslant 110^\circ$ [40]. The bands represent 1σ uncertainty of the calculations.

The value of $E^{\rm kin}_{\rm sym}(\rho_0)$ determined from the IBUU transport analysis of the neutron to proton ratios in Sn+Sn collisions is consistent with that calculated using our CFG model (see Fig. 3).

We now turn to extracting the total symmetry energy at supra-nuclear densities and the density dependence of its potential part using the CFG model. We use the general form of the total symmetry energy given by Eq. (1), with the CFG corrections to the kinetic energy term given by Eq. (7) and (8). As detailed above, by comparing the CFG model results to the known values of the total symmetry energy ($E_{\rm sym}(\rho_0) = 31.0 \pm 1(1\sigma)$ MeV [19]) we can extract the value of the potential part of the symmetry energy at saturation density: $E^{\rm pot}_{\rm sym}(\rho_0) = E_{\rm sym}(\rho_0) - E^{\rm kin}_{\rm sym}(\rho_0)$. Simillarly, using the known density dependence of the total symmetry energy at saturation density ($L = 50 \pm 5(1\sigma)$ MeV [19]) we can extract the density dependence of the potential part of the symmetry energy:

$$\gamma = \frac{\frac{1}{3}L - \frac{dE^{\rm kin}_{\rm sym}(\rho)}{d\rho}\Big|_{\rho_0}}{E_{\rm sym}(\rho_0) - E^{\rm kin}_{\rm sym}(\rho_0)}.$$

Our results are summarized in Table I where we list the value of γ extracted using the CFG model. This is compared with free fermi gas model results (i.e. $\alpha = 2/3$) assuming different values for the kinetic symmetry energy (i.e. $E^{\rm kin}_{\rm sym}(\rho_0) = -10, 0, 12.5, 17$ MeV), and with recent analyses of heavy ion collisions [6] and neutron star data [12], which

TABLE I. Density dependence parameter, γ, of the potential part of the symmetry energy extracted within the Correlated Fermi Gas (CFG) and Free Fermi Gas (FG) models, assuming a total symmetry energy of $E_{\mathrm{sym}}(\rho_0) = 31$ MeV. Also shown are the value of γ and its 1σ and 2σ confidence intervals, extracted from analysis of heavy ion collision data [6] and neutron stars observations [12], assuming a Free FG model. The assumed value of the kinetic symmetry energy at saturation density used in each extraction is also listed.

	$E^{\mathrm{kin}}_{\mathrm{sym}}(\rho_0)$ [MeV]	γ $\pm 1\sigma(2\sigma)$
CFG	-10 ± 3	0.25 ± 0.05
FG	-10 ± 3	0.58 ± 0.05
	0	0.55 ± 0.06
	12.5	0.48 ± 0.10
	17	0.41 ± 0.13
Tsang *et al.* [6]	12.5	$0.7^{+0.1(0.35)}_{-0.2(0.3)}$
Steiner *et al.* [12]	17.0	$0.3^{+0.1(0.5)}_{-0.1(0.3)}$

also assume a free fermi gas model (i.e. $\alpha = 2/3$). As can be seen, even within the FG model, the value of γ varies significantly depending on the value of the kinetic symmetry energy. Furthermore, CFG and FG results for the same kinetic symmetry energy also differ due to the density dependence of the SRC correction term [Eq. (8)]. The value of γ obtained from the neutron star analysis of Ref. [12] is very similar to that of the CFG model.

Figure 5 shows the density dependence of the kinetic, potential and total symmetry energy obtained using both the CFG and FG models. While the two models differ significantly in the values and density dependences of their kinetic and potential parts, their total symmetry energies are almost identical.

To summarize, we provide an analytical expression for a kinetic symmetry energy of correlated nucleonic matter at $\rho = \rho_0$, using the dominance of short-range correlated neutron-proton pairs at high momentum observed in electron scattering data. Our model yields $E^{\mathrm{kin}}_{\mathrm{sym}}(\rho_0) = -10 \pm 7.5$ MeV, significantly lower than $E^{\mathrm{kin}}_{\mathrm{sym}}(\rho_0) = +12.5$ MeV of the widely-used free Fermi gas model. This result is consistent with our analysis of recent data on the free proton-to-neutron ratios measured in intermediate energy nucleus-nucleus collisions as well as with microscopic many-body calculations, and previous phenomenological extractions. We also extract the density dependence of $E^{\mathrm{pot}}_{\mathrm{sym}}(\rho)$ and $E_{\mathrm{sym}}(\rho)$ from our model of $E^{\mathrm{pot}}_{\mathrm{sym}}(\rho)$ together with the value of the total symmetry energy and its density dependence at saturation density. While the total symmetry energy exacted using different models is consistent, its separation into kinetic and potential parts is not.

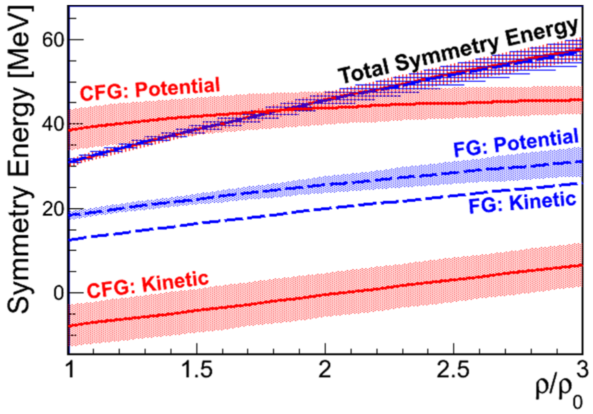

FIG. 5. (Color online) The density dependence of the kinetic, potential and total symmetry energy extracted using the CFG and FG models. See text for details.

ACKNOWLEDGMENTS

We thank F. J. Fattoyev, X. H. Li, W. G. Newton, Z. Z. Shi, A. Gal, M. M. Sargsian, G. A. Miller, D. W. Higinbotham, M. Strikman, and L. Frankfurt for helpful discussions. O. Hen and E. Piasetzky are supported by the Israel Science Foundation. B. A. Li is supported in part by the U.S. National Science Foundation under Grant No. PHY-1068022, U.S. National Aeronautics and Space Administration under Grant No. NNX11AC41G issued through the Science Mission Directorate, the CUSTIPEN (China-U.S. Theory Institute for Physics with Exotic Nuclei) under DOE Grant No. DE-FG02-13ER42025, and the National Natural Science Foundation of China under Grant No. 11320101004. W. J. Guo is supported by the National Natural Science Foundation of China (10905041) and the China Scholarship Council Foundation (201208310156). L. B. Weinstein is supported by the U.S. Department of Energy under Grants No. DE-SC00006801 and No. DE-FG02-96ER40960.

---

[1] J. M. Lattimer, C. J. Pethick, M. Prakash, and P. Haensel, Phys. Rev. Lett. **66**, 2701 (1991).

[2] M. Prakash, T. L. Ainsworth, and J. M. Lattimer, Phys. Rev. Lett. **61**, 2518 (1988).

[3] N. Nikolov, N. Schunck, W. Nazarewicz, M. Bender, and J. Pei, Phys. Rev. C **83**, 034305 (2011).

[4] B. A. Li, C. M. Ko, and Z. Z. Ren, Phys. Rev. Lett. **78**, 1644 (1997).

[5] L. W. Chen, C. M. Ko, and B. A. Li, Phys. Rev. Lett. **94**, 032701 (2005).

[6] M. B. Tsang, Y. Zhang, P. Danielewicz, M. Famiano, Z. Li, W. G. Lynch, and A. W. Steiner, Phys. Rev. Lett. **102**, 122701 (2009).

[7] A. B. Balantekin *et al.*, Mod. Phys. Lett. A **29**, 1430010 (2014).

[8] C. Kouveliotou *et al.*, arXiv:1401.3741 (2014).

[9] A. W. Steiner, M. Prakash, J. M. Lattimer, and P. J. Ellis, Phys. Rep. **411**, 325 (2005).

[10] B. A. Li and A. W. Steiner, Phys. Lett. B **642**, 436 (2006).

[11] W. G. Newton, M. Gearheart, and B. A. Li, APJ Suppl. Ser. **204**, 9 (2013).

[12] A. W. Steiner, J. M. Lattimer, and E. F. Brown, Astrophys. J. **722**, 33 (2010).
[13] W. G. Lynch *et al.*, Prog. Nucl. Part. Phys. **62**, 427 (2009).
[14] W. Trautmann and H. H. Wolter, Int. J. Mod. Phys. E **21**, 1230003 (2012).
[15] M. B. Tsang *et al.*, Phys. Rev. C **86**, 015803 (2012).
[16] B. A. Li, A. Ramos, G. Verde, and I. Vidaña, eds., Eur. Phys. J. A **50**, 2 (2014).
[17] C. J. Horowitz *et al.*, J. Phys. G **41**, 093001 (2014).
[18] J. M. Lattimer, Annu. Rev. Nucl. Part. Sci. **62**, 485 (2012).
[19] J. M. Lattimer and Y. Lim, Astrophys. J. **771**, 51 (2013).
[20] B. A. Li and X. Han, Phys. Lett. B **727**, 276 (2013).
[21] S. Gandolfi, J. Carlson, S. Reddy, A. W. Steiner, and R. B. Wiringa, Eur. Phys. J A **50**, 10 (2014).
[22] K. Hebeler and A. Schwenk, Eur. Phys. J A **50**, 11 (2014).
[23] A. W. Steiner and S. Gandolfi, Phys. Rev. Lett. **108**, 081102 (2012).
[24] K. Hebeler, J. M. Lattimer, C. J. Pethick, and A. Schwenk, Astrophys. J. **773**, 11 (2013).
[25] A. Gezerlis, I. Tews, E. Epelbaum, S. Gandolfi, K. Hebeler, A. Nogga, and A. Schwenk, Phys. Rev. Lett. **111**, 032501 (2013).
[26] B. A. Li, W. J. Guo, and Z. Z. Shi, arXiv:1408.6415.
[27] C. Xu and B. A. Li, arXiv:1104.2075; C. Xu, A. Li, and B. A. Li, J. Phys: Conf. Ser. **420**, 012190 (2013).
[28] I. Vidana, A. Polls, and C. Providencia, Phys. Rev. C **84**, 062801(R) (2011).
[29] A. Lovato, O. Benhar, S. Fantoni, A. Yu. Illarionov, and K. E. Schmidt, Phys. Rev. C **83**, 054003 (2011).
[30] A. Carbone, A. Polls, and A. Rios, Eur. Phys. Lett. **97**, 22001 (2012).
[31] A. Rios, A. Polls, and W. H. Dickhoff, Phys. Rev. C **89**, 044303 (2014).
[32] V. Baran, M. Colonna, V. Greco, and M. Di Toro, Phys. Rep. **410**, 335 (2005).
[33] B. A. Li, L. W. Chen, and C. M. Ko, Phys. Rep. **464**, 113 (2008).
[34] K. Egiyan *et al.* (CLAS Collaboration), Phys. Rev. C **68**, 014313 (2003).
[35] K. Egiyan *et al.* (CLAS Collaboration), Phys. Rev. Lett. **96**, 082501 (2006).
[36] N. Fomin *et al.* (Hall C. Collaboration), Phys. Rev. Lett. **108**, 092502 (2012).
[37] O. Hen *et al.* (The CLAS Collaboration), Science **346**, 614 (2014).
[38] R. Subedi *et al.* (Hall A. Collaboration), Science **320**, 1476 (2008).
[39] M. A. Famiano *et al.*, Phys. Rev. Lett. **97**, 052701 (2006).
[40] D. S. Coupland *et al.*, arXiv:1406.4546.
[41] R. B. Wiringa, R. Schiavilla, S. C. Pieper, and J. Carlson, Phys. Rev. C **89**, 024305 (2014).
[42] C. Ciofi degli Atti and S. Simula, Phys. Rev. C **53**, 1689 (1996).
[43] H. A. Bethe, Ann. Rev. Nucl. Part. Sci. **21**, 93 (1971).
[44] A. N. Antonov, P. E. Hodgson, and I. Z. Petkov, *Nucleon Momentum and Density Distributions in Nuclei* (Clarendon Press, Oxford, 1988).
[45] S. Fantoni and V. R. Pandharipande, Nucl. Phys. A **427**, 473 (1984).
[46] S. C. Pieper, R. B. Wiringa, and V. R. Pandharipande, Phys. Rev. C **46**, 1741 (1992).
[47] D. B. Day *et al.*, Phys. Rev. C **40**, 1011 (1989).
[48] C. Ciofi degli Atti, E. Pace, and G. Salme, Phys. Rev. C **43**, 1155 (1991).
[49] M. McGauley and M. M. Sargsian, arXiv:1102.3973.
[50] E. Piasetzky, O. Hen, and L. B. Weinstein, AIP Conf. Proc. **1560**, 355 (2013).
[51] E. Piasetzky, M. Sargsian, L. Frankfurt, M. Strikman, and J. W. Watson, Phys. Rev. Lett. **97**, 162504 (2006).
[52] A. Tang *et al.*, Phys. Rev. Lett. **90**, 042301 (2003).
[53] H. Baghdasaryan *et al.* (CLAS Collaboration), Phys. Rev. Lett. **105**, 222501 (2010).
[54] L. Frankfurt, M. Sargsian, and M. Strikman, Int. J. Mod. Phys. A **23**, 2991 (2008).
[55] J. Arrington, D. W. Higinbotham, G. Rosner G., and M. Sargsian, Prog. Part. Nucl. Phys. **67**, 898 (2012).
[56] I. Passchier *et al.*, Phys. Rev. Lett. **88**, 102302 (2002).
[57] O. Hen, L. B. Weinstein, E. Piasetzky, G. A. Miller, M. M. Sargsian, and Y. Sagi, arXiv:1407.8175.
[58] X. H. Li *et al.* arXiv:1403.5577 (2014).
[59] J. Dobaczewski, W. Nazarewicz, and P.-G. Reinhard, J. Phys. G: Nucl. Part. Phys. **41**, 074001 (2014).
[60] J. Piekarewicz, W.-C. Chen, and F. J. Fattoyev, arXiv:1407.0911.
[61] Z. Chajecki and B. Tsang (private communication).
[62] B. A. Li, C. B. Das, S. Das Gupta, and C. Gale, Nucl. Phys. A **735**, 563 (2004).

Analysis of Neutron Stars Observations Using a Correlated Fermi Gas Model

O. Hen,[1] A.W. Steiner,[2, 3, 4] E. Piasetzky,[1] and L.B. Weinstein[5]
[1] *Tel Aviv University, Tel Aviv 69978, Israel*
[2] *Institute for Nuclear Theory, University of Washington, Seattle, Washington 98195, USA*
[3] *Department of Physics and Astronomy, University of Tennessee, Knoxville, Tennessee 37996, USA*
[4] *Physics Division, Oak Ridge National Laboratory, Oak Ridge, Tennessee 37831, USA*
[5] *Old Dominion University, Norfolk, VA 23529, USA*
(Dated: November 9, 2015)

Background: The nuclear symmetry energy is one of the fundamental ingredients in determining the equation of state (EOS) of neutron stars. Recent terrestrial experiments constrain both its value and slope at nuclear saturation density ($\rho_0 = 0.17$ nucleons/fm^3), however, its high-density extrapolation is unknown. Assuming a Free Fermi-gas (FFG) model for the kinetic symmetry energy, the high-density extrapolation depends on a single parameter - the density dependence of the potential symmetry energy. Recently, a new Correlated Fermi-gas (CFG) model was proposed, which includes the effect of short-range correlated, high-momentum, nucleons in nuclear matter. Using constrains obtained at saturation density, the CFG model was shown to obtain a soft density dependences for the symmetry potential.

Purpose: Examine the ability of the FFG and CFG models to describe neutron stars observables that are directly sensitive to the symmetry energy at high-density. Specifically, the ability of the CFG model, with its soft density dependences for the symmetry potential, to support a two solar-mass neutron star.

Methods: Using Bayesian analysis of neutron stars observables, we use the CFG and FFG models to describe the symmetry energy and examine the resulting parameters in the neutron star EOS and the density dependence of the potential symmetry energy.

Results: We find that both models can describe the data and support a two solar-mass NS. The obtained density dependence for the potential part of the symmetry energy is very different between the two models, but has a small effect on the NS EOS.

Conclusions: While sensitive to the high-density values of the symmetry energy, neutron stars observables alone are not enough to distinguish between the CFG and FFG models. This indicated that the NS EOS, obtain from Bayesian analysis of neutron stars observables, that is of vast intreats for astrophysics, is robust and is not sensitive to the exact nuclear model used for the kinetic term of the nuclear symmetry energy.

PACS numbers:

INTRODUCTION:

Determining the equation of state (EOS) of dense nuclear matter, such as that found in neutron stars (NS), has been a long-sought goal of nuclear physics. The EOS encapsulates the energy-density relation of cold and dense nuclear matter and is therefore a fundamental property of quantum chromodynamics. While considerable progress had been made in theoretical studies of nuclear and neutron matter at high densities [1–3], experimental constraints from terrestrial experiments and astrophysical observations are still sparse.

One of the largest uncertainties in the NS EOS is the density dependence of the nuclear symmetry energy [4]. This describes the change in the energy of nuclear matter as one replaces a proton with a neutron. The symmetry energy is constrained by terrestrial measurements up to nuclear saturation density, ρ_0 (= 0.17 nucleons/fm^3 $\approx$ 160 MeV/fm^3) [5–12]. Specifically at saturation density, the value and slope of the symmetry energy were recently determined to about 2 MeV and 20 MeV respectively [5, 6]. The symmetry energy behavior at supra-nuclear densities, required for the description of NS, is not well known.

A common method used to simplify the extraction of the density dependence of the symmetry energy is to split the symmetry energy into kinetic and potential parts and study them separately [13]. The kinetic term is usually determined analytically using a zero-temperature Free-Fermi Gas (FFG) model, which fully determines the value at saturation density and the density dependence to supra-nuclear densities. Combined with the known total symmetry energy at saturation density, this determines the potential symmetry energy at saturation density, leaving its density dependence as the only unknown [13, 14].

While the analytical FFG model is simple and easy to use, we know that it fails to describe many relevant properties of nuclear systems. In particular, microscopic calculations have shown that the FFG model underestimates the kinetic energy carried by nucleons in nuclei and nuclear matter [1, 15–19]. Results from recent electron-scattering experiments indicate that 20 - 25 % of nucleons in medium and heavy nuclei have momentum greater than the Fermi momentum [20–22].

These high-momentum nucleons dominate the kinetic energy of nucleons in nuclei and are predominantly in the form of neutron-proton (np) short-range correlated (SRC) pairs [23–28]. These SRC pairs are pairs of nucleons with large relative momentum and small center-of-mass momentum, where large and small are relative to the Fermi momentum. Omitting these SRC pairs in the FFG model cause an underestimate of the kinetic energy carried by nucleons in nuclei [29].

The effect of np-SRC pairs on the nuclear symmetry energy was recently investigated using the Correlated Fermi-Gas (CFG) model [29]. This model describe the momentum distribution of nucleons in symmetric nuclear-matter by:

$$n_{SNM}^{SRC}(k) = \begin{cases} A_0 & k < k_F \\ C_\infty/k^4 & k_F < k < \lambda k_F^0, \\ 0 & k > \lambda k_F^0 \end{cases} \qquad (1)$$

where A_0 stands for a depleted Fermi gas distribution that extends up to k_F. Above the Fermi momentum the momentum distribution is assumed to be dominated by np-SRC pairs who's momentum distribution is given by C_∞/k^4 [30] that extends from k_F to a constant cutoff given by λk_F^0, where k_F^0 is the Fermi-momentum of symmetric nuclear matter at saturation density. All constants in Eq. 1 (i.e. C_∞ and λ) are extracted from data, see Ref. [29] for details.

The kinetic symmetry energy calculated using the FFG and the CFG models showed a very large difference in the kinetic symmetry [29]. While the total symmetry energy at supra-nuclear density was almost unchanged, the saturation value and density dependence of the potential symmetry energy changed significantly. Intermediate energy heavy-ion collision experiments are directly sensitive to the potential symmetry energy. Incorporating np-SRC pairs into the transport codes used to interpret these collisions should have a large impact on the extracted density dependence of the potential symmetry energy.

This work examines the sensitivity of the NS EOS, extracted from Bayesian analysis of NS mass and radius observations [14], to the inclusion of np-SRC using the CFG model. This is a complementary and independent approach to the previous use of terrestrial observations at saturation density and has a larger sensitivity to the high-density behavior of the symmetry energy. We start with a short overview of NS observables, EOS parameterizations, and Bayesian analysis used to constrain free parameters in the NS EOS. We then discuss our results with emphasis on similarities and differences in the NS EOS obtained using the FFG and CFG models. We highlight the robustness of the resulting EOS and discuss the differences in the extracted potential symmetry energy.

BAYESIAN ANALYSIS OF NS OBSERVABLES AND THE NS EOS:

Bayesian analysis allows constraining the NS EOS by performing a global fit of NS EOS to NS mass-radius extractions, taking into account external constraints from terrestrial measurements, astrophysical observations (e.g., observation of a two solar-mass NS) and physical limitations such as causality (i.e., speed of sound $\leq$ speed of light), and hydrodynamical stability [14, 31].

The NS observations used in the analysis presented here include high precision mass extractions from Pulsar-timing measurements, simultaneous mass-radius extractions from photospheric radius expansion (PRE) X-ray burst measurements, and thermal spectra measurement of low-mass X-ray Binaries (LMXB), see Ref. [31] for details.

The parameterization of the NS EOS is divided into three energy-density regions: low ($\leq$ 15 MeV/fm^3), medium (15 to $\approx$ 350 MeV/fm^3), and high ($\leq\approx$ 350 MeV/fm^3). The low energy-density region describes the NS crust and its functional form is assumed to be well constrained. The high energy-density region is parameterized by a one or two polytropes. The medium energy-density region has a physically motivated functional form, with two fit parameters (Incompressibility, K, and Skewness, K) and the density dependent symmetry energy. See Ref. [14] for details.

As described in the introduction, the total symmetry

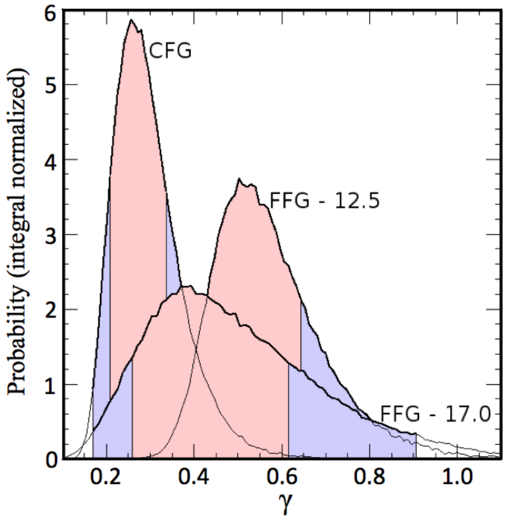

FIG. 1: (color online) The probability distribution of the extracted potential symmetry energy density dependence parameter γ (detailed in Eq. 3), obtained from a Bayesian analysis of NS observations using the CFG, FFG$_{12.5}$, and FFG$_{17.0}$ models for the kinetic symmetry energy. The inner and outer shaded region mark the 1- and 2-σ limits of each distribution, see text for details.

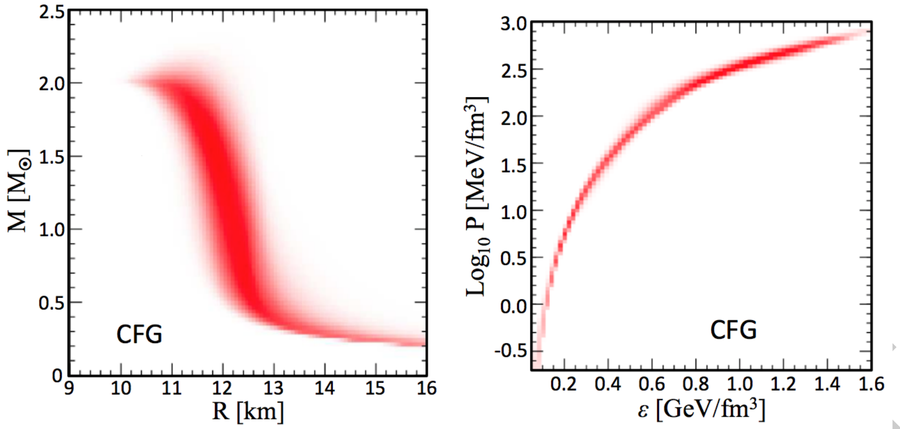

FIG. 2: The extracted mass-radius (left) and pressure energy-density (right) relations for the CFG model. The results for the FFG models are almost identical.

energy is generally given by:

$$E_{sym}(\rho/\rho_0) = E^{kin}_{sym}(\rho/\rho_0) + E^{pot}_{sym}(\rho/\rho_0), \quad (2)$$

where $E^{kin}_{sym}(\rho/\rho_0)$ and $E^{pot}_{sym}(\rho/\rho_0)$ are the kinetic and potential parts of the total symmetry energy. At nuclear saturation density the total symmetry energy, S_v, and its slope, L, are well constrained by terrestrial measurements [5, 6]. The kinetic term can be analytically calculated assuming a FFG or CFG model, and the potential symmetry energy at saturation energy is calculated as: $S_{pot} = S_v - S_{kin}$, where S_{kin} is the kinetic symmetry energy at saturation density. The density dependence of the potential symmetry energy is parameterized as:

$$\begin{aligned} E^{pot}_{sym}(\rho/\rho_0) &= S_{pot} \cdot (\rho/\rho_0)^{\gamma} \\ &= (S_v - S_{kin}) \cdot (\rho/\rho_0)^{\gamma}, \end{aligned} \quad (3)$$

where, assuming knowledge of S_{kin}, γ is the only unknown.

To constrain the NS EOS in a self-consistent way, we follow Steiner et al. [14] and perform a Bayesian analysis of all available NS observations and terrestrial measurements, using the FFG or the CFG models to express the kinetic symmetry energy at saturation and the density dependence. There are two FFG models used in the literature with $S_{kin} = 12.5$ and 17.0 MeV. We examine both options and refer to them as FFG$_{12.5}$ and FFG$_{17.0}$ respectively.

BAYESIAN ANALYSIS RESULTS:

We start by examining the details of the potential symmetry energy. Fig. 1 shows the density dependence of the symmetry energy for the three models. As can be seen, this variable is very sensitive to the choice of the kinetic symmetry energy model. The CFG kinetic symmetry energy is significantly lower than that of the FFG at saturation density. Because the total symmetry energy and its slope are fixed at saturation density, this increases the potential symmetry energy at ρ_0 and drastically decreases its density dependence, γ.

We note that the results shown in Fig. 1 for the FFG$_{17.0}$ model differ from the once previously obtained from a similar Bayesian analysis using the FFG$_{17.0}$ model [14]. This difference is due to the inclusion of additional observables in the analysis described here and changes in the fit parameter phase-space limitations. Unlike previous works, the results obtained using the FFG models are consistent with that extracted from heavy-ion analysis using the FFG$_{12.5}$ model [13].

The dramatically different potential symmetry energy and density dependence obtained using the CFG and FFG models does not appear to have a large effect on the bulk properties of the resulting NS EOS. Fig. 2 shows the EOS obtained from the Bayesian analysis using the CFG model, which is the same as obtained using the FFG$_{12.5}$ and FFG$_{17.0}$ models. Notice that despite the soft density dependence of the potential symmetry energy the resulting CFG EOS supports a two solar-mass NS. Fig. 3 shows the extracted energy per nucleon as a function of the baryonic density for the CFG and FFG$_{12.5}$ models (results for the FFG$_{17.0}$ model are practically identical to the FFG$_{12.5}$ model). The FFG results here are also very similar to the CFG model, although the latter yields a slightly larger energy. Both models are consistent with the empirical value of E/A = 16 MeV at saturation density.

The almost identical EOS and energy-density relations for the CFG, FFG$_{12.5}$ and FFG$_{17.0}$ models (as shown in Figs. 1 and 2) support the robustness of the Bayesian analysis and indicates that it is insensitive to the exact nuclear model used for the kinetic term of the nuclear symmetry energy. This is not surprising, since these are

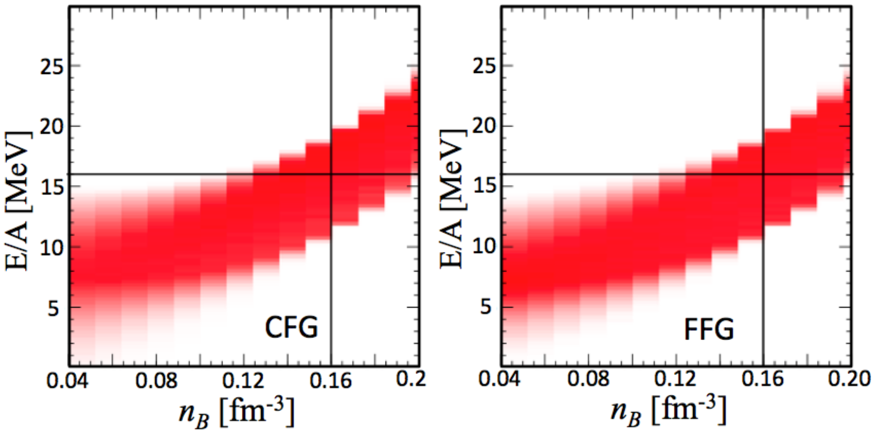

FIG. 3: (color online) The extracted energy per particle as a function of the baryonic density for the CFG (left) and FFG12.5 (right) models. The horizontal and vertical black lines mark the empirical value of 16 MeV at saturation density..

bulk properties of nuclear matter, which depends on the sum of the kinetic and potential symmetry energies which is the same for both the CFG and FFG models.

The bulk properties of NS are robust and largely insensitive to the choice of the kinetic symmetry energy model. However, it is desired to know (1) which model captures the nuclear dynamics better and (2) are there other observables that can differentiate between them? Recent calculations done using a Relativistic Mean-Field (RMF) model for the symmetry potential obtained very different results for the nuclear incompressibility when calculated using the CFG and FFG models. The result of the CFG model was consistent with recent experimental constraints. Another test suggested was to analyze pion production and isospin diffusion observables measured in intermedium-energy heavy-ion collisions. These experiments are directly sensitive to the symmetry potential but traditional analyzed using the FFG model alone. By incorporating SRCs into transport models one could preform a more details test.

SUMMARY:

The kinetic part of the nuclear symmetry energy can be parametrized using two models: CFG and FFG. These models differ based on their treatment of short-range high-momentum pairs of nucleons in nuclei. Using Bayesian analysis of neutron stars observables, we examined the ability of the CFG and FFG models to describe the data and examined the resulting parameters in the neutron star EOS and the density dependence of the potential symmetry energy. We find that both models can describe the data and support a two solar-mass NS. The obtained density dependence for the potential part of the symmetry energy is very different between the two models, but has a small effect on the NS EOS.

While sensitive to the high-density values of the symmetry energy, neutron stars observables alone are not enough to distinguish between the CFG and FFG models. This indicated that the NS EOS, obtain from Bayesian analysis of neutron stars observables, that is of vast intreats for astrophysics, is robust and is not sensitive to the exact nuclear model used for the kinetic term of the nuclear symmetry energy.

We thank lots of people for Bao-An Li and Misak Sargsian for many fruitful discussions. This work was partially supported by the U.S. Department of Energy under Grants No. DE-SC00006801 and No. DE-FG02-96ER40960 and by the Israel Science Foundation.

[1] A. Rios, A. Polls, and W. H. Dickhoff, Phys. Rev. **C89**, 044303 (2014), 1312.7307.
[2] S. Gandolfi, J. Carlson, and S. Reddy, Phys. Rev. **C85**, 032801 (2012), 1101.1921.
[3] K. Hebeler, J. M. Lattimer, C. J. Pethick, and A. Schwenk, Phys. Rev. Lett. **105**, 161102 (2010), 1007.1746.
[4] M. Prakash, T. L. Ainsworth, and J. M. Lattimer, Phys. Rev. Lett. **61**, 2518 (1988).
[5] J. M. Lattimer and A. W. Steiner, Eur. Phys. J. **A50**, 40 (2014), 1403.1186.
[6] B.-A. Li and X. Han, Phys. Lett. **B727**, 276 (2013), 1304.3368.
[7] W. G. Lynch, M. B. Tsang, Y. Zhang, P. Danielewicz, M. Famiano, Z. Li, and A. W. Steiner, Prog. Part. Nucl. Phys. **62**, 427 (2009), 0901.0412.
[8] W. Trautmann and H. H. Wolter, Int. J. Mod. Phys. **E21**, 1230003 (2012), 1205.2585.
[9] M. B. Tsang et al., Phys. Rev. **C86**, 015803 (2012), 1204.0466.
[10] B.-A. Li, A. Ramos, G. Verde, and I. Vidana, Eur. Phys.

J. **A50**, 9 (2014).

[11] C. J. Horowitz, E. F. Brown, Y. Kim, W. G. Lynch, R. Michaels, A. Ono, J. Piekarewicz, M. B. Tsang, and H. H. Wolter, J. Phys. **G41**, 093001 (2014), 1401.5839.

[12] J. M. Lattimer, Ann. Rev. Nucl. Part. Sci. **62**, 485 (2012), 1305.3510.

[13] M. B. Tsang, Y. Zhang, P. Danielewicz, M. Famiano, Z. Li, W. G. Lynch, and A. W. Steiner, Phys. Rev. Lett. **102**, 122701 (2009), [Int. J. Mod. Phys.E19,1631(2010)], 0811.3107.

[14] A. W. Steiner, J. M. Lattimer, and E. F. Brown, Astrophys. J. **722**, 33 (2010), 1005.0811.

[15] R. B. Wiringa, R. Schiavilla, S. C. Pieper, and J. Carlson, Phys. Rev. C **89**, 024305 (2014).

[16] C. Ciofi degli Atti and S. Simula, Phys. Rev. C **53**, 1689 (1996), URL `http://link.aps.org/doi/10.1103/PhysRevC.53.1689`.

[17] A. Carbone, A. Polls, and A. Rios, Euro. Phys. Lett. **97**, 22001 (2012).

[18] I. Vidaña, A. Polls, and C. m. c. Providência, Phys. Rev. C **84**, 062801 (2011), URL `http://link.aps.org/doi/10.1103/PhysRevC.84.062801`.

[19] A. Lovato, O. Benhar, S. Fantoni, A. Yu. Illarionov, and K. E. Schmidt, Phys. Rev. **C83**, 054003 (2011), 1011.3784.

[20] K. Egiyan et al. (CLAS Collaboration), Phys. Rev. C **68**, 014313 (2003).

[21] K. Egiyan et al. (CLAS Collaboration), Phys. Rev. Lett. **96**, 082501 (2006).

[22] N. Fomin et al., Phys. Rev. Lett. **108**, 092502 (2012).

[23] E. Piasetzky, M. Sargsian, L. Frankfurt, M. Strikman, and J. W. Watson, Phys. Rev. Lett. **97**, 162504 (2006).

[24] A. Tang et al., Phys. Rev. Lett. **90**, 042301 (2003).

[25] R. Shneor et al., Phys. Rev. Lett. **99**, 072501 (2007).

[26] R. Subedi et al., Science **320**, 1476 (2008).

[27] I. Korover, N. Muangma, O. Hen, et al., Phys.Rev.Lett. **113**, 022501 (2014), 1401.6138.

[28] O. Hen et al. (CLAS Collaboration), Science **346**, 614 (2014).

[29] O. Hen, B.-A. Li, W.-J. Guo, L. B. Weinstein, and E. Piasetzky, Phys. Rev. C **91**, 025803 (2015), URL `http://link.aps.org/doi/10.1103/PhysRevC.91.025803`.

[30] O. Hen, L. B. Weinstein, E. Piasetzky, G. A. Miller, M. M. Sargsian, and Y. Sagi, Phys. Rev. **C92**, 045205 (2015), 1407.8175.

[31] A. W. Steiner, J. M. Lattimer, and E. F. Brown, Astrophys. J. **765**, L5 (2013), 1205.6871.

4.3. Contact Interactions

"Correlated Fermion Pairs in Nuclei and Ultracold Atomic Gasses",
*O. Hen et al., Phys. Rev. C **92**, 045205 (2015).*

PHYSICAL REVIEW C **92**, 045205 (2015)

Correlated fermions in nuclei and ultracold atomic gases

O. Hen,[1,*] L. B. Weinstein,[2] E. Piasetzky,[1] G. A. Miller,[3] M. M. Sargsian,[4] and Y. Sagi[5]
[1]*Tel Aviv University, Tel Aviv 69978, Israel*
[2]*Old Dominion University, Norfolk, Virginia 23529, USA*
[3]*University of Washington, Seattle, Washington 98195-1560, USA*
[4]*Florida International University, Miami, Florida 33199, USA*
[5]*Department of Physics, Technion Israel Institute of Technology, Haifa 32000, Israel*

(Received 2 August 2014; revised manuscript received 25 August 2015; published 23 October 2015)

Background: The high-momentum distribution of atoms in two spin-state ultracold atomic gases with strong short-range interactions between atoms with different spins, which can be described by using Tan's contact, are dominated by short-range pairs of different fermions and decreases as k^{-4}. In atomic nuclei the momentum distribution of nucleons above the Fermi momentum ($k > k_F \approx 250$ MeV/c) is also dominated by short-range-correlated different-fermion (neutron-proton) pairs.

Purpose: Compare high-momentum unlike-fermion momentum distributions in atomic and nuclear systems.

Methods: We show that, for $k > k_F$ MeV/c, nuclear momentum distributions are proportional to that of the deuteron. We then examine the deuteron momentum distributions derived from a wide variety of modern nucleon-nucleon potentials that are consistent with NN-scattering data.

Results: The high-momentum tail of the deuteron momentum distribution, and hence of the nuclear momentum distributions, appears to decrease as k^{-4}. This behavior is shown to arise from the effects of the tensor part of the nucleon-nucleon potential. In addition, when the dimensionless interaction strength for the atomic system is chosen to be similar to that of atomic nuclei, the probability for finding a short-range different-fermion pair in both systems is the same.

Conclusions: Although nuclei do not satisfy all of the conditions for Tan's contact, the observed similarity of the magnitude and k^{-4} shape of nuclear and atomic momentum distributions is remarkable because these systems differ by about 20 orders of magnitude in density. This similarity may lead to a greater understanding of nuclei and the density dependence of nuclear systems.

DOI: 10.1103/PhysRevC.92.045205 PACS number(s): 21.65.−f, 21.30.−x, 03.75.Ss, 67.85.−d

I. INTRODUCTION

Interacting many-body fermionic systems are abundant in nature. In noninteracting Fermi systems at zero temperature, the maximum momentum of any fermion in the system is the Fermi momentum, k_F. Independent fermions moving in a mean-field potential have only a small probability to have $k > k_F$. However, an additional short-range interaction between fermions creates a significant high-momentum tail. In this work we discuss two very different systems, each composed of two dominant kinds of fermions: protons and neutrons in atomic nuclei and two spin-state ultracold atomic gases. While these systems differ by more than 20 orders of magnitude in density, and the fermion-fermion interactions are very different, both exhibit a strong short-range interaction between unlike fermions creating short-range-correlated (SRC) pairs of unlike fermions that dominate the high-momentum tail.

The momentum distribution of a dilute two-component atomic Fermi gas with contact interactions is known to exhibit a C/k^4 tail for $k > k_F$, where C is the contact as defined by Tan [1–12]. The value of C depends on the strength of interaction between the two components, as parametrized by a, the scattering length. Here we will show that, although nuclei do not fulfill the stringent conditions of Tan's relations, their momentum distribution is remarkably similar to that of ultracold Fermi gases with the same dimensionless interaction strength $(k_F a)^{-1}$. The similarity is in both its functional scaling and the spectral weight of the tail.

While this remarkable similarity may be accidental, it is plausible that Fermi systems with a complicated noncontact interaction may still posses universal properties on scales much larger than the scale of the interaction. This approach might lead to greater insight into nuclear pair correlations as well as the behavior of the density dependence of nuclear systems.

This paper is structured as follows: we review our knowledge of nucleon-nucleon pair correlations in nuclei, emphasizing that (1) the momentum distribution of nucleons in nuclei at $k > k_F$ is dominated by proton-neutron (np) pairs and (2) the momentum distribution of nucleons in medium to heavy nuclei is proportional to that of deuterons at high momenta. We then show that (3) the momentum distribution of nucleons in the deuteron and hence in all nuclei decreases approximately as k^{-4} at high momenta, which (4) can be understood from the short distance structure of correlations. This k^{-4} distribution is (5) the same momentum distribution as for the previously measured atoms in ultracold two-spin-state atomic gases with a contact interaction. We also show that (6) the pair-correlation probability for unlike fermions (i.e., the magnitude of the momentum distribution at high momentum) is the same for nuclei and for atomic systems when the dimensionless interaction strength of the atomic system is

---

[*] or.chen@mail.huji.ac.il

chosen to be the same as for nuclei. We then explore (7) the applicability of the conditions of Tan's theory to atomic nuclei. We discuss soft and hard nucleon-nucleon interactions in the Appendix.

Previous papers explored the nuclear momentum distribution as well as relationships between atomic and nuclear systems. Amado and Woloshyn [13] showed that the nuclear momentum distribution $n(k) \propto [k^{-2}v(k)]^2$ where $v(k)$ is the Fourier transform of the nucleon-nucleon potential. This decreases as k^{-4} if $v(k)$ is momentum independent. Sartor and Mahaux found a more complicated form for the momentum distribution at $k > k_F$ for a dilute Fermi gas [14,15], although their momentum distribution also decreases approximately as k^{-4} for large momenta. Studies of the ^{3}He Fermi liquid might also be relevant to this topic [16]. Carlson *et al.* compared quantum monte carlo approaches to neutron matter and atomic physics [17]. Özen and Zinner [18] proposed creating a two-component cold Fermi gas closely analogous to nuclear systems. Zinner and Jensen [19,20] explored the differences and similarities between nuclei and cold atomic gases. They point out that, "as the contact parameters are expected to be universal, they should be the same for a nuclear system in the limit of large scattering length." This work builds on these studies and examines quantitatively the connections and similarities between two-component atomic and nuclear systems. Our analysis is different than that of recent work that relates the nuclear contact to the Levinger constant [21].

II. SHORT-RANGE CORRELATIONS IN NUCLEI

Atomic nuclei are among the most common many-body Fermi systems. Analysis of electron-nucleus scattering [22] confirmed that medium and heavy nuclei, with atomic weight $A \geqslant 12$, exhibit the properties of a degenerate system with a characteristic Fermi momentum, $k_F \approx 250$ MeV/c. However, experiments also show that nuclei are not completely described by the independent-particle approximation and that, as expected [23,24], two-particle correlations are a leading correction [25–31]. Nuclei are composed of protons and neutrons with up and down spins, which can create six different types of nucleon pairs. However, isospin invariance reduces the types of independent pairs to four: spin-singlet proton-proton (pp), neutron-neutron (nn), and proton-neutron (pn) pairs and spin-triplet pn pairs. Isospin symmetry further implies that all three types of spin-singlet pairs are similar to each other, reducing the types of pairs to two: spin singlet and spin triplet. These pairs have either even or odd values of the orbital angular momentum L according to the generalized Pauli principle, $(-1)^{L+S+T} = -1$.

Experiments show that short-range-correlated nucleon-nucleon pairs account for approximately all of the high-momentum, $k > k_F$, nucleons in nuclei and about 20%–25% of all the nucleons in nuclei [25–31]. They also show that short-range np pairs dominate over pp pairs with a ratio $np/pp = 18 \pm 5$ [29–31], even in heavy asymmetric nuclei such as lead [32]. As np pairs include contributions from both spin-singlet and spin-triplet pairs whereas pp pairs are entirely spin singlet, the observed np/pp ratio implies that spin-triplet np pairs account for 85% ± 3% of all pairs with spin-singlet isospin-triplet pp, nn, and np pairs contributing 5% ± 1% each for a total of 15% ± 3% spin-singlet pairs. This is due to the dominant tensor interaction (which acts only in spin-triplet states) between nucleons at relative momenta between 300 and 600 MeV/c [33–35]. Corrections due to correlations among three nucleons or more are small [23,26] and appear only for nucleon momenta greater than about 800 MeV/c.

III. NUCLEAR-MOMENTUM DISTRIBUTIONS

Because of the observed dominance of np pairs in SRCs we can use the independent-pair approximation [36] to write the momentum density at $k > k_F$ for heavier nuclei as

$$n_A(k) = a_2(A) n_d(k), \tag{1}$$

where $n_A(k)$ and $n_d(k)$ are the high-momentum parts of the nucleon-momentum distribution for a nucleus of atomic number A and deuterium, respectively, and the factor $a_2(A)$ is independent of k and is the probability of finding a high-momentum pair in nucleus A relative to deuterium.

This simple picture was validated experimentally by measurements of the ratios of per-nucleon inclusive electron scattering cross sections for nuclei of atomic number A relative to deuterium at four-momentum transfer squared, $Q^2 = \vec{q}^{\,2} - \omega^2 > 1.5$ GeV^2 and Bjorken scaling parameter $1.5 < x < 1.9$ where $x = Q^2/(2m\omega)$, $\vec{q}$ and ω are the three-momentum and energy transferred to the nucleus, respectively, and m is the nucleon mass. Cross sections in this kinematic region are sensitive to the integral of the nucleon momentum distribution from a threshold momentum to infinity where $k_{\text{thresh}} = k_{\text{thresh}}(Q^2,x)$ depends on x and Q^2 [37]. These cross-section ratios are independent of x for $1.5 \leqslant x \leqslant 1.9$ and $1.5 \leqslant Q^2 \leqslant 3$ GeV^2 [25–28], showing that the momentum distributions have similar shapes for approximately $k_F \leqslant k \lesssim 3k_F$ ($275 \pm 25 \leqslant k \lesssim 700$ MeV/c) validating Eq. (1). The value of the ratio gives the proportionality constant for the different nuclei:

$$a_2(A) = \frac{\sigma_A/A}{\sigma_d/2}. \tag{2}$$

IV. DEUTERON MOMENTUM DISTRIBUTIONS

Since the momentum distributions of all nuclei at high momentum are proportional to that of the deuteron for about $k_F \leqslant k \leqslant 3k_F$, we now examine the deuteron momentum distribution. We will show that the nucleon momentum distribution for deuterium, and hence for all nuclei, decreases approximately as k^{-4} for the momentum range $1.3\,k_F \leqslant k \leqslant 2.5\,k_F$. (In anticipation of the coming discussion of heavy nuclei, we use $k_F = 250$ MeV/c, the typical Fermi momentum for medium and heavy nuclei.)

In order to study the range of possible deuteron-momentum distributions, we considered ten modern nucleon-nucleon (NN) potentials that are consistent with the nucleon-nucleon scattering world data set, the Nijmegen 1, 2, and 3 [38], AV18 [39], CD Bonn [40], wjc1 and 2 [41], IIB [42], and n3lo500 and n3lo600 [43] nucleon-nucleon interactions.

The chiral effective-field theory (χEFT) N3LO potentials [43] have an explicit momentum cutoff of the form

$\exp[-(p/\Lambda)^n]$ where $n = 4, 6,$ or 8 and $\Lambda = 500$ or 600 MeV. While we use the N3LO potentials with 500 and 600 MeV cutoffs, the χEFT neutron-proton phase shifts differ dramatically in some partial waves (especially at higher energy) as the cutoff is varied from 0.7 to 1.5 GeV or as the expansion order is increased from N3LO to N4LO [44]. In addition, "the N2LO, N3LO, and N4LO contributions are all about of the same size, thus raising some concern about the convergence of the chiral expansion for the NN potential" [45]. The N5LO contribution is much smaller, indicating convergence [45]. It is unclear how these convergence issues affect the ability of N3LO potentials to describe the high-momentum tail of the deuteron. However, high-precision deuteron-momentum distributions are not yet available for higher-order χEFT.

There is also some disagreement over the utility of bare interactions versus soft phase-equivalent interactions. This is discussed in detail in the Appendix.

The momentum distribution of a nucleon bound in deuterium, $n_d(k)$, was calculated by using each of the modern nucleon-nucleon potentials. The proton and neutron momentum distributions in the deuteron are equal, $n_p(k/k_F) = n_n(k/k_F) = n_d(k/k_F)$, and are normalized so that

$$\frac{1}{(2\pi)^3}\int_0^\infty n(k/k_F)d^3(k/k_F) = \frac{1}{2}. \tag{3}$$

We can see the k^{-4} dependence of the momentum distribution clearly in Fig. 1(a), which shows the scaled dimensionless momentum distribution, $(k/k_F)^4 n_d(k/k_F)$, for a nucleon bound in deuterium for each of these potentials [43]. We observe k^{-4} scaling in seven of the ten different realistic models, all showing that the ratio

$$R_d = (k/k_F)^4 n_d(k/k_F) = 0.64 \pm 0.10 \tag{4}$$

for $1.3 \leqslant k/k_F \leqslant 2.5$ is constant within about 15%, as shown by the red dashed line and uncertainty band in Fig. 1(a). Note that k^{-4} changes by a factor of 14 in this range and even the outlying potentials only differ by at most a factor of two from the average.

The experimental reduced $d(e,e'p)$ cross sections for $1.3\,k_F \leqslant k \leqslant 2.5\,k_F$ also appear to scale as k^{-4} and provide more evidence for the scaling of the momentum distribution. Figure 1(a) also shows the measured $d(e,e'p)$ scaled reduced cross sections, $(k/k_F)^4\sigma_{\mathrm{red}}(k/k_F)$, for proton knockout by electron scattering from deuterium in two kinematics where the effects of rescattering of the knocked-out proton (final-state interactions or FSIs) are expected to be small [46]. The two kinematics are for the angle between the undetected neutron and the momentum transfer, $\theta_{nq} = 35^\circ$ and 45°. If the electron interacts directly with an on-shell proton and the proton does not rescatter as it leaves the nucleus, then the reduced cross section equals the momentum distribution. Corrections for these effects are model dependent and are on the order of 30% to 40% (see Ref. [46] and references therein). These effects should be significantly smaller for $\theta_{nq} = 35^\circ$ than for 45°. The momentum dependence of these effects should also be significantly smaller.

We fit these momentum distributions by $n_d(k) \propto k^{-\alpha}$ for $1.3k_F \leqslant k \leqslant 2.5k_F$ [except for N3LO500 and N3LO600 which we fit up to their cutoffs of 500 MeV/c ($2k_F$) and 600 MeV/c ($2.4k_F$), respectively]. We varied the lower and upper fitting bounds by $\pm 0.1k_F$ and $\pm 0.2k_F$, respectively, to determine the uncertainty in the exponent α (see Fig. 2). We observe k^{-4} scaling in seven of the ten different realistic models of the nucleon-momentum distribution in deuterium.

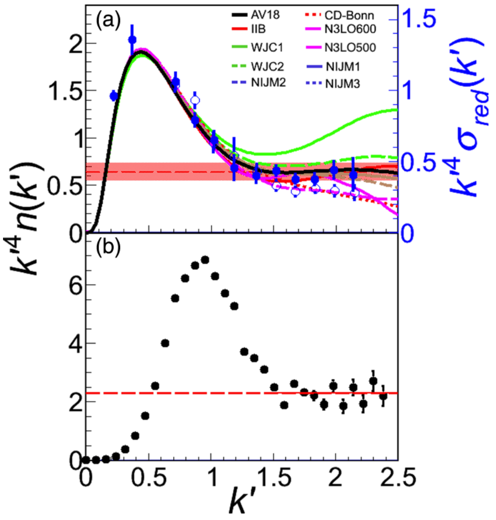

FIG. 1. (Color online) The scaled momentum distribution, $k'^4 n(k')$ where $k' = k/k_F$, for (a) deuteron and (b) atomic systems. (a) The curves show the scaled proton-momentum distribution for the deuteron calculated from the Nijmegen 1, 2, and 3 [38], AV18 [39], CD Bonn [40], wjc1 and 2 [41], IIB [42], and n3lo500 and n3lo600 [43] nucleon-nucleon interactions. The dashed red line is the average of eight of the calculated momentum distributions for $k \geqslant 1.3k_F$. The red band shows the $\pm 15\%$ uncertainty. The points show the scaled reduced cross sections (using the right-hand y axis), $k'^4\sigma_{\mathrm{red}}(k')$, for electron-induced proton knockout from deuterium, $d(e,e'p)$, at $\theta_{nq} = 35^\circ$ (filled circles) and at $\theta_{nq} = 45^\circ$ (open circles) [46]. The curves and points are plotted in units of $k_F = 250$ MeV/c, the typical Fermi momentum for medium and heavy nuclei. This choice of k_F affects the normalization but not the observed k^{-4} scaling. (b) The points show the measured momentum distribution of ^{40}K atoms in a symmetric two-spin-state ultracold gas with a short-range interaction between the different spin states [5]. The dimensionless interaction strength $(k_F a)^{-1} = -0.08 \pm 0.04$. The Fermi momentum is $k_F \approx 1.6$ eV/c.

This scaling behavior arises from the sum of the S and D wave contributions to the density. Due to the tensor interaction, the high-momentum tail is predominantly produced by $J = 1$, S- and D-wave np nucleon pairs ($T = 0, S = 1, L = 0,2$ or ${}^3S_1 - {}^3D_1$) [47]. For larger momenta, $k > 2.5k_F$, the momentum distribution falls more rapidly with k. However, this accounts for less than 1% of the fermions in the system [26]. The momentum distribution of pp pairs does not scale, since there is a minimum in the momentum distribution at $k/k_F \approx 1.6$.

In agreement with the np-pair-dominance model, exact calculations of the ^{12}C-momentum distribution by using the AV18 potential also show k^{-4} scaling [35]. Rios, Polls, and Dickhoff calculated the momentum distribution for infinite symmetric nuclear matter using a self-consistent Green's

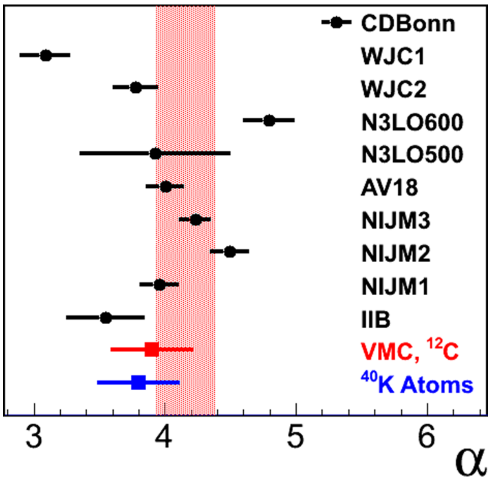

FIG. 2. (Color online) The power α obtained by fitting the momentum distribution of the nucleon in deuterium to the form: $n_d(k) \propto k^{-\alpha}$ over $1.3k_F \leqslant k \leqslant 2.5k_F$ for the nucleon-nucleon interactions of Fig. 1. The momentum distributions from n3lo500 and n3lo600 are sharply regulated (forced to decrease rapidly) at around 500 ($k = 2k_F$) and 600 MeV/c ($k/k_F = 2.4k_F$), respectively, so we restricted the upper limit of their fit ranges to $2.0k_F$ and $2.4k_F$. The uncertainty of the nuclear momentum distribution exponent comes predominantly from varying the lower and upper bounds of the fitting range by $\pm 0.1k_F$ and $\pm 0.2k_F$ respectively. The red band is the average α ($\pm 2\sigma$) obtained from the deuteron distributions, excluding the two outlier wave functions: CDBonn and WJC1. Also shown is the result of the power-law fits for the momentum distributions of a nucleon in ^{12}C [35] and an atom in an ultracold two-spin-state ^{40}K gas [5].

function (SCGF) approach for the AV18, CDBonn and N3LO500 interactions [48,49]. They show that the N3LO500 potential fails to reproduce the measured deuteron-momentum distributions. Their AV18 and CDBonn nuclear-matter-momentum distributions decrease with approximately the same exponent α as do the AV18 and CDBonn deuteron-momentum distributions shown in Fig. 2.

Based on the inclusive $A(e,e')$ cross-section ratios discussed above, the np-pair dominance model, and the calculations of nuclear- and nuclear-matter-momentum distributions, we conclude that the momentum distributions of all nuclei decrease approximately as k^{-4}.

V. UNDERSTANDING THE k^{-4} SCALING

This scaling should not be surprising. Colle *et al.* [50] found that the nuclear-mass dependence of the number of SRC pp and pn pairs in nuclei can be described by tensor operators acting on NN pairs in a nodeless relative S state of the mean-field basis [47,51]. This very-short-range behavior of the correlated part of the NN interaction leads to k^{-4} momentum dependence at high momentum, as is shown next.

This k^{-4} behavior can be understood to arise from the importance of the one-pion-exchange (OPE) contribution to the tensor potential V_T, acting in second order. The Schrödinger equation for the spin-one two-nucleon system, which involves S- and D-state components, can be expressed as an equation involving the S state only by using $(-B - H_0)|\Psi_D\rangle = V_T|\Psi_S\rangle$, where B is the binding energy of the system and H_0 is the Hamiltonian excluding the tensor potential. Thus, one obtains an effective S-state potential: $V_{00} = V_T(-B - H_0)^{-1}V_T$, where V_T connects the S and D states. The intermediate Hamiltonian H_0 is dominated by the effects of the centrifugal barrier and can be approximated by the kinetic-energy operator. This second-order term is large because it contains an isospin factor $(\vec{\tau}_1 \cdot \vec{\tau}_2)^2 = 9$, and because $S_{12}^2 = 8 - 2S_{12}$. Evaluation of the S-state potential, neglecting the small effects of the central potential in the intermediate D state, yields

$$V_{00}(k,k') \approx -M\frac{16f^4}{\mu^4\pi^4}\int \frac{p^2\,pdp}{MB + p^2} I_{02}(k,p)I_{20}(p,k'), \qquad (5)$$

where M is the nucleon mass, $f^2 \approx 0.08$ is the coupling constant, μ is the pion mass, and $I_{LL'}$ are Fourier transforms of the OPE tensor potential,

$$I_{02}(p,k) = I_{20}(p,k) = \frac{k^2 Q_2(z) + p^2 Q_0(z)}{2pk} - Q_1(z),$$

with $z \equiv (p^2 + k^2 + \mu^2)/(2pk)$, and Q_i are Legendre functions of the second kind. The important property is that $\lim_{p\to\infty} I_{02}(p,k) = 1 - (k^2 + \mu^2)/p^2 + \cdots$. Thus, the integrand of Eq. (5) is dominated by large values of p and diverges unless there is a cutoff. This means that $V_{00}(k',k)$ is approximately a constant, independent of k and k'. This is the signature of a short-range interaction. As discussed in the Introduction, this is the necessary and sufficient condition to obtain an asymptotic two-nucleon wave function $\sim 1/k^2$ and a momentum density $n(k) \sim 1/k^4$. Potentials that do not yield this behavior either have a very weak tensor force or a momentum cutoff at low momenta.

VI. COMPARING NUCLEAR AND ATOMIC HIGH-MOMENTUM TAILS

Figure 1(b) shows the k^{-4} scaling of ^{40}K atoms. Note the remarkable similarity between the data depicted in Figs. 1(a) and 1(b). The nuclear-momentum distributions have the same k^{-4} dependence as the momentum distribution measured for two spin-state ultracold ^{40}K atoms of Ref. [5] and as Tan's predictions.

VII. NUCLEAR- AND ATOMIC-PAIR-CORRELATION PROBABILITIES

After establishing the similarity in k^{-4} scaling of the momentum-distribution tail of the nuclear and cold atom systems, we now compare the spectral weight contained in these tails. Similar to atomic gases, we define the normalized dimensionless scaling coefficient per particle as

$$\frac{C}{k_F A} \equiv (k/k_F)^4 n(k/k_F) \qquad (6)$$

at high momentum, where A is the number of fermions in the system and $n(k/k_F)$ is the dimensionless scaled fermion momentum distribution in units of k_F, normalized according to Eq. (3). $C/(k_F A)$ is a measure of the per particle number of

TABLE I. The scaling coefficient extracted for different nuclei. $a_2(A)$ is the ratio of the per nucleon inclusive (e,e') cross sections for nucleus A relative to deuterium for $Q^2 > 1.5\ (\text{GeV}/c)^2$ and $1.5 \leqslant x \leqslant 1.9$ [28] [see Eq. (1)]. C is defined by Eq. (7).

Nucleus	$a_2(A)$	$C/(k_F A)$
^{12}C	4.75 ± 0.16	3.04 ± 0.49
^{56}Fe	5.21 ± 0.20	3.33 ± 0.54
^{197}Au	5.16 ± 0.22	3.30 ± 0.53

short-range-correlated pairs. For nuclei,

$$\frac{C}{k_F A} = a_2(A) R_d, \tag{7}$$

where $C/(k_F A)$, for nuclei, is the sum of all four possible coefficients, dominated by spin-triplet np pairs, and the ratios $a_2(A)$ are taken from Ref. [28] (see Table I).

Figure 3 shows the nuclear coefficients from Table I and the scaled atomic contact as extracted from measurements of the momentum distribution of trapped two-spin-state mixtures of ultracold ^{40}K [5] and ^{6}Li [6] atomic gases as a function of the dimensionless interaction strength $(ak_F)^{-1}$. The ultracold atomic gas measurements span a wide range of interaction strengths near unitary, in the BCS-BEC crossover regime. In the nuclear case, all medium and heavy nuclei are in the unitary regime where $|k_F a|^{-1} \ll 1$, using the typical nuclear Fermi momentum, $k_F = 250\ \text{MeV}/c = 1.27\ \text{fm}^{-1}$ [22] and the $^3S_1$ neutron-proton scattering length, $a = 5.42$ fm [52]. As can be seen, when the dimensionless interaction strength is the same, the scaled atomic contact and the nuclear coefficient agree remarkably well. The integral of the k^{-4} tail of the momentum density is about 0.2. Thus, each fermion has a ≈20% probability of belonging to a high-momentum different-fermion pair in both the atomic and nuclear systems.

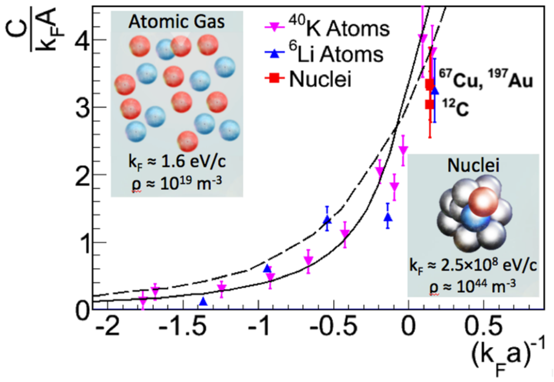

FIG. 3. (Color online) The magenta inverted and blue upright triangles show the scaled contact plotted versus $(k_F a)^{-1}$, the inverse of the product of the scattering length and Fermi momentum, as extracted from measurements of ultracold two-spin-state atomic systems at finite temperature [5,6]. The red squares show the equivalent coefficient extracted from atomic nuclei (see Table I), which are essentially at zero temperature. The dashed and solid lines show the theoretical predictions of Refs. [8] and [53], respectively, for atomic systems at zero temperature.

This agreement between the shape and magnitude of the momentum distributions between such wildly disparate systems is remarkable. We now look for the underlying reasons for this agreement.

VIII. POSSIBLE CONNECTIONS TO TAN'S CONTACT

Tan [1–3] and later others [4] showed that a short-range interaction between two different fermion types leads to a high-momentum tail that falls as k^{-4} (where k is the fermion momentum), and derived a series of universal relations that relate the contact (i.e., the number of short-range-correlated pairs) to various thermodynamic properties of the system such as the total energy and pressure. These were recently validated experimentally in ultracold two-spin-state atomic gas systems [5,6] (see Ref. [4] for a review).

Tan obtained relations for dilute systems with scattering length a and interfermion distance d, which are much larger than the range of the interaction, r_0: $a \gg r_0$ and $d \gg r_0$. In such systems the k^{-4} scaling of the momentum distribution is only expected for $ka \gg 1$ and $kr_0 \ll 1$.

As we have shown, atomic nuclei exhibit some of the same key properties as cold atomic Fermi systems. They are characterized by a Fermi momentum k_F, and have a strong short-range interaction between (spin-triplet) unlike fermions. The nuclear momentum distributions also fall as k^{-4} for $300 \leqslant k \leqslant 600\ \text{MeV}/c$.

However, unlike systems of atoms, atomic nuclei are self-bound. The nucleon-nucleon force provides both the long-range interactions that cause atomic nuclei to resemble Fermi gases and the short-range interaction between fermions. The binding interaction arises in part from the iterated effects of the long-distance one-pion-exchange potential and has a range of about $r_0^{\text{bind}} \approx \hbar/(m_\pi c) \approx 1.4$ fm, where $m_\pi = 140\ \text{MeV}/c^2$ is the pion mass. The range of the short-range part of the nucleon-nucleon interaction responsible for the spin-triplet pn pairs in the high-momentum tail is less well defined. The NN-pairs in a nodeless relative S state [50] are at much closer distances than typical nucleons. Similarly, the second-order action of the tensor interaction described in Eq. (5) also must have an effective range much shorter than the long-distance pion exchange that binds the nucleus. Quantitatively, various tensor correlation functions shown in Ref. [54] peak at an internucleon distance of about 1 fm, so we estimate that $r_0 \approx 1$ fm.

The typical distance between same-type nucleons in nuclei is $d = (\rho_0/2)^{-1/3} \approx 2.3$ fm, where $\rho_0 \approx 0.17\ \text{nucleons}/\text{fm}^3$ is the saturation nuclear density. The nucleon-nucleon scattering length in the $^3S_1$ channel is 5.424 ± 0.003 fm [52].

Therefore, for nuclei, both the interaction length and the internucleon distance are greater, but not much greater, than the range of the short-distance interaction (i.e., $a \approx 5.4\ \text{fm} > d \approx 2\ \text{fm} > r_0 \approx 1$ fm). Other required conditions for $1/k^4$ scaling are $k \gg 1/a \approx 40\ \text{MeV}/c$ and $k \ll 1/r_0 \approx 200\ \text{MeV}/c$ for $r_0 \approx 1$ fm. As can be seen in Fig. 1(a), scaling occurs for $300 \leqslant k \leqslant 600\ \text{MeV}/c$, much greater than the lower limit of $40\ \text{MeV}/c$. However, k is definitely not much less (or even less) than the upper limit of $200\ \text{MeV}/c$.

The required kinematic conditions discussed above are sufficient, but perhaps not necessary. The scaling of quark distributions measured in deep inelastic electron scattering was observed at momentum transfers much below that expected. This is referred to as "precocious scaling" [55]. Additionally the $1/k^4$ tail in ultracold Fermi gases was experimentally observed to start at a much lower momentum than predicted [5,56].

Our extraction is different than a recent work by Weiss, Bazak, and Barnea [21] that relates the nuclear contact term to the Levinger constant. They attempt to extract it from photodisintegration data, which are driven by the electric-dipole operator that operates on neutron-proton pairs. Photodisintegration is not a measure of the ground-state nucleon momentum density. Furthermore their analysis is restricted to photon energies below 140 MeV, which corresponds to wavelengths $\lambda \geqslant 2\pi\hbar c/E = 8.8$ fm which sample the entire nucleus and are not short-range. Also, these photon energies correspond to nucleon momenta less than about 340 MeV$/c$ ($\approx 1.35 k_F$). This is below the k^{-4} scaling region shown in Fig. 1 above. Their average contact (singlet plus triplet over two) equals our triplet contact alone, so that their total contact is double ours and also double that of an atomic system with the same value of $k_F a$.

IX. SUMMARY

We have shown that the momentum distribution of nucleons in nuclei for $k > k_F$ is dominated by spin-triplet pn pairs and falls approximately as k^{-4}. This is very similar to the momentum distribution of two-spin-state ultracold atomic gases with a strong short-range interaction between atoms in the different spin states. Remarkably, despite a 20-order-of-magnitude difference in density, when both systems have the same dimensionless interaction strength $(k_F a)^{-1}$, and the magnitudes of the momentum distributions are also equal, indicating that fermions in the two systems have equal probabilities to belong to correlated pairs.

This leads to the question of whether this agreement between atomic and nuclear systems at remarkably different length, energy, and momentum scales is accidental or has a deeper reason. If the agreement has a deeper reason, then perhaps relations like Tan's can be developed for atomic nuclei and a better extrapolation to supra-dense nuclear systems may be possible.

ACKNOWLEDGMENTS

We thank W. Boeglin, E. Braaten, W. Cosyn, L. Frankfurt, D. Higinbotham, S. Moroz, J. Ryckebusch, R. Schiavilla, M. Strikman, J. W. Van Orden, and J. Watson for many fruitful discussions. We particularly thank J. W. Van Orden for providing the deuteron-momentum distributions. We also thank D. Jin for the atomic data presented in Fig. 2. This work was partially supported by the US Department of Energy under Grants No. DE-FG02-97ER-41014, No. DE-FG02-96ER-40960, and No. DE-FG02-01ER-41172 and by the Israel Science Foundation.

APPENDIX: SOFT AND HARD NN INTERACTIONS

Nuclear theory must describe a broad range of phenomena from low energies to high energies and from low momentum transfer to high momentum transfer. Therefore one must contend with the fact that the general baryon-baryon interaction includes matrix elements that connect low relative momenta to high relative momenta. These terms can be handled by using so-called soft NN potentials and by generating soft phase-equivalent effective interactions obtained from the bare interactions by means of unitary transformations [57–63].

Calculations of low-energy and low-momentum processes are indeed simplified by using soft interactions, and it is reasonable to obtain such interactions using a unitary transformation. A consistent application of this idea involves transforming the Hamiltonian and all other operators, especially including the currents that account for interactions with external probes [63]. Such transformation are known to convert single-nucleon operators into multinucleon operators. The effect on long-range operators such as the radius or electromagnetic transition operators is small [62,63]. However, the effect on short-range or high-momentum observables is large [63].

To posit the soft interaction to be the fundamental bare interaction is to deny the reality of high-momentum-transfer processes. Therefore, the fundamental bare interaction must allow high-momentum-transfer processes.

In particular, consider that two-body densities in coordinate space have a correlation "hole" near $r = 0$. By transforming only the Hamiltonian and not the two-body density, these correlation holes disappear [63]. Similarly, these Hamiltonian-only transformations dramatically reduce the high-momentum part of the momentum density.

As an example, consider coherent neutrino-nuclear interactions [64–66]. The neutrino interacts weakly and the cross section is proportional to the square of the elastic nuclear form factor. Following Ref. [66] we note that the neutrino-nucleus elastic-scattering cross section $d\sigma/d\Omega$ is [67,68]

$$\frac{d\sigma}{d\Omega} = \frac{G^2}{16\pi^2} k^2 (1 + \cos\theta) F^2(Q^2) \tag{A1}$$

for a neutrino of energy k scattering at angle θ, and G is the Fermi coupling constant. The ground-state elastic form factor $F(Q^2)$ at momentum transfer Q, $Q^2 = 2k^2(1 - \cos\theta)$, is the matrix element of the single-nucleon operator $e^{i\mathbf{q}\cdot\mathbf{r}_i}$, for a nucleon i weighted by the weak charge of the proton or neutron. One could ideally contemplate probing the high-momentum components of nuclear wave functions by using neutrino-nuclear interactions. Now imagine that one wished to describe the nuclear wave function by using soft interactions. The necessary unitary transformation would transform the simple single-nucleon operator $e^{i\mathbf{q}\cdot\mathbf{r}_i}$ into a complicated multibody operator, which would ruin the simplicity of using the neutrino as a probe.

If one wishes to use simple probes to investigate high-momentum aspects of nucleon structure, it is necessary to start with a theory involving bare interactions, which are necessarily hard interactions.

[1] S. Tan, Ann. Phys. (NY) **323**, 2952 (2008).
[2] S. Tan, Ann. Phys. (NY) **323**, 2971 (2008).
[3] S. Tan, Ann. Phys. (NY) **323**, 2987 (2008).
[4] E. Braaten, in *The BCS-BEC Crossover and the Unitary Fermi Gas*, edited by W. Zwerger (Springer, Berlin, 2012).
[5] J. T. Stewart, J. P. Gaebler, T. E. Drake, and D. S. Jin, Phys. Rev. Lett. **104**, 235301 (2010).
[6] E. D. Kuhnle, H. Hu, X.-J. Liu, P. Dyke, M. Mark, P. D. Drummond, P. Hannaford, and C. J. Vale, Phys. Rev. Lett. **105**, 070402 (2010).
[7] G. B. Partridge, K. E. Strecker, R. I. Kamar, M. W. Jack, and R. G. Hulet, Phys. Rev. Lett. **95**, 020404 (2005).
[8] F. Werner, L. Tarruell, and Y. Castin, Eur. Phys. J. B **68**, 401 (2009).
[9] A. Schirotzek, Ph.D. thesis, Massachusetts Institute of Technology, 2010 (unpublished).
[10] Y. Sagi, T. E. Drake, R. Paudel, and D. S. Jin, Phys. Rev. Lett. **109**, 220402 (2012).
[11] S. Gandolfi, K. E. Schmidt, and J. Carlson, Phys. Rev. A **83**, 041601 (2011).
[12] S. Hoinka, M. Lingham, K. Fenech, H. Hu, C. J. Vale, J. E. Drut, and S. Gandolfi, Phys. Rev. Lett. **110**, 055305 (2013).
[13] R. Amado and R. Woloshyn, Phys. Lett. B **62**, 253 (1976).
[14] R. Sartor and C. Mahaux, Phys. Rev. C **21**, 1546 (1980).
[15] R. Sartor and C. Mahaux, Phys. Rev. C **25**, 677 (1982).
[16] F. Mazzanti, A. Polls, J. Boronat, and J. Casulleras, Phys. Rev. Lett. **92**, 085301 (2004).
[17] J. Carlson, S. Gandolfi, and A. Gezerlis, Prog. Theor. Exp. Phys. (2012) 01A209.
[18] C. Ozen and N. T. Zinner, Eur. Phys. J. D **68**, 225 (2014).
[19] N. T. Zinner and A. S. Jensen, J. Phys.: Conf. Ser. **111**, 012016 (2008).
[20] N. T. Zinner and A. S. Jensen, J. Phys. G **40**, 053101 (2013).
[21] R. Weiss, B. Bazak, and N. Barnea, Phys. Rev. Lett. **114**, 012501 (2015).
[22] E. J. Moniz, I. Sick, R. R. Whitney, J. R. Ficenec, R. D. Kephart, and W. P. Trower, Phys. Rev. Lett. **26**, 445 (1971).
[23] H. Bethe, Annu. Rev. Nucl. Sci. **21**, 93 (1971).
[24] L. L. Frankfurt and M. I. Strikman, Phys. Rep. **76**, 215 (1981).
[25] CLAS Collaboration, K. Egiyan *et al.*, Phys. Rev. C **68**, 014313 (2003).
[26] CLAS Collaboration, K. Egiyan *et al.*, Phys. Rev. Lett. **96**, 082501 (2006).
[27] L. L. Frankfurt, M. I. Strikman, D. B. Day, and M. Sargsyan, Phys. Rev. C **48**, 2451 (1993).
[28] N. Fomin *et al.*, Phys. Rev. Lett. **108**, 092502 (2012).
[29] E. Piasetzky, M. Sargsian, L. Frankfurt, M. Strikman, and J. W. Watson, Phys. Rev. Lett. **97**, 162504 (2006).
[30] R. Subedi *et al.*, Science **320**, 1476 (2008).
[31] I. Korover, N. Muangma, O. Hen *et al.*, Phys. Rev. Lett. **113**, 022501 (2014).
[32] CLAS Collaboration, O. Hen *et al.*, Science **346**, 614 (2014).
[33] M. M. Sargsian, T. V. Abrahamyan, M. I. Strikman, and L. L. Frankfurt, Phys. Rev. C **71**, 044615 (2005).
[34] R. Schiavilla, R. B. Wiringa, S. C. Pieper, and J. Carlson, Phys. Rev. Lett. **98**, 132501 (2007).
[35] R. B. Wiringa, R. Schiavilla, S. C. Pieper, and J. Carlson, Phys. Rev. C **89**, 024305 (2014).
[36] A. de Shalit and H. Feshbach, *Theoretical Nuclear Physics, Volume I: Nuclear Structure* (John Wiley & Sons, Inc., New York, 1974).
[37] J. Arrington, D. Higinbotham, G. Rosner, and M. Sargsian, Prog. Part. Nucl. Phys. **67**, 898 (2012).
[38] V. G. J. Stoks, R. A. M. Klomp, C. P. F. Terheggen, and J. J. de Swart, Phys. Rev. C **49**, 2950 (1994).
[39] R. B. Wiringa, V. G. J. Stoks, and R. Schiavilla, Phys. Rev. C **51**, 38 (1995).
[40] R. Machleidt, Phys. Rev. C **63**, 024001 (2001).
[41] F. Gross and A. Stadler, Few-Body Syst. **44**, 295 (2008).
[42] F. Gross, J. W. Van Orden, and K. Holinde, Phys. Rev. C **45**, 2094 (1992).
[43] R. Machleidt and D. Entem, Phys. Rep. **503**, 1 (2011).
[44] D. R. Entem, N. Kaiser, R. Machleidt, and Y. Nosyk, Phys. Rev. C **91**, 014002 (2015).
[45] D. R. Entem, N. Kaiser, R. Machleidt, and Y. Nosyk, arXiv:1505.03562.
[46] Hall A Collaboration, W. Boeglin *et al.*, Phys. Rev. Lett. **107**, 262501 (2011).
[47] Jan Ryckebusch *et al.*, J. Phys. G: Nucl. Part. Phys. **42**, 055104 (2015).
[48] A. Rios, A. Polls, and W. H. Dickhoff, Phys. Rev. C **79**, 064308 (2009).
[49] A. Rios, A. Polls, and W. H. Dickhoff, Phys. Rev. C **89**, 044303 (2014).
[50] C. Colle, O. Hen, W. Cosyn, I. Korover, E. Piasetzky, J. Ryckebusch, and L. B. Weinstein, Phys. Rev. C **92**, 024604 (2015).
[51] J. Ryckebusch (private communication).
[52] L. Koester and W. Nistler, Z. Phys. A **272**, 189 (1975).
[53] R. Haussmann, M. Punk, and W. Zwerger, Phys. Rev. A **80**, 063612 (2009).
[54] M. Vanhalst, J. Ryckebusch, and W. Cosyn, Phys. Rev. C **86**, 044619 (2012).
[55] H. Georgi and H. D. Politzer, Phys. Rev. Lett. **36**, 1281 (1976).
[56] H. Hu, X.-J. Liu, and P. D. Drummond, New J. Phys. **13**, 035007 (2011).
[57] S. Bogner, T. Kuo, and A. Schwenk, Phys. Rep. **386**, 1 (2003).
[58] H. Feldmeier, T. Neff, R. Roth, and J. Schnack, Nucl. Phys. A **632**, 61 (1998).
[59] R. Roth, T. Neff, and H. Feldmeier, Prog. Part. Nucl. Phys. **65**, 50 (2010).
[60] S. K. Bogner, R. J. Furnstahl, and R. J. Perry, Phys. Rev. C **75**, 061001 (2007).
[61] S. Bogner, R. Furnstahl, and A. Schwenk, Prog. Part. Nucl. Phys. **65**, 94 (2010).
[62] K. A. Wendt, R. J. Furnstahl, and R. J. Perry, Phys. Rev. C **83**, 034005 (2011).
[63] T. Neff, H. Feldmeier, and W. Horiuchi, Phys. Rev. C **92**, 024003 (2015).
[64] K. Scholberg, Phys. Rev. D **73**, 033005 (2006).
[65] D. Akimov *et al.*, arXiv:1310.0125.
[66] C. J. Horowitz, K. J. Coakley, and D. N. McKinsey, Phys. Rev. D **68**, 023005 (2003).
[67] D. Z. Freedman, D. N. Schramm, and D. L. Tubbs, Annu. Rev. Nucl. Sci. **27**, 167 (1977).
[68] A. Drukier and L. Stodolsky, Phys. Rev. D **30**, 2295 (1984).

5. Summary and Conclusions

From atomic nuclei to neutron stars, nuclear systems lay at the heart of our universe. The strong, non-perturbative nature of nuclear interactions makes the theoretical description of many-body nuclear systems a challenge. Effective nuclear models successfully describe many bulk properties of nuclear systems; however, full understanding of nuclear dynamics requires a detailed description of the short-range structure of nuclei. As of today, the latter still represents a considerable challenge for both experimental and theoretical research.

Recent measurements of 2N-SRC pairs in ^{4}He and ^{12}C showed that high-momentum nucleons in nuclei are predominantly due to 2N-SRC pairs [33-37]. These pairs are predominantly np- rather than pp- or nn-SRC pairs [36,37]. This np-SRC pair dominance indicates the important role played by the tensor part of the nucleon-nucleon interaction at short distances [38-40]. Based on these results the possible effect of SRC pairs on heavier nuclear systems such as neutron stars was examined [41,42]. However, due to the possible existence of odd-l pairs in heavy nuclear systems, whether np-SRC pairs would dominate in these systems was not clear.

The first part of this work (chapters 2 and 3) extends previous exclusive studies of 2N-SRC pairs to heavy atomic nuclei. This was done by measuring one- and two-nucleon knockout processes, A(e,e'p) and A(e,e'pp), off ^{12}C, ^{27}Al, ^{56}Fe, and ^{208}Pb, in kinematics dominated by scattering off 2N-SRC pairs ($x_B > 1.2$, large-Q^2, $|P_{miss}| > 300$ MeV/c). The analysis includes identification and characterization of pp-SRC events in all measured nuclei, and extraction of single and double nucleon knockout cross-section ratios for nuclei relative to ^{12}C.

These measurements yielded:

1. **A first direct observation of pp-SRC pairs in nuclei heavier than ^{12}C using exclusive reactions.**
   The use of hard exclusive reactions is the most successful tool for studying the detailed structure of SRC pairs in nuclei [34,44]. These studies allow extracting the detailed c.m. motion of the pairs, their isospin structure and more [34-37]. Previous studies of exclusive reactions focused on medium and light symmetric nuclei (^{12}C and ^{4}He) where, in the measured kinematics, the effects of FSI are thought to be under control [35,45]. Extending these measurements to heavy nuclei is highly desirable as they allow the exploration of the role played by SRC in a true many-body, asymmetric, nuclear environment. By observing for the first time pp-SRC pairs in heavy nuclei, and comparing their characteristics to medium nuclei (^{12}C), we showed experimentally the validity of hard exclusive measurements in resolving the detailed short-range structure of heavy nuclei.

2. **Extraction of the ratio of np- to pp-SRC pairs in heavy nuclei.**
   The relative number of np- to pp-SRC pairs in the measured nuclei was extracted using the single-to-double nucleon knockout cross-section ratios for different nuclei relative to ^{12}C. The extracted np/pp ratios showed, for the first time, the persistence of np-SRC pair dominance in heavy asymmetric atomic nuclei.
   This observation also indicates a new *universal* feature of two-component Fermi systems with a short-range interaction that is strong between different fermions and weak between fermions of the same type: the probability of finding a high-momentum fermion is higher for the minority species (protons) than the majority species (neutrons). This indicates that SRC can potentially invert the energy sharing between protons and neutrons in heavy nuclei, giving the protons a larger average kinetic energy [46].
3. **Extraction of nuclear transparency ratios for proton knockout from the hard breakup of 2N-SRC pairs.**
   Previous transparency measurements focused on quasielastic proton knockout from the mean-field protons in the nucleus (i.e. $x_B \approx 1$, high-Q^2, low-P_{miss} kinematics) [47-49]. Compared to Glauber calculations, these measurements showed a Q^2 independent, ~20% deviation for heavy nuclei [50]. Theoretical analysis indicated that the observed deviation can be explained by over-correction for missing mean-field strength due to 2N-SRC contamination in the previous measurements [51]. The transparency extraction reported in this work was done in different kinematics (large-x_B, large-Q^2 high-P_{miss} kinematics), where one focuses on SRC pairs instead of correcting for them. This new method allows one to perform a largely theory-independent analysis. The resulting transparency ratios agreed with Glauber calculations, supporting the proposed 'over-correction' explanation for the observed deviation of the mean-field measurements from the Glauber calculations.

The second part of this work (chapter 4) uses the experimental results reported in chapter 3 to perform a phenomenological study of SRC effects (specifically np-SRC dominance) on a variety of systems:

1. **Deep-Inelastic scattering off bound nucleons.**
   Measurements of the per-nucleon DIS cross-section ratio for nuclei relative to deuterium were first reported by the EMC collaboration in the early 80s [52]. Contrary to expectations, the observed x_B dependence of the measured per nucleon cross section ratio is different from unity over a wide range of x_B. This became known as the 'EMC Effect'. Comparing the EMC measurements with theoretical calculations showed large disagreement, especially for $0.3 < x_B < 0.7$ [53]. This indicated the possible

existence of unknown nuclear effects. While over 1000 theoretical papers have tried to explain the origin of the EMC effect, as of today there is still no widely accepted explanation. Considering all available experimental constraints, it seems very unlikely that the EMC effect could be explained without introducing modifications to the structure function of bound nucleons in nuclei. Detailed measurements of the EMC effect in a variety of nuclei show that the strength of the effect grows with A [54,55]. The strength is defined as the slope of the per nucleon cross-section ratio for $0.3 < x_B < 0.7$. Attempts to find a nuclear variable (binding energy / density etc.) for which this dependence is regular have been largely unsuccessful until now. Our observation that the magnitude of the EMC effect is linearly proportional to the number of 2N-SRC pairs over the entire periodic table (from ^{3}He to ^{197}Au) constitutes the first identification of such a variable. This is known as the EMC/SRC correlation and indicates that both the EMC effect and SRC might have the same common origin – high momentum nucleons in nuclei. Applying different theoretical corrections to the experimental data showed that the EMC/SRC correlation is robust, supporting the physical interpretation of this correlation. Inspired by the fact that the strong short-range interaction of SRC pairs implies that their structure does not depend on the detailed nuclear structure, we demonstrated that one can fully describe the EMC data for all measured nuclei using a theoretical model which includes global, nucleus independent, modification of SRC / mean-field nucleons.

2. **Free neutron structure and the large-x_B d/u ratio of the proton.**
   The partonic structure of the neutron is of vast interest for understanding SU(6) symmetry-breaking mechanisms in QCD [56]. Assuming isospin symmetry, the proton-to-neutron structure function ratio at high-x_B (where valence quarks dominate the structure function) is directly related to the d/u ratio of the proton [56]. Extracting the structure function of the neutron from DIS cross-section measurements requires a free neutron target. The short lifetime and neutral charge of the neutron makes this unpractical. To overcome this limitation, many analyses approximate the deuteron as a free proton plus neutron pair, and extract the neutron DIS cross-section by subtracting the proton DIS cross-section from that of the deuteron DIS [57]. One should note that more modern extractions also include a model-dependent correction for Fermi motion effects in the deuteron [58]. However, even after correcting for Fermi motion effects one cannot be sure that the deuteron does not have an EMC-like effect, referred to in this work as the IMC effect. By extrapolating the EMC-SRC correlation to the limit of no correlations ($a_2 \rightarrow 0$), we extracted the magnitude of the IMC effect, i.e. the slope of the DIS cross-section ratio for the deuteron relative to a free proton-neutron pair. Using

measured proton and deuteron DIS cross sections this allowed the extraction of the free neutron DIS cross-section and the ratio of the free proton-to-neutron DIS cross-section. Using the extracted, IMC corrected, proton-to-neutron DIS cross-section, we constrained theoretical models for the off-shell structure of nucleons bound in deuterium used in a global QCD analysis by the CTEQ-JLab collaboration. This allowed us to strengthen the constraint on the d/u ratio as x_B -> 1.

3. **Pairing mechanisms in nuclei and the quantum numbers of SRC nucleon pairs.**
   The underlying pairing mechanism that is responsible for the creation of 2N-SRC pairs is highly model-dependent and is currently not well understood. By examining the A-dependence of the a_2 scaling parameter (i.e. the total number of high-momentum nucleons in nuclei relative to deuterium) one can see that simple combinatorial considerations do not apply, showcasing the need for a much more selective mechanism. To gain further experimental insight into this process, we used the measured A(e,e'p) and A(e,e'pp) cross-sections ratios to extract the relative number of pp- and np-SRC pairs in nuclei relative to ^{12}C. The results indicate a very soft A-dependence for both the number of pp- and np-SRC pairs. Obtaining separately the scaling of the relative number of pp- and np-SRC pairs allows detailed comparison to theoretical calculations. One such comparison to the calculations of Ryckebusch et al. [59] is shown as part of this work. This model assumes that correlation operators acting on mean-field wave functions can describe the formation of 2N-SRC pairs. By restricting the action of the correlation operators to mean-field pairs with specific relative quantum numbers, one can obtain different predictions for the scaling of the number of np- and pp-SRC pairs in nuclei. The result of this comparison indicates that only when considering 2N pairs in a node-less relative S-state, could the soft A-dependence of the data be reproduced. This is a clear indication of the selectivity of the 2N-SRC pairing mechanism.
4. **The nuclear symmetry energy and neutron stars equation of state.**
   Understanding the equation of state of high-density asymmetric nuclear matter is crucial for describing many astrophysical phenomena, from core-collapse supernova to neutron stars mergers, gravitational wave emission, r-process nuclear synthesis, and more [60]. The nuclear symmetry energy, which describes the change in the energy of nuclear systems as a proton is replaced with a neutron, is one of the main unknowns in this equation of state [61]. Focusing on the kinetic part of this energy, previous works assumed a free Fermi gas model, which neglects correlations. Taking into account the observed np-SRC dominance, this work proposes a new Correlated Fermi Gas (CFG) model

which includes the effect of np-SRC pairs in the description of symmetric nuclear matter. We observed a negative kinetic symmetry energy, which is also supported by transport analysis of medium-energy heavy ion collisions. Combined with data from other terrestrial measurements, we observed a very soft density dependence for the potential symmetry energy. When the CFG model was incorporated into Bayesian analysis of neutron stars observables, this picture persisted, indicating that the inclusion of correlations softens the density dependence of the potential symmetry energy, but still allow neutron stars with mass that is greater than two times the solar mass.

5. **Contact interactions in strongly interacting Fermi systems.**
   Dilute two-component Fermi systems with a short-range interaction between the different components can be described using universal relations [62]. The short-range interaction creates different Fermion pairs with high relative momentum and low center-of-mass momentum, where high and low are relative to the Fermi momentum of the system. These pairs create a high-momentum tail to the one body momentum distribution that drops as C/k^4, where C is a scaling constant known as the 'Contact'. The contact measures the number of pairs and depends on the strength of the short-range interaction [62].
   While the extent to which one can describe atomic nuclei as 'dilute' Fermi system is unclear, our analysis of the high-momentum, np-SRC dominated tail of the nuclear momentum distribution shows similar behavior. By analyzing 10 different nucleon-nucleon interactions and using the experimentally extracted scaling of high-momentum tails in nuclear momentum distribution, we observe strong indications that C/k^4 scaling exists in nuclei. This is understood as a result of the second order effect of the tensor part of the nucleon-nucleon interaction. When comparing the momentum distribution of nuclear and atomic systems with the same dimensionless interaction strength, the same value of C is observed. This result is fascinating and surprising as the atomic and nuclear systems are dominated by very different interactions and differ by over 20 orders of magnitude in density.

The experimental results and phenomenological analyses detailed above lay the groundwork for the development of an experimental program that will study energy sharing in imbalanced nuclear systems and the dependence of bound nucleon structure functions on virtuality (see appendix-B for details). This program currently consists of three approved experiments that should run in the next few years at Jefferson Lab.

References

[1] E. Rutherford, Philosophical Magazine **12**, 134 (1907).

[2] H. Geiger, Proc. Roy. Soc. July 17 (1908).

[3] H. Geiger and E. Marsden, Proc. Roy. Soc. A **82**, 495 (1909).

[4] H. Geiger, Proc. Roy. Soc. **83**, 492 (1910).

[5] J. Chadwick, Nature **192**, 312 (1932).

[6] R.B. Wiringa, R. Schiavilla, S.C. Pieper, and J. Carlson, Phys. Rev. C **89**, 024305 (2014).

[7] A. Rios, A. Polls, and W. H. Dickhoff, Phys. Rev. C 79, 064308 (2009),

[8] A. Rios, A. Polls, and W. H. Dickhoff, Phys. Rev. C 89, 044303 (2014).

[9] E. J. Moniz, Phys. Rev. **184**, 1154 (1969).

[10] E. J. Moniz et al., Phys. Rev. Lett. **26**, 445 (1971).

[11] M.G. Mayer, Physical Review **75**, 1969 (1949).

[12] O. Haxel, J.H.D. Jensen, H.E. Suess, Physical Review **75**, 1766 (1949).

[13] D.R. Entem, R. Machleidt, Phys. Rev. C **68**, 041001(R) (2003).

[14] R. Machleidt, D.R. Entem, Phys. Rep. **503**, 1(2011).

[15] E. Epelbaum, W. Glöckle, U.-G. Meissner, Nucl. Phys. A **747** (2012).

[16] E. Epelbaum, H.-W. Hammer, U.-G. Meißner, Rev. Mod. Phys. **81**, 1773 (2009).

[17] S. Frullani, and J. Mougey, Adv. Nucl. Phys. 14, 1-283 (1984).

[18] L. Lapikas, Nucl. Phys. A **553**, 297 (1993).

[19] V. G. J. Stoks, R. A. M. Klomp, C. P. F. Terheggen, and J. J. de Swart, Phys. Rev. C 49, 2950 (1994).

[20] F. Gross and A. Stadler, Few-Body Systems **44**, 295 (2008), ISSN 0177-7963.

[21] F. Gross, J. W. Van Orden, and K. Holinde, Phys. Rev. C **45**, 2094 (1992).

[22] R. Machleidt and D. Entem, Physics Reports **503**, 1 (2011), ISSN 0370-1573.

[23] S.K. Bogner, R.J. Furnstahl, and A. Schwenk, Prog. Part. Nucl. Phys. **65**, 94 (2010).

[24] R.J. Furnstahl and K. Ebeler, Rep. Prog. Phys. **76**, 126301 (2013).

[25] K. Wendt, R.J. Furnsthal, and S. Ramanan, Phys. Rev. C **86**, 014003 (2003).

[26] R.V. Reid, Ann. Phys. N.Y. **50**, 411 (1968).

[27] R. Machleidt, Adv. Nucl. Phys. **19**, 189 (1989).

[28] R. Machleidt, Phys. Rev. C **63**, 024001 (2001).

[29] R.B. Wiringa, V.G.J. Stoks, and R. Schiavilla, Phys. Rev. C **51**, 38 (1955).

[30] K.S. Egiyan et al. (CLAS Collaboration), Phys. Rev. C 68, 014313 (2003).

[31] K.S. Egiyan et al. (CLAS Collaboration), Phys. Rev. Lett. **96**, 082501 (2006).

[32] N. Fomin et al., Phys. Rev. Lett. **108**, 092502 (2012).

[33] A. Tang, J.W. Watson, J.L.S. Aclander, J. Alster, and G. Asryan, et al., Phys. Rev. Lett. **90**, 042301 (2003).

[34] E. Piasetzky, M. Sargsian, L. Frankfurt, M. Strikman, and J.W. Watson, Phys. Rev. Lett. **97**, 162504 (2006).

[35] R. Shneor et al., Phys. Rev. Lett. **99**, 072501 (2007).

[36] R. Subedi et al., Science **320**, 1476 (2008).
[37] I. Korover et al., Phys. Rev. Lett. **113**, 022501 (2014).
[38] R. Schiavilla et al., Phys. Rev. Lett. **98**, 132501 (2007).
[39] M. Sargsian et al., Phys. Rev. C **71**, 044615 (2005).
[40] M. Alvioli, C. Ciofi and H. Morita, Phys. Rev. Lett. **100**, 162503 (2008).
[41] L. Frankfurt, M. Sargsian, and M. Strikman, Int. J. Mod. Phys. A 23, 2991 (2008).
[42] C. Xu, A. Li, B.A. Li, J. of Phys: Conference Series **420**, 012190 (2013)
B.A. Li, L.W. Chen and C. M. Ko, Phys. Rep. **464**, 113 (2008).
[43] L.B. Weinstein, S.E. Kuhn, "Short distance structure of nuclei: Mining the wealth of existing Jefferson lab data", DOE Grant DE-SC0006801.
[44] J. Arrington, D. W. Higinbotham, G. Rosner, and M. Sargsian, Prog. Part. Nucl. Phys. **67**, 898 (2012).
[45] L. L. Frankfurt, M. M. Sargsian, and M. I. Strikman, Phys. Rev. C **56**, 1124 (1997).
M. M. Sargsian, Int. J. Mod. Phys. E **10**, 405 (2001).
[46] M. Sargsian, Phys. Rev. C **89**, 034305 (2014).
[47] T.G. O'Neill et al., Phys. Lett. B **351**, 87 (1995).
[48] G. Garino et al., Phys. Rev. C **45**, 780 (1992).
[49] D. Abbott, et al., Phys. Rev. Lett. **80**, 5072 (1998).
K. Garrow, et al., Phys. Rev. C **66**, 044613 (2002).
[50] D. Dutta, K. Hafidi, and M. Strikman, Prog. Part. Nucl. Phys. **69**, 1 (2013).
[51] L.L. Frankfurt, M.I. Strikman, and M. Zhalov, Phys. Lett. B **503**, 73 (2001).
[52] J. Aubert et al., Phys. Lett. B **123**, 275 (1983).
[53] P. R. Norton, Rep. Prog. Phys. **66**, 1253 (2003).
D. Geesaman, K. Saito, and A. Thomas, Annu. Rev. Nucl. Part. Sci. **45**, 337 (1995).
[54] J. Gomez et al., Phys. Rev. D **49**, 4348 (1994).
[55] J. Seely et al., Phys. Rev. Lett. **103**, 202301 (2009).
[56] W. Melnitchouk and A. W. Thomas, Phys. Lett. B **377**, 11 (1996).
R. J. Holt and C. D. Roberts, Rev. Mod. Phys. **82**, 2991 (2010).
[57] A. Accardi et al., Phys. Rev. D **84**, 014008 (2011).
[58] J. Arrington, F. Coester, R. Holt, and T.-S. H. Lee, J. Phys. G **36**, 025005 (2009).
[59] J. Ryckebusch, M. Vanhalst, and W. Cosyn, J. Phys. G **42**, 055104 (2015).
[60] J. M. Lattimer and Y. Lim, Astro. Phys. J **771**, 51 (2013).
[61] M. Prakash, T. L. Ainsworth, and J. M. Lattimer, Phys. Rev. Lett. 61, 2518 (1988).
[62] S. Tan, Annals of Physics 323, 2952 (2008).
S. Tan, Annals of Physics 323, 2971 (2008).
S. Tan, Annals of Physics 323, 2987 (2008).
E. Braaten, Lect. Notes Phys. 836, 193 (2012).
[63] O. Hen et al., JLab Experiment E14-011: "Proton and Neutron Momentum

Distributions in A=3 Asymmetric Nuclei", arXiv: 1410.4451 (2014).
[64] O. Hen et al., JLab Experiment E11-003A: "In Medium Proton Structure functions, SRC, and the EMC effec" (2015).
[65] O. Hen et al., JLab Experiment E11-107: "In Medium Nucleon Structure functions, SRC, and the EMC effec", arXiv: 1409.1717 (2011).
[66] W. U. Boeglin et al., Phys. Rev. Lett. **107**, 262501 (2011).
[67] W. Melnitchouk, M. Sargsian, and M.I. Strikman, Z. Phys. A **359**, 99 (1997).

Appendix-A: New EMC Data Base

O. Hen et al., Int. J. Mod. Phys. E ***22****, 1330017 (2013) – Appendix.*

Appendix A. EMC Data Base

In this appendix, we present a new data-base for the structure function ratio of nuclei (F_2^A) relative to deuterium (F_2^d). The ratio is taken using F_2^A and F_2^d each extracted in its own reference frame, at equivalent kinematical regions, defined by x_A and Q^2. The extraction of the structure function follows the formalism of Sec. 2.3, and is shown only for the range of $0.3 \leq x_A \leq 0.7$.

We use JLab and SLAC high precision data on DIS cross-section ratios for nuclei relative to deuterium as input to Eq. (9).[8,12] We use a parametrization of $F_2^d(x, Q^2)$ from Ref. 44 to move the deuteron measurement to x_A, and reapply isoscalar corrections using a parametrization of $R_{np}(x_A, Q^2) = F_2^n(x_A, Q^2)/F_2^p(x_A, Q^2)$ from Ref. 46. The results are presented in Tables A.1–A.8 are for the SLAC data and Tables A.9–A.12 are for the JLab data. Note that the SLAC results are averaged over $Q^2 = 2$, 5 and 10 GeV/c^2.

Table A.1. EMC data for ^{4}He from SLAC. The left side of the table shows the original as published data from Table VIII of Ref. 8. The right side is the same data, corrected for the definition of x_A according to Eq. (9).

x	$F_2^{^4\mathrm{He}}/F_2^d(x)$	$\Delta F_2^{^4\mathrm{He}}/F_2^d(x)$	x_A	$F_2^{^4\mathrm{He}}/F_2^d(x_A)$	$\Delta F_2^{^4\mathrm{He}}/F_2^d(x_A)$
0.36	0.998	0.021	0.362	1.005	0.021
0.40	0.968	0.017	0.402	0.976	0.017
0.44	0.949	0.019	0.443	0.958	0.019
0.48	0.954	0.017	0.483	0.963	0.017
0.52	0.951	0.017	0.523	0.969	0.017
0.56	0.943	0.017	0.563	0.958	0.017
0.60	0.928	0.017	0.604	0.949	0.017
0.64	0.935	0.018	0.644	0.961	0.018
0.68	0.917	0.020	0.684	0.936	0.020

Table A.2. Same as Table A.1, for ^{9}Be.

x	$F_2^{^9\mathrm{Be}}/F_2^d(x)$	$\Delta F_2^{^9\mathrm{Be}}/F_2^d(x)$	x_A	$F_2^{^9\mathrm{Be}}/F_2^d(x_A)$	$\Delta F_2^{^9\mathrm{Be}}/F_2^d(x_A)$
0.36	0.993	0.014	0.362	1.007	0.014
0.40	0.957	0.009	0.402	0.972	0.009
0.44	0.980	0.014	0.443	0.997	0.014
0.48	0.951	0.011	0.483	0.968	0.011
0.52	0.955	0.011	0.523	0.979	0.011
0.56	0.945	0.011	0.563	0.967	0.011
0.60	0.928	0.010	0.604	0.955	0.010
0.64	0.917	0.011	0.644	0.947	0.011
0.68	0.912	0.013	0.684	0.935	0.013

Table A.3. Same as Table A.1, for ^{12}C.

x	$F_2^{^{12}\mathrm{C}}/F_2^d(x)$	$\Delta F_2^{^{12}\mathrm{C}}/F_2^d(x)$	x_A	$F_2^{^{12}\mathrm{C}}/F_2^d(x_A)$	$\Delta F_2^{^{12}\mathrm{C}}/F_2^d(x_A)$
0.36	0.987	0.017	0.362	0.995	0.017
0.40	0.974	0.011	0.403	0.983	0.011
0.44	0.975	0.018	0.443	0.986	0.018
0.48	0.953	0.014	0.483	0.963	0.014
0.52	0.926	0.012	0.523	0.945	0.012
0.56	0.924	0.010	0.564	0.940	0.010
0.60	0.905	0.009	0.604	0.928	0.009
0.64	0.903	0.010	0.644	0.930	0.010
0.68	0.888	0.012	0.685	0.909	0.012

Table A.4. Same as Table A.1, for ^{27}Al.

x	$F_2^{^{27}\mathrm{Al}}/F_2^d(x)$	$\Delta F_2^{^{27}\mathrm{Al}}/F_2^d(x)$	x_A	$F_2^{^{27}\mathrm{Al}}/F_2^d(x_A)$	$\Delta F_2^{^{27}\mathrm{Al}}/F_2^d(x_A)$
0.36	0.993	0.013	0.362	1.005	0.013
0.40	0.966	0.009	0.403	0.977	0.009
0.44	0.959	0.012	0.443	0.973	0.012
0.48	0.934	0.010	0.483	0.948	0.010
0.52	0.926	0.010	0.524	0.950	0.010
0.56	0.923	0.009	0.564	0.944	0.009
0.60	0.906	0.009	0.604	0.934	0.009
0.64	0.892	0.009	0.645	0.923	0.009
0.68	0.876	0.011	0.685	0.900	0.011

Table A.5. Same as Table A.1, for ^{40}Ca.

x	$F_2^{^{40}\mathrm{Ca}}/F_2^d(x)$	$\Delta F_2^{^{40}\mathrm{Ca}}/F_2^d(x)$	x_A	$F_2^{^{40}\mathrm{Ca}}/F_2^d(x_A)$	$\Delta F_2^{^{40}\mathrm{Ca}}/F_2^d(x_A)$
0.36	1.004	0.021	0.363	1.013	0.021
0.40	0.966	0.012	0.403	0.975	0.012
0.44	0.960	0.019	0.443	0.972	0.019
0.48	0.954	0.014	0.484	0.966	0.014
0.52	0.912	0.013	0.524	0.934	0.013
0.56	0.915	0.012	0.564	0.933	0.012
0.60	0.904	0.011	0.605	0.930	0.011
0.64	0.895	0.012	0.645	0.925	0.012
0.68	0.870	0.015	0.685	0.893	0.015

Table A.6. Same as Table A.1, for ^{56}Fe.

x	$F_2^{^{56}\mathrm{Fe}}/F_2^d(x)$	$\Delta F_2^{^{56}\mathrm{Fe}}/F_2^d(x)$	x_A	$F_2^{^{56}\mathrm{Fe}}/F_2^d(x_A)$	$\Delta F_2^{^{56}\mathrm{Fe}}/F_2^d(x_A)$
0.36	0.972	0.012	0.363	0.986	0.012
0.40	0.955	0.009	0.403	0.970	0.009
0.44	0.940	0.012	0.443	0.957	0.012
0.48	0.917	0.009	0.484	0.934	0.009
0.52	0.904	0.009	0.524	0.931	0.009
0.56	0.893	0.009	0.564	0.916	0.009
0.60	0.869	0.008	0.605	0.899	0.008
0.64	0.860	0.009	0.645	0.894	0.009
0.68	0.852	0.010	0.685	0.879	0.010

Table A.7. Same as Table A.1, for ^{108}Ag.

x	$F_2^{^{108}\mathrm{Ag}}/F_2^d(x)$	$\Delta F_2^{^{108}\mathrm{Ag}}/F_2^d(x)$	x_A	$F_2^{^{108}\mathrm{Ag}}/F_2^d(x_A)$	$\Delta F_2^{^{108}\mathrm{Ag}}/F_2^d(x_A)$
0.36	1.012	0.023	0.363	1.031	0.023
0.40	0.968	0.013	0.403	0.988	0.013
0.44	0.957	0.021	0.443	0.979	0.021
0.48	0.926	0.015	0.484	0.948	0.015
0.52	0.897	0.014	0.524	0.928	0.014
0.56	0.891	0.013	0.564	0.918	0.013
0.60	0.881	0.012	0.605	0.915	0.012
0.64	0.842	0.013	0.645	0.878	0.013
0.68	0.842	0.016	0.685	0.871	0.016

Table A.8. Same as Table A.1, for ^{197}Au.

x	$F_2^{^{197}\mathrm{Au}}/F_2^d(x)$	$\Delta F_2^{^{197}\mathrm{Au}}/F_2^d(x)$	x_A	$F_2^{^{197}\mathrm{Au}}/F_2^d(x_A)$	$\Delta F_2^{^{197}\mathrm{Au}}/F_2^d(x_A)$
0.36	0.956	0.014	0.362	0.979	0.014
0.40	0.930	0.010	0.403	0.953	0.010
0.44	0.931	0.014	0.443	0.957	0.014
0.48	0.914	0.011	0.483	0.939	0.011
0.52	0.892	0.011	0.524	0.926	0.011
0.56	0.881	0.011	0.564	0.911	0.011
0.60	0.837	0.010	0.604	0.871	0.010
0.64	0.846	0.011	0.644	0.884	0.011
0.68	0.829	0.013	0.685	0.859	0.013

Table A.9. EMC data for ^{3}He from JLab. The left side of the table shows the original as published data from Ref. 12. The right side is the same data, corrected for the definition of x_A according to Eq. (9).

x	$F_2^{^3\mathrm{He}}/F_2^d(x)$	$\Delta F_2^{^3\mathrm{He}}/F_2^d(x)$	x_A	$F_2^{^3\mathrm{He}}/F_2^d(x_A)$	$\Delta F_2^{^3\mathrm{He}}/F_2^d(x_A)$
0.325	0.9774	0.011453	0.325	0.970073	0.0113672
0.350	0.9763	0.0113158	0.350	0.968431	0.0112246
0.375	0.9796	0.0113219	0.375	0.971228	0.0112251
0.400	0.9684	0.0107239	0.400	0.959746	0.0106281
0.425	0.9725	0.0114144	0.425	0.963504	0.0113089
0.450	0.9713	0.0112523	0.450	0.961924	0.0111437
0.475	0.9696	0.0108533	0.476	0.960588	0.0107524
0.500	0.9629	0.0114935	0.501	0.95354	0.0113818
0.525	0.9599	0.0112036	0.526	0.949848	0.0110863
0.550	0.964	0.0118444	0.551	0.955055	0.0117345
0.575	0.9653	0.0113391	0.576	0.955923	0.0112289
0.600	0.9644	0.0109817	0.601	0.954435	0.0108683
0.625	0.949	0.0118153	0.626	0.94051	0.0117096
0.650	0.9611	0.0115051	0.651	0.951985	0.0113959
0.675	0.9562	0.0116562	0.676	0.945647	0.0115276
0.700	0.9479	0.0125035	0.701	0.938561	0.0123803

Table A.10. Same as Table A.9, for ^{4}He.

x	$F_2^{^4\text{He}}/F_2^d(x)$	$\Delta F_2^{^4\text{He}}/F_2^d(x)$	x_A	$F_2^{^4\text{He}}/F_2^d(x_A)$	$\Delta F_2^{^4\text{He}}/F_2^d(x_A)$
0.325	1.011	0.0116698	0.327	1.01653	0.0117336
0.350	0.9998	0.0114398	0.352	1.00644	0.0115158
0.375	0.9996	0.0114471	0.377	1.00753	0.0115379
0.400	0.9784	0.0108174	0.402	0.987558	0.0109187
0.425	0.9727	0.0114294	0.427	0.983079	0.0115513
0.450	0.9724	0.0112776	0.453	0.98331	0.0114042
0.475	0.9688	0.0108597	0.478	0.983158	0.0110206
0.500	0.9695	0.0115953	0.503	0.984013	0.0117688
0.525	0.9613	0.0112505	0.528	0.975085	0.0114118
0.550	0.955	0.0117935	0.553	0.973823	0.0120259
0.575	0.9542	0.0112231	0.578	0.973198	0.0114466
0.600	0.9491	0.0107922	0.604	0.966896	0.0109946
0.625	0.9361	0.0115938	0.629	0.960513	0.0118962
0.650	0.9389	0.0111987	0.654	0.961687	0.0114705
0.675	0.9315	0.0113139	0.679	0.949143	0.0115282
0.700	0.9238	0.0121262	0.704	0.947597	0.0124385

Table A.11. Same as Table A.9, for ^{9}Be.

x	$F_2^{^9\text{Be}}/F_2^d(x)$	$\Delta F_2^{^9\text{Be}}/F_2^d(x)$	x_A	$F_2^{^9\text{Be}}/F_2^d(x_A)$	$\Delta F_2^{^9\text{Be}}/F_2^d(x_A)$
0.325	1.027	0.0134537	0.327	1.03628	0.0135753
0.350	1.018	0.0131816	0.352	1.02794	0.0133104
0.375	1.014	0.0130497	0.377	1.02575	0.0132009
0.400	0.9977	0.0124262	0.402	1.0112	0.0125944
0.425	0.9907	0.0127738	0.427	1.00495	0.0129575
0.450	0.9821	0.0124847	0.452	0.997484	0.0126803
0.475	0.9745	0.0120235	0.477	0.992554	0.0122463
0.500	0.9709	0.012429	0.503	0.989694	0.0126696
0.525	0.9567	0.0119992	0.528	0.974422	0.0122215
0.550	0.9538	0.0123411	0.553	0.976809	0.0126388
0.575	0.9469	0.0118303	0.578	0.969655	0.0121146
0.600	0.9403	0.0114402	0.603	0.961711	0.0117006
0.625	0.9459	0.0122301	0.628	0.974281	0.0125971
0.650	0.9322	0.0116412	0.653	0.958901	0.0119747
0.675	0.9269	0.0116589	0.679	0.948751	0.0119338
0.700	0.9201	0.0122438	0.704	0.947675	0.0126108

Table A.12. Same as Table A.9, for ^{12}C.

x	$F_2^{^{12}\mathrm{C}}/F_2^d(x)$	$\Delta F_2^{^{12}\mathrm{C}}/F_2^d(x)$	x_A	$F_2^{^{12}\mathrm{C}}/F_2^d(x_A)$	$\Delta F_2^{^{12}\mathrm{C}}/F_2^d(x_A)$
0.325	1.015	0.0123864	0.327	1.0211	0.0124609
0.350	1.011	0.0122230	0.352	1.01838	0.0123122
0.375	1.003	0.0120969	0.377	1.01175	0.0122024
0.400	0.9859	0.0115927	0.403	0.996045	0.011712
0.425	0.9798	0.0119255	0.428	0.991303	0.0120655
0.450	0.9743	0.0117119	0.453	0.986333	0.0118566
0.475	0.9617	0.0113265	0.478	0.977356	0.0115109
0.500	0.9553	0.0117368	0.503	0.971005	0.0119297
0.525	0.9485	0.0114379	0.528	0.963524	0.0116191
0.550	0.9401	0.0117128	0.554	0.960463	0.0119665
0.575	0.938	0.0113657	0.579	0.958495	0.0116141
0.600	0.9274	0.0110039	0.604	0.946495	0.0112305
0.625	0.9291	0.0119147	0.629	0.955914	0.0122586
0.650	0.9191	0.0113583	0.654	0.943392	0.0116585
0.675	0.9162	0.0114603	0.680	0.93512	0.011697
0.700	0.9107	0.0121902	0.705	0.936063	0.0125297

Appendix-B: 12 GeV Experiments at Jefferson Lab

The results described in this dissertation led us to propose three new experiments. These experiments were all reviewed by the Jefferson-Lab program advisory committee and approved for running as part of the 12 GeV program of JLab. This appendix describes the general concept of each experiment and the expected results. Full details are given in the proposals [63-65].

E14-011: "Proton and Neutron Momentum Distributions in A=3 Asymmetric Nuclei" (spokespersons: O. Hen, L. Weinstein, S. Gilad, and W. Boeglin)

This experiment will to utilize the planned ^{3}H target in Hall A of JLab to measure the quasielastic ^{3}H(e,e′p) and ^{3}He(e,e'p) reactions. The scattered electron and knockout proton will be detected using the two Hall A High Resolution Spectrometers (HRSs). The measurement will be done in large-Q^2 high-x_B kinematics that suppresses final state interactions (FSI) [66], covering a missing momentum range up to 450 MeV/c. It is scheduled to take take data in early 2017.

The measured data will be used to extract: (a) the proton momentum distributions of both ^{3}He and ^{3}H, which will help constrain detailed calculations of the A = 3 system, (b) the ratio of ^{3}He(e,e′p)/^{3}H(e, e′p) cross sections where the residual affect of FSI will mostly cancel, and (c) the average kinetic energy of protons in the two nuclei as a function of the maximum cutoff momentum.

In the simplest picture, one would expect that at low missing momentum the ^{3}He(e,e′p)/^{3}H(e, e′p) cross sections ratio would equal two (simple nucleon counting). At larger missing momentum ($300 \leq p_{miss} \leq 500$ MeV/c) this ratio should decrease to one, due to the dominance of short-range np-SRC pairs (and to the fact that there are two np pairs in both ^{3}He and ^{3}H). However, taking into account the full effect of np-SRC dominance, the fraction of high-momentum protons in ^{3}He should be smaller than that in ^{3}H, which should increase the low-P_{miss} ratio to above two. This measurement will confirm these values and will map out the transition region where the ratio changes from above two to one. Theoretical predictions for the measured quantities and the expected experimental accuracy are shown in Fig. B.1.

The importance of this measurement stems from the rare availability of a ^{3}H target and from the fact that the A = 3 system is the simplest system of mirror nuclei for which precise calculations of the (e,e′p) reaction exist. These data will offer a direct test of these calculations.

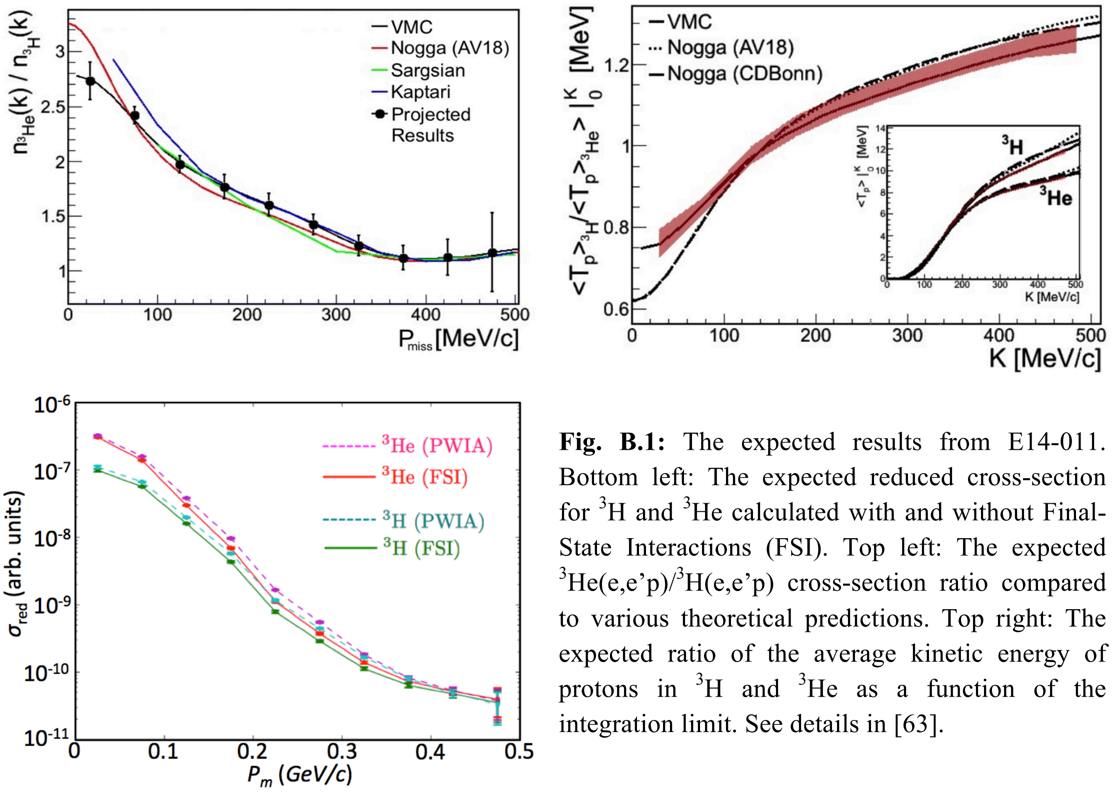

Fig. B.1: The expected results from E14-011. Bottom left: The expected reduced cross-section for ^{3}H and ^{3}He calculated with and without Final-State Interactions (FSI). Top left: The expected ^{3}He(e,e'p)/^{3}H(e,e'p) cross-section ratio compared to various theoretical predictions. Top right: The expected ratio of the average kinetic energy of protons in ^{3}H and ^{3}He as a function of the integration limit. See details in [63].

E11-107: "In Medium Neutron Structure functions, SRC, and the EMC effect" (spokespersons: O. Hen, L. Weinstein, S. Gilad, and S. Wood)

E11-003A: "In Medium Proton Structure functions, SRC, and the EMC effect" (spokespersons: O. Hen, L. Weinstein, E. Piasetzky, and H. Hakobyan)

These experiments will measure semi-inclusive deep inelastic scattering (DIS) off the deuteron by "tagging" the DIS scattering with high-momentum recoiling protons (E11-107) or neutrons (E11-003A) emitted at a large angle relative to the momentum transfer.

While the EMC effect has been observed many times, there is no generally accepted explanation of its origin. Many theoretical models predict that the EMC effect is due to the modification of the nucleon structure functions in the nuclear medium and that this modification increases with nucleon virtuality. In addition, the recently observed correlation between the strength of the EMC effect and the amount of 2N-SRC pairs in nuclei indicates that most of the EMC effect stems from DIS scattering on high-momentum (i.e., high-virtuality) nucleons in the nucleus. By measuring whether nucleon structure is modified in the nucleus and how this modification depends on nucleon virtuality, Experiments E11-107 and E11-003A will offer new insight to the origin of the EMC-SRC correlation.

The proposed measurement will focus on the simplest nuclear system available – the deuteron. In the deuteron one can use the d(e,e'N_S)X reaction to perform DIS on one nucleon, tagged by a backward-recoiling partner nucleon. In appropriate kinematics (large-W, large-Q^2 and large-recoil angles relative to the momentum transfer), allowed by the 12 GeV upgrade of JLab, the momentum of the recoil nucleon equals the initial momentum of the nucleon the electron scattered off. Therefore, the recoil tagging technique allows extracting the dependence of the DIS cross-section on the nucleon initial momentum / virtuality.

The proposed observable is the ratio of high x' to low x' DIS scattering from a tagged partner nucleon in deuterium divided by the same ratio for the untagged scattering. $x' = Q^2 / 2p_\mu q^\mu$ is the equivalent value of Bjorken-x for scattering off a moving nucleon. This ratio should be sensitive to the modification of the nucleon structure functions in the medium. At low x' ($0.25 < x' < 0.35$), any modification of in-medium nucleon structure functions should be small. At high x' ($0.5 < x' < 0.6$) much larger effects are expected. Fig. B.2 shows the expected accuracy in the bound-to-free structure function extraction as a function of the light cone momentum of the recoil nucleon. The results are compared to three different theoretical models.

E11-107 will run in Hall-C of Jefferson Lab, measuring the d(e,e'p_S)X reaction. The scattered electrons will be detected by the SHMS and HMS spectrometers, simultaneously covering the high and low ranges of x'. A new dedicated Large-Acceptance Detector (LAD) covering the backward lab angles from 85^o to 175^o will be used to detect the recoiling protons. LAD will be made of 40 plastic scintillators, placed 4 meters from the target offering 1 Sr coverage at the backward hemisphere, see Fig. B.3. In order to achieve the experimental goals at low cost, LAD will utilize the surplus time-of-flight (TOF) counters of the CLAS6 spectrometer that will not be used in the upgraded CLAS12 spectrometer. A dedicated scattering chamber with a large thin backward window will be constructed to allow the protons to reach the LAD.

E11-003A will run in Hall-B of JLab, measuring the d(e,e'n_S)X reaction. The electrons will be detected by CLAS12, covering a wide and continuous range of x'. A new dedicated Backward Angle Neutron Detector (BAND), covering the backward lab angles from 160^o to 170^o, will be used to detect the recoiling neutrons (Fig. B.4). BAND will be placed 3.5 meters from the target. It will be composed of four “rings” of plastic scintillators perpendicular to the beam line with an inner radius of 60 cm, outer radius of 120 cm, and a total thickness of 24 cm. The experiment will run during the CLAS12 deuteron run period (2018).

The combined data from both experiments will give new insight to medium modification mechanisms in nuclei, the EMC effect and its isospin dependence, and more.

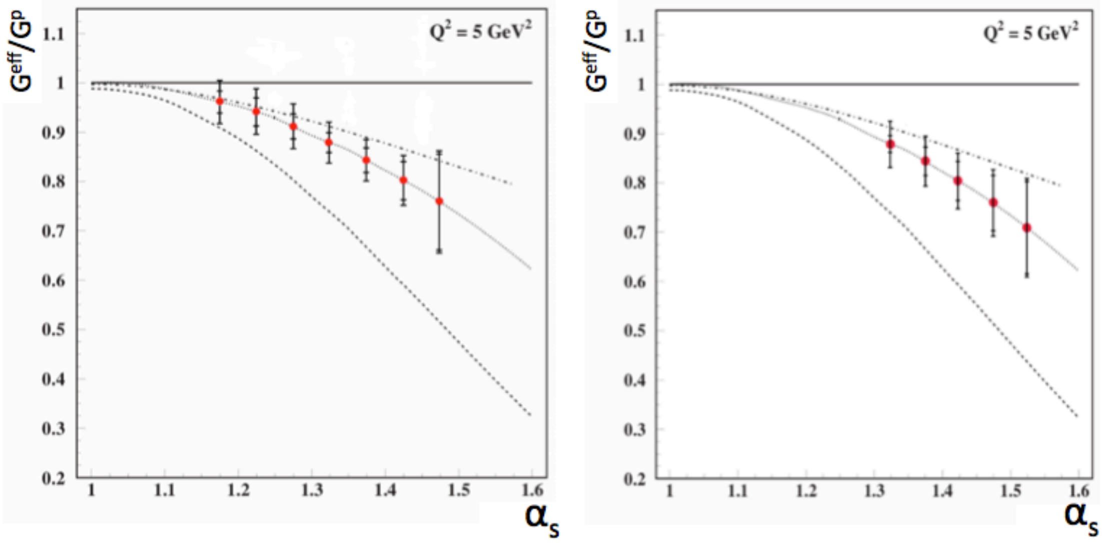

Fig. B.2: Expected sensitivity of the E11-107 (left) and E11-003A (right) experiments to the bound neutron (left) and proton (right) structure function modification $F^{eff}_{2p(n)} / F_{2p(n)}$ in deuterium as a function of α (the light cone momentum fraction). The simulated data points show the expected statistical (inner error bars) and total (outer error bars) uncertainties. The different lines show model calculations for: Point Like Configuration (PLC) suppression model (dashed line), rescaling model (dotted line), and binding/off-shell model (dot-dashed line) [67].

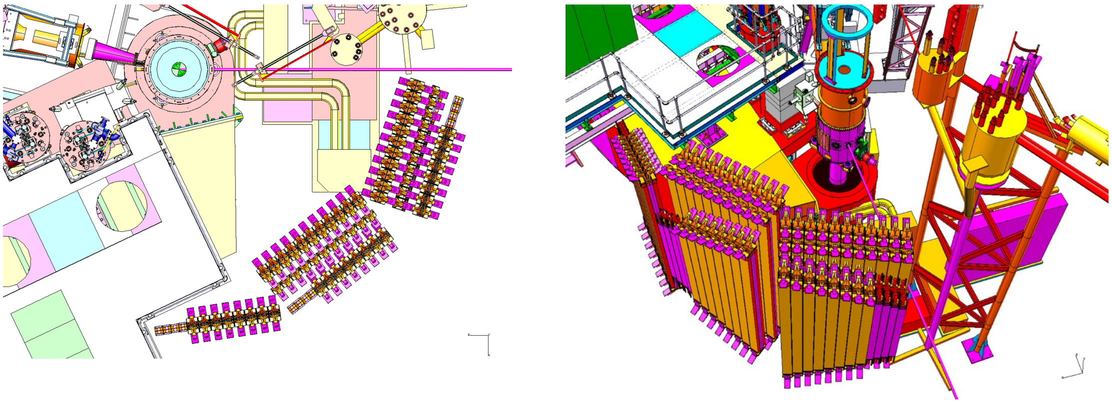

Fig. B.3: The proposed layout and structure of the LAD detector at Hall C of Jefferson lab. **Left:** Plan view of the layout. The incoming beam line is shown by the purple horizontal line. The scattering chamber is shown by the light blue circle in the middle toward the top of the figure. The HMS entrance is shown in the upper left and the SHMS structure is shown on the left side. There are three sectors of LAD in the lab, covering 85° – 175°. **Right:** A view from upstream. The panels of the LAD (on the lower left) are shown in yellow with magenta support structures. The beam line is the thin magenta line entering from the bottom, the scattering chamber is the magenta and brown column in the middle of the figure, parts of the SHMS structure can be seen on the upper right, and the cryogen service infrastructure is on the lower left. For E11-107 we plan to use only the front layer of LAD to detect the recoil protons.

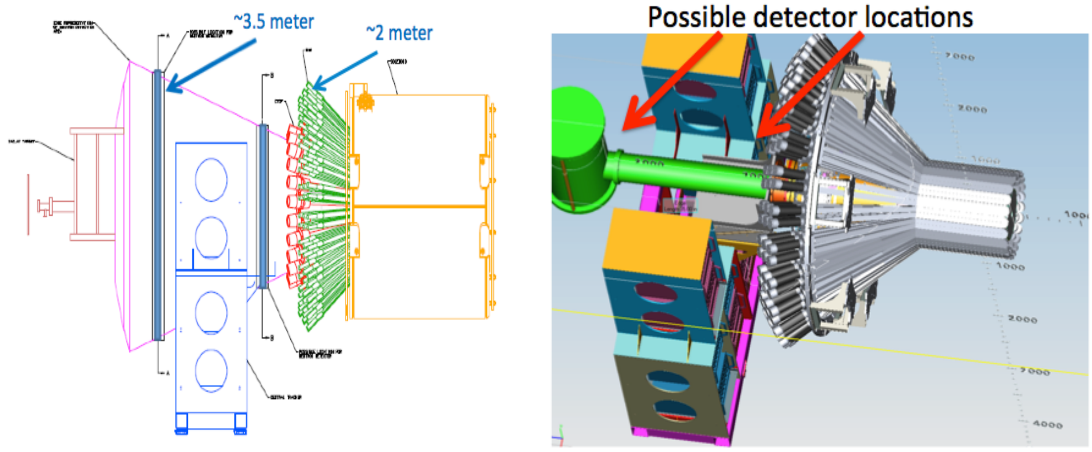

Fig. B.4: The preliminary design of the experimental setup for CLAS12+BAND. The left figure shows an elevation view of equipment racks (blue outline), light guides and phototubes of the central detectors (green and red), and the outside of the solenoid magnet (orange). Possible locations of the BAND detector are shown in solid blue. The right side shows the cryogenic system and beamline (green), the central detectors, light guides and PMTs (gray), and the equipment racks. The solenoid magnet is not shown. Red arrows indicate the possible BAND locations.

Appendix-C: Popular Presentation of EMC / SRC Studies

"The EMC Effect Still Puzzles After 30 Years",
D. Higinbotham, G.A. Millar, O. Hen and K. Rith, CERN Cour. ***53/4****, 35 (2013).*

INTERNATIONAL JOURNAL OF HIGH-ENERGY PHYSICS

CERNCOURIER

VOLUME 53 NUMBER 4 MAY 2013

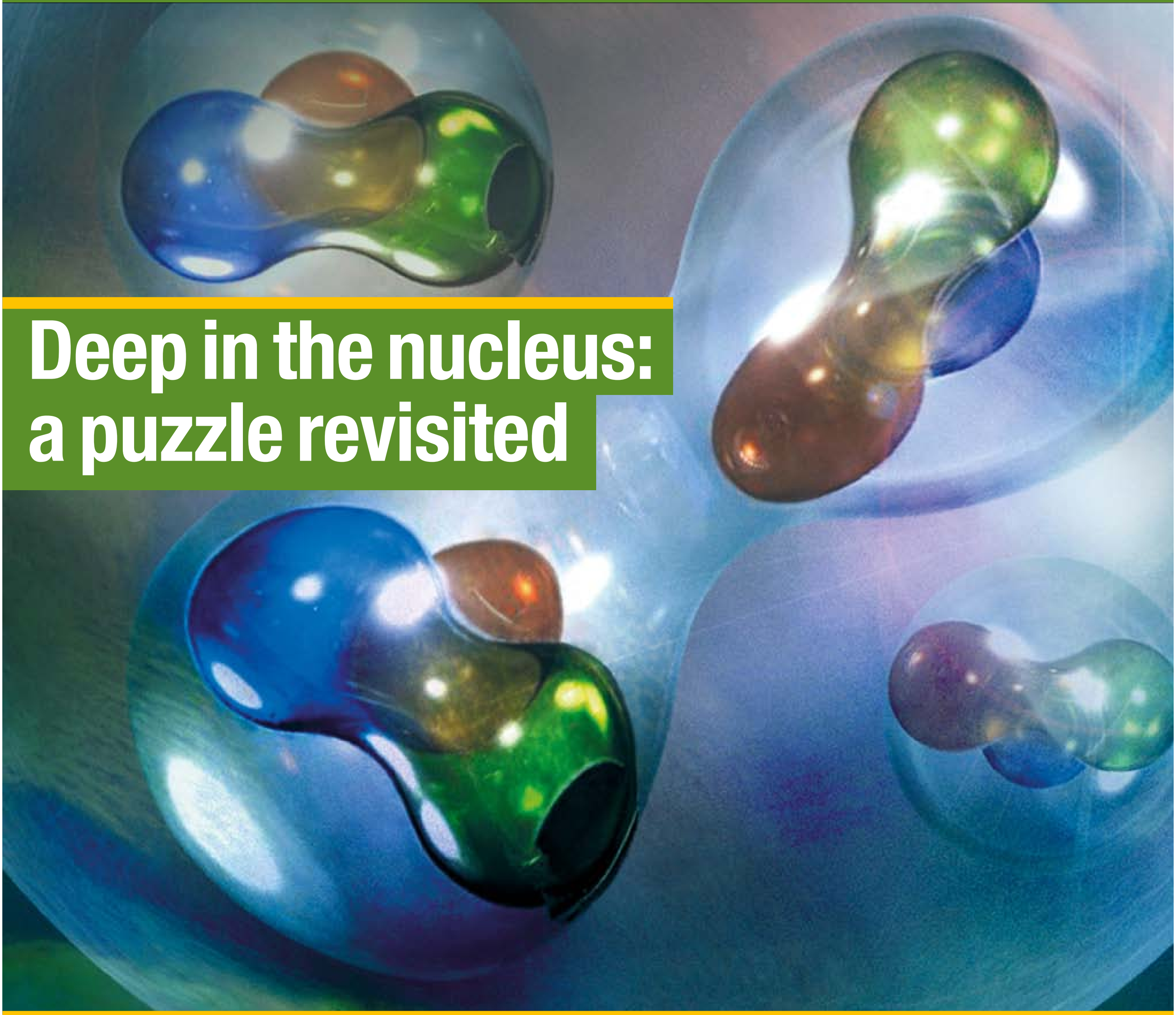

Deep in the nucleus: a puzzle revisited

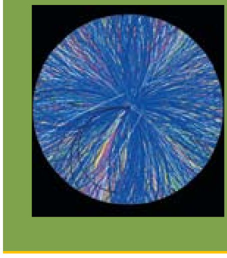

HEAVY IONS

The key to finding out if a collision is head on **p31**

ASTROWATCH

Planck reveals an almost perfect universe **p12**

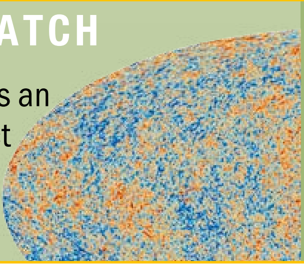

IT'S A HIGGS BOSON

The new particle is identified **p21**

The EMC effect still puzzles after 30 years

Thirty years ago, high-energy muons at CERN revealed the first hints of an effect that puzzles experimentalists and theorists alike to this day.

Contrary to the stereotype, advances in science are not typically about shouting “Eureka!”. Instead, they are about results that make a researcher say, “That’s strange”. This is what happened 30 years ago when the European Muon collaboration (EMC) at CERN looked at the ratio of their data on per-nucleon deep-inelastic muon scattering off iron and compared it with that of the much smaller nucleus of deuterium.

The data were plotted as a function of Bjorken-x, which in deep-inelastic scattering is interpreted as the fraction of the nucleon’s momentum carried by the struck quark. The binding energies of nucleons in the nucleus are several orders of magnitude smaller than the momentum transfers of deep-inelastic scattering, so, naively, such a ratio should be unity except for small corrections for the Fermi motion of nucleons in the nucleus. What the EMC experiment discovered was an unexpected downwards slope to the ratio (figure 1) – as revealed in *CERN Courier* in November 1982 and then published in a refereed journal the following March (Aubert *et al.* 1983).

This surprising result was confirmed by many groups, culminating with the high-precision electron- and muon-scattering data from SLAC (Gomez *et al.* 1994), Fermilab (Adams *et al.* 1995) and the New Muon collaboration (NMC) at CERN (Amaudruz *et al.* 1995 and Arneodo *et al.* 1996). Figure 2 shows representative data. The conclusions from the combined experimental evidence were that: the effect had a universal shape; was independent of the squared four-momentum transfer, Q^2; increased with nuclear mass number A; and scaled with the average nuclear density.

A simple picture

The primary theoretical interpretation of the EMC effect – the region $x > 0.3$ – was simple: quarks in nuclei move throughout a larger confinement volume and, as the uncertainty principle implies, they carry less momentum than quarks in free nucleons. The reduction of the ratio at lower x, named the shadowing region, was attributed either to the hadronic structure of the photon or, equivalently, to the overlap in the longitudinal ▷

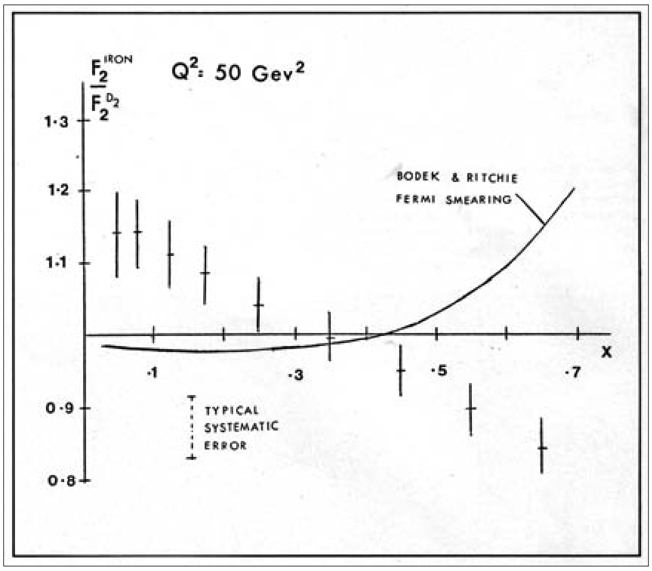

Fig. 1. A plot of the EMC data as it appeared in the November 1982 issue of CERN Courier. *This image nearly derailed the highly cited refereed publication (Aubert* et al. *1983) because the editor argued that the data had already been published.*

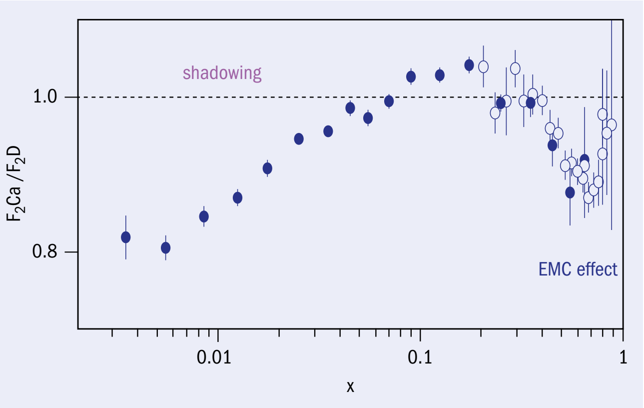

Fig. 2. The ratio of the deep-inelastic cross-sections of calcium (Ca) to that of deuterium (D) from NMC (solid circles) and SLAC (open circles). The downward slope from $0.3 < x < 0.7$ and subsequent rise from $x > 0.7$ is a universal characteristic of EMC data and has became known as the EMC effect. The reduction of the ratio at lower values of x, where valence quarks should no longer play a significant role, is known as the shadowing region.

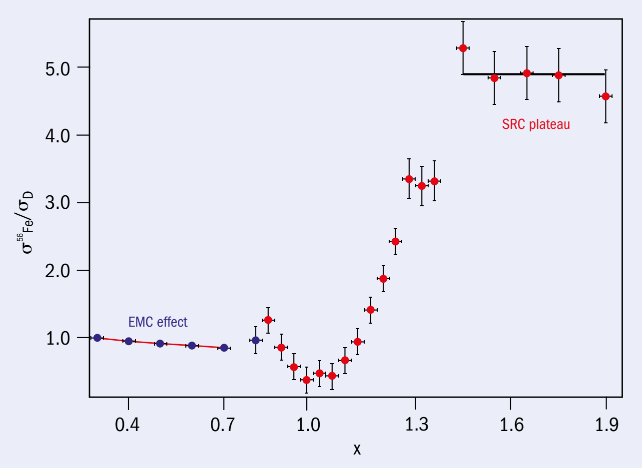

Fig. 3. While figure 2 focuses on lower values of x, this focuses on the valence-quark region. In this region, the slope of the EMC effect in the region $0.3 < x < 0.7$ and the $x > 1$ plateaux from nucleon–nucleon short-range correlation (SRC) can be clearly seen. Both the EMC effect and the plateaux are more or less independent of Q^2, while the dip at $x = 1$ fills in as Q^2 increases.

direction of small-x partons from different nuclei. These notions gave rise to a host of models: bound nucleons are larger than free ones; quarks in nuclei move in quark bags with 6, 9 and even up to 3A quarks, where A is the total number of nucleons. More conventional explanations, such as the influence of nuclear binding, enhancement of pion-cloud effects and a nuclear pionic field, were successful in reproducing some of the nuclear deep-inelastic scattering data.

It was even possible to combine different models to produce new ones; this led to a plethora of models that reproduced the data (Geesaman *et al.* 1995), causing one of the authors of this article to write that "EMC means Everyone's Model is Cool". It is interesting to note that none of the earliest models were that concerned with the role of two-nucleon correlations, except in relation to six-quark bags.

The initial excitement was tempered as deep-inelastic scattering became better understood and the data became more precise. Some of the more extreme models were ruled out by their failure to match well known nuclear phenomenology. Moreover, inconsistency with the baryon-momentum sum rules led to the downfall of many other models. Because some of them predicted an enhanced nuclear sea, the nuclear Drell-Yan process was suggested as a way to disentangle the various possible models. In this process, a quark from a proton projectile annihilates with a nuclear antiquark to form a virtual photon, which in turn becomes a leptonic pair (Bickerstaff *et al.* 1984). The experiment was done and none of the existing models provided an accurate description of both sets of data – a challenge that remains to this day (Alde *et al.* 1984).

New data

A significant shift in the experimental understanding of the EMC effect occurred when new data on ^{9}Be became available (Seely *et al.* 2009). These data changed the experimental conclusion that the EMC effect follows the average nuclear density and instead suggested that the effect follows local nuclear density. In other words, even in deep-inelastic kinematics, ^{9}Be seemed to act like two alpha particles with a single nearly free neutron, rather than like a collection of nucleons whose properties were all modified.

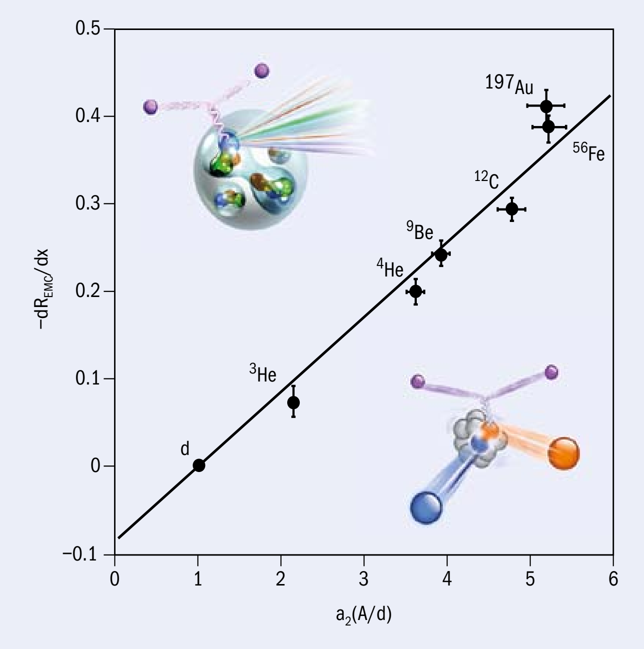

Fig. 4. The slope of the EMC effect, dR/dx for $0.3 < x < 0.7$ with $R = F_2^A/F_2^D$, versus the magnitude of the observed $x > 1$ plateaux, denoted as a_2, for various nuclei. For data that were taken by completely different groups, the linearity is striking and has caused renewed interest in understanding the cause of both effects. The inset drawings illustrate the kinematic difference of deep-inelastic EMC-effect scattering and the scattering from a correlated pair in $x > 1$ kinematics.

This led experimentalists to ask if the $x > 1$ scaling plateaux (*CERN Courier* November 2005 p37) that have been attributed to short-range nucleon–nucleon correlations – a phenomenon that is also associated with high local densities (*CERN Courier* January/February 2009 p22) – could be related to the EMC effect. Figure 3 shows the kinematic range of the EMC effect together with the $x > 1$ short-range correlation (SRC) region. While the dip at $x = 1$ has been shown to vary rapidly with Q^2, the EMC effect and the magnitude of the $x > 1$ plateaux are basically constant within the Q^2 range of the experimental data. Plotting the slope of the EMC effect, $0.3 < x < 0.7$, against the magnitude of scaling $x > 1$ plateaux for all of the available data, as shown in figure 4, revealed a striking correlation (Weinstein *et al.* 2011). This phenomenological relationship has led to renewed interest in understanding how strongly correlated nucleons in the nucleus may be affecting the deep-inelastic results. ▷

A significant shift in experimental understanding occurred when new data on ^{9}Be became available

Anniversary

In February 2013, on nearly the 30th anniversary of the EMC publication, experimentalists and theorists came together at a special workshop at the University of Washington Institute of Nuclear Theory to review understanding of the EMC effect, discuss recent advances and plan new experimental and theoretical efforts. In particular, an entire series of EMC and SRC experiments are planned for the new 12 GeV electron beam at Jefferson Lab and analysis is underway of new Drell-Yan experimental data from Fermilab.

A new life

Although the EMC effect is now 30 years old, the recent experimental results have given new life to this old puzzle; no longer is Every Model Cool. Understanding the EMC effect implies understanding how partons behave in the nuclear medium. It thus has far-reaching consequences for not only the extraction of neutron information from nuclear targets but also for understanding effects such as the NuTeV anomaly (*CERN Courier* September 2009 p9) or the excesses in the neutrino cross-sections observed by the MiniBooNe experiment (*CERN Courier* May 2007 p8).

● Further reading

For more about the workshop at the University of Washington Institute of Nuclear Theory, see www.int.washington.edu/PROGRAMS/13-52w/.

A Adams *et al.* 1995 *Z. Phys. C* **67** 403.
D Alde *et al.* 1990 *Phys. Rev. Lett.* **64** 2479.
P Amaudruz *et al.* 1995 *Nucl. Phys.* **B441** 3.
M Arneodo *et al.* 1996 *Nucl. Phys.* **B481** 3.
J J Aubert *et al.* 1983 *Phys. Lett. B* **123** 275.
R Bickerstaff *et al.* 1984 *Phys. Rev. Lett.* **53** 2532.
D F Geesaman *et al.* 1995 *Ann. Rev. Nucl. Part. Phys.* **45** 337.
J Gomez *et al.* 1994 *Phys.Rev. D* **49** 4348.
J Seely *et al.* 2009 *Phys. Rev. Lett.* **103** 202301.
L Weinstein *et al.* 2011 *Phys. Rev. Lett.* **106** 052301.

Résumé

L'effet EMC, encore une énigme 30 ans après

Il y a trente ans, les membres de la collaboration EMC (Collaboration européenne du muon) au CERN découvraient un effet inattendu en rapportant leurs mesures de la diffusion profondément inélastique du muon au nombre de nucléons : les fonctions de structure étaient différentes s'agissant du fer et s'agissant du deutérium, qui est un noyau beaucoup plus léger. En représentant le rapport fer/deutérium en fonction de la fraction de l'impulsion du nucléon portée par le quark frappé, les expérimentateurs ont découvert une pente descendante inattendue. Ce résultat surprenant a été confirmé par de nombreux groupes, mais il reste une énigme. Des données récentes sur le ^{9}Be ont relancé l'intérêt pour cette question, en montrant que des corrélations nucléon-nucléon à courte distance pouvaient être liées à l'effet EMC.

Douglas Higinbotham, Jefferson Lab, **Gerald A Miller**, University of Washington, **Or Hen**, Tel Aviv University, and **Klaus Rith**, University of Erlangen-Nürnberg.

תקציר

האינטראקציה בין נוקלאונים הקשורים בגרעין האטום נקבעת ברובה על ידי מאפייני הכוח הגרעיני החזק. לאורך המאה הקודמת הושקע מאמץ אדיר בחקר תכונותיו של הכוח הגרעיני החזק והאופן בו הוא יוצר גרעינים יציבים וקובע את מאפייניהם. למרות מאמץ זה, נצבר ידע מוגבל לגבי אופיו של הכוח הגרעיני החזק במרחקים הקצרים ביחס לגודל הנוקלאון.

בשנים האחרונות, עם התפתחותם של מאיצי אלקטרונים ופרוטונים באנרגיה וזרם גבוהים, ניתן היה לחקור לראשונה באופן ניסיוני וישיר את המבנה קצר הטווח, גבוה התנע, של הגרעין. תוצאות ממדידות אלו, וחישובים תאורטיים משלימים, מראים כי בין נוקלאונים הנמצאים במרחק יחסי קצר יש אינטראקציה קצרת טווח חזקה, היוצרת זנב בעל תנע גבוה לפונקציית הגל הגרעינית. זנב זה מתחיל באזור תנע פרמי של הגרעין, k_F, וממשיך מעבר אליו לתנע גבוה יותר. יצירת זנב זה, כתוצאה מאינטראקציות קצרות טווח חזקות, הנו מאפיין אוניברסלי של מערכות פרמיוניות בעלות 2 רכיבים. מכיוון שלנוקלאונים מבנה הפנימי, ישנה אפשרות שמבנה זה משתנה כאשר המרחק בין מרכזיהם קטן מהרדיוס שלהם כך שישנה חפיפה גדולה בין התפלגות הקוורקים שלהם. הבנה זו של השפעתה של האינטראקציה קצרת הטווח של הכוח הגרעיני החזק משנה את תפיסתנו לגבי מבנה הגרעין והתפקיד אותו ממלאים זוגות נוקלאונים קצרי טווח במערכות גרעיניות ובתהליכים אסטרופיזיקליים.

עבודה זו דנה בזוגות קורלטיביים במרחק קצר בגרעינים כבדים. העבודה מורכבת מ- 2 חלקים עיקריים: (1) חקר ניסיוני של זוגות קורלטיביים במרחקים קצרים בגרעיני פחמן, אלומיניום, ברזל ועופרת (^{12}C, ^{27}Al, ^{56}Fe, ^{208}Pb). ו- (2) חקר פנומנולוגי של ההשפעה של זוגות אלו על: פיזור אינלסטי עמוק (Deep-Inelastic Scattering),תהליכי זיווג ומבנה גרעינים, חומר גרעיני, וכוכבי ניטרונים, ואינטראקציות מגע (Contact Interactions) במערכות פרמיונויות בעלות אינטראקציה חזקה.

בחלק הניסיוני מדווחות תוצאות ממדידת שליפת נוקלאון בודד וזוג נוקלאונים מגרעיני פחמן, אלומיניום, ברזל ועופרת. המדידות נעשה תוך שימוש בגלאי CLAS (CEBAF Large Acceptance Spectrometer) במעבדת ג'פרסון שבארה"ב. הקינמטיקה שנבחרה לניסוי מאופיינת על-ידי מעבר תנע גבוה, פרמטר x_B גדול מ-1, ותנע חסר גבוה, ונשלטת על ידי פיזור מזוגות קורלטיביים במרחק קצר. התוצאות ממדידות אלו מהוות גילוי ישיר ראשון של קורלציות קצרות טווח בגרעינים הכבדים מפחמן, וכוללות קביעה של היחס של מספר הזוגות פרוטון-פרוטון לזוגות פרוטון-ניטרון בגרעינים שנמדדו, וקביעת השקיפות הגרעינית של גרעינים אלו לפרוטון שנשלף באנרגיה גבוה מפירוק זוג קורלטיבי.

בחלק הפנומנולוגי מדווחות תוצאות של בחינת השפעת התוצאות הניסיוניות על מגוון רחב של מערכות שונות. מחקר זה כולל את הקשר שבין כמות הזוגות קורלטיביים במרחק קצר בגרעינים והחוזק של אפקט ה- EMC (יחס פונקציית המבנה הלא אלסטית של נוקלאונים הקשורים לגרעין וזה של נוקלאונים הקשורים בדאוטריום) בגרעינים אלו; קביעת חוזק אפקט ה- IMC (יחס פונקציית המבנה הלא אלסטית של נוקלאונים הקשורים בדאוטריום לזוג פרוטון-ניטרון חופשי) וקביעה של פונקציית המבנה של ניטרון חופשי; אילוץ פרמטרים חופשיים במודלים של שינוי במבנה של נוקלאונים המשמשים באנליזות גלובליות של כרומודינאמיקה קוונטית וקביעת חסם על יחס קוורקים d/u בפרוטון; בחינה של מנגנוני זיווג של נוקלאונים בגרעין וקביעה של המספרים הקוונטים של זוגות נוקלאונים בגרעין בעלי יכולת לעבור למצב של קורלציה קצרת טווח; השפעת זוגות קורלטיביים במרחק קצר על אנרגיה האסימטריה הקינטית של חומר גרעיני, אנרגיית האסימטריה הגרעינית, משוואת מצב של כוכבי ניטרונים, ותכונות אוניברסליות של אינטראקציות מגע במערכות פרמיוניות בעלות אינטראקציה חזקה.

לתוצאות המוצגות בעבודה זו השלכות רחבות להבנת המבנה ותהליכי חלוקת אנרגיה במערכות גרעיניות אסימטריות כבדות, והיוו בסיס לפיתוח תכנית ניסויים עתידית המורכבת מ- 3 ניסויים שאושרו לרוץ במעבדת המאיץ Jefferson שבארה"ב לאחר שדרוג המאיץ של המעבדה לאנרגיה של 12 ג'יגה אלקטרון-וולט.

TEL AVIV UNIVERSITY אוניברסיטת תל-אביב

נוקלאונים בעלי תנע גבוה בגרעין

חיבור זה הוגש כחלק מן הדרישות
לשם התואר "דוקטור לפילוסופיה"

על ידי

אור חן

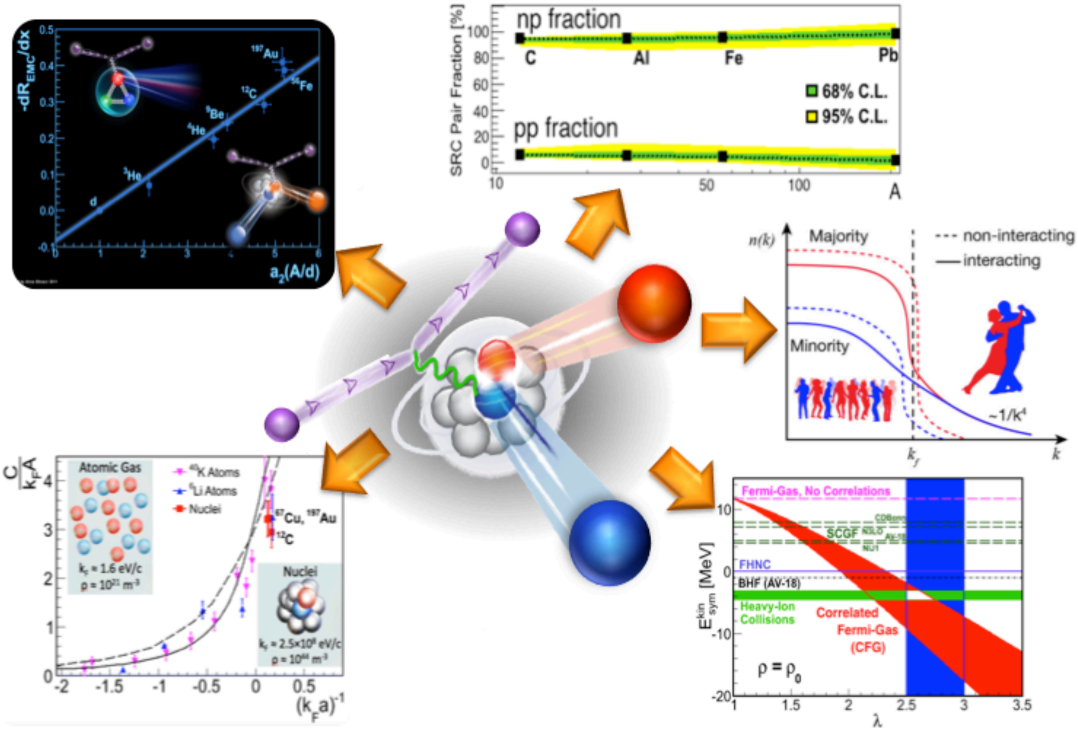

הוגש לסנאט של אוניברסיטת תל-אביב
אוקטובר 2015

המחקר נערך תחת הנחייתו של
פרופסור אלי פיאסצקי